# The Detection of Antibiotic Drugs in Aquatic Environments: Developing Sensitive Electrochemical Sensors Engineered from Transition Metal Dichalcogenides, Spinels, and Advanced Carbon Materials

Maynooth University
National University of Ireland Maynooth

A thesis submitted to Maynooth University in fulfilment of the requirements for the degree of

**Doctor of Philosophy**

**By**

**Yiran Luo, M.Sc.**

Department of Chemistry
Maynooth University
Maynooth
Co. Kildare

**December 2025**

**Research Supervisor: Prof. Carmel B. Breslin**
**Dr. Eithne Dempsey**
**Head of Department: Dr. Diego Montagner**

# Table of Contents

# Declaration

I hereby certify this thesis has not been submitted before, in whole or part, to this or any other university for any degree, and is, except where stated otherwise, the original work of the author.

Signed 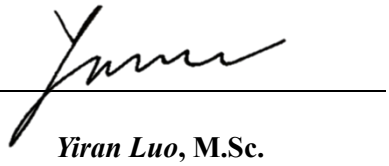 Date 11/11/2025

***Yiran Luo*, M.Sc.**

# Acknowledgements

This is a journey from fearing the unknown to feeling exhilaration and joy at the uncharted path to the future. Time has flown by so swiftly that only when we realise it must end do we perceive so many regrets and things worth cherishing. Delight thankful to my supervisor Prof. Carmel B. Breslin. As an amazing P.I., Prof. Carmel Breslin her patient advice, high standards, and steady encouragement shaped this work from the start to the end. I am grateful to my co-supervisor Dr. Eithne Dempsey and my progression meeting's examiners Prof. John G. McCaffrey, Prof. John P. Lowry, and Dr. Robert Elmes for their time and nice feedback. Their comments helped me improve the study and clarify my ideas. I also thank the internal and external examiners for reading the thesis and offering valuable suggestions.

This project would not have been possible without financial and institutional support. I thank Maynooth University and the Science Foundation Ireland (SFI) and Research Ireland for funding and resources. Access to core facilities and training made a real difference to the quality of the results. I also thank the technical and administrative staff for their reliable support with instruments, safety, and purchasing.

Tara Barwa, thanks for your all-interesting chats and accompany; your messages, late-night calls and all the delicious food we had in different restaurants kept me going when the work was hard. To my fellow postdoc Dr. Rupa and Dr. Dani and all my colleagues (who I am not going to name individually for fear of omitting anyone), thanks for all the help and make me feel that these four years were accomplished in a pleasant and warm group.

Thanks to all the technical staffs for all your kind help! Thanks to Mr. Noel Williams, without your help, my computer would not function properly, not to mention your

invaluable support with other experimental equipment and, most crucially, your timely intervention to salvage all my data before my USB drive dead. Karen, thanks for your kind help with the SEM and EDX measurements. To Donna, Carol and Barbara, thanks for your kind help when encountering some problems. To Anne, Orla and Michelle, thanks for your kind help during my time demonstrating. To the research analysts at Bernal Insitute, University of Limerick, thanks for your kind help with the XRD, XPS, and Raman. Also, thanks to my friend Liu bin for your instruction and assistance in drawing molecular structure images and software.

To my dear friend Nuriye•Nurlan, thank you for your patience and constant encouragement. Though time differences and distance separate us physically, they draw our hearts ever closer, making us each other's most steadfast and warmest support. I would also like to extend my best wishes to my dear friend Xu Qian, hoping she will successfully become Dr. Xu in June 2026. We shall celebrate this wonderful moment together.

Finally, to the best mother and father for me, with all my love and pride. Your love, trust, and sacrifices give me the strength to complete this journey. This thesis is dedicated to them.

To all of us: May the Mother Goddess thrice close her eyes for you, keeping your blood eternally pulsing. May your journey be forever peaceful and your schemes forever concealed.
Farewell and May this journey lead us starward.
Ends, then begins.

# Abstract

With the rapid advancement of global healthcare and economic development, the antimicrobial resistance (AMR) and antibiotic-residue contamination in aquatic environments and their implications for human health have become a critical issue worldwide. Consequently, the development of highly efficient, sensitive and field-deployable analytical techniques for determining antibiotic concentrations in water bodies has become more crucial than ever before, particularly for rapid screening in complex environmental matrices.

In this thesis, a series of highly sensitive, selective electrochemical sensors with excellent long-term stability for Metronidazole (MTZ), Sulfanilamide (SFD), Flutamide (FLD), Sulfamerazine (SRZ), and Sparfloxacin (SPAR) were developed, addressing the overall research question of whether structurally tunable hybrid interfaces can provide sensitive, selective, and stable antibiotic detection across multiple analytes. The sensors involved modifying glassy carbon electrodes (GCE), screen-printed electrodes (SPE), and carbon cloth (CC) with diverse catalyst materials to increase surface area, improve electron transfer and ensure stability, with a comparative design strategy spanning laboratory and deployable electrode formats. The sensors were then used to detect antibiotics in real aquatic environments and in artificial urine, thereby evaluating practical matrix compatibility and selectivity beyond ideal electrolyte systems.

These nanocomposites incorporate two-dimensional transition metal dichalcogenides (TMDs), spinel oxides, and carbon-based materials (reduced graphene oxide (rGO), carbon particles (CPs), and carbon nanofibres (CNFs)), and the novelty of this thesis lies in systematically comparing how these TMD/spinel/carbon materials, prepared via simplified and partially green processing routes, control electroanalytical performance across different targets and electrode substrates.

Excellent results were achieved in electrochemical detection experiments: (1) Exfoliated molybdenum disulfide ($MoS_2$) demonstrated detection of MTZ across an exceptionally broad range from 40 nM to 2000 μM, addressing the Chapter 3 question

of whether exfoliated $MoS_2$ can deliver high sensitivity and wide-range MTZ detection; (2) Reduced graphene oxide/graphite (rGO/G) demonstrated superior performance to pure reduced graphene oxide, and an impressive limit of detection (LOD) of 86 nM was achieved for SFD, addressing the Chapter 4 question of whether rGO/G coupled with exfoliated $MoS_2$ can improve SFD sensing; (3) Carbon particles (CPs) and tungsten disulfide ($WS_2$) platelets synergistically detected FLD with an LOD of 0.74 nM, addressing the Chapter 5 question of CPs-$WS_2$ interfacial synergy for FLD electroanalysis; (4) Cerium oxide ($CeO_2$) nano-powders sprinkled over the spinel provided excellent stability and the LOD for SRZ was 13.8 nM, addressing the Chapter 6 question of stable and selective SRZ sensing using a $CeO_2$/spinel/$WS_2$; and (5) a novel sustainable spinel was synthesised and applied to two distinct electrodes, giving LODs of 49.0 nM with cerium ferrite ($CeFe_2O_4$) spinel oxide supported by CNFs on GCE and 14.0 nM when immobilised on CC, addressing the Chapter 7 question of transferable SPAR detection on conventional and flexible substrates.

Moreover, these composites not only detect these diverse antibiotics in water but also maintain selectivity towards corresponding antibiotics when deployed in complex real-world aquatic environments, demonstrating the practical potential of rationally engineered TMDs/spinel/carbon materials electrochemical platforms for environmental pharmaceutical monitoring.

# Chapter 1 Introduction and Literature Review

# 1.1. Research Background and Motivation

## 1.1.1. Significance of Aquatic Environments

Aquatic ecosystems represent indispensable environmental components that support tremendous biodiversity and provide essential ecosystem services [1], [2], [3]. These systems encompass marine ecosystems (covering over 70 % of Earth's surface and accounting for more than 97 % of Earth's water supply) and freshwater ecosystems (including systems like lakes, ponds, rivers, streams, and wetlands) [4], [5], [6]. Aquatic environments perform crucial environmental functions, including nutrient recycling [7], water purification [8], flood attenuation [9], groundwater recharge [5], and wildlife habitat provision [7]. The self-purification capacity of aquatic ecosystems relies on diverse biota, including microorganisms, phytoplankton, aquatic plants, invertebrates, and fish that collectively participate in organic matter destruction and water filtration processes [10], [11], [12]. These ecosystems also hold immense value for human recreation, tourism, religious practices, and scientific education, making their protection a paramount global priority [7], [13].

Water is a core part of the human habitat. It supports the survival and growth of society. Rapid industrial and economic development, together with population growth, has led to heavy discharges of domestic sewage, industrial and agricultural wastewater, and solid waste into rivers and lakes [11]. As a result, global ecosystems have deteriorated [14]. Pollution incidents now occur often and threaten public health. Ensuring clean and safe water, especially drinking water, has become a significant challenge.

Pollutants in aquatic systems are usually grouped as inorganic, organic, and microbial. Typical organic pollutants include pesticides, nitrophenols, and antibiotics [15]. When these compounds build up, they harm water quality and damage ecosystems, with risks

to human health. Many methods are used to remove them, such as physical, chemical, and biological treatments [16]. Yet complete removal is difficult. Even at low levels, organic pollutants can remain toxic. They can also accumulate in the body and trigger acute or chronic illness, including reproductive, neurological, and immune disorders, and even cancer [17]. Long-term exposure to low concentrations therefore threatens both ecological security and human health.

### 1.1.2. Application and Importance of Antibiotic Drugs

Antibiotics are a class of secondary metabolites produced by microorganisms (including bacteria, fungi, and actinomycetes) or higher plants and animals during their life processes [18]. These substances possess antimicrobial or other biological activities and can interfere with the developmental functions of other living cells. The history of antibiotics dates back to the early 20$^{th}$ century, but it was not until 1928 that a revolutionary discovery was made [18]. The first antibiotic to be isolated was penicillin, discovered by Alexander Fleming in 1928 in the natural substances produced by the Penicillium fungus. In 1939, Gerhard Domagk discovered sulfonamide drugs, which were used to treat various infections caused by streptococci [19]. In the following years, Fleming and his colleagues, including Howard Florey and Ernst Boris Chain, conducted further research, ultimately developing penicillin into an effective medicinal form by 1940. This discovery completely revolutionised the medical community's approach to treating bacterial infections. Penicillin, with its broad-spectrum antibacterial activity and minimal side effects, quickly became the drug of choice for treating bacterial infections [20]. Meanwhile, other antibiotics were discovered at different times. For example, in 1943, Selman Waksman, a researcher of Gram-positive bacteria, discovered Streptomycin, which was later found to be effective against Mycobacterium Tuberculosis, making it one of the most important antibiotics in clinical practice. Additionally, tetracycline was first discovered in 1949 and widely used as a broad-spectrum antibiotic [18], [20].

Antibiotics represent powerful medications that treat bacterial infections by either killing bacteria (bactericidal) or preventing their multiplication (bacteriostatic) [21]. These pharmaceutical agents function through multiple mechanisms including inhibition of cell wall biosynthesis (Penicillins, Cephalosporins), modification of membrane permeability, disruption of protein synthesis (Macrolides, Tetracyclines), and suppression of genetic material replication (Fluoroquinolones) [22], [23]. Since the landmark discovery of penicillin by Alexander Fleming, antibiotics have fundamentally transformed modern medicine, significantly reducing mortality from bacterial infections and enabling advanced medical procedures including surgery, chemotherapy, and organ transplantation. Beyond human medicine, antibiotics are extensively employed in veterinary practices and animal husbandry for disease prevention and growth promotion, contributing substantially to global food security [24]. The classification of antibiotics encompasses numerous structural classes, including Penicillins, Macrolides, Cephalosporins, Fluoroquinolones, Tetracyclines, and Aminoglycosides, each with distinct antibacterial spectra and clinical applications [18], [21]. The antibiotics used in this research are outlined below.

***Metronidazole (MTZ)*:** Metronidazole (MTZ; structure shown in Fig. 1.1) is a nitroimidazole drug. It is widely used for its anti-inflammatory and antimicrobial effects. Doctors prescribe it for infections caused by Helicobacter pylori [25], Giardia lamblia, and Trichomonas vaginalis [26]. It also treats oral and dental infections, respiratory tract infections, and Crohn's disease [27]. MTZ is used in both human and veterinary medicine. However, it has genotoxic and mutagenic risks. Long-term or excessive use may lead to leucopenia, peripheral neuritis, and even cancer [28]. Because MTZ is highly soluble and stable in water, it can persist in aquatic systems. High concentrations have been detected in urban water supplies [29], posing risks to people, animals, and aquatic life.

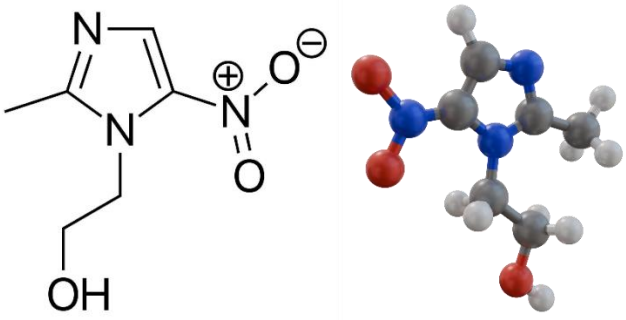


**Figure 1.1.** The molecular structure of MTZ.

***Sulfanilamide (SFD):*** Sulfanilamide (SFD; structure shown in Fig. 1.2) is a notable sulfonamide. It treats bacterial infections and acts as a key intermediate during the breakdown of other widely used sulfonamides [30]. Historically, SFD was among the first drugs to show broad-spectrum activity against bacterial disease. Today, it is more often found in newer formulations derived from the parent compound [31][32], [33]. Beyond medicine, SFD is used in dye synthesis and appears as the main residual product when azo dyes degrade, making its detection in water especially important [34][35].

These concerns have led to a strong interest in methods for measuring sulfonamides in aquatic systems. Chromatographic and spectrophotometric techniques are widely applied [36]. A simpler and more cost-effective option is electrochemical sensing. With suitable electrocatalysts, such sensors achieve low detection limits and wide linear ranges, enabling the quantification of antibiotics and other antimicrobials [37][38].

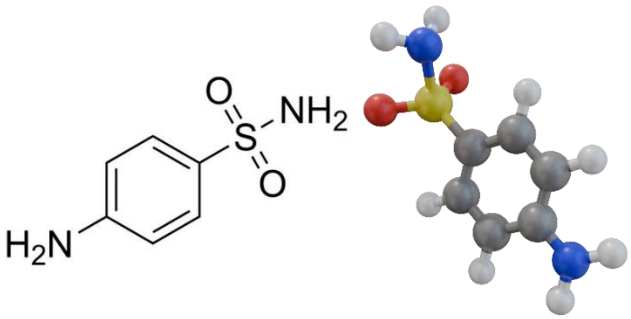


**Figure 1.2.** The molecular structure of SFD.

***Flutamide (FLD):*** Flutamide (FLD; structure shown in Fig. 1.3), 4-nitro-3-trifluoromethyl-isobutylaniline. It has been widely used to effectively control the growth and spread of prostate cancer [39]. It is also employed in the treatment of polycystic ovary syndrome [40]. However, with its significant use in the healthcare sector, and its ineffective removal from wastewater treatment plants, it has been detected in the aquatic ecosystem [41]. Anticancer drugs, such as FLD, can be extremely toxic, and this is alarming in terms of the health of aquatic species, impacting on their reproductive endocrine systems [42], [43]. FLD sensors have previously been reported, including sensors fabricated from different oxide phases, such as nickel oxides [43], molybdenum oxides [44], and cobalt oxides [45], [46], [47], [48], and various sensors that employ graphene or reduced graphene oxide [49], [50], [51].

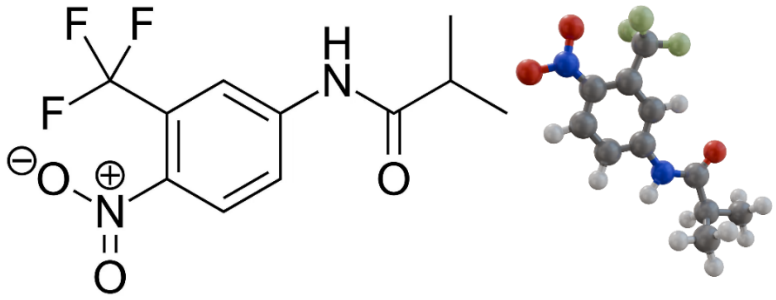


**Figure 1.3.** The molecular structure of FLD.

***Sulfamerazine (SRZ):*** Sulfamerazine (SRZ; structure shown in Fig. 1.4) is a sulfonamide antibiotic that is used extensively to treat bacterial infections and promote animal growth. Like other antibiotics, it has been detected in aquatic environments [52], [53], threatening the ecological health of essential eco-systems, and contributing to the emergence of antibiotic resistance. Indeed, concentrations as high as 4.3 μg $L^{-1}$ have been detected in lakes [54]. This is becoming even more of a concern as the production and use of antibiotics continue to increase each year. With the quality of aquatic environments deteriorating at an alarming rate, there is a clear need for simple and sensitive analytical devices that are capable of detecting antibiotics, such as SRZ.

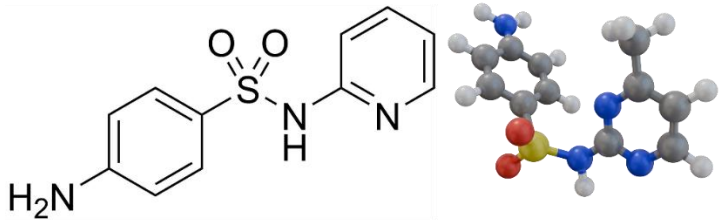


**Figure 1.4.** The molecular structure of SRZ.

***Sparfloxacin (SPAR):*** Sparfloxacin (SPAR; structure shown in Fig. 1.5), a well-known third-generation fluoroquinolone, has a broad spectrum of antibacterial action, making it widely used in veterinary medicine [55]. SPAR and other fluoroquinolone family members are attracting increasing attention due to their growing presence in aquatic environments. This can have detrimental effects on all aquatic life [55], [56]. SPAR has been detected in various aquatic environments, reaching levels of 2.4 μg $L^{-1}$ in India [57], and ranging from 0.99 to 9.66 μg $L^{-1}$ elsewhere [58]. Moreover, higher levels of SPAR (17–19 μg $L^{-1}$) have been detected in wastewaters [59]. Therefore, its detection and removal from aquatic systems is becoming increasingly important in terms of both the protection of the environment and the health of the world's population.

SPAR can be detected using a range of approaches, such as the commonly used HPLC and fluorescence techniques [59], including chromatography with electrospray tandem mass spectrometry [60], and fluorescence methods [61][62].

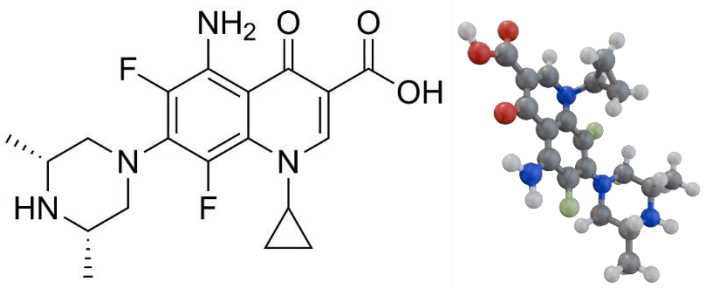


**Figure 1.5.** The molecular structure of SPAR.

A summary of all antibiotic drugs used in this thesis is presented in Table 1.1.

**Table 1.1.** The names, structures, types, therapeutic effects, and side effects of the antibiotic drugs used in this thesis.

| Antibiotic drug | Structures | Types | Detection Challenge | Uses | Side Effects | Refs. |
|---|---|---|---|---|---|---|
| Metronidazole (MTZ) | 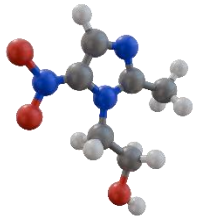 | Nitroimidazole | Low electroactivity | Bacterial infections | Nausea, a metallic taste, and headaches | [63] |
| Sulfonamide (SFD) | 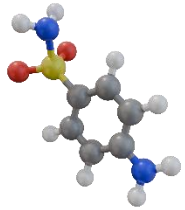 | Sulfonamides (SAs) | Organic matter interference | Bacterial infections | Gastrointestinal effects, candidiasis, dizziness and itchy skin (rash) | [64] |
| Flutamide (FLD) | 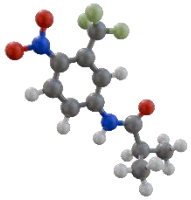 | Nonsteroidal antiandrogen (NSAA) | Sulfonamide cross-reactivity | Prostate cancer | Hot flashes, diarrhea, and sexual problems | [65] |

| | | | | | | |
|---|---|---|---|---|---|---|
| Sulfamerazine (SRZ) | 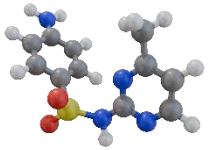 | Sulfonamides (SAs) | pH-dependent response | Bacterial infections | Nausea, vomiting, diarrhea and hypersensitivity reactions | [66] |
| Sparfloxacin (SPAR) | 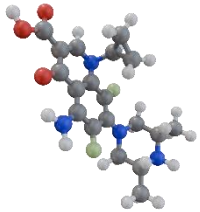 | Fluoroquinolone | Biofouling in complex matrices | Bacterial infections (respiratory infections) | Muscle or joint pain | [67] |
| Sulfapyridine (SAD) | 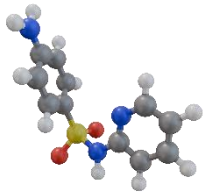 | Sulfonamides (SAs) | - (Used in interference detection) | Help control skin problem (dermatitis herpetiformis) | Fever, headache (continuing), itching, skin rash | [68] |
| Cefadroxil (CEX) | 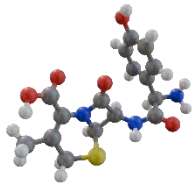 | Cephalosporin | - (Used in interference detection) | Various infections | Feeling of discomfort, fever with or without chills, flushing or redness of the skin | [69] |

### 1.1.3. Hazards of AMR and Antibiotic Residue Accumulation in Aquatic Environments

Antimicrobial resistance (AMR) gives germ-like bacteria and fungi the power to defeat the drugs designed to kill them. As a result, standard infections become harder to treat, raising the threat of severe illness and death, as presented in Scheme 1.1. Although AMR is a natural process, it is being dangerously worsened by the overuse and incorrect use of antimicrobial medicines in people, animals, and farming. The rampant overuse and inappropriate disposal of antibiotics, such as those listed in Table 1.1, have precipitated severe environmental contamination and public health crises globally [70].

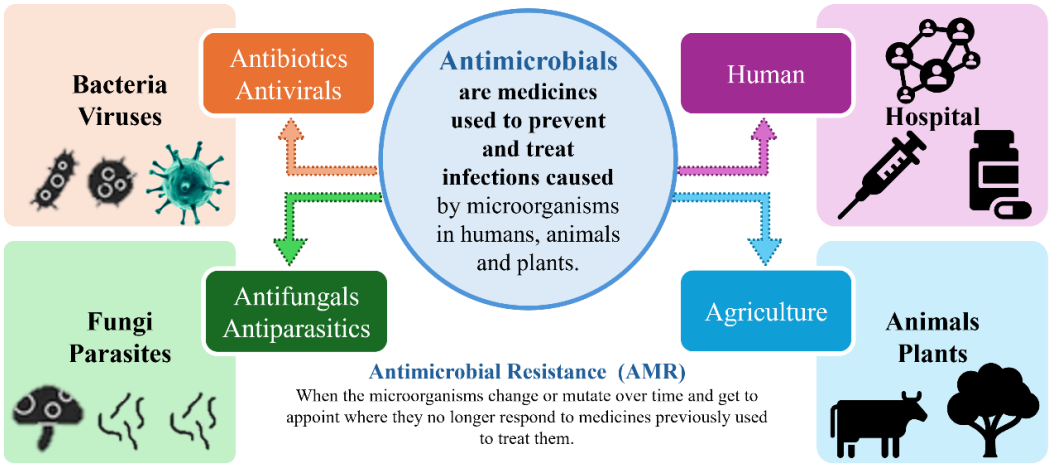


**Scheme 1.1.** Classification and scope of application of antimicrobial agents and Antimicrobial Resistance (AMR).

Antibiotic residues enter aquatic environments through multiple pathways, including hospital effluents, municipal wastewater, agricultural runoff, and pharmaceutical manufacturing discharges [71]. These residues persist in various environmental compartments, with concentrations detected from ng/L to mg/L levels in wastewater, surface waters, and even drinking water sources [72], [73]. Particular concern is the role of aquatic environments as hotspots for antibiotic resistance development, where

sub-therapeutic antibiotic concentrations selectively pressure bacteria [74], leading to the emergence and dissemination of antibiotic-resistant genes (ARGs) [75] and antibiotic-resistant bacteria (ARB) [76].

The probabilistic environmental hazard assessment conducted by the World Health Organisation (WHO), Western Pacific and South-East Asia regions identified that antibiotic concentrations in various aquatic compartments frequently exceed predicted no-effect concentrations (PNECs) for resistance selection [77]. Wastewater treatment plants and receiving waters constitute potential reservoirs, with ciprofloxacin in drinking water of the WHO Western Pacific Region (WPR) and China presenting particularly high risk (high probability of exceeding PNECs) [78]. The human health risks associated with environmental antibiotic contamination include direct toxic effects, allergic reactions, potential organ toxicity, teratogenicity, carcinogenicity, and most critically, the compromised efficacy of antibiotic therapies due to widespread resistance. Agricultural systems irrigated with contaminated water facilitate antibiotic uptake by crops, introducing these residues into the human food chain and creating additional exposure routes beyond direct water consumption, as shown in Scheme 1.2 [76], [79].

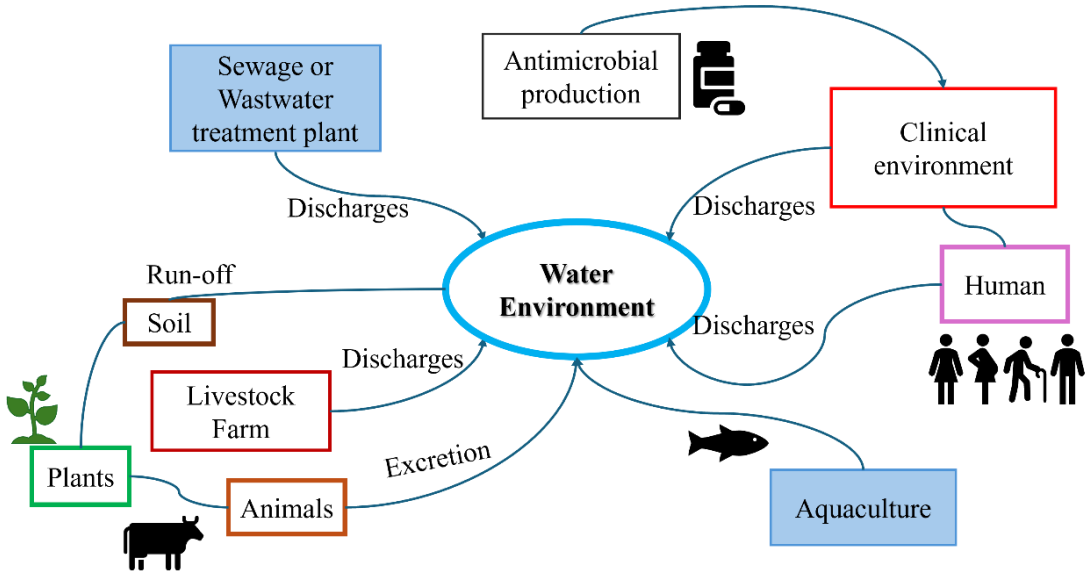


**Scheme 1.2.** Schematic diagram of antibiotic accumulation in the water cycle.

### 1.1.4. Importance of Researching and Developing Sensors for Antibiotic Detection in Water

Conventional antibiotic detection methodologies like high-performance liquid chromatography (HPLC), liquid chromatography-tandem mass spectrometry (LC-MS/MS), and enzyme-linked immunosorbent assay (ELISA) offer sensitive and selective determination but present significant limitations for routine environmental monitoring. These techniques require sophisticated instrumentation, extensive sample preparation, skilled personnel, and laboratory-based settings, rendering them impractical for rapid, on-site screening and continuous monitoring applications. The complex matrices of environmental samples further complicate analysis due to matrix interference. These limitations have stimulated intense research interest in developing alternative detection platforms that offer rapid, sensitive, cost-effective, and field-deployable solutions for antibiotic monitoring [80], [81].

Electrochemical sensors have emerged as particularly promising platforms for antibiotic detection, offering unparalleled advantages of cost-effectiveness, rapid analysis, high sensitivity, ease of operation, and miniaturization potential for portable and on-site applications. The fundamental principle of electrochemical sensors involves measuring electrical signals (current, potential, impedance) generated from redox reactions of target analytes at modified electrode surfaces.

Advanced electrode modification materials including two-dimensional transition metal dichalcogenides (TMDs) [82], spinel oxides [83], and carbon nanomaterials [35] have significantly enhanced sensor performance through increased electroactive surface area, improved electron transfer kinetics, and selective recognition capabilities. The ongoing technological evolution in this field includes the development of wearable sensors and smartphone-integrated platforms that enable real-time environmental monitoring and point-of-care testing, potentially revolutionising antibiotic detection and resistance

management strategies [38].

Sensitive detection of trace organic pollutants is essential for water monitoring and management. For these reasons, this thesis focuses on developing accurate, fast, and sensitive electrochemical sensors for the detection of antibiotic drugs. MTZ, SFD, FLD, SRZ, and SPAR, as shown in Table 1.1, represent the targeted antibiotics. In total, five electrochemical sensors were created and applied to detect these targets. The materials selected for the design of electrochemical sensors for these targets include two-dimensional (2D) transition-metal dichalcogenides, spinel oxides, and carbon materials. These materials are introduced in Section 1.2.

# 1.2. Materials Landscape for Electrochemical Antibiotic Sensing

## 1.2.1. Two-Dimensional Transition Metal Dichalcogenides (TMDs)

### 1.2.1.1. Definition, Classification, and Applications

Transition metal dichalcogenides (TMDs), abbreviated as $MX_2$ (M = Mo, W, etc.; X = S, Se, Te), have garnered significant attention from researchers worldwide due to their two-dimensional layered structure similar to graphene [84]. TMDs are held together by van der Waals forces between layers, and single-layer or multi-layer TMDs can be exfoliated from bulk materials [85]. TMDs exhibit broad application prospects in electrochemical catalysis, electrochemical sensor and energy storage, optoelectronic devices, and other fields due to their layered structure, tunable bandgaps, enabling efficient electron transfer [86].

The methods commonly employed for the synthesis of 2D TMDs include both top-down approaches (mechanical exfoliation, liquid phase exfoliation and sputtering) and bottom-up approaches (physical vapor deposition (PVD), chemical vapor deposition (CVD), atomic layer deposition (ALD) and chemical solutions) [87], [88]. Sensors based on TMDs offer low-cost and convenient solutions for detecting variable analytes, finding widespread application in fields such as biology, medicine, agriculture, food, and the petroleum industry.

Extensive research on two-dimensional transition metal dichalcogenides has shown that these 2D nanomaterials possess unique physical, chemical, and optoelectronic properties, including high mobility, excellent mechanical properties, large specific surface area, narrow bandgap, strong photoluminescence and exciton binding energy, and the ability to transition from an indirect bandgap to a direct bandgap. These properties make them highly attractive and promising for various applications,

including optoelectronic, photocatalysis, nanoenzyme catalysis, and energy devices. [89], [90]. These properties also make them highly attractive and promising in the development of electrochemical sensors [91].

### 1.2.1.2. Molybdenum Disulfide ($MoS_2$)

Molybdenum disulfide ($MoS_2$) is hailed as the 'king of high-grade solid lubricants. $MoS_2$ occurs in several polymorphs. $MoS_2$ consists of three atomic layers, with molybdenum atoms sandwiched between two layers of sulfur atoms, forming a unique layered structure resembling a 'sandwich' as shown in Fig. 1.6. This structure confers exceptional anisotropy, catalytic properties, and a low coefficient of friction.

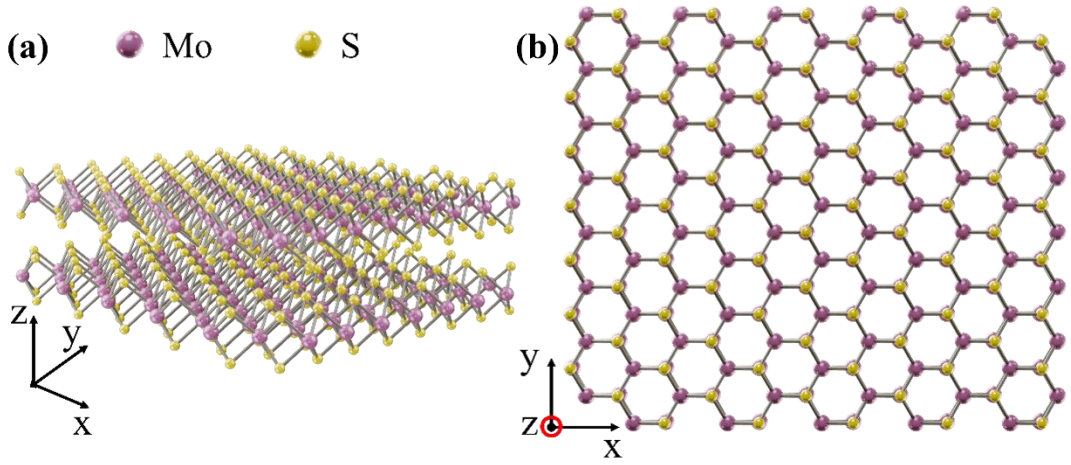


**Figure 1.6.** $MoS_2$ consists of 3 atomic layers, with molybdenum (Mo) atoms sandwiched between 2 layers of sulfur (S) atoms, forming a unique layered structure. $MoS_2$ structural forms (a) and (b).

The 2H phase has a layered hexagonal lattice with parameters a = 0.316 nm and c = 1.229 nm [92]. This gives an interlayer spacing of 0.615 nm [93], as shown schematically in Fig. 1.7. Bulk 2H-$MoS_2$ is an indirect-band-gap semiconductor ($\approx$ 1.29 eV). As thickness decreases, the band gap increases. In the monolayer, $MoS_2$ has

a direct band gap of about 1.90 eV [94], which suits many electronic devices. $MoS_2$ can be synthesised by top-down or bottom-up routes, such as exfoliation and chemical vapour deposition.

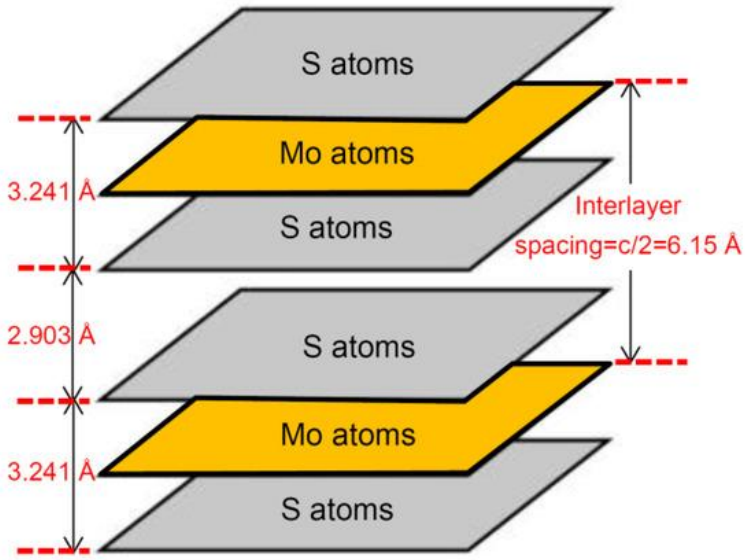


**Figure 1.7.** Distances between different layers in 2H $MoS_2$ [87].

***Micromechanical Exfoliation:*** Like graphene, $MoS_2$ flakes can be made by tape exfoliation on a substrate. Bulk $MoS_2$ is pressed with sticky tape onto the surface. When the tape is lifted, some layers remain because of van der Waals attraction to the substrate. Repeating the steps yields flakes with random shapes, sizes, and layer numbers. This route gives very high-quality 2D material, suitable for probing intrinsic properties and peak device performance. Using this method, Kis and co-workers prepared monolayer $MoS_2$ for ultrasensitive photodetectors [95], analogue [96] and digital circuits [97], and studies of mobility engineering and the metal–insulator transition [98].

***Liquid Phase Exfoliation:*** This method also begins with bulk $MoS_2$ and yields flakes with varied shapes, sizes, and layer numbers. The quantities are higher, but the quality is lower. Two main routes are used. The first applies mechanical energy-sonication, high-shear mixing, stirring, grinding, or gas bubbling [99]. The action is mostly physical, though additives can help [100], [101]. Surfactants such as sodium

deoxycholate bile salt [101] and chitosan [100] stabilise the sheets and limit re-aggregation. In some setups, electrolysis generates microbubbles that enter the interfaces and pry the layers apart [102]. Yields are far better than tape exfoliation, yet still too low for industry applications.

The second route uses atomic intercalation introduced by solution chemistry [103] or electrochemistry [104]. Lithium commonly inserts between $MoS_2$ layers, expands the spacing, and makes sonication more effective. Fan et al. reported efficient delamination via sonication-assisted Li intercalation, while complete intercalation with butyllithium was achieved in about 1.5 h [105]. Flakes produced this way (shown in Fig. 1.8) often lose semiconducting behaviour because the structure changes during Li insertion. Partial recovery is possible by annealing above 300 °C [103].

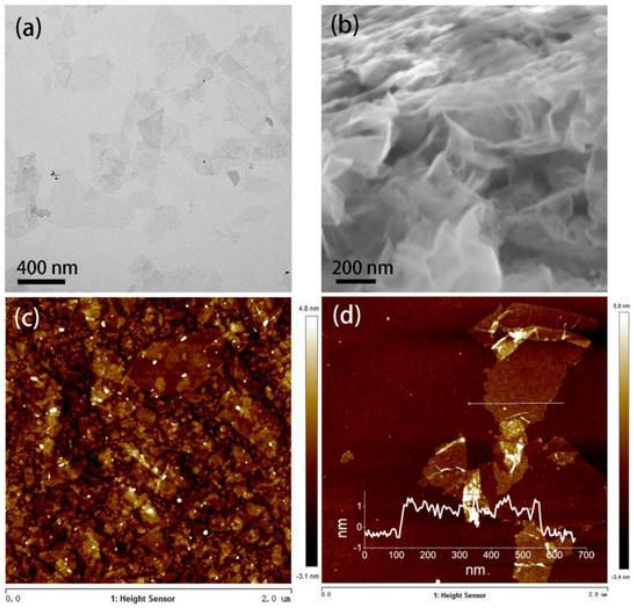


**Figure 1.8.** TEM, SEM and AFM images of $MoS_2$ flakes exfoliated by Li intercalation and sonication [105].

Liquid-phase exfoliation is a simple, low-cost method that produces large amounts of 2D nanosheets with reasonably high quality. It is therefore considered the most practical route for low-expense, large-scale production of one- to few-layer flakes [106]. The approach can yield wet suspensions, dry powders, and even continuous thin films [107].

By drop-casting a suspension onto a substrate and drying it, Walia et al. prepared $MoS_2$ thin films for optical and electrical studies [108].

***Chemical Vapor Deposition (CVD):*** Among the available methods, CVD fits best with established semiconductor processes. It grows films directly on a substrate through chemical reactions. Uniform, large-area $MoS_2$ enables batch fabrication of atomically thin devices and circuits. Most studies start from solid molybdenum sources such as $MoO_3$ [109] or metallic Mo [110]. When the Mo source is not vaporised, the process is often called sulfurisation [109]. Sulfur is supplied as $H_2S$ gas [111] or evaporated sulfur [112]. Some reports indicate that $MoCl_5$ helps achieve continuous monolayers over large areas [112]. Early films were sometimes discontinuous, but this issue is now largely resolved. Typical growth temperatures are 700-1000 °C, and adding a metal catalyst, such as Au, improves film quality [111]. In essence, the reactions convert $MoO_3$ or Mo to $MoS_2$ in sulfur- or $H_2S$-containing vapours.

Metal-organic CVD (MOCVD) is a form of CVD that uses organometallic precursors. It is widely applied in the semiconductor industry to grow single-crystal epitaxial films. Recent studies have extended this method to $MoS_2$ thin films [113], [114]. Kang et al. [115] grew $MoS_2$ and $WS_2$ on 4-inch oxidised silicon wafers using gaseous $Mo(CO)_6$ (boiling point 156 °C) and $(C_2H_5)_2S$.

***Other Processes:*** Although molecular beam epitaxy (MBE) is a leading method for growing single-crystal semiconductor thin films, its use for 2D materials still needs development, and the grain sizes obtained are smaller than expected [116]. Conventional physical vapour deposition is also rarely applied. For example, a $MoS_2$–Ti composite grown by vacuum sputtering with Ti and $MoS_2$ targets produced an amorphous $MoS_2$ phase [117].

$MoS_2$ can be produced by several solution-based routes. In hydrothermal [118] and solvothermal syntheses [119], molybdate reacts with sulfide or elemental sulfur in a

stainless-steel autoclave. Reactions proceed at elevated temperature (≈200 °C) and pressure for hours or longer, yielding $MoS_2$ powders with varied morphologies. Particle size can be tuned to some extent. High-temperature post-annealing is often used to improve crystallinity and purity. The key difference is that solvothermal processing typically uses a non-aqueous precursor solution.

Other wet-chemical methods operate near room temperature and atmospheric pressure, though post-annealing remains common [120]. Depending on conditions, products can be powders or thin films. A widely used precursor is ammonium tetrathiomolybdate, $(NH_4)_2MoS_4$, which decomposes to $MoO_3$ at 120-360 °C and then converts to $MoS_2$. Electrochemical deposition [121] and photo-assisted deposition [122] are also employed. For example, Li et al. fabricated $MoS_2$ nanowires and nanoribbons from an $MoO_x$ precursor [121]. Exposing $MoO_x$ to $H_2S$ at 500-800 °C produced $MoS_2$; the processing temperature can yield either the 2H or 3R phase. The nanoribbons reached ~50 μm in length and formed parallel arrays suited to device fabrication.

***Sensor Application:*** Geng et al. used $MoS_2$ doped with functional hybrids of Ni and rGO (Ni-$MoS_2$/rGO composite) for oxidation studies of glucose. This sensor showed excellent electrocatalytic performance with a rapid response time, good reproducibility and stability, high electron transport rates, large effective surface area and electrical conduction efficiency. In employing Ni-$MoS_2$/rGO to determine glucose oxidation, a linear range of 0.005-8.2 mM, and a limit of detection (LOD) of 2.7 μM were achieved [123].

In another example, Fang et al. used a 3D $MoS_2$ nanoflower and $Cu_2O$ composite on GCE for the detection of glucose in 0.1 M KOH/NaOH. Leveraging its unique structure and large surface area, the $MoS_2$-$Cu_2O$ composite showed excellent electrochemical activity for glucose detection. The mechanism involves glucose isomerising to 1,2-enediol in an alkaline medium, followed by its oxidation to gluconolactone via interaction with $Cu^+$ ions. The fabricated sensor achieved a detection limit of 1.0 μM

and a sensitivity of 3108.87 μA $mM^{-1}$ $cm^{-2}$, validating the promise of metal oxide-$MoS_2$ based platforms for sensing small biomolecules [124].

Moving to another sensing application, Xia et al. constructed a novel 3D nanoflower-like Cu/multi-layer $MoS_2$ composite (CuNFs/$MoS_2$) modified on glassy carbon electrode (GCE). This was applied for hydrogen peroxide ($H_2O_2$) and glucose detection, as shown in Fig. 1.9. By combining the advantages of CuNFs and $MoS_2$, high electrocatalytic activity towards $H_2O_2$ and glucose was achieved. For $H_2O_2$, the linear detection range spans 0.04-1.88 μM and 1.88-35.6 μM, with a corresponding limit of detection (LOD) of 0.021 μM. For glucose, the linear detection range covers 1-20 μM and 20-70 μM, with a corresponding LOD of 0.32 μM [125].

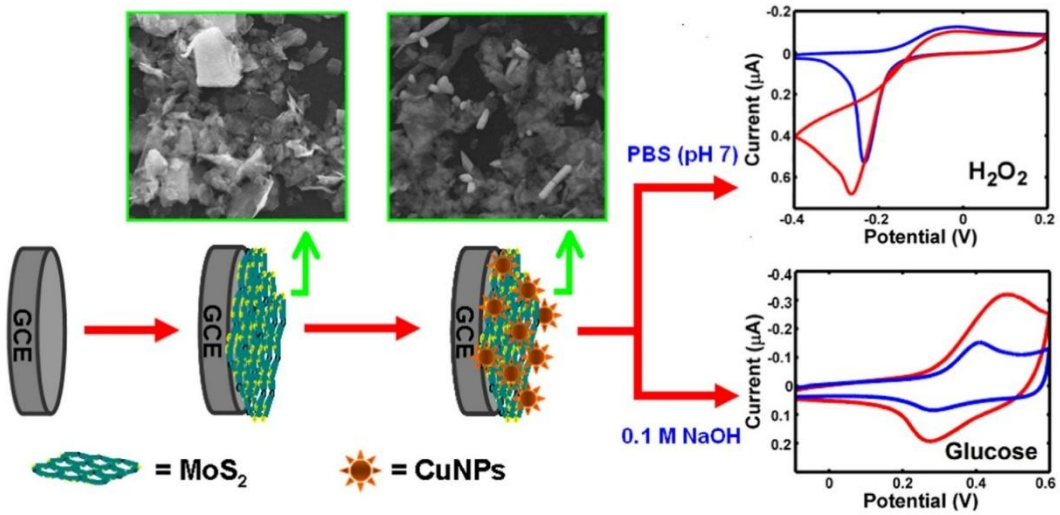


**Figure 1.9.** A schematic representation of the fabrication of the CuNFs-$MoS_2$/GCE, and possible reaction mechanisms at the electrode during the analysis for $H_2O_2$ and glucose. The bule line represents of the CuNFs-$MoS_2$/GCE recorded in blank supporting electrolyte; and the red line represents the CV of the same electrode recorded after adding the analyte (in the presence of $H_2O_2$ in PBS, pH 7.0 or in the presence of glucose in 0.1 M NaOH) showing the enhanced electrocatalytic activity [125].

Amino acids are the fundamental building blocks of proteins and are vital for human health. They play a pivotal role in metabolic regulation. Among these, tryptophan (Try)

is an essential α-amino acid whose monitoring helps determine whether stem cells are impaired. Xia et al. developed a method that combines Ag-$MoS_2$-chitosan (as shown in Fig. 1.10) on a gold carbon electrode (GCE) to detect the oxidation reaction of tryptophan. This sensor exhibits a detection limit of 0.05 µM (S/N=3) across a linear tryptophan concentration range of 0.5-120.0 µM. Furthermore, the Ag-$MoS_2$/CS/GCE exhibits selectivity towards tryptophan in mixtures containing other amino acids, without interference from these other compounds [126].

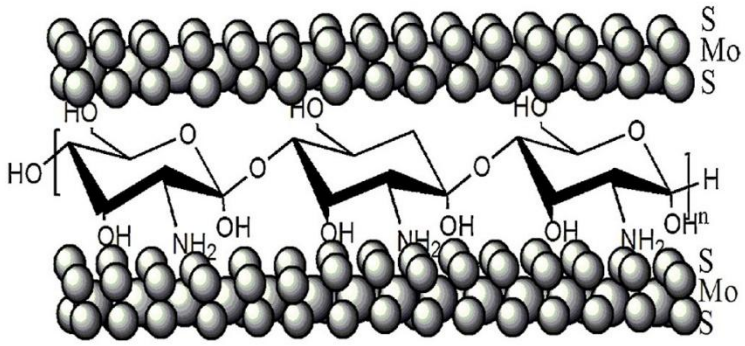


**Figure 1.10.** The simply structure of proposed lamellar arrangement of $MoS_2$-CS nanocomposites. [126]

For another vital human nutrient, folic acid (FA), which aids in the production of healthy red blood cells. Mani et al. employed a straightforward method to prepare a ternary nanocomposite comprising graphene, $MoS_2$, and gold nanoparticles (AuNPs) as an electrocatalytic sensor for FA detection. Deposited onto a screen-printed electrode (SPCE), this composite exhibits outstanding electrocatalytic performance for folic acid, owing to synergistic interactions between $MoS_2$ and AuNPs, with a detection limit of 38.5 nM and a broad linear range of 50 nM to 1150 µM. The electrode exhibits excellent repeatability, reproducibility, and stability. Its practicality was validated using human urine samples, yielding favourable recovery rates [127].

### 1.2.1.3. Tungsten Disulfide ($WS_2$)

$WS_2$ adopts a sandwich-like structure, with tungsten (W) atomic layers sandwiched between two layers of sulphur (S) atoms as shown in Fig. 1.11. This structure endows $WS_2$ with unique properties [128]. For example, this structure can adjust the electronic properties of $WS_2$, enabling it to achieve different electronic states. Additionally, $WS_2$ exhibits high thermal conductivity, excellent corrosion resistance, and superior mechanical strength [129]. $WS_2$ has a wide range of applications across diverse fields. In sensors, due to its outstanding optoelectronic properties and sensitivity, $WS_2$-based chemical sensors for detecting environmental pollutants such as formaldehyde and nitrogen oxides have become a research trend. These sensors feature high sensitivity, a wide detection range, low energy consumption, and excellent stability [129].

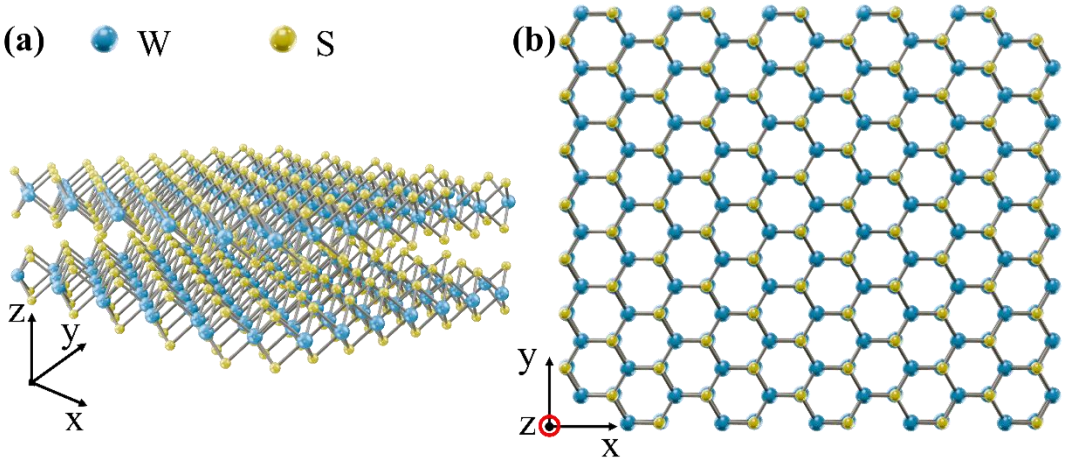


**Figure 1.11.** $WS_2$ adopts a characteristic sandwich-like (S-W-S) layered structure, in which a hexagonally coordinated tungsten (W) atomic layers sandwiched between two sulphur (S) atomic layers, forming a stacked two-dimensional lamellar framework. $WS_2$ structural forms (a) and (b).

$WS_2$ can be synthesised using the same method as for synthesising $MoS_2$. In this thesis, the focus is on liquid phase exfoliation. This method begins with bulk $WS_2$ and produces flakes with various shapes, sizes, and layer numbers. Systems such as NaCl, NMP, n-BuLi, LiCl, tannic acid, and $H_2O$ can all be used as liquid-phase solvents for

exfoliated bulk $WS_2$ [130], [131].

***Sensor Application:*** A novel approach utilising non-lysed phage M13 (as the biological receptor) was developed to prepare a nanobiocomposite of $WS_2$ quantum dots, gold nanoparticles (AuNPs) and M13 phage, as shown in Fig. 1.12. The high specific surface area of $WS_2$ quantum dots, the specificity of the phage, and the efficient chemical bonding between M13 and the uniformly dispersed AuNPs provided an efficient biosensor. The biosensor exhibits favourable stability across broad temperature and time ranges, coupled with high sensitivity and selectivity in the analysis of the amount of c-Met protein in standard solutions [132].

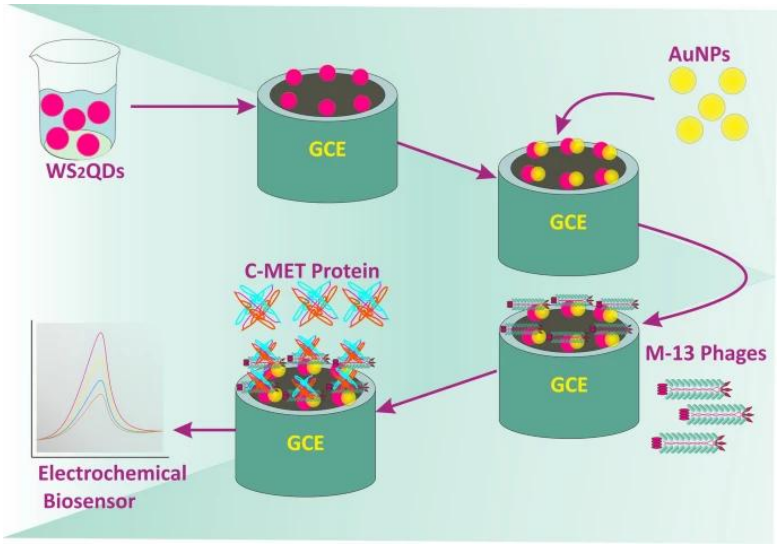


**Figure 1.12.** Summary of colon cancer using tungsten disulfide quantum dots and bacteriophage nano-biocomposite as an efficient electrochemical platform. [132]

$WS_2$ quantum dots have also been employed as ferritin immunosensors, as shown in Fig. 1.13. The 2D layered quantum dots were synthesised via a one-step liquid-phase exfoliation method, with both quantum dot synthesis and in situ functionalisation achieved through biosurfactants, providing a clean and environmentally friendly approach. The resulting functionalised quantum dots ($WS_2$-B QDs) yielded linear detection ranges for ferritin (10-1500 ng $mL^{-1}$). The detection limits were 3.8 ng $mL^{-1}$

for differential pulse voltammetry (DPV) and 6.048 ng $mL^{-1}$ for cyclic voltammetry (CV, demonstrating superior performance of DPV. High selectivity, excellent reproducibility, and stability (≈ 60 days) were seen [133].

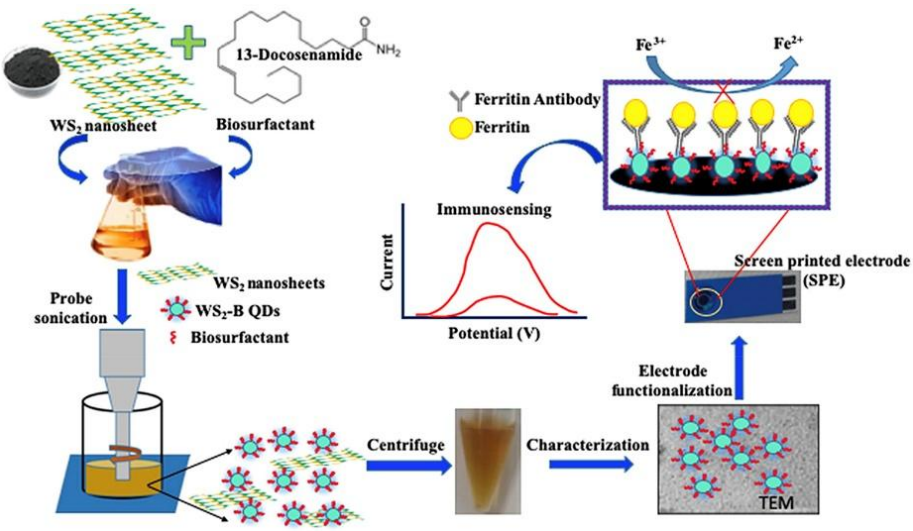


**Figure 1.13.** Summary of $WS_2$-B QDs/SPE for a novel biosurfactant-stabilised/functionalised sensor [133].

In the development of sensors, $WS_2$ has also been combined with carbon materials (like carbon quantum dots, graphene and carbon nanotubes) [134][135]. For example, $WS_2$ and hydroxylated multi-walled carbon nanotubes (MWCNTs-OH) have been employed in the detection of aquatic pollutants (2,4, 6-trichlorophenol) and two emerging pollutants (bisphenol and polystyrene nanoplastics), as shown in Fig. 1.14 [134].

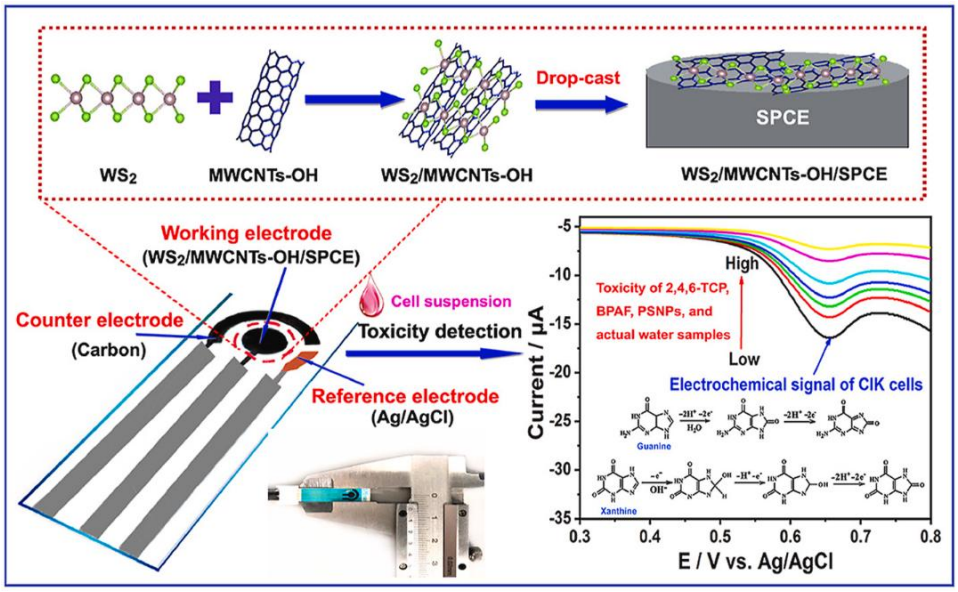


**Figure 1.14.** Summary of $WS_2$/MWCNTs-OH/SPCE working for water toxicity [134].

Likewise, $WS_2$ was combined with carbon quantum dots CQDs to form a novel electroactive material for the determination of sulfamethazine [135]. Similarly, graphene has been coupled with $WS_2$. The graphene serves as a two-dimensional electrical scaffold supporting nano-sized $WS_2$. AuNPs were also anchored with chitosan onto the $WS_2$-graphene-chitosan composites to yield a DNA biosensor with outstanding electrochemical performance for capturing single-stranded DNA sequences [136].

## 1.2.2. Spinel materials and oxides

### 1.2.2.1. Definition, Classification, and Applications

Metal oxides have been widely used in the development of electrochemical sensors, due to their good conductivity, good stability and the availability of a high density of active sites that can facilitate electron transfer [137], [138]. Spinel-type oxides are an important class of functional metal oxides with widespread applications in fields such as electronics, magnetism, catalysis, energy storage, and energy conversion [139]. Spinel-type oxides can be described as $AB_2O_4$, to give a cubic close-packed lattice arrangement, where A and B represent the cations positioned in the tetrahedral and octahedral sites ($AB_2O_4$, A = Co, Ni, Cu, Zn, Fe, abbreviated as ABO, where A and B are metal elements and O is an oxygen-group element) [140].

Spinel oxides have high thermal stability, corrosion resistance, and excellent chemical and mechanical properties. They are also highly versatile, acting as efficient electrocatalysts for reactions like the oxygen evolution reaction, being used in high-temperature self-lubrication systems, and sensing technologies [141], [142]. The ability to tune their electronic and surface properties further enhances their performance for specific applications. Among these, the most commonly used methods to synthesis spinel-type oxides include the solid-state method, sol-gel method [143], coprecipitation method [141], hydrothermal/solvothermal method [144], ultrasonic/microwave method, co-precipitation method and electrodeposition method [138]. Additionally, recent studies have explored alternative synthesis strategies such as combustion, ion exchange, reflux, and microemulsion methods. Each method has its own advantages and unique characteristics [138], [140], [143]. These are now briefly discussed.

***Hydrothermal Method:*** This method for synthesizing $ZnMn_2O_4$ involves mixing zinc and manganese precursors (like nitrates or acetates) in an aqueous solution, often with a pH regulator and sometimes a surfactant or complexing agent. This solution is then

heated in a sealed, Teflon-lined autoclave to a specific temperature (120-200 ℃) for a set amount of time (12-48 h). After cooling, the resulting solid product is collected by centrifugation, washed, and dried [145].

***Co-precipitation Method:*** This method is typically carried out at room temperature using appropriate salts such as nitrates or acetates (zinc, manganese, iron, etc.). A specific precipitating agent is added to a particular solvent (a solution containing multiple cations), and through reaction, a uniformly composed precipitate is formed [146]. This method has low requirements on equipment, short production cycle and is suitable for commercial production.

### 1.2.2.2. Zinc Manganite ($ZnMn_2O_4$) Spinel Oxide

Zinc-based oxides have attracted much attention, due to the abundance of zinc coupled with the tunable morphology, high surface areas, and semiconducting properties [139]. Among the various oxides, spinel-type Zn oxides are finding increasing applications in the electroanalysis of analytes in biological and environmental analysis [142]. In particular, Zinc manganese oxides, $ZnMn_2O_4$ spinels (ZMO) shown in Fig. 1.15, are environmentally acceptable and cost-effective. In this structure, the $Zn^{2+}$ cations are positioned at the tetrahedral sites, while the $Mn^{3+}$ ions occupy the octahedral sites. ZMO is typically formed using sol-gel synthesis [147], or co-precipitation methods [148], which are then followed by a thermal process.

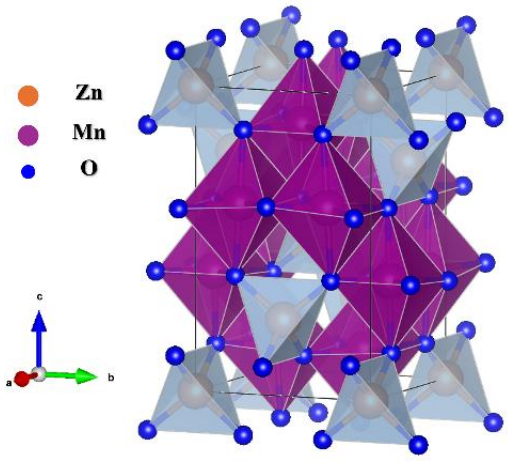


**Figure 1.15.** Structure of $ZnMn_2O_4$.

Various ZMO composites have been designed and formulated, including composites with hexagonal boron nitride [142], reduced graphene oxide [149], carbon nanotubes [150], MXenes [151], and oxides such as $MgFe_2O_4$ [152], and sulfides such as CdS [153]. ZMO and its composites have been employed as gas sensors [154], and in the design of supercapacitors [152]. It has also been employed for the electrochemical analysis of $H_2O_2$ [144], and mesotrione, a widely used herbicide [142], making it an interesting material in the development of electrochemical sensors.

### 1.2.2.3. Cerium Ferrite ($CeFe_2O_4$) Spinel Oxide

While $CeO_2$/rGO [155] and $Ce_2O_3$/rGO [156] have been designed for the electrochemical analysis of biomolecules, there are no reports to the best of our knowledge on the application of $CeFe_2O_4$-based composites as electrochemical sensors. Therefore, a $CeFe_2O_4$-$CeO_2$ composite (CFO) was synthesised and supported with conducting carbon fibres (CNFs) to produce CFO-CNFs for Chapter 7. The structure of $CeFe_2O_4$ is shown in Fig. 1.16.

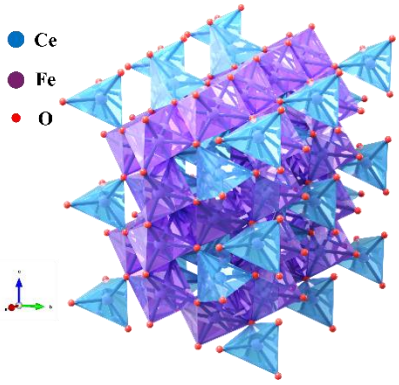


**Figure 1.16.** Structure of $CeFe_2O_4$.

Although there is yet no further literature evidence of the application of $CeFe_2O_4$ in sensors, this particular Ce and Fe spinel oxide exhibits superior catalytic performance compared to copper, manganese, nickel, cobalt, and magnesium. For example, Guo et al. demonstrated that the synergistic effect between A-metal and iron significantly enhances the catalytic performance of $AFe_2O_4$ catalysts prepared using the sol-gel method. The performance ranking of the $AFe_2O_4$ spinel catalysts is as follows: $CeFe_2O_4$ > $CuFe_2O_4$ > $MnFe_2O_4$ > $NiFe_2O_4$ > $CoFe_2O_4$ > $MgFe_2O_4$ > no catalyst [157].

The practical application of $CeFe_2O_4$/GO hybrid synthesised via a simplified hydrothermal method holds critical significance for achieving high-performance superhydrophobic electromagnetic (EM) materials under harsh environmental conditions, particularly in high-humidity settings. The nanocomposite shows a stable EM wave absorption ability; this approach offers a viable solution for mitigating electromagnetic pollution in outdoor environment [158].

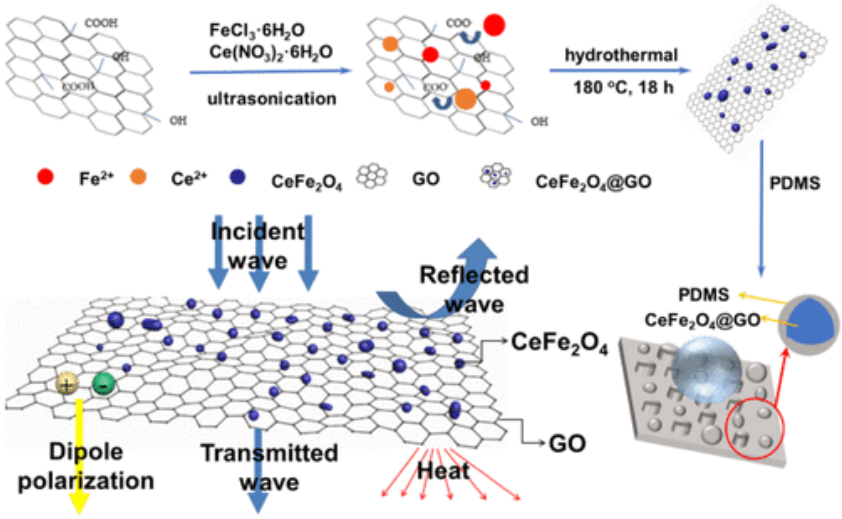


**Figure 1.17.** Summary of $CeFe_2O_4$/GO hybrid for the EM pollution in the outdoor environment [158].

$CeFe_2O_4$ has been combined with multi-walled carbon nanotubes (MWCNTs) to fabricate microwave-absorbing materials and multifunctional coatings [159]. $CeFe_2O_4$ also serves as an activator for peroxymonosulphate (PMS) and as an adsorbent for removing Terdizolamide phosphate (TZD). Magnetic biochar (CF-biochar) loaded with $CeFe_2O_4$ was prepared via microwave ablation-anaerobic carbonisation. This material exhibits smaller particle size, larger specific surface area, broader pore size distribution, and high magnetic properties. By establishing removal kinetics and adsorption isotherm models, the CF-biochar/PMS system was demonstrated to be an efficient, promising, and sustainable technical solution for TZD removal [160]. These studies demonstrate that the $CeFe_2O_4$ spinel oxides exhibit high catalytic activity, structural stability and adsorption capacity, making them suitable for applications in sensors and pollutant removal [160], [161].

### 1.2.2.4. Cerium Dioxide ($CeO_2$)

Cerium dioxide ($CeO_2$), shown in Fig. 1.18, is an interesting oxide that is currently attracting much attention [27-29]. For example, it has been doped with Mn and employed in the electrochemical sensing of urea [30] and it is attracting much attention

in the field of biosensors [31]. It has been shown to exhibit antioxidant, anti-bacterial [29], and anti-biofouling characteristics [27] and has promising wound-healing properties [28]. $CeO_2$ can enhance the stability of spinels as a sensor; hence, it is frequently observed working in tandem with spinels to improve electrochemical performance [162], [163], [164].

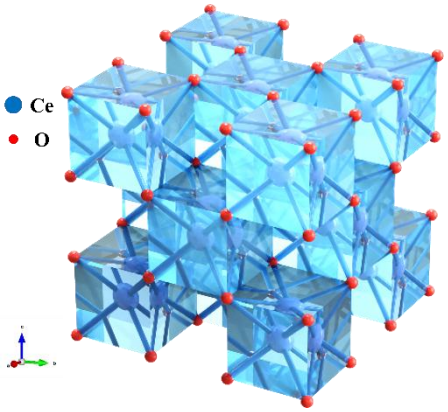


**Figure 1.18.** Structure of $CeO_2$.

### 1.2.2.5. Sensor Application for Ferrite ($ZnFe_2O_4$) Spinel Oxides

Liu et al. prepared $ZnFe_2O_4$/ZnO composite materials via a mild hydrothermal method, featuring a substantial number of $ZnFe_2O_4$ nanoparticles modified onto the surface of ZnO microflowers (as shown in Fig. 1.19). Enhanced gas sensing performance was achieved through increased surface area and reaction zone, synergistic effects between materials, formation of heterojunctions, and an optimised dispersion structure. The response value of the $ZnFe_2O_4$/ZnO microflowers to 50 ppm acetone at 250 °C was approximately 8.3, representing an increase of nearly 5.4-fold compared to the response value of the original ZnO microflowers under identical conditions [165].

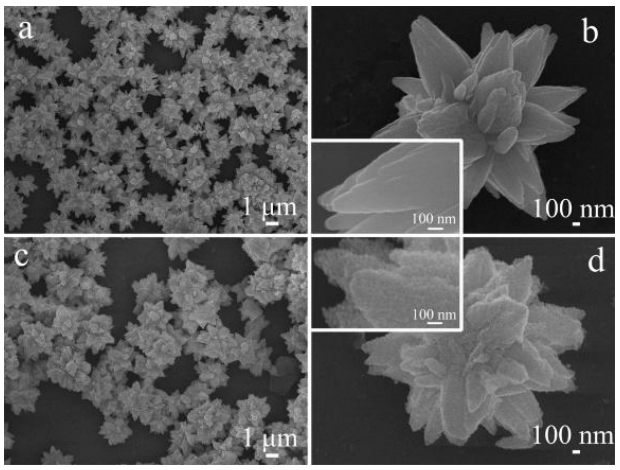


**Figure 1.19.** FESEM images of the pure (a and b) and $ZnFe_2O_4$-decorated (c and d) ZnO hierarchical flower-like structures [165].

Cetyltrimethylammonium bromide (CTAB) promotes the mutual association of $Zn(OH)_4^{2-}$ ions, which decompose into ZnO crystal nuclei. These nuclei self-assemble and grow into rod-like structures with specific axial orientation. Wang et al. [166] employed ferrous sulphate heptahydrate and zinc nitrate dihydrate as reactants. Following conventional procedures, the resulting $ZnFe_2O_4$/ZnO morphology is depicted in Fig. 1.20. Owing to the unique structure formed by the surfactant and the heterojunction effect, the $ZnFe_2O_4$/ZnO nano heterostructure exhibits outstanding gas sensitivity. Compared to the zinc oxide nanowires synthesised by Zou et al. [167], the heterojunction nanowire structure synthesised in this experiment enables operation at lower temperatures and faster gas response.

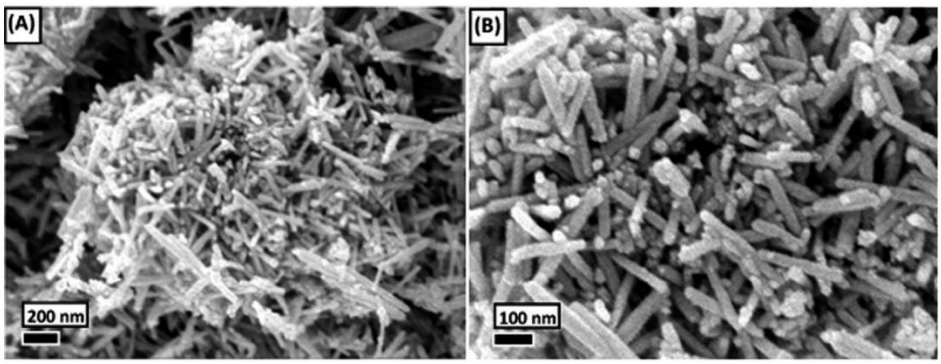


**Figure 1.20.** SEM images of the as-prepared $ZnFe_2O_4$/ZnO nano heterostructures [166].

## 1.2.3. Carbon Materials

Various nanomaterials and signal amplification strategies have been prepared and used as construction materials for electrochemical sensors, such as gold nanoparticles, bimetallic nanoparticles, functionalised graphene, carbon nanotubes, graphene quantum dots, and metal-organic frameworks [168], [169]. Carbon-based materials exhibit outstanding properties, including rich pore structures, high specific surface areas, tunable surface functionality, excellent conductivity, and ease of chemical functionalisation, demonstrating broad application prospects in the field of electrochemical sensing [170]. Choosing an appropriate electrocatalyst is crucial to enhancing the sensing capabilities of electrochemical sensors; therefore, combining TMDs, or metal oxides, with carbon materials could be an effective strategy. Some of the carbon-based materials chosen in this study are described below.

### 1.2.3.1. Graphene-based Materials

Graphite and graphene sound similar, but graphene is actually a single-layer structure of graphite. Graphite is formed by stacking multiple layers of graphene, with approximately 3 million layers of graphene in 1 millimetre of graphite. Graphene can be considered as a single layer of graphite, while graphite is composed of multiple layers of graphene stacked together. Graphene consists of a single layer of carbon atoms, whereas graphite is formed by stacking multiple layers of graphene, resulting in a thickness greater than that of graphene [171]. Graphite and graphene are two different carbon materials, but they are closely related. Graphene is the basic building block of graphite and can be regarded as a single-layer structure of graphite [172], as illustrated in Fig. 1.21.

Graphene oxide (GO) and reduced graphene oxide (rGO) are two graphene-related materials that differ in structure and properties. GO contains various oxygen-containing functional groups, while rGO is the product obtained by removing or reducing these

functional groups through a reduction process [173]. GO can be viewed as single-layer graphene with various oxygen-containing functional groups, such as epoxy groups, hydroxyl groups, and carboxyl groups, attached to it. This provides GO with good solubility, making it easy to disperse in water, making it a precursor for other materials [174]. The rGO is obtained by using various reducing agents (such as hydrazine hydrate, sodium borohydride, etc.), thereby removing or reducing the oxygen-containing functional groups in graphene oxide [175]. The reduced material may still contain a small amount of functional groups and defects. However, the conductivity and mechanical properties of rGO are closer to those of graphene, though typically not as good as those of pristine graphene. In applications, GO is frequently used to prepare various composite materials, sensors, and biomaterials, while rGO is primarily used to prepare transparent conductive films, supercapacitors, and electrode materials [174], [176].

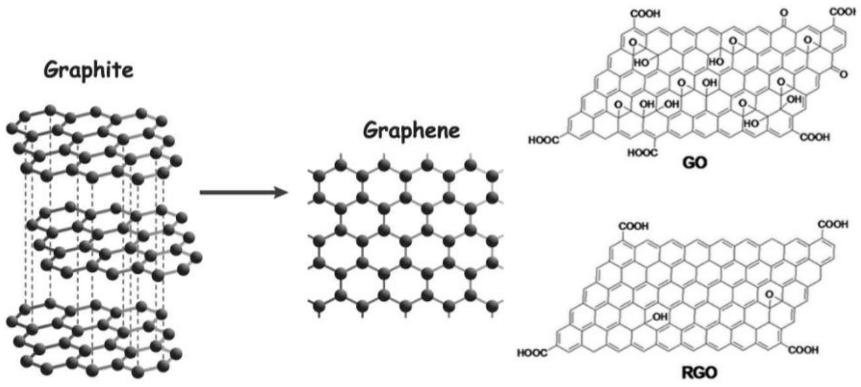


**Figure 1.21.** Structure of graphite, graphene, graphene oxide (GO) and reduced graphene oxide (RGO) [171].

### 1.2.3.2. Carbon Quantum Dots (CQDs) and Carbon Particles (CPs)

Carbon particles (CPs) and carbon dots (CQDs) are two related carbon-based materials that differ in size and structure. CPs are a broader term that can refer to carbon-based particles of any size, including CQDs, as well as larger carbon materials such as coal

and coke. CQDs typically refer to carbon-based nanomaterials with fluorescent properties that are smaller than 10-20 nm. CQDs can be synthesised from fruits or kitchen waste while adhering to green chemistry principles [177], [178]. A general core-shell structure of CQDs is shown in Fig. 1.22, highlighting the graphitic and crystalline core and the functional groups.

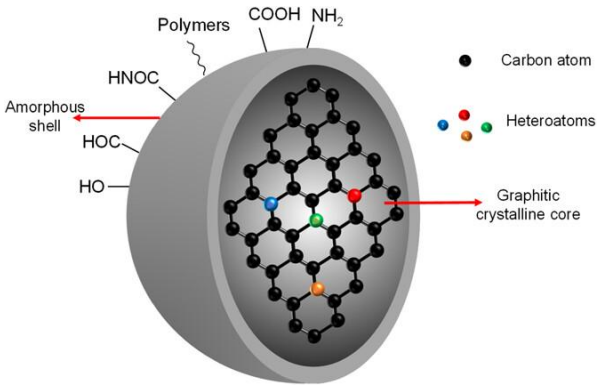


**Figure 1.22.** A general core-shell structure of CQDs [179].

CPs can refer to carbon-based particles of any size, and their advantage lies in their structural diversity, which can include amorphous carbon, graphite, diamond, and other forms of carbon-based materials. Due to their varying structures, different materials can exhibit distinct properties such as conductivity and adsorption capacity [180].

In Chapter 5, a green synthesis method to produce CQDs from kiwi fruit is described. The fluorescent properties could be observed initially, but after a few hours, the fluorescent properties could no longer be detected. This was due to the instability of the CQDs. However, when performing FLD detection, larger CPs were obtained instead.

### 1.2.3.3. Carbon Nanofibers (CNFs)

Carbon nano fibers (CNFs) are a type of quasi-one-dimensional carbon material with exceptional properties (SEM shown in Fig. 1.23). They can be viewed as carbon nanofibers formed by the curling of graphite sheets, similar to carbon nanotubes, but

more akin to a material intermediate between nanotubes and traditional carbon fibers. They typically have diameters ranging from 10 nm to 500 nm and lengths from 0.5 μm to 100 μm or longer [181], [182], [183]. CNFs combine some of the properties of carbon nanotubes and traditional carbon fibers. This makes them stronger than ordinary carbon fibres. They have excellent electrical and thermal conductivity, making them promising for electrochemical applications. CNFs exhibit good high-temperature resistance in non-oxidising environments and have a high strength-to-weight ratio, giving them an advantage over other high-performance carbon materials [183]. These notable advantages also expand the application scope of CNFs as reinforcing phases added to various composite materials. This can lead to enhanced mechanical properties for manufacturing electronic devices, sensors, catalysts and for producing filtration materials, absorptive materials, and more [182].

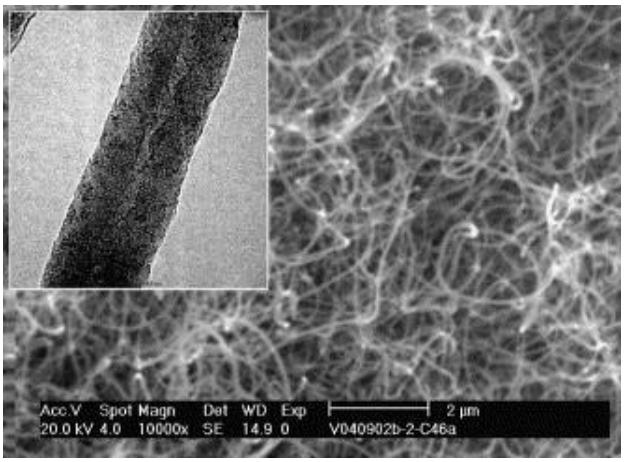


**Figure 1.23.** SEM and TEM image of CNFs [184].

Carbon fibres are usually produced by high-temperature sintering of polymer fibers, offering high strength and stiffness, but with inferior conductivity and thermal conductivity compared to carbon nanotubes. Carbon nanofibres, however, strike a balance between the two, combining strength, conductivity, and thermal conductivity while maintaining relatively lower production costs [181].

# 1.3. Research Objectives and Thesis Structure

## 1.3.1. Main Research Goals

The work reported in this thesis has five objectives and highlights:

1. To compare the electrochemical sensors formed using electrodeposition of $MoS_x$ and the formation of $MoS_2$ sheets dispersed in DL-tryptophan solution for metronidazole (MTZ) detection. MTZ is extensively employed in treating bacterial infections in humans and animals, yet exhibits genotoxic and mutagenic side effects. Its accumulation in aquatic environments may pose hazards to both humans and aquatic organisms. Consequently, establishing a simple, rapid, and efficient analytical method for MTZ is paramount.

2. To form a sensor for the electrochemical detection of sulfanilamide (SFD), which is a sulfonamide. This was developed using exfoliated $MoS_2$ (by tannic acid) and reduced graphene oxide/graphite. By studying graphene oxide and the reduced graphene oxide/graphite, it was observed that the latter was superior to pure reduced graphene oxide. Sulfonamides are antibiotics that inhibit bacterial folic-acid synthesis, a pathway essential for growth. They are linked to frequent allergic and hypersensitivity reactions; in severe cases, adverse effects can include anaemia, crystalluria, and liver failure. Elevated levels in water pose risks to human health and aquatic life.

3. To fabricate a CPs-$WS_2$ composite, which was based on a green electrochemical sensor for the determination of flutamide (FLD) via successive *Actinidia*-derived carbon particles (CPs) and tungsten disulfide ($WS_2$). Flutamide helps inhibit the growth and spread of cancer cells. Stopping the drug may be followed by fever, headache, loss of appetite, nausea, vomiting, and unusual fatigue. In addition,

heavy use in some farms and animal-production settings can lead to substantial accumulation in aquatic environments. This new composite, CPs-$WS_2$, has a high surface area and good electrical conductivity, and it enables the electrochemical detection of nM concentrations of FLD.

4. To develop a spinel-carbon composite-based electrochemical sensor for sulfamerazine (SRZ). A highly effective sensor was designed for the analysis of sulfamerazine. A $ZnMn_2O_4$ spinel, combined with $CeO_2$ and $WS_2$ was used as the sensor. The $CeO_2$ nano-powder sprinkled over the spinel provided good stability. Sulfamerazine is an antibacterial agent widely used for various bacterial infections. As an antimicrobial, it may cause blood disorders, potentially increase the risk of certain infections, delay wound healing, and trigger gum bleeding.

5. To find a new sustainable spinel, an iron-cerium spinel oxide was designed for the detection of sparfloxacin (SPAR), a water contaminant, which belongs to the class of medicines known as new antibiotics. It is used to treat bacterial bronchitis and pneumonia. SPAR works by killing bacteria or preventing their growth. However, this medicine will not work for colds, flu, or other viral infections. This study highlights the detection of an antibiotic using this new spinel oxide, $CeFe_2O_4$-$CeO_2$, and CNFs.

## 1.3.2. Chapter Summaries

In this Introduction chapter (***Chapter 1***), an introduction to the pollutants to be determined, electrochemical sensors, and the materials used in electrode modification processes and their contribution to electrochemical sensors is provided.

In ***Chapter 2***, the relevant experimental materials, preparation of the solutions, techniques and apparatus used, along with an overview of the theories and related equations employed in this thesis are detailed.

In ***Chapter 3***, molybdenum disulfide, $MoS_2$, sheets were obtained by exfoliation of the bulk powders in an aqueous solution containing 1.0 mM tryptophan and then drop-cast onto a glassy carbon electrode to give GCE/$MoS_2$. For comparative purposes, amorphous $MoS_x$ was electrodeposited directly onto the glassy carbon electrode from a 5 mM $(NH_4)_2MoS_4$ solution. Both electrodes were employed in the electrochemical detection of the antibiotic metronidazole (MTZ). (Summary shown in Scheme 1.3).

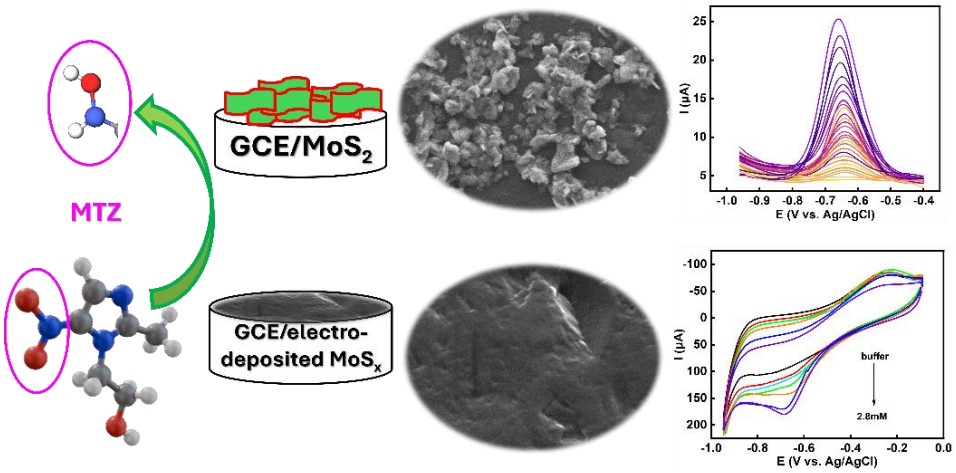


**Scheme 1.3.** Summary of Chapter 3.

In ***Chapter 4***, sulfonamides were selected. These are a family of synthetic drugs with broad-spectrum antimicrobial activity. Like other antimicrobials, they have been found

in aquatic environments, making their detection important. Herein, an electrochemical sensor was designed using tannic acid exfoliated few-layered $MoS_2$ sheets, which were combined with a mixture of reduced graphene oxide (rGO) and graphite flakes (G). The rGO/G was formed using electrodeposition, by cycling from −0.5 to −1.5 V in an acidified sulfate solution with well dispersed GO and G. The exfoliated $MoS_2$ sheets were drop cast over the wrinkled rGO/G surface to form the final sensor, GCE/rGO/G/ta-$MoS_2$. (Summary shown in Scheme 1.4).

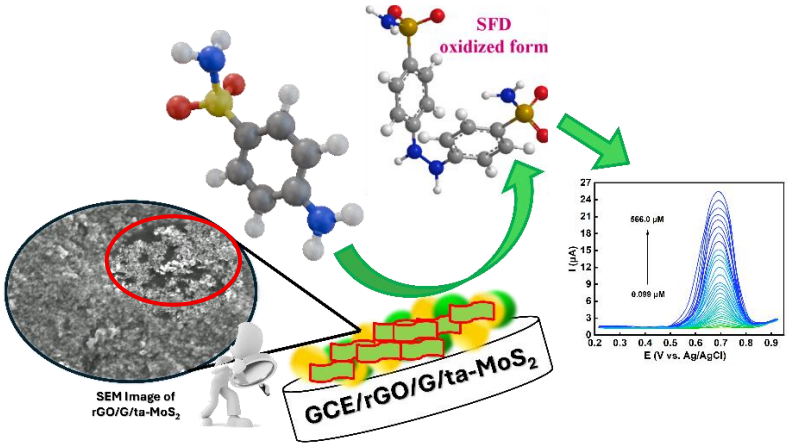


**Scheme 1.4.** Summary of Chapter 4.

In ***Chapter 5***, the development of electrochemical sensors for flutamide detection is a crucial step in biomedical research and environmental monitoring. In this study, a composite of Actinidia-derived carbon particles (CPs) and tungsten disulfide ($WS_2$) was formed and used as an electrocatalyst for the electrochemical detection of flutamide. The CPs carry surface hydroxyl and carbonyl groups that facilitate anchoring onto $WS_2$ platelets, forming a CPs-$WS_2$ nanocomposite with high surface area and a percolated conductive network that promotes electron transfer. (Summary shown in Scheme 1.5).

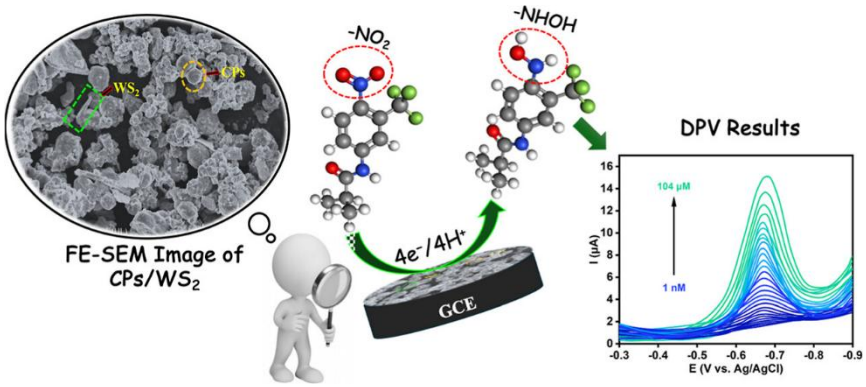


**Scheme 1.5.** Summary of Chapter 5.

In ***Chapter 6***, sulfamerazine is an extensively used antibiotic, and in recent years it has been discovered in various aquatic environments, making its detection highly relevant. In this study, an electrochemical sensor for the sensitive detection of sulfamerazine was designed by decorating a $ZnMn_2O_4$ (ZMO) spinel with $CeO_2$ and $WS_2$. The ZMO adopted a sphere-like morphology. On combining ZMO with $CeO_2$, the $CeO_2$ appeared sprinkled over the surface of the ZMO, forming a powder-like coating. The $WS_2$ sheets were exfoliated in sodium cholate and dispersed onto the $CeO_2$-coated ZMO to enhance its conducting properties. (Summary shown in Scheme 1.6).

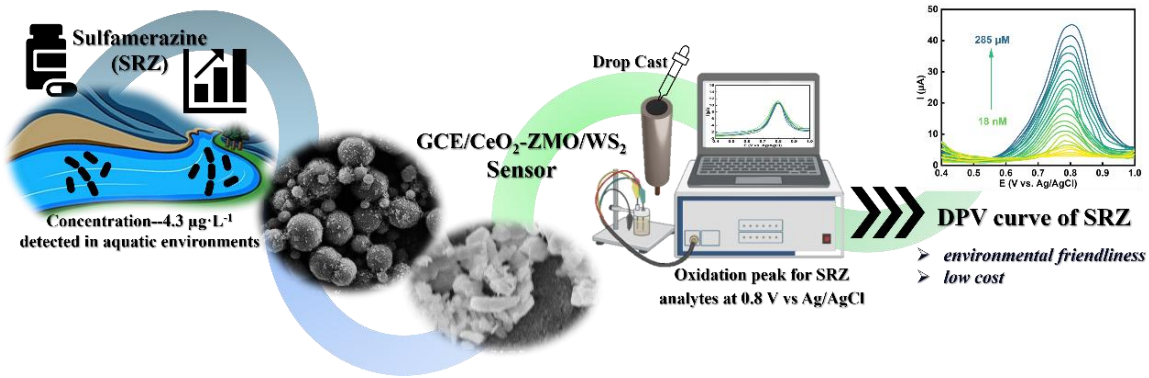


**Scheme 1.6.** Summary of Chapter 6.

In ***Chapter 7***, antibiotics, such as fluoroquinolones, are frequently found in aquatic environments, making their detection and removal crucial from both an environmental and health perspective. In this study, a $CeFe_2O_4$ spinel was combined with $CeO_2$ to give a new composite material (CFO), which was then supported by carbon nanofibers

(CNFs). (Summary shown in Scheme 1.7).

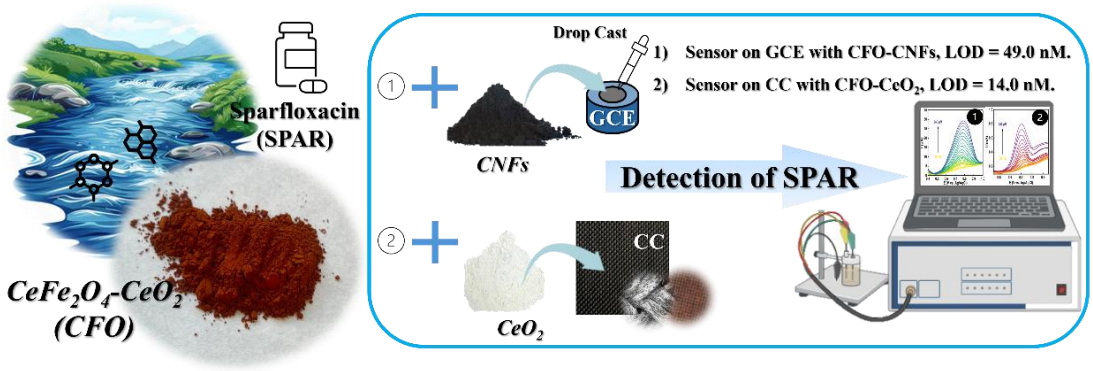


**Scheme 1.7.** Summary of Chapter 7.

In ***Chapter 8***, the final conclusions for the results and findings in this thesis are summarised, relating to both the developed sensors and future work for the removal of different pollutants from aqueous solutions.

# References


[1] A. Nasrul, A. Anwar, M. P. Aulia, C. M. Rosnelly, and I. Ramli, "Effectiveness of Microplastic Removal from River Water Using Conventional and Ultrafiltration Techniques: Correlation with Physicochemical Parameters," *International Journal of Engineering, Transactions B: Applications*, vol. 39, no. 6, pp. 1357–1368, 2026, doi: 10.5829/ije.2026.39.06c.05.

[2] I. Hamid and W. A. Khanday, "Recent advances in antibiotic removal methods from wastewater: A comprehensive review," *Sep Purif Technol*, vol. 381, 2026, doi: 10.1016/j.seppur.2025.135478.

[3] Q. Sun, J. C. P. Gabriel, and L. P. Tan, "Advancing sustainable closed-loop solutions: Supercritical carbon dioxide technology for aquatic biological waste valorization," *Applied Food Research*, vol. 5, no. 2, 2025, doi: 10.1016/j.afres.2025.101384.

[4] J. Sheffield, E. F. Wood, M. Pan, H. Beck, G. Coccia, A. Serrat‐Capdevila, and K. Verbist, "Satellite Remote Sensing for Water Resources Management: Potential for Supporting Sustainable Development in Data-Poor Regions," Dec. 01, 2018, *Blackwell Publishing Ltd*. doi: 10.1029/2017WR022437.

[5] B. R. Scanlon, "Global water resources and role of groundwater in a more resilient water future."

[6] D. Yang, Y. Yang, and J. Xia, "Hydrological cycle and water resources in a changing world: A review," Jun. 01, 2021, *Beijing Normal University Press*. doi: 10.1016/j.geosus.2021.05.003.

[7] N. Nath, "A Study on: Aquatic Ecosystem, Its Features, Functions & Threats," *Jamshedpur Research Review*, vol. 9, no. 59, pp. 57–65, 2023.

[8] M. Shaikh and F. Birajdar, "Groundwater and ecosystems: understanding the critical interplay for sustainability and conservation," *EPRA International Journal of Multidisciplinary Research*, vol. 10, no. 3, pp. 181–186, 2024.

[9] S. Apostolaki, E. Akinsete, P. Koundouri, and P. Samartzis, "Freshwater: The importance of freshwater for providing ecosystem services," *Encyclopedia of the World's biomes*, pp. 71–79, 2020.

[10] A. Inyinbor Adejumoke, O. Adebesin Babatunde, P. Oluyori Abimbola, A. Adelani Akande Tabitha, O. Dada Adewumi, and A. Oreofe Toyin, "Water pollution: effects, prevention, and climatic impact," *Water challenges of an urbanizing world*, vol. 33, pp. 33–47, 2018.

[11] J. Singh, P. Yadav, A. K. Pal, and V. Mishra, "Water pollutants: Origin and status," in *Sensors in water pollutants monitoring: Role of material*, Springer, 2019, pp. 5–20.

[12] J. Mateo-Sagasta, S. M. Zadeh, and H. Turral, "More people, more food, worse water?: a global review of water pollution from agriculture," Food and Agriculture Organization of the United Nations, 2018.

[13] L. Lin, H. Yang, and X. Xu, "Effects of Water Pollution on Human Health and Disease Heterogeneity: A Review," Jun. 30, 2022, *Frontiers Media S.A.* doi: 10.3389/fenvs.2022.880246.

[14] M. Hasanova, B. Amanullayeva, M. Safarova, B. Palecz, and R. Mammadov, "The effect of deteriorate ecosystems on the world," *Journal of Life Sciences and Biomedicine of ANAS*, no. 01, p. 60, 2025, doi: 10.59849/2710-4915.2025.1.60.

[15] O. M. L. Alharbi, R. A. Khattab, and I. Ali, "Health and environmental effects of persistent organic pollutants," *J Mol Liq*, vol. 263, pp. 442–453, 2018.

[16] S. Wang, W. Yan, and F. Zhao, "Recovery of solid waste as functional heterogeneous catalysts for organic pollutant removal and biodiesel production," *Chemical Engineering Journal*, vol. 401, p. 126104, 2020.

[17] J. Hartmann, I. van Driezum, D. Ohana, G. Lynch, B Berendsen, S. Wuijts, J. P. van der Hoek, and A. M. de Roda Husman, "The effective design of sampling campaigns for emerging chemical and microbial contaminants in drinking water and its resources based on literature mining," *Science of the Total Environment*, vol. 742, p. 140546, 2020.

[18] M. A. Cook and G. D. Wright, "The past, present, and future of antibiotics," *Sci Transl Med*, vol. 14, no. 657, p. eabo7793, 2022.

[19] E. Grundmann, *Gerhard Domagk: The First Man to Triumph Over Infectious Diseases*, vol. 17. LIT Verlag Münster, 2004.

[20] M. I. Hutchings, A. W. Truman, and B. Wilkinson, "Antibiotics: past, present and future," *Curr Opin Microbiol*, vol. 51, pp. 72–80, 2019.

[21] E. Etebu and I. Arikekpar, "Antibiotics: Classification and mechanisms of action with emphasis on molecular perspectives," *International journal of applied microbiology and biotechnology research*, vol. 4, no. 2016, pp. 90–101, 2016.

[22] M. F. Haddad, B. A. Abdullah, H. A. AlObeidi, A. M. Saadi, and M. F. Haddad, "Antibiotic classification, mechanisms, and indications: A review," *International Journal of Medical and All Body Health Research*, vol. 5, no. 3, pp. 39–46, 2024.

[23] C. Chiu, "Definitions, classifications, and antibiotics," in *Urinary Tract Infection: Clinical Perspectives on Urinary Tract Infection*, Springer, 2013, pp. 1–10.

[24] M. Zimina, O. Babich, A. Prosekov, S. Sukhikh, S. Ivanova, M. Shevchenko, and S. Noskova, "Overview of global trends in classification, methods of preparation and application of bacteriocins," *Antibiotics*, vol. 9, no. 9, p. 553, 2020.

[25] P. Malfertheiner, F. Megraud, C. O'Morain, F. Bazzoli, E. El-Omar, D. Graham, R. Hunt, T. Rokkas N. Vakil, and E. J. Kuipers, "Current concepts in the management of Helicobacter pylori infection: the Maastricht III Consensus Report," *Gut*, vol. 56, no. 6, pp. 772–781, 2007.

[26] C. D. Freeman, N. E. Klutman, and K. C. Lamp, "Metronidazole: a therapeutic review and update," *Drugs*, vol. 54, no. 5, pp. 679–708, 1997.

[27] A. H. Ceruelos, L. C. Romero-Quezada, J. C. R. Ledezma, and L. L. Contreras, "Therapeutic uses of metronidazole and its side effects: an update," *Eur Rev Med Pharmacol Sci*, vol. 23, no. 1, pp. 397–401, 2019.

[28] A. T. E. Vilian, K. S. Ranjith, S. J. Lee, R. Umapathi, S. K. Hwang, C. W. Oh, Y. S. Huh, and Y. K. Han, "Hierarchical dense Ni− Co layered double hydroxide supported carbon nanofibers for the electrochemical determination of metronidazole in biological samples," *Electrochim Acta*, vol. 354, p. 136723,

2020.

[29] D. J. Quincey, P. Kay, J. Wilkinson, L. J. Carter, and L. E. Brown, "High concentrations of pharmaceuticals emerging as a threat to Himalayan water sustainability," *Environmental Science and Pollution Research*, vol. 29, no. 11, pp. 16749–16757, 2022.

[30] Q. Cai and J. Hu, "Decomposition of sulfamethoxazole and trimethoprim by continuous UVA/LED/$TiO_2$ photocatalysis: Decomposition pathways, residual antibacterial activity and toxicity," *J Hazard Mater*, vol. 323, pp. 527–536, Feb. 2017, doi: 10.1016/j.jhazmat.2016.06.006.

[31] F. M. Hamed, B. A. Hassan, and M. M. Abdulridha, "The antitumor activity of sulfonamides derivatives," *Int. J. Pharm. Res*, vol. 12, pp. 2512–2519, 2020.

[32] M. Mackeviciute, V. Rita, A. Kazimieras, S. Jurate, L. Raimundas, K. Povilas, and M. Vytautas, "Synthesis and characterization of sulphanilamide and benzimidazole pharmacophores containing γ-amino acid derivatives as dual antimicrobial and anticancer agents," *Arkivoc.*, vol. 2023, no. 7, pp. 1–13, 2023.

[33] H. Turkmen, G. Zengin, and B. Buyukkircali, "Synthesis of sulfanilamide derivatives and investigation of in vitro inhibitory activities and antimicr obial and physical properties," *Bioorganic Chemistry*, vol. 39, no. 3, pp. 114–119, Mar. 2011, doi: 10.1016/j.bioorg.2011.02.004.

[34] S. J. Zhang, H. Q. Yu, and Q. R. Li, "Radiolytic degradation of Acid Orange 7: A mechanistic study," *Chemosphere*, vol. 61, no. 7, pp. 1003–1011, Nov. 2005, doi: 10.1016/j.chemosphere.2005.03.008.

[35] H. Liu, G. Li, J. Qu, and H. Liu, "Degradation of azo dye Acid Orange 7 in water by Fe0/granular activated carbon system in the presence of ultrasound," *J Hazard Mater*, vol. 144, no. 1–2, pp. 180–186, May 2007, doi: 10.1016/j.jhazmat.2006.10.009.

[36] S. G. Dmitrienko, E. V. Kochuk, V. V. Apyari, V. V. Tolmacheva, and Y. A. Zolotov, "Recent advances in sample preparation techniques and methods of sulfonamides detection - A review," Nov. 19, 2014, *Elsevier B.V.* doi: 10.1016/j.aca.2014.08.023.

[37] A. Ait Lahcen, S. Ait Errayess, and A. Amine, "Voltammetric determination of sulfonamides using paste electrodes based on various carbon nanomaterials," *Microchimica Acta*, vol. 183, no. 7, pp. 2169–2176, 2016.

[38] A. Joshi and K. H. Kim, "Recent advances in nanomaterial-based electrochemical detection of antibiotics: Challenges and future perspectives," Apr. 01, 2020, *Elsevier Ltd*. doi: 10.1016/j.bios.2020.112046.

[39] E. D. Crawford *et al.*, "Androgen receptor targeted treatments of prostate cancer: 35 years of progress with antiandrogens," *J Urol*, vol. 200, no. 5, pp. 956–966, 2018.

[40] N. F. Goodman, R. H. Cobin, W. Futterweit, J. S. Glueck, R. S. Legro, and E. Carmina, "American Association of Clinical Endocrinologists, American College of Endocrinology, and Androgen Excess and PCOS Society Disease State Clinical Review: Guide to the Best Practices in the Evaluation and Treatment of Polycystic Ovary Syndrome - Part 1," *Endocrine Practice*, vol. 21,

no. 11, pp. 1291–1300, Nov. 2015, doi: 10.4158/EP15748.DSC.

[41] T. I. A. Gouveia, I. H. Mota, A. M. T. Silva, A. Alves, and M. S. F. Santos, "Are cytostatic drugs in surface waters a potential threat?," *Science of the Total Environment*, vol. 853, Dec. 2022, doi: 10.1016/j.scitotenv.2022.158559.

[42] "Effects of the commercial antiand".

[43] Z. Fathi, S. Jahani, and M. M. Foroughi, "Electrode material fabricated by doping holmium in nickel oxide and its application in electrochemical sensor for flutamide determination as a prostate cancer drug," *Monatsh Chem*, vol. 152, no. 7, pp. 757–766, Jul. 2021, doi: 10.1007/s00706-021-02794-8.

[44] N. Nataraj, T. W. Chen, S. M. Chen, T. Kokulnathan, F. Ahmed, T. Alshahrani, and N. Arshi, "Electrochemical detection of anti-cancer drug flutamide in biological fluids with calcium molybdate/molybdenum oxide as an effective electrocatalyst," *J Taiwan Inst Chem Eng*, vol. 156, Mar. 2024, doi: 10.1016/j.jtice.2024.105348.

[45] R. Keerthika Devi, G. Muthusankar, S.-M. Chen, and G. Gopalakrishnan, "In situ formation of $Co_3O_4$ nanoparticles embedded N-doped porous carbon nanocomposite: a robust material for electrocatalytic detection of anticancer drug flutamide and supercapacitor application", doi: 10.1007/s00604-021-04860-8/Published.

[46] N. M. Umesh, J. A. Jesila, S. F. Wang, M. Govindasamy, R. A. Alshgari, M. Ouladsmane, and I. V. Asharani, "Fabrication of highly sensitive anticancer drug sensor based on heterostructured ZnO-$Co_3O_4$ capped on carbon nitride nanomaterials," *Microchemical Journal*, vol. 167, Aug. 2021, doi: 10.1016/j.microc.2021.106244.

[47] "A low-cost and facile electrochemical sensor for the trace-level recognition of".

[48] T. Ravele, N. W. Hlongwa, T. T. I. Nkambule, N. N. Gumbi, and K. E. Sekhosana, "Electrochemical Sensors Based on Manganese and Cobalt Oxide Nanostructures for the Detection of Flutamide and its Derivatives in Real Water Samples," *J Clust Sci*, vol. 35, no. 1, pp. 285–297, Jan. 2024, doi: 10.1007/s10876-023-02474-z.

[49] T. W. Tseng, U. Rajaji, T. W. Chen, S. M. Chen, Y. C. Huang, V. Mani, and A. I. Jothi, "Sonochemical synthesis and fabrication of perovskite type calcium titanate interfacial nanostructure supported on graphene oxide sheets as a highly efficient electrocatalyst for electrochemical detection of chemotherapeutic drug," *Ultrason Sonochem*, vol. 69, Dec. 2020, doi: 10.1016/j.ultsonch.2020.105242.

[50] A. Sangili, V. Vinothkumar, S. M. Chen, P. Veerakumar, and K. C. Lin, "Gold Nanoparticle Embedded on a Reduced Graphene Oxide/ polypyrrole Nanocomposite: Voltammetric sensing of furazolidone and flutamide," *Langmuir*, vol. 36, no. 46, pp. 13949–13962, Nov. 2020, doi: 10.1021/acs.langmuir.0c02448.

[51] T. S. K. Sharma and K. Y. Hwa, "Rational design and preparation of copper vanadate anchored on sulfur doped reduced graphene oxide nanocomposite for electrochemical sensing of antiandrogen drug nilutamide using flexible electrodes," *J Hazard Mater*, vol. 410, May 2021, doi:

10.1016/j.jhazmat.2020.124659.

[52] G. Zhang, X. Liu, S. Lu, J. Zhang, and W. Wang, "Occurrence of typical antibiotics in Nansi Lake's inflowing rivers and antibiotic source contribution to Nansi Lake based on principal component analysis-multiple linear regression model," *Chemosphere*, vol. 242, p. 125269, 2020.

[53] J. Wu, J. Liu, Z. Pan, B. Wang, and D. Zhang, "Spatiotemporal distributions and ecological risk assessment of pharmaceuticals and personal care products in groundwater in North China," *Hydrology Research*, vol. 51, no. 5, pp. 911–924, 2020.

[54] S. Xiao, J. Wan, Y. Wang, Z. Yan, Y. Ma, J. Sun, M. Tang, J. Cao, and J. Chen, "Distribution, sources, and risk assessment of emerging contaminants in the effluents from large-scale wastewater treatment plants in Guangzhou central districts, South China," *Water Air Soil Pollut*, vol. 234, no. 7, p. 455, 2023.

[55] M. A. Makary, K. Kaczmarski, and K. Nachman, "A call for doctors to recommend antibiotic-free foods: agricultural antibiotics and the public health crisis of antimicrobial resistance," *J Antibiot (Tokyo)*, vol. 71, no. 8, pp. 685–687, 2018.

[56] A. Sengar and A. Vijayanandan, "Human health and ecological risk assessment of 98 pharmaceuticals and personal care products (PPCPs) detected in Indian surface and wastewaters," Feb. 10, 2022, *Elsevier B.V.* doi: 10.1016/j.scitotenv.2021.150677.

[57] N. Ranjan, P. K. Singh, and N. S. Maurya, "Pharmaceuticals in water as emerging pollutants for river health: A critical review under Indian conditions," *Ecotoxicol Environ Saf*, vol. 247, p. 114220, 2022.

[58] X. Zhou, G. J. P. Cuasquer, Z. Li, H. P. Mang, and Y. Lv, "Occurrence of typical antibiotics, representative antibiotic-resistant bacteria, and genes in fresh and stored source-separated human urine," *Environ Int*, vol. 146, Jan. 2021, doi: 10.1016/j.envint.2020.106280.

[59] M. Ashfaq, K. N. Khan, M. S. Ur Rehman, G. Mustafa, M. F. Nazar, Q. Sun, J. Iqbal, S.I. Mulla, and C. P. Yu, "Ecological risk assessment of pharmaceuticals in the receiving environment of pharmaceutical wastewater in Pakistan," *Ecotoxicol Environ Saf*, vol. 136, pp. 31–39, 2017.

[60] Y. Xiao, H. Chang, A. Jia, and J. Hu, "Trace analysis of quinolone and fluoroquinolone antibiotics from wastewaters by liquid chromatography-electrospray tandem mass spectrometry," *J Chromatogr A*, vol. 1214, no. 1–2, pp. 100–108, Dec. 2008, doi: 10.1016/j.chroma.2008.10.090.

[61] S. Sa-Nguanprang, A. Phuruangrat, and O. Bunkoed, "Fluorescent probe of quantum dots and zinc oxide in a highly selective polymer simultaneously determined florfenicol and sparfloxacin," *Microchimica Acta*, vol. 190, no. 4, p. 129, 2023.

[62] N. Chansud, R. Kaewnok, P. Nurerk, F. Davis, and O. Bunkoed, "Ultrasensitive and highly selective fluorescence probe of nitrogen-doped graphene quantum dots and zinc oxide decorated carbon foam incorporated molecularly imprinted polymer for trace sparfloxacin determination," *Mater Today Commun*, vol. 35, p.

105687, 2023.

[63] C. D. Freeman, N. E. Klutman, and K. C. Lamp, “Metronidazole: a therapeutic review and update,” *Drugs*, vol. 54, no. 5, pp. 679–708, 1997.

[64] A. Tačić, V. Nikolić, L. Nikolić, and I. Savić, “Antimicrobial sulfonamide drugs,” *Adv. Technol*, vol. 6, no. 1, pp. 58–71, 2017.

[65] B. R. Goldspiel and D. R. Kohler, “Flutamide: an antiandrogen for advanced prostate cancer,” *Dicp*, vol. 24, no. 6, pp. 616–623, 1990.

[66] W. H. HALL and W. W. SPINK, “Sulfamerazine: clinical evaluation in 116 cases,” *J Am Med Assoc*, vol. 123, no. 3, pp. 125–131, 1943.

[67] J. J. Schentag, “Sparfloxacin: A review,” *Clin Ther*, vol. 22, no. 4, pp. 372–387, 2000.

[68] P. H. Long, “Sulfapyridine,” *J Am Med Assoc*, vol. 112, no. 6, pp. 538–539, 1939.

[69] R. E. Buck and K. E. Price, “Cefadroxil, a new broad-spectrum cephalosporin,” *Antimicrob Agents Chemother*, vol. 11, no. 2, pp. 324–330, 1977.

[70] B. Aslam, R. Asghar, S. Muzammil, M. Shafique, A. B. Siddique, M. Khurshid, M. Ijaz, M. H. Rasool, T. H. Chaudhry, A. Aamir, and Z. Baloch, “AMR and Sustainable Development Goals: at a crossroads,” *Global Health*, vol. 20, no. 1, p. 73, 2024.

[71] D. G. J. Larsson, W. H. Gaze, R. Laxminarayan, and E. Topp, “AMR, One Health and the environment,” *Nat Microbiol*, vol. 8, no. 5, pp. 754–755, 2023.

[72] K. W. K. Tang, B. C. Millar, and J. E. Moore, “Antimicrobial resistance (AMR),” *Br J Biomed Sci*, vol. 80, p. 11387, 2023.

[73] S. Amann, K. Neef, and S. Kohl, “Antimicrobial resistance (AMR),” *European Journal of Hospital Pharmacy*, vol. 26, no. 3, pp. 175–177, 2019.

[74] J. Wang, L. Chu, L. Wojnárovits, and E. Takács, “Occurrence and fate of antibiotics, antibiotic resistant genes (ARGs) and antibiotic resistant bacteria (ARB) in municipal wastewater treatment plant: An overview,” *Science of the Total Environment*, vol. 744, p. 140997, 2020.

[75] R. K. Manoharan, F. Ishaque, and Y.-H. Ahn, “Fate of antibiotic resistant genes in wastewater environments and treatment strategies-A review,” *Chemosphere*, vol. 298, p. 134671, 2022.

[76] R. Capita and C. Alonso-Calleja, “Antibiotic-resistant bacteria: a challenge for the food industry,” *Crit Rev Food Sci Nutr*, vol. 53, no. 1, pp. 11–48, 2013.

[77] A. K. Murray, I. C. Stanton, H. J. Tipper, H. Wilkinson, W. Schmidt, A. Hart, A. C. Singer, and W. H. Gaze, “A critical meta-analysis of predicted no effect concentrations for antimicrobial resistance selection in the environment,” *Water Res*, vol. 266, p. 122310, 2024.

[78] Q. Yan, X. Gao, Y.P. Chen, X.Y. Peng, Y.X. Zhang, X.M. Gan, C.F. Zi, and J.S. Guo, “Occurrence, fate and ecotoxicological assessment of pharmaceutically active compounds in wastewater and sludge from wastewater treatment plants in Chongqing, the Three Gorges Reservoir Area,” *Science of the Total Environment*, vol. 470, pp. 618–630, 2014.

[79] R. O. Carey and K. W. Migliaccio, “Contribution of wastewater treatment plant effluents to nutrient dynamics in aquatic systems: a review,” *Environ Manage*,

vol. 44, no. 2, pp. 205–217, 2009.

[80] A. Elbehiry, E. Marzouk, A. Abalkhail, M.H. Abdelsalam, M.E.A. Mostafa, M. Alasiri, and M. Ibrahe, "Detection of antimicrobial resistance via state-of-the-art technologies versus conventional methods," *Front Microbiol*, vol. 16, p. 1549044, 2025.

[81] M. A. Salam, M. Y. Al-Amin, J. S. Pawar, N. Akhter, and I. B. Lucy, "Conventional methods and future trends in antimicrobial susceptibility testing," *Saudi J Biol Sci*, vol. 30, no. 3, p. 103582, 2023.

[82] R. Sukanya, D. C. da Silva Alves, and C. B. Breslin, "Recent developments in the applications of 2D transition metal dichalcogenides as electrocatalysts in the generation of hydrogen for renewable energy conversion," *J Electrochem Soc*, vol. 169, no. 6, p. 064504, 2022.

[83] Z. K. Heiba, M. B. Mohamed, and S. I. Ahmed, "Modifying the structure and optical characteristics of $ZnMn_2O_4$ by alloying with CdS to form heterostructure nanocomposite," *Applied Physics A*, vol. 127, no. 11, p. 883, 2021.

[84] S. Manzeli, D. Ovchinnikov, D. Pasquier, O. V Yazyev, and A. Kis, "2D transition metal dichalcogenides," *Nat Rev Mater*, vol. 2, no. 8, pp. 1–15, 2017.

[85] R. Roldán, M. P. López-Sancho, F. Guinea, E. Cappelluti, J. A. Silva-Guillén, and P. Ordejón, "Momentum dependence of spin-orbit interaction effects in single-layer and multi-layer transition metal dichalcogenides," *2d Mater*, vol. 1, no. 3, Dec. 2014, doi: 10.1088/2053-1583/1/3/034003.

[86] E. A. Marseglia, "Transition metal dichalcogenides and their intercalates," *Int Rev Phys Chem*, Aug. 2008, doi: https://doi.org/10.1080/01442358309353343.

[87] J. Sun *et al.*, "Synthesis methods of two-dimensional MoS2: A brief review," Jul. 01, 2017, *MDPI AG*. doi: 10.3390/cryst7070198.

[88] O. Samy, S. Zeng, M. D. Birowosuto, and A. El Moutaouakil, "A review on MoS2 properties, synthesis, sensing applications and challenges," *Crystals (Basel)*, vol. 11, no. 4, 2021, doi: 10.3390/cryst11040355.

[89] Q. Fu, J. Han, X. Wang, P. Xu, T. Yao, J. Zhong, W. Zhong, S. Liu, T. Gao, Z. Zhang, L. Xu, and B. Song, "2D Transition Metal Dichalcogenides: Design, Modulation, and Challenges in Electrocatalysis," Feb. 01, 2021, *Wiley-VCH Verlag*. doi: 10.1002/adma.201907818.

[90] W. Choi, N. Choudhary, G. H. Han, J. Park, D. Akinwande, and Y. H. Lee, "Recent development of two-dimensional transition metal dichalcogenides and their applications," *Materials Today*, vol. 20, no. 3, pp. 116–130, 2017.

[91] M. Donarelli and L. Ottaviano, "2D Materials for Gas Sensing Applications: A Review on Graphene Oxide, $MoS_2$, $WS_2$ and Phosphorene," 2018, *MDPI AG*. doi: 10.3390/s18113638.

[92] J. A. Stewart and D. E. Spearot, "Atomistic simulations of nanoindentation on the basal plane of crystalline molybdenum disulfide ($MoS_2$)," *Model Simul Mat Sci Eng*, vol. 21, no. 4, p. 045003, 2013.

[93] K. Ai, C. Ruan, M. Shen, and L. Lu, "$MoS_2$ Nanosheets with Widened Interlayer Spacing for High-Efficiency Removal of Mercury in Aquatic Systems," *Adv Funct Mater*, vol. 26, no. 30, pp. 5542–5549, Aug. 2016, doi:

10.1002/adfm.201601338.

[94] A. Splendiani, L. Sun, Y. Zhang, T. Li, J. Kim, C.Y. Chim, G. Galli, and F. Wang, "Emerging photoluminescence in monolayer $MoS_2$," *Nano Lett*, vol. 10, no. 4, pp. 1271–1275, Apr. 2010, doi: 10.1021/nl903868w.

[95] O. Lopez-Sanchez, D. Lembke, M. Kayci, A. Radenovic, and A. Kis, "Ultrasensitive photodetectors based on monolayer $MoS_2$," *Nat Nanotechnol*, vol. 8, no. 7, pp. 497–501, 2013.

[96] B. Radisavljevic, M. B. Whitwick, and A. Kis, "Small-signal amplifier based on single-layer $MoS_2$," *Appl Phys Lett*, vol. 101, no. 4, 2012.

[97] B. Radisavljevic, M. B. Whitwick, and A. Kis, "Integrated circuits and logic operations based on single-layer $MoS_2$," *ACS Nano*, vol. 5, no. 12, pp. 9934–9938, 2011.

[98] B. Radisavljevic and A. Kis, "Mobility engineering and a metal–insulator transition in monolayer $MoS_2$," *Nat Mater*, vol. 12, no. 9, pp. 815–820, 2013.

[99] V. Forsberg, R. Zhang, J. Bäckström, C. Dahlström, B. Andres, M. Norgren, M. Andersson, "Exfoliated $MoS_2$ in water without additives," *PLoS One*, vol. 11, no. 4, p. e0154522, 2016.

[100] W. Zhang, Y. Wang, D. Zhang, S. Yu, W. Zhu, J. Wang, F. Zheng, S. Wang, and J. Wang, "A one-step approach to the large-scale synthesis of functionalized $MoS_2$ nanosheets by ionic liquid assisted grinding," *Nanoscale*, vol. 7, no. 22, pp. 10210–10217, 2015.

[101] M. Zhang, R.C.T. Howe, R.I. Woodward, E.J.R. Kelleher, F. Torrisi, G. Hu, S.V. Popov, and J.R. Taylor, "Solution processed $MoS_2$-PVA composite for sub-bandgap mode-locking of a wideband tunable ultrafast Er: fiber laser," *Nano Res*, vol. 8, no. 5, pp. 1522–1534, 2015.

[102] N. Liu, P. Kim, J. H. Kim, J. H. Ye, S. Kim, and C. J. Lee, "Large-area atomically thin $MoS_2$ nanosheets prepared using electrochemical exfoliation," *ACS Nano*, vol. 8, no. 7, pp. 6902–6910, 2014.

[103] G. Eda, H. Yamaguchi, D. Voiry, T. Fujita, M. Chen, and M. Chhowalla, "Photoluminescence from chemically exfoliated $MoS_2$," *Nano Lett*, vol. 11, no. 12, pp. 5111–5116, 2011.

[104] Z. Zeng, Z. Yin, X. Huang, H. Li, Q. He, G. Lu, F. Boey, H. Zhang, "Single-layer semiconducting nanosheets: high-yield preparation and device fabrication," *Angewandte Chemie-International Edition*, vol. 50, no. 47, pp. 11093–11097, 2011.

[105] X. Fan, P. Xu, D. Zhou, Y. Sun, Y.C. Li, M.A.T. Nguyen, M. Terrones, T.E. Mallouk, "Fast and efficient preparation of exfoliated 2H $MoS_2$ nanosheets by sonication-assisted lithium intercalation and infrared laser-induced 1T to 2H phase reversion," *Nano Lett*, vol. 15, no. 9, pp. 5956–5960, 2015.

[106] J. N. Coleman, M. Lotya, A. O'Neill, S. D. Bergin, P. J. King, U. Khan, K. Young, A. Gaucher, "Two-dimensional nanosheets produced by liquid exfoliation of layered materials," *Science (1979)*, vol. 331, no. 6017, pp. 568–571, 2011.

[107] A. R. Rezk, "Acoustic–Excitonic Coupling for Dynamic Photoluminescence Manipulation of Quasi-2D $MoS_2$ Nanoflakes," *Adv Opt Mater*, vol. 3, no. 7, pp.

888–894, 2015.

[108] S. Walia, S. Balendhran, Y. Wang, R. A. Kadir, A. S. Zoolfakar, P. Atkin, J. Z. Ou, S. Sriram, K. Kalantar-zadeh, and M. Bhaskaran, "Characterization of metal contacts for two-dimensional $MoS_2$ nanoflakes," *Appl Phys Lett*, vol. 103, no. 23, 2013.

[109] G. M. Cai, J. K. Jian, X. L. Chen, M. Lei, and W. Y. Wang, "Regular hexagonal $MoS_2$ microflakes grown from $MoO_3$ precursor," *Applied Physics A*, vol. 89, no. 3, pp. 783–788, 2007.

[110] Y. Zhan, Z. Liu, S. Najmaei, P. M. Ajayan, and J. Lou, "Large area vapor phase growth and characterization of $MoS_2$ atomic layers on $SiO_2$ substrate," *arXiv preprint arXiv:1111.5072*, 2011.

[111] I. Song, C. Park, M. Hong, J. Baik, H. Shin, and H. C. Choi, "Inside Back Cover: Patternable Large-Scale Molybdenium Disulfide Atomic Layers Grown by Gold-Assisted Chemical Vapor Deposition (Angew. Chem. Int. Ed. 5/2014)," *Angewandte Chemie International Edition*, vol. 53, no. 5, p. 1449, 2014.

[112] Y. Yu, C. Li, Y. Liu, L. Su, Y. Zhang, and L. Cao, "Controlled scalable synthesis of uniform, high-quality monolayer and few-layer $MoS_2$ films," *Sci Rep*, vol. 3, no. 1, p. 1866, 2013.

[113] V. Kranthi Kumar, S. Dhar, T. H. Choudhury, S. A. Shivashankar, and S. Raghavan, "A predictive approach to CVD of crystalline layers of TMDs: The case of $MoS_2$," *Nanoscale*, vol. 7, no. 17, pp. 7802–7810, May 2015, doi: 10.1039/c4nr07080a.

[114] B. Olofinjana, G. Egharevba, B. Taleatu, O. Akinwunmi, and E. O. Ajayi, "MOCVD of Molybdenum Sulphide Thin Film Via Single Solid Source Precursor Bis-(Morpholinodithioato-s,s')-Mo," *Journal of Modern Physics*, vol. 02, no. 05, pp. 341–349, 2011, doi: 10.4236/jmp.2011.25042.

[115] K. Kang, S. Xie, L. Huang, Y. Han, P.Y. Huang, K.F. Mak, C.J. Kim, D. Muller, and J Park, "High-mobility three-atom-thick semiconducting films with wafer-scale homogeneity," *Nature*, vol. 520, no. 7549, pp. 656–660, 2015.

[116] S. Vishwanath, X. Liu, S. Rouvimov, P.C. Mende, A. Azcatl, S. McDonnell, R.M. Wallace, "Comprehensive structural and optical characterization of MBE grown $MoSe_2$ on graphite, $CaF_2$ and graphene," *2d Mater*, vol. 2, no. 2, p. 024007, 2015.

[117] X. Qin, P. Ke, A. Wang, and K. H. Kim, "Microstructure, mechanical and tribological behaviors of $MoS_2$-Ti composite coatings deposited by a hybrid HIPIMS method," *Surf Coat Technol*, vol. 228, pp. 275–281, 2013.

[118] X. Zhou, B. Xu, Z. Lin, D. Shu, and L. Ma, "Hydrothermal synthesis of flower-like $MoS_2$ nanospheres for electrochemical supercapacitors," *J Nanosci Nanotechnol*, vol. 14, no. 9, pp. 7250–7254, 2014.

[119] X. Feng, Q. Tang, J. Zhou, J. Fang, P. Ding, L. Sun, and L. Shi., "Novel mixed–solvothermal synthesis of $MoS_2$ nanosheets with controllable morphologies," *Crystal Research and Technology*, vol. 48, no. 6, pp. 363–368, 2013.

[120] H. Liao, Y. Wang, S. Zhang, and Y. Qian, "A solution low-temperature route to $MoS_2$ fiber," *Chemistry of Materials*, vol. 13, no. 1, pp. 6–8, 2000.

[121] Q. Li, E.C. Walter, W.E. Van der Veer, B.J. Murray, J.T. Newberg, E.W.

Bohannan, and J.A. Switzer, "Molybdenum disulfide nanowires and nanoribbons by electrochemical/chemical synthesis," *J Phys Chem B*, vol. 109, no. 8, pp. 3169–3182, 2005.

[122] M. Nguyen, P.D. Tran, S.S. Pramana, R.L. Lee, S.K. Batabyal, N. Mathews, L.H. Wong, and M. Graetzel, "In situ photo-assisted deposition of $MoS_2$ electrocatalyst onto zinc cadmium sulphide nanoparticle surfaces to construct an efficient photocatalyst for hydrogen generation," *Nanoscale*, vol. 5, no. 4, pp. 1479–1482, 2013.

[123] D. Geng, X. Bo, and L. Guo, "Ni-doped molybdenum disulfide nanoparticles anchored on reduced graphene oxide as novel electroactive material for a non-enzymatic glucose sensor," *Sens Actuators B Chem*, vol. 244, pp. 131–141, 2017, doi: 10.1016/j.snb.2016.12.122.

[124] L. Fang, F. Wang, Z. Chen, Y. Qiu, T. Zhai, M. Hu, C. Zhang, and K. Huang, "Flower-like $MoS_2$ decorated with $Cu_2O$ nanoparticles for non-enzymatic amperometric sensing of glucose," *Talanta*, vol. 167, pp. 593–599, May 2017, doi: 10.1016/j.talanta.2017.03.008.

[125] X. Lin, Y. Ni, and S. Kokot, "Electrochemical and bio-sensing platform based on a novel 3D Cu nano-flowers/layered $MoS_2$ composite," *Biosens Bioelectron*, vol. 79, pp. 685–692, May 2016, doi: 10.1016/j.bios.2015.12.072.

[126] X. Xia, Z. Zheng, Y. Zhang, X. Zhao, and C. Wang, "Synthesis of Ag-$MoS_2$/chitosan nanocomposite and its application for catalytic oxidation of tryptophan," *Sens Actuators B Chem*, vol. 192, pp. 42–50, 2014, doi: 10.1016/j.snb.2013.10.096.

[127] V. Mani, M. Govindasamy, S. M. Chen, B. Subramani, A. Sathiyan, and J. P. Merlin, "Determination of folic acid using graphene/molybdenum disulfide nanosheets/gold nanoparticles ternary composite," *Int J Electrochem Sci*, vol. 12, no. 1, pp. 258–267, 2017, doi: 10.20964/2017.01.35.

[128] Y. Q. Zhu, W. K. Hsu, H. Terrones, N. Grobert, B. H. Chang, M. Terrones, B. Q. Wei, and H. W. Kroto, "Morphology, structure and growth of $WS_2$ nanotubes," *J Mater Chem*, vol. 10, no. 11, pp. 2570–2577, 2000.

[129] C. Lan, C. Li, J. C. Ho, and Y. Liu, "2D $WS_2$: from vapor phase synthesis to device applications," *Adv Electron Mater*, vol. 7, no. 7, p. 2000688, 2021.

[130] S. Ott, M. Lakmann, and C. Backes, "Impact of pretreatment of the bulk starting material on the efficiency of liquid phase exfoliation of $WS_2$," *Nanomaterials*, vol. 11, no. 5, May 2021, doi: 10.3390/nano11051072.

[131] F. Rashvand, "CHEMICAL DOPING OF LIQUID EXFOLIATED 2D-MATERIALS." heiDOK-The Heidelberg Document Repository, 12 November 2021, doi: 10.11588/heidok.00030764.

[132] R. Pourakbari, M. Yousefi, B. Khalilzadeh, M. H. Irani-nezhad, A. Khataee, L. Aghebati-Maleki, "Early stage evaluation of colon cancer using tungsten disulfide quantum dots and bacteriophage nano-biocomposite as an efficient electrochemical platform," *Cancer Nanotechnol*, vol. 13, no. 1, Dec. 2022, doi: 10.1186/s12645-022-00113-2.

[133] M. Garg, M. Chatterjee, A. L. Sharma, and S. Singh, "Label-free approach for

electrochemical ferritin sensing using biosurfactant stabilized tungsten disulfide quantum dots," *Biosens Bioelectron*, vol. 151, Mar. 2020, doi: 10.1016/j.bios.2019.111979.

[134] G. Wu, H. Zheng, Y. Xing, C. Wang, X. Yuan, and X. Zhu, "A sensitive electrochemical sensor for environmental toxicity monitoring based on tungsten disulfide nanosheets/hydroxylated carbon nanotubes nanocomposite," *Chemosphere*, vol. 286, Jan. 2022, doi: 10.1016/j.chemosphere.2021.131602.

[135] Y. Wang, C. Gong, Y. Zhu, Q. Wang, and L. Geng, "Signal-on electrochemical aptasensor for sensitive detection of sulfamethazine based on carbon quantum dots/tungsten disulfide nanocomposites," *Electrochim Acta*, vol. 393, Oct. 2021, doi: 10.1016/j.electacta.2021.139054.

[136] K. J. Huang, Y. J. Liu, H. B. Wang, T. Gan, Y. M. Liu, and L. L. Wang, "Signal amplification for electrochemical DNA biosensor based on two-dimensional graphene analogue tungsten sulfide-graphene composites and gold nanoparticles," *Sens Actuators B Chem*, vol. 191, pp. 828–836, 2014, doi: 10.1016/j.snb.2013.10.072.

[137] K. Balamurugan, R. Karthik, S.M. Chen, R. Sukanya, B. T. Subramanian, V. M. Nair Biju d, J.J. Shim, and C. B. Breslin, "Heterostructures of mixed metal oxides (ZnMnO3/ZnO) synthesized by a wet-chemical approach and their application for the electrochemical detection of the drug chlorpromazine," *Compos B Eng*, vol. 236, p. 109822, 2022.

[138] R. Rajakumaran, R. Sukanya, S. M. Chen, R. Karthik, C. B. Breslin, and P. M. Shafi, "Synthesis and characterization of pyrochlore-type praseodymium stannate nanoparticles: an effective electrocatalyst for detection of nitrofurazone drug in biological samples," *Inorg Chem*, vol. 60, no. 4, pp. 2464–2476, 2021.

[139] A. A. Ansari *et al.*, "ZnO nanostructures – Future frontiers in photocatalysis, solar cells, sensing, supercapacitor, fingerprint technologies, toxicity, and clinical diagnostics," Sep. 15, 2024, *Elsevier B.V.* doi: 10.1016/j.ccr.2024.215942.

[140] Q. Zhao, Z. Yan, C. Chen, and J. Chen, "Spinels: controlled preparation, oxygen reduction/evolution reaction application, and beyond," *Chem Rev*, vol. 117, no. 15, pp. 10121–10211, 2017.

[141] Y. Zhu, Q. Lin, Y. Zhong, H. A. Tahini, Z. Shao, and H. Wang, "Metal oxide-based materials as an emerging family of hydrogen evolution electrocatalysts," Oct. 01, 2020, *Royal Society of Chemistry*. doi: 10.1039/d0ee02485f.

[142] B. Karuppaiah, J. Anupriya, S. M. Chen, and S. J. Park, "An emergent electrochemical sensor based on spinel zinc manganese oxide decorated on amine-functionalized boron nitride for enhanced electrochemical determination of herbicide mesotrione," *Process Safety and Environmental Protection*, vol. 176, pp. 292–303, Aug. 2023, doi: 10.1016/j.psep.2023.06.008.

[143] I. Ganesh, "A review on magnesium aluminate (MgAl2O4) spinel: Synthesis, processing and applications," Feb. 2013. doi: 10.1179/1743280412Y.0000000001.

[144] M. Annalakshmi, S. Kumaravel, T. S. T. Balamurugan, S. M. Chen, and J. L. He,

"Facile solvothermal synthesis of ultrathin spinel ZnMn2O4 nanospheres: An efficient electrocatalyst for in vivo and in vitro real time monitoring of H2O2," *Journal of Electroanalytical Chemistry*, vol. 900, Nov. 2021, doi: 10.1016/j.jelechem.2021.115674.

[145] F. M. Courtel, Y. Abu-Lebdeh, and I. J. Davidson, "ZnMn2O4 nanoparticles synthesized by a hydrothermal method as an anode material for Li-ion batteries," *Electrochim Acta*, vol. 71, pp. 123–127, Jun. 2012, doi: 10.1016/j.electacta.2012.03.108.

[146] J. Song, T. Guo, Q. Wang, M. Yao, and Y. Mao, "Preparation of Mesoporous Structure Electrode Materials ZnMn 2 O 4 by Co-precipitation Method", doi: 10.1051/e3sconf/20.

[147] Z. K. Heiba, M. B. Mohamed, A. M. El-Naggar, and Y. Altowairqi, "Structure and dielectric properties of ZnMn2O4/NiFe2O4 nanocomposite," *Applied Physics A*, vol. 127, no. 8, p. 577, 2021.

[148] Z. K. Heiba, M. B. Mohamed, and A. Badawi, "Structure and optical properties of nano-ZnMn2O4/CuS solid solution heterostructure," *J Solgel Sci Technol*, vol. 101, no. 3, pp. 637–648, 2022.

[149] S. Aman, N. Ahmad, S. Manzoor, M. M. Alanazi, S.A.M. Abdelmohsen, R. Y. Khosa, and A. G. Al-Sehemi, "Effect of Copper Substitution on the Electrocatalytic Activity of ZnMn2O4 Spinel Embedded on Reduced Graphene Oxide Nanosheet for the Oxygen Evolution Process," *Catalysis Surveys from Asia*, vol. 27, no. 2, pp. 165–179, Jun. 2023, doi: 10.1007/s10563-023-09389-9.

[150] S. Singh, A. Shrivastava, D. K. Singh, M. Yadav, V. Singh, V. Rathour, A. Tiwari, I Sinha, "ZnMn2O4 spinel nanocrystals-decorated multi-walled carbon nanotubes for oxygen reduction: Experimental and theoretical studies on the strong coupling facilitated four-electron selectivity," *Int J Hydrogen Energy*, vol. 56, pp. 188–198, Feb. 2024, doi: 10.1016/j.ijhydene.2023.12.157.

[151] M. Shi, B. Wang, Y. Shen, J. Jiang, W. Zhu, Y. Su, M. Narayanasamy, S. Angaiah, C Yan, and Q Peng, "3D assembly of MXene-stabilized spinel ZnMn2O4 for highly durable aqueous zinc-ion batteries," *Chemical Engineering Journal*, vol. 399, Nov. 2020, doi: 10.1016/j.cej.2020.125627.

[152] Z. K. Heiba, A. A. Shaltout, S. I. Ahmed, E. Alzahrani, H. H. Wahba, M. A. Deyab, and M. B. Mohamed, "Functional properties of quaternary metals (1− x) ZnMn2O4/(x) MgFe2O4 as supercapacitor electrode," *Applied Physics A*, vol. 127, no. 1, p. 12, 2021.

[153] Z. K. Heiba, M. B. Mohamed, and S. I. Ahmed, "Modifying the structure and optical characteristics of ZnMn2O4 by alloying with CdS to form heterostructure nanocomposite," *Applied Physics A*, vol. 127, no. 11, p. 883, 2021.

[154] J. M. Gonçalves, "Sensing performances of spinel ferrites MFe2O4 (M = Mg, Ni, Co, Mn, Cu and Zn) based electrochemical sensors: A review," Nov. 15, 2022, *Elsevier B.V.* doi: 10.1016/j.aca.2022.340362.

[155] B. Wu, L. Xiao, M. Zhang, C. Yang, Q. Li, G. Li, Q. He, and J. Liu, "Facile synthesis of dendritic-like CeO2/rGO composite and application for detection of uric acid and tryptophan simultaneously," *J Solid State Chem*, vol. 296, Apr.

2021, doi: 10.1016/j.jssc.2021.122023.

[156] S. Zhang, P. Ling, Y. Chen, J. Liu, and C. Yang, "2D/2D porous Co3O4/rGO nanosheets act as an electrochemical sensor for voltammetric tryptophan detection," *Diam Relat Mater*, vol. 135, May 2023, doi: 10.1016/j.diamond.2023.109811.

[157] H. Guo, X. Wang, H. Li, M. Liu, L. Xing, and H. Zhai, "AFe2O4 (A= Cu, Ni, Co, Mg, Ce, Mn) Catalysts for Hydrogen-Rich Syngas Production from Corn Straw Pyrolysis-Catalytic Steam Reforming," *Energy Technology*, vol. 13, no. 1, p. 2401302, 2025.

[158] Y. Guo, X. Chen, W. Ma, and X. Zhao, "CeFe2O4Nanoparticle/Graphene Oxide Composites with Synergistic Superhydrophobicity and Microwave Absorption," *ACS Appl Nano Mater*, vol. 5, no. 5, pp. 6513–6522, May 2022, doi: 10.1021/acsanm.2c00546.

[159] X. Chen, M. Yang, X. Zhao, D. Hu, W. Liu, and W. Ma, "Tailoring superhydrophobic PDMS/CeFe2O4/MWCNTs nanocomposites with conductive network for highly efficient microwave absorption," *Chemical Engineering Journal*, vol. 432, Mar. 2022, doi: 10.1016/j.cej.2021.134226.

[160] L. Zhang, T. Ai, S.Dai, G. Xiao, X. Xiong, N. Zhang, J. Si, G. Wang, W. Xue, and J. Xu, "Mechanisms of removing terdizolamide phosphate from water by the activation of potassium peroxymonosulfate with CeFe2O4 biochar," *Environmental Science and Pollution Research*, vol. 32, no. 8, pp. 4690–4706, 2025.

[161] S. S. Khan, J. P. Steffy, M. B. Safa, H. A. AL-Shwaiman, V. Subhiksha, A. Syed, L. S. Wong, and M. Verma, "Fabrication of Ag0 preluded CeFe2O4 for boosted catalytic degradation of Rhodamine B by Al3+ activation: Interfacial engineering, synergistic behavior and mechanism insight," *Colloids Surf A Physicochem Eng Asp*, vol. 727, Dec. 2025, doi: 10.1016/j.colsurfa.2025.138214.

[162] Y. He, Y. Zhu, J. Qian, P. Wang, Y. Zhang, K. Xu, B. Lu, Y. Liu, and J. She, "Revealing the crystal phase effect of CeO2 in spinel-based nanocatalysts toward the peroxymonosulfate activation for organics degradation," *Chemical Engineering Journal*, vol. 474, Oct. 2023, doi: 10.1016/j.cej.2023.145737.

[163] Z. Quan, Z. Wang, X. Wang, H. Liu, and Y. Ma, "Effect of CeO2 addition on the sintering behavior of pre-synthesized magnesium aluminate spinel ceramic powders," *Ceram Int*, vol. 45, no. 1, pp. 488–493, Jan. 2019, doi: 10.1016/j.ceramint.2018.09.194.

[164] H. W. Ha, N. J. Yun, and K. Kim, "Improvement of electrochemical stability of LiMn2O4 by CeO2 coating for lithium-ion batteries," *Electrochim Acta*, vol. 52, no. 9, pp. 3236–3241, Feb. 2007, doi: 10.1016/j.electacta.2006.09.066.

[165] C. Liu, B. Wang, T. Wang, J. Liu, P. Sun, X. Chuai, and G. Lu, "Enhanced gas sensing characteristics of the flower-like ZnFe2O4/ZnO microstructures," *Sens Actuators B Chem*, vol. 248, pp. 902–909, 2017, doi: 10.1016/j.snb.2017.01.133.

[166] S. Wang, J. Zhang, J. Yang, X. Gao, H. Zhang, Y. Wang, and Z. Zhu, "Spinel ZnFe2O4 nanoparticle-decorated rod-like ZnO nanoheterostructures for enhanced gas sensing performances," *RSC Adv*, vol. 5, no. 13, pp. 10048–10057,

2015, doi: 10.1039/c4ra14033h.

[167] T. Zou, R. Zhao, Z. Wang, R. Zhao, Z. Wang, Y. Yang, X. Xing, and Y. Wang, "Sensitive and selective n-butanol gas detection based on ZnO nanocrystalline synthesized by a low-temperature solvothermal method," *Physica E Low Dimens Syst Nanostruct*, vol. 103, pp. 143–150, Sep. 2018, doi: 10.1016/j.physe.2018.06.002.

[168] C. Q. Zhao and S. N. Ding, "Perspective on signal amplification strategies and sensing protocols in photoelectrochemical immunoassay," Jul. 15, 2019, *Elsevier B.V.* doi: 10.1016/j.ccr.2019.03.018.

[169] S. A. Lim and M. U. Ahmed, "Electrochemical immunosensors and their recent nanomaterial-based signal amplification strategies: A review," 2016, *Royal Society of Chemistry*. doi: 10.1039/c6ra00333h.

[170] J. Lei and H. Ju, "Signal amplification using functional nanomaterials for biosensing," Mar. 21, 2012. doi: 10.1039/c1cs15274b.

[171] A. D. da Silva, W. J. Paschoalino, J. P. V. Damasceno, and L. T. Kubota, "Structure, Properties, and Electrochemical Sensing Applications of Graphene-Based Materials," Nov. 16, 2020, *Wiley-VCH Verlag*. doi: 10.1002/celc.202001168.

[172] V. Singh, D. Joung, L. Zhai, S. Das, S. I. Khondaker, and S. Seal, "Graphene based materials: Past, present and future," Oct. 10, 2011, *Elsevier Ltd*. doi: 10.1016/j.pmatsci.2011.03.003.

[173] X. Huang, Z. Yin, S. Wu, X. Qi, Q. He, Q. Zhang, Q. Yan, F. Boey, and H. Zhang, "Graphene-based materials: Synthesis, characterization, properties, and applications," Jul. 18, 2011. doi: 10.1002/smll.201002009.

[174] J. Liu, S. Bao, and X. Wang, "Applications of Graphene-Based Materials in Sensors: A Review," Feb. 01, 2022, *MDPI*. doi: 10.3390/mi13020184.

[175] D. Li and R. B. Kaner, "Graphene-based materials," *Science (1979)*, vol. 320, no. 5880, pp. 1170–1171, 2008.

[176] J. Zhu, D. Yang, Z. Yin, Q. Yan, and H. Zhang, "Graphene and graphene-based materials for energy storage applications," *Small*, vol. 10, no. 17, pp. 3480–3498, 2014.

[177] A. Molla and J. H. Youk, "Recent progress on electroanalytical sensing of small molecules and biomolecules using carbon dots: A review," Nov. 25, 2023, *Korean Society of Industrial Engineering Chemistry*. doi: 10.1016/j.jiec.2023.07.037.

[178] H. E. S. K. B. Mustafa Çeşme, "Fluorescent Carbon Dots from Vegetable and Fruit Wastes and Their Applications," *Fruits and Vegetable Wastes*, Nov. 2022, Accessed: Nov. 03, 2025. [Online]. Available: https://link.springer.com/chapter/10.1007/978-981-16-9527-8_15

[179] W. You, W. Zou, S. Jiang, J. Zhang, Y. Ge, G. Lu, D. W. Bahnemann, and J. H. Pan, "Fluorescent carbon quantum dots with controllable physicochemical properties fantastic for emerging applications: A review," Mar. 01, 2024, *John Wiley and Sons Inc*. doi: 10.1002/cnl2.120.

[180] L. Cui, X. Ren, M. Sun, H. Liu, and L. Xia, "Carbon dots: Synthesis, properties

and applications," Dec. 01, 2021, *MDPI*. doi: 10.3390/nano11123419.

[181] J. Huang, Y. Liu, and T. You, "Carbon nanofiber based electrochemical biosensors: A review," *Analytical Methods*, vol. 2, no. 3, pp. 202–211, Mar. 2010, doi: 10.1039/b9ay00312f.

[182] E. Hammel, X. Tang, M. Trampert, T. Schmitt, K. Mauthner, A. Eder, and P. Pötschke, "Carbon nanofibers for composite applications," in *Carbon*, 2004, pp. 1153–1158. doi: 10.1016/j.carbon.2003.12.043.

[183] M. H. Al-Saleh and U. Sundararaj, "Review of the mechanical properties of carbon nanofiber/polymer composites," Dec. 2011. doi: 10.1016/j.compositesa.2011.08.005.

# Chapter 2 Experimental and Research Methods

## 2.1. Introduction

The main research in this thesis is focused on the fabrication and characterisation of transition metal dichalcogenides (TMDs), carbon materials and spinels on glassy carbon electrodes (GCE), screen printed electrodes (SPE) and carbon cloth (CC) for electrochemical monitoring of aquatic contaminants, specifically antibiotic drugs. The sensing work couples transition-metal dichalcogenides (TMDs) with spinels and diverse carbon materials, produced via ultrasonic technology, simple grinding, and a straightforward electrodeposition protocol. The resulting materials were comprehensively examined by scanning electron microscopy (SEM), energy-dispersive X-ray spectroscopy (EDX) with elemental mapping, Fourier-transform infrared (FTIR) and UV–visible spectroscopy (UV-vis), alongside a suite of electrochemical measurements. The optimised modified electrodes were then deployed as analytical platforms for five representative pollutants in water: Metronidazole (MTZ), Sulfanilamide (SFD), Flutamide (FLD), Sulfamerazine (SRZ), and Sparfloxacin (SPAR).

The sections that follow set out the electrochemical measurements, characterisation techniques and experimental methods used. The specific preparation procedures for each material are detailed within their respective chapters.

## 2.2. Experimental Chemical and Methods

### 2.2.1. Chemical Reagents

All the chemical reagents used in this thesis were of analytical grade. They were purchased from Sigma-Aldrich™ and used as received, without any further purification steps. All the chemical reagents used are listed in Table 2.1. The drugs employed in the electrochemical sensing studies are summarised in Table 2.2.

**Table 2.1**: Chemicals, formula and purity.

| Reagent name | Chemical formula and Purity |
|---|---|
| Molybdenum disulfide powders | $MoS_2$ (< 2 μM), 98.0 % |
| Tungsten disulfide powders | $WS_2$ (< 2 μM), 99.0 % |
| Ammonium tetrathiomolybdate | $(NH_4)_2MoS_4$, 99.97 % |
| L-tryptophan | $C_{11}H_{12}N_2O_2$, 98.0 % |
| tannic acid | $C_{76}H_{52}O_{46}$ |
| sulfuric acid | $H_2SO_4$, 98.0 % |
| Hydrochloric acid | HCl, 97.0 % |
| Acetic acid | $CH_3COOH$ (HAc) |
| Phosphoric acid | $H_3PO_4$, 99.9 % |
| Sodium hydroxide | NaOH, 98.0 % |
| Potassium dihydrogen phosphate | $KH_2PO_4$, 99.0 % |
| Potassium ferricyanide | $K_3[Fe(CN)_6]$, 99.0 % |
| Potassium ferrocyanide | $K_4[Fe(CN)_6]$, 99.0 % |
| Potassium phosphate | $K_3PO_4$, 97.0 % |
| Sodium chloride | NaCl, 99.0 % |
| Sodium nitrate | $NaNO_3$, ≥99.0 % |
| Sodium nitrite | $NaNO_2$, 97.0 % |
| Sodium sulfate | $Na_2SO_4$, ≥99.0 % |
| Ammonium nitrate | $NH_4NO_3$, ≥98.0 % |
| Magnesium nitrate hexahydrate | $Mg(NO_3)_2 \cdot xH_2O$, ≥98.0 % |
| Ammonium Carbonate | $(NH_4)_2CO_3$, ≥30.0 % $NH_3$ basis |
| Potassium phosphate monobasic | $KH_2PO_4$, ≥99.0 % |
| Potassium phosphate dibasic | $K_2HPO_4$, ≥98.0 % |
| Potassium chloride | KCl, 99.0-100.5 % |
| Sodium acetate | $CH_3COONa$, ≥99.0 % |
| Natural fine flake graphite powder | G, 99.98 % |
| Sodium hydrogen phosphate | $Na_2HPO_4 \cdot 2H_2O$, ≥98.0 % |
| Sodium nitrate | $NaNO_3$, ≥99.0 % |

| | |
|---|---|
| Potassium permanganate | $KMnO_4$, 97.0 % |
| Hydrogen peroxide | $H_2O_2$, 35.0 % |
| Sodium sulfate | $Na_2SO_4$, ⩾99.0 % |
| Calcium chloride | $CaCl_2$, ⩾96.0 % |
| Copper sulphate | $CuSO_4$, ⩾98.0 % |
| Ferrous sulfate | $FeSO_4$, ⩾99.0 % |
| Magnesium chloride | $MgCl_2$, ⩾97.0 % |
| Sodium acetate | $CH_3COONa$ (NaAc), ⩾99.0 % |
| Sodium carbonate | $Na_2CO_3$, ⩾99.5 % |
| Cerium(III) nitrate hexahydrate | $Ce(NO_3)_3$, 99 % |
| Potassium hydroxide | KOH, ⩾85 % |
| Acetic acid | $Zn(CH_3CO_2)_2$, 96 % |
| Manganese(II) acetate | $Mn(CH_3CO_2)_2$, 98 % |
| Urea | $NH_2CONH_2$, 99.0-100.5 % |
| K-carrageenan | - |
| Carbon Nanofibers | CNFs |
| Ethanol | EtOH, ⩾95 % |
| Iron (II) Chloride Tetrahydrate | $FeCl_2 \cdot 4H_2O$, 98 % |
| Cerium (III) Chloride Heptahydrate | $CeCl_2 \cdot 7H_2O$, 98 % |
| Hexammine cobalt(III) chloride | $Ru(NH_3)_6Cl_3$, 98 % |
| Polyvinylidene fluoride | PVDF |
| N-Methyl-2-pyrrolidone | NMP, ⩾99.0 % |

**Table 2.2**. Antibiotic Chemicals.

| Antibiotic drugs | Abbreviation | Structure |
|---|---|---|
| Metronidazole | MTZ | 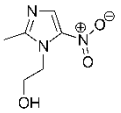 |
| Sulfanilamide | SFD | 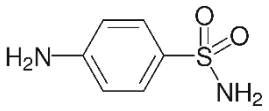 |
| Sulfamerazine | SRZ | 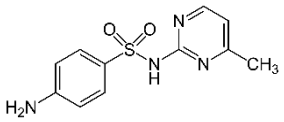 |
| Sulfapyridine | SAD | 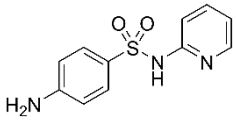 |
| Flutamide | FLD | 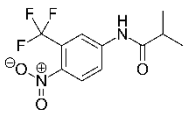 |
| Sparfloxacin | SPAR | 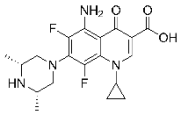 |

| | | |
|---|---|---|
| Cefadroxil | CEX | 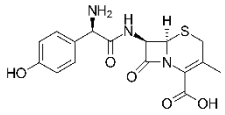 |

## 2.2.2. Instruments, Electrodes and Software

All the instruments, electrodes, and software used in this thesis are listed below, with the instruments summarised in Table 2.3, the electrodes used in Table 2.4, and the software employed in Table 2.5.

**Table 2.3**. Instrumentation and models

| Equipment Name | Model |
|---|---|
| Potentiostat | Cyclic voltammetry (CV): Solartron 1287 coupled with a 1255 FRA |
| Electrochemical workstation | Differential Pulse Voltammetry (DPV): CHI440 CH Instruments, Inc. |
| Electrochemical Impedance Spectroscopy (EIS) | Solartron 1287 potentiostat<br>1255 FRA (Solartron) |
| SEM | Hitachi, S-4800 and phenom world pro X |
| EDX instrument | Oxford Instrument INCAz-act ESX |
| Electronic balance | Sartorius Models TE612 and TE214s |
| High speed tabletop centrifuge | Thermoscientific SORVALL ST 8 |
| Magnetic stirrer apparatus | Fisherbrand |
| pH meter | METTLER TOLEDO |
| Thermo Fisher IR spectrometer | Nicolet iS50 FT-IR microscope |
| Ultrasonic cleaner | BRANSON 1510 |
| Ultrasonic processors | AC/DC input 220 V AC, Schuko plug |
| UV-Vis Spectrometer | CARY 50 Conc |
| Raman Spectrometer | inVia Reflex Raman Microscope (532 and 632.8 nm) |
| X-ray photoelectron spectroscopy (XPS) | Kratos AXIS ULTRA spectrometer |
| X-ray diffraction (XRD) | PANalytical, X'Pert-PRO MPD system |
| Fluorescence spectroscopy | Agilent® Cary Eclipse Fluorescence Spectrometer |
| Benchtop Ovens | Genlab® 50 Litre Base Mount Design MINO50/TDIG |
| Calcination Oven | Gallenkamp® |

| | | |
|---|---|---|
| Hydrothermal Autoclave Reactor | Synthesis | Teflon (100 mL) |

**Table 2.4.** Electrodes employed.

| Application | Electrodes |
|---|---|
| Working Electrode (WE) | Glassy Carbon Electrode (GCE 3 mm diameter)<br>Screen Printed Electrode (SPE)<br>Carbon Cloth (CC) |
| Reference Electrode (RE) | Silver/Silver Chloride (Ag/AgCl) |
| Counter Electrode (CE) | High surface area Platinum Wire |
| ITO Electrodes | Indium Tin Oxide (ITO) Electrode |

**Table 2.5.** Software employed.

| Software | Company |
|---|---|
| Origin2021 | OriginLab Corporation |
| Chi660e | CH Instruments, Inc. |
| CorrWare® | Scribner |
| CView™ | |
| ZPlot® | |
| ZView® | |
| Digital Micrograph | Gatan, Inc. |
| Image J | National Institutes of Health (NIH) |
| ChemDraw | Revvity Signals |
| VESTA | Koichi Momma |
| Microsoft Word | Microsoft® |
| Microsoft Excel | |
| Microsoft Power Point | |

## 2.2.3. Synthesis Method of Sensor Materials

### 2.2.3.1. Exfoliation Synthesis

Exfoliation synthesis is a method used to separate the stacked layers of materials like TMDs into single, double, or few-layer sheets, creating 2D materials. This process typically involves weakening the weak van der Waals forces between layers using

mechanical, chemical, or electrochemical forces, with techniques like intercalation, sonication, or electrochemistry being common [1]. Exfoliation can be combined with other methods, such as using ultrasound to help disperse the exfoliated sheets and prevent them from re-aggregating. It is often combined with chemical intercalation, where guest species are introduced between layers to weaken the interlayer forces [1], [2]. In this study, exfoliation was employed to $MoS_2$ by DL-tryptophan in Chapter 3 and tannic acid in Chapter 4, and $WS_2$ sheets using sodium cholate in Chapter 6.

#### 2.2.3.2. Hydrothermal Synthesis

Hydrothermal synthesis is a method for creating substances from high-temperature aqueous solutions in a closed, pressurized system, like an autoclave. It uses high temperatures (above water's boiling point) and pressures to dissolve and recrystallize materials that are difficult to synthesize under normal conditions, such as spinels oxides and other materials [3]. This approach was used in the synthesis of Carbon Particles (CPs) in Chapter 5, $ZnMn_2O_4$ spinel oxides and $CeO_2$ in Chapter 6.

### 2.2.4. Preparation of Solutions

#### 2.2.4.1. Phosphate-Buffered (PB) Solution

Phosphate-buffered (PB) solutions were prepared at 0.1 M and 0.05 M using potassium phosphate monobasic ($KH_2PO_4$) and deionised water. The pH was adjusted using small volumes of HCl or NaOH solutions.

#### 2.2.4.2. Phosphate-Buffered Saline (PBS) with Sodium Chloride

Sodium Chloride (NaCl) was added to the phosphate-buffered solutions to form a phosphate saline buffer. This solution was prepared with a concentration of 0.1 M potassium phosphate monobasic ($KH_2PO_4$) and 0.01M sodium chloride (NaCl), with pH values of 7.0, adjusted by NaOH.

### 2.2.4.3. Artificial Urine Solution

The artificial urine media was prepared by dissolving $NH_4NO_3$ (0.85 g), NaCl (14.1 g), KCl (2.8 g), $CaCl_2$ (0.6 g), $Mg(NO_3)_2 \cdot xH_2O$ (0.43 g), $Na_2SO_4$ (0.42 g), and $CO(NH_2)_2$ (17.3 g) in deionised water, to give a final volume of 80 mL [4]. The pH was adjusted to 6.0 using a few drops of 0.02 M HCl.

### 2.2.4.4. Antibiotic Drugs Solution

The antibiotic drug solutions were prepared at concentrations of 1.0, 0.1 or 0.2 mM, dissolved in PB solution. These solutions served as stock solutions and were prepared regularly and stored in the fridge when not in use. Other concentrations were prepared through serial dilution.

### 2.2.4.5. NaOH Solution

0.1 M NaOH was prepared in deionised water.

### 2.2.4.6. Potassium Ferricyanide and Potassium Ferrocyanide Solution

The solution (2.5 mM) was prepared using the mixture of $K_3[Fe(CN)_6]$ and $K_4[Fe(CN)_6]$ dissolved in 0.1 M KCl solution. This solution was employed as an electrochemical probe and used to estimate the electroactive surface area of the sensors.

### 2.2.4.7. $Ru(NH_3)_6Cl_3$ Solution

The solution (2.5 mM) was prepared using $Ru(NH_3)_6Cl_3$ dissolved in 0.1 M KCl solution. This solution was employed as an electrochemical probe and used to estimate the electroactive surface area of the sensors.

### 2.2.4.8. Real Water Samples

Two different water samples were used. Tap water was collected directly from the laboratory, while the river water sample was collected freshly from the Royal Canal in

Maynooth, Ireland. The samples were centrifuged and filtered to remove insoluble particles. They were stored in the fridge and used within 6 h. A stock solution of drugs was added to the water samples, and the recorded current was compared with the calibration curve obtained with deionised water to compute the recovery.

## 2.3. Electrochemical Experiments

### 2.3.1. Electrochemistry

In electrochemistry, the two fundamental observables are current (I) and potential (E). Current is the rate of charge flow induced by an applied potential. In a typical electrochemical experiment, one of the two observables is normally controlled whilst the evolution of the other one is recorded. The response of electrochemical systems to the applied stimulus depends on multiple factors, notably the analyte's properties and its concentration.

### 2.3.2. The Electrochemical Cell Set-up

All composite materials developed in this thesis were fabricated and characterised using electrochemical techniques. Unless otherwise stated, measurements were performed at ambient laboratory temperature. Experiments employed either a Solartron 1287 potentiostat coupled with a 1255 FRA, a Solartron 1285 potentiostat or a CHI440 CH Instruments, Inc. electrochemical workstation, each operated via computer control (CorrWare® for Windows, v3.6a; Chi660e from CH Instruments software). A schematic of the experimental configuration is provided in Fig. 2.1.

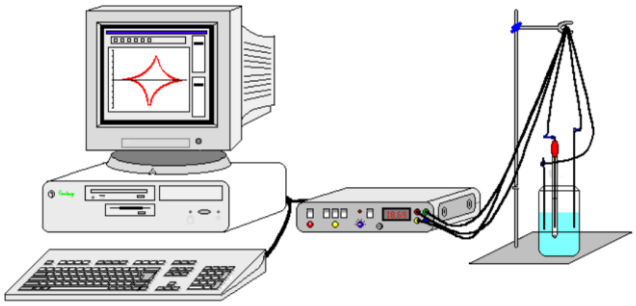

**Figure 2.1.** General schematic of an electrochemical system [5].

The electrochemical cell typically consists of three electrodes. The working electrode is the electrode where the electrochemical reactions are studied. When studying solution electroactive species, the working electrode should be made of an inert material that does not undergo significant chemical or structural changes during the measurement. Examples of suitable electrodes are platinum, gold, or glassy carbon [6]. The reference electrode is the electrode with a fixed, known potential, against which the applied potential is measured. The characteristics of the reference electrode are that it should be stable during the measurement and allow for the focus to be on changes at the working electrode. The counter or auxiliary electrode completes the circuit and allows current to flow between the counter and working electrode, enabling the electrochemical reaction of interest to be studied. It should also be composed of an inert material with a larger area than the working electrode. Examples of counter electrodes are coiled platinum wires or platinum gauzes.

The electrolyte solution used in experiments is an important component of the electrochemical system. The electrolyte solution consists of several ingredients, including the electrolyte salt and the solvent. The ideal properties of the electrolyte solution are chemical and electrochemical inertness in the proposed experiment, with good conductivity. The modes of transport of the reactants in an electrochemical cell are diffusion, migration, and convection. To simplify the understanding of the electrochemical system, migration and convection are undesirable and should be

mitigated. Migration is reduced by maintaining a high concentration of electrolyte salt relative to the reactant, and convection is prevented by eliminating stirring and vibrations.

A schematic of the electrochemical cell employed in this study is shown in Figure 2.2. It consists of a glass cylinder sealed with a Teflon® lid, providing three ports for the electrodes and inlets and outlets for deoxygenating the solution. A silver/silver chloride electrode was used as the reference electrode, represented as Ag/AgCl/KCl (saturated aqueous solution). Its potential relative to the conventional standard hydrogen electrode (NHE) is 0.197 V. When this electrode is used as the reference electrode, it is commonly denoted as 'vs. Ag/AgCl'. The counter electrode (CE) was a coiled platinum wire providing a high surface area. The working electrode (WE) was a glassy carbon electrode (GCE) with a geometric diameter of 3 mm, or the GCE modified with the relevant composite films [7].

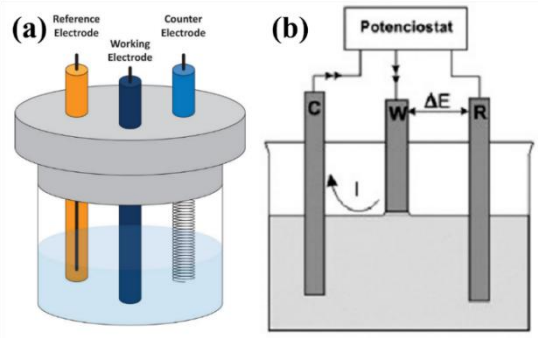


**Figure 2.2.** Schematic representation of the electrochemical cell used in this study. Working electrochemical cell with WE, CE and RE [8], [9].

Prior to use, the GCE were mechanically polished and cleaned. The GCE was polished on a micro-cloth (Aka-Napel cloth), using progressively smaller diamond suspensions (Akasol) with a final 1 μm particle size, until a mirror finish was obtained. Then, the polished GCE was sonicated for a short period of time, typically 2 min, and rinsed thoroughly with deionised water. The silver/silver chloride electrode was stored in

saturated KCl to prevent frit desiccation and, immediately before immersion, was rinsed thoroughly with deionised water to minimise KCl carryover into the supporting electrolyte. For each experiment, the three electrodes were immersed in the supporting electrolyte and connected to the potentiostat/workstation. As illustrated in Fig. 2.2 (b), current is driven between the WE and CE, while the WE potential is measured with respect to the RE.

## 2.3.3. Electrochemical Techniques

The two main techniques employed consisted of cyclic voltammetry (CV), and differential pulse voltammetry (DPV). The theoretical basis, and data-analysis procedures for these techniques are detailed below.

### 2.3.3.1. Cyclic Voltammetry (CV)

Cyclic Voltammetry (CV) is a standard electrochemical research method, and it has been recognised as one of the most useful electrochemical techniques for initial studies and the characterisation of an electrochemical system. During the recording of CVs, the electrode potentials are scanned repeatedly for one or more times at different scan rates with a triangular waveform, as shown in Fig. 2.3, meaning CV is a dynamic electrochemical technique. The initial applied potential ($E_i$) is scanned to a vertex potential ($E_v$), then scanning is reversed, and the vertex potential is swept back to the final potential ($E_f$), generating a triangular waveform over time. Usually, the final applied potential is equal to the initial applied potential, $E_f = E_i$. The potential range is chosen based on the electrolyte and depending on the reduction and oxidation reactions that occur at the electrode surface.

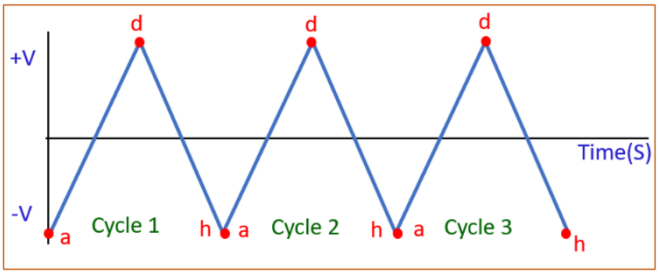


**Figure 2.3.** Triangular waveform formed as potential is changed over time [10].

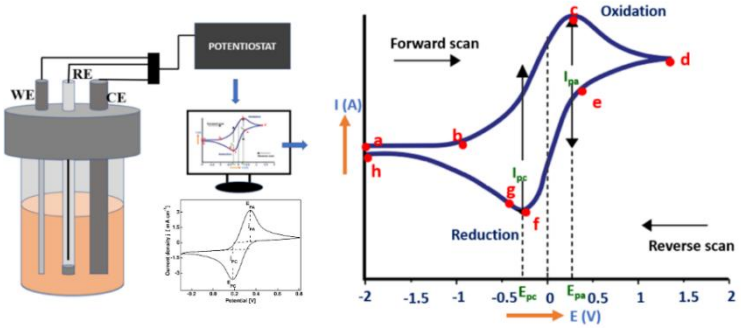


**Figure 2.4.** Cyclic Voltammogram (CV) obtained from cyclic voltammetry measurements [10].

In a typical experiment, as shown in Fig. 2.4 (for a reversible redox reaction), at the beginning of the experiment, the current is minimal because the WE displays only capacitive behaviour, resulting in a very low initial current. As the potential is cycled forward, a point is reached in a CV where the current begins to increase significantly, often referred to as the "Onset Potential" ($E_{onset}$). At the onset, electrons attain sufficient energy, enabling them to actively participate in the redox reaction. Once the reaction initiates, it continuously generates or consumes electrons, leading to a distinctive region of the voltammogram where the current demonstrates exponential growth. At some point, a peak is observed, and this is termed an anodic peak. It represents the highest current response observed during the oxidation of a substance at the WE surface. When the voltage is increased further, the current decreases; this behaviour represents a clear departure from Ohmic characteristics. According to Ohm's law, an increase in voltage should result in a corresponding increase in current, but in the realm of electrochemistry,

this non-Ohmic behavior is common and indicative of the unique electrochemical nature of the system. With increasing time, the diffusion layer continues to grow, and when this is combined with higher potentials, the diffusion process lags behind the reaction rate. Consequently, the system attempts to catalyse additional reactions, but there is an insufficient supply of reactants available at the working electrode, resulting in a decline in current.

During the reverse-scanning phase, oxidation continues because the applied voltage remains sufficient to sustain the reaction. However, the current remains low as the diffusion layer is now extended. As the potential is scanned further in the negative direction, the reverse reaction begins, leading to a rapid and significant change in the current direction. As the voltage polarity is reversed during the negative scan, the current likewise reverses its direction, quickly surging and reaching a peak current again. This cathodic peak represents the maximum current response observed during the reduction of a substance at the working electrode. Beyond this point, the electrode's supply of available oxidised species becomes limited, causing a decrease in current.

For illustration, consider the one-electron redox couple $A/A^+$ in solution, as shown in Eq. (2.1).

$$A - e^- = A^+ \quad \textbf{(2.1)}$$

During the forward scan (Fig. 2.4), the working-electrode potential is swept from $E_i$ to more positive values $E_v$, and oxidation occurs at the electrode surface ($A \rightarrow A^+ + e^-$). This results in an anodic current that increases with potential, attaining a maximum at the anodic peak potential ($E_{PA}$) and giving the anodic peak current ($I_{PA}$). The current then diminishes as the diffusion layer becomes depleted. Upon reversing the scan from $E_v$ to $E_f$, the oxidised species is reduced at the surface via $A^+ + e^- \rightarrow A$ yielding a cathodic peak characterised by the cathodic peak current ($I_{PC}$) at the cathodic peak potential ($E_{PC}$), as shown in Fig. 2.4.

The role of the applied potential can be further analysed and explained in terms of the Fermi energy level and the LUMO and HOMO levels of the solution molecules. The highest occupied molecular orbital (HOMO) is the uppermost filled molecular orbital in a given electronic configuration. The lowest unoccupied molecular orbital (LUMO) is the next available energy level for electron occupation. As shown in Fig. 2.5, variations in the potential at the WE can alter the energy of the electrons, and this in turn will influence the electron-transfer reactions at the electrode-solution interface. In Fig. 2.5(a), the applied potential leads to the occupation of lower energy levels on the electrode. Now the HOMO level is higher in energy, and electron transfer is from the HOMO level to the electrode. This leads to the oxidation of the molecules in solution. In Fig. 2.5(b), the energy of the electrons is high due to the applied potential. Now, the direction of electron flow is from the electrode to the solution phase, with electrons transferring into the LUMO levels, giving rise to the reduction of the solution species.

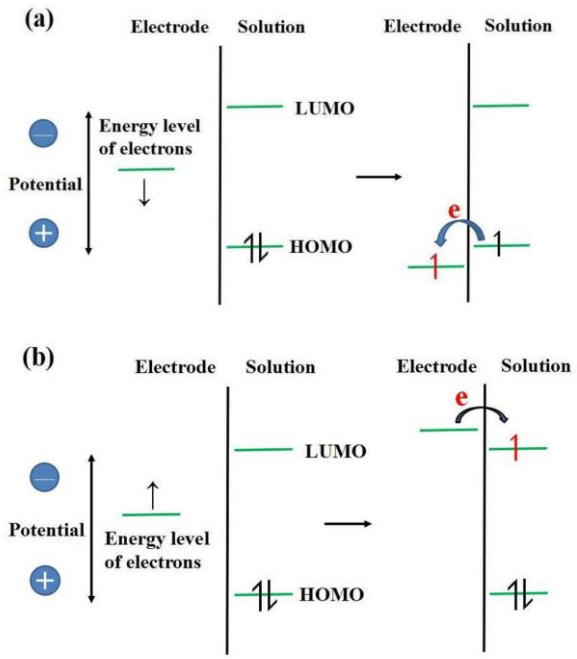


**Figure 2.5** Representation of (a) oxidation and (b) reduction process of a species, A, in solution. HOMO represents the highest occupied molecular orbitals and LUMO expresses the lowest unoccupied molecular orbitals [7].

Shown in Figure 2.6 are two CVs, representing a quasi-reversible system (Fig. 2.6(a)) and an irreversible system (Fig. 2.6(b)). As detailed earlier, the maximum current, $I_{PA}$ or $I_{PC}$, is due to diffusion processes and the formation of a diffusion layer [11]. The principal diagnostic parameters are the peak current $I_p$, peak potential $E_p$, the half-peak width $w_{1/2} \equiv |E_p - E_{1/2}|$, and the potential scan rate $v$. For reversible diffusion- or surface-confined systems, $E_p$ is independent of $v$; in contrast, irreversible responses exhibit systematic peak-potential shifts to more extreme values with increasing $v$. Peak-current analysis further distinguishes between: diffusion-controlled processes (reversible or irreversible), $I_p \propto v^{1/2}$ (Randles–Ševčík behaviour), whereas for reversible adsorption-controlled processes, $I_p \propto v$ [12], [13].

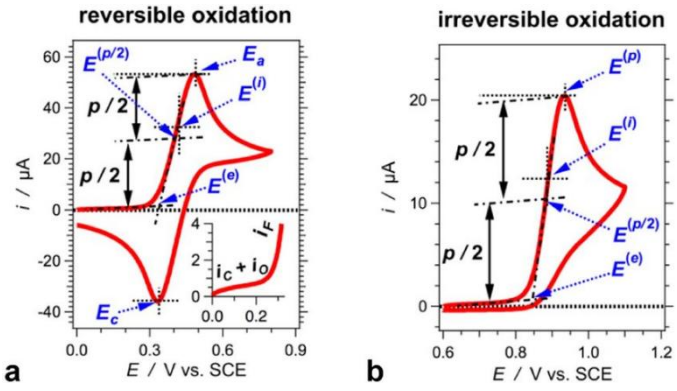


**Figure 2.6.** Cyclic voltammograms showing chemically reversible and irreversible oxidation with designated potentials: $E_a$, anodic potential, $E_c$, cathodic potential, $E_i$, inflection-point potential, $E_{p/2}$, half-peak potential, $E_e$, edge potential [11].

Representative CVs recorded at varying scan rates are shown in Fig. 2.7. The peak current increases monotonically with scan rate, reflecting the shorter experimental timescale at higher scan rate ($v$). At low $v$, the diffusion layer grows thicker, diminishing the concentration gradient at the electrode surface and thus the diffusive flux. At high $v$, the diffusion layer is thinner, the gradient is steeper, and the resulting current is larger. The dependence of peak current on scan rate provides kinetic/transport diagnostics of

the electrochemical process (e.g., diffusion-controlled vs adsorption-controlled). A linear relationship between $I_p$ and $v^{1/2}$ indicates diffusion control and is described by the Randles–Ševčík formalism. For reversible and quasi-reversible systems, the relevant expression is given in Eq. (2.2), whereas for irreversible systems Eq. (2.3) applies [13]. By contrast, a linear dependence of $I_p$ on $v$ is characteristic of a surface-confined (adsorption-controlled) process.

$$I_p = (2.69 \times 10^5) n^{3/2} D^{1/2} v^{1/2} AC \quad \textbf{(2.2)}$$

$$I_p = -(2.99 \times 10^5) n(\alpha n')^{1/2} D^{1/2} v^{1/2} AC \quad \textbf{(2.3)}$$

Here, $I_p$ denotes the peak current (A); n is the number of electrons transferred; D is the diffusion coefficient ($cm^2\ s^{-1}$); $v$ is the potential scan rate ($V\ s^{-1}$); C is the bulk analyte concentration ($mol\ cm^{-3}$); α is the charge–transfer coefficient; n' is the number of electrons involved up to and including the rate-determining step; and A is the (electroactive) electrode area ($cm^2$).

When both redox species are chemically stable and electron-transfer kinetics are rapid, reversible behaviour is observed [14]. For the $K_3Fe(CN)_6/K_4Fe(CN)_6$ couple, quasi-reversible behaviour is often obtained owing to the high stability of both ferri- and ferrocyanide; consequently, this redox probe is widely employed to evaluate the electroactive surface area of electrodes. In Chapters 3 to 6, the electroactive area of the activated GCE was determined using mixed solutions of $Fe(CN)_6^{3-}$ and $Fe(CN)_6^{4-}$. In Chapter 7, the well-known anionic $K_3Fe(CN)_6/K_4Fe(CN)_6$ system was not chosen due to its potential electrostatic repulsion with the oxygenated species at the surface of the CFO. For $Ru(NH_3)_6Cl_3$ solution, the peak currents were plotted as a function of the square root of the scan rate according to the Randles-Sevcik relationship, Eq. (2.2), where D corresponds to the diffusion coefficient of the $Ru(NH_3)_6^{3+}$, which was taken as $9.0 \times 10^{-6}\ cm^2\ s^{-1}$ [15].

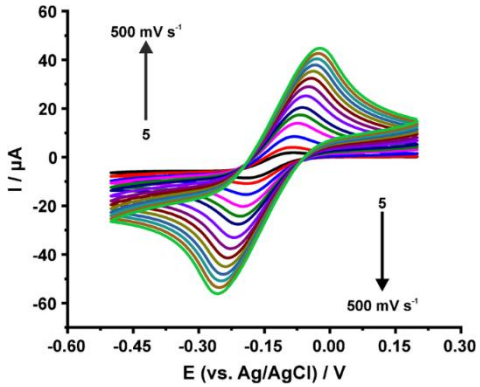


**Figure 2.7** An example of representative voltammograms at different scan rates [15].

CV was employed to determine the redox behaviour, charge-transfer characteristics, and electroactive surface properties of the fabricated electrodes. All electrochemical measurements were conducted using a computer-controlled potentiostat operated. Unless otherwise specified, experiments were performed at ambient temperature (approximately 20-25 °C). CV was performed by sweeping the working electrode potential linearly between a defined initial potential and vertex potentials, followed by reversal to complete the cycle after connecting the reaction cell. The potential window was selected based on the electrochemical stability of the electrolyte and the anticipated redox processes of the analyte and/or electrode material. To ensure stability and repeatability, several initial cycles were typically applied until consecutive scans overlapped, indicating that the electrode/electrolyte interface had reached a quasi-steady state. The voltammograms presented and analyzed were then acquired under identical conditions (electrolyte composition, scan rate, and electrode surface area).

### 2.3.3.2. Differential Pulse Voltammetry (DPV)

Pulse voltammetric techniques were employed to enhance analytical sensitivity by increasing the faradaic-to-nonfaradaic current ratio. In these methods, the potential is applied in discrete pulses and the current is sampled after a defined delay, permitting the double-layer (capacitive) current to decay so that the recorded signal is predominantly faradaic. Representative pulse methods include normal pulse voltammetry (NPV), differential pulse voltammetry (DPV), and square-wave

voltammetry (SWV). In this thesis, DPV was used for quantifying target analytes and for examining the pH dependence of their oxidation/reduction peak potentials. The CH instrument used in these studies is depicted in Fig. 2.8.


**Figure. 2.8.** The CHI440 CH Instruments, Inc. potentiostat for used in the differential pulse voltammetry (DPV) analyses.

Differential pulse voltammetry (DPV) applies a sequence of potential pulses of fixed amplitude superimposed on a staircase baseline (stepwise ramp). A baseline (starting) potential is chosen where faradaic processes are negligible, and the staircase is advanced in small increments. During each pulse period, the current is sampled twice—immediately before the pulse and at the end of the pulse—and the difference is plotted versus the baseline potential. This is shown in the schematic provided in Figure 2.9.

By allowing the capacitive (double-layer) current to decay between the two sampling instants, DPV markedly suppresses non-faradaic contributions, yielding high sensitivity and characteristically narrow peaks. The small step sizes and well-defined pulse parameters (step height, pulse amplitude, pulse width) provide enhanced resolution, enabling discrimination between analytes with closely spaced redox potentials. Consequently, DPV is widely used for trace determinations across diverse matrices, including pharmaceuticals, dyes, insecticides, and pesticides [16].

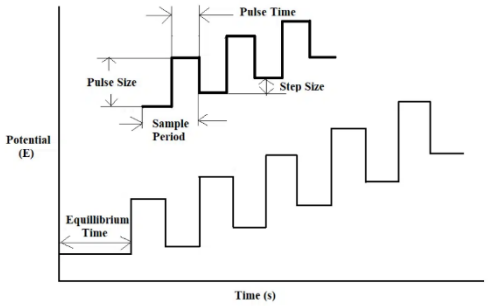


**Figure. 2.9.** Schematic of potential wave form for differential pulse voltammetry [17].

### 2.3.3.3. Electrochemical Impedance Spectroscopy (EIS)

Electrochemical impedance spectroscopy (EIS) was employed to probe the interfacial properties and operational stability of the modified electrodes in the presence of various analytes. Measurements were performed using a Solartron 1287 potentiostat coupled to a Solartron 1255 or 1250 frequency-response analyzer. The DC potential was set at the analyte's characteristic oxidation or reduction potential, as determined from cyclic voltammetry, and a small-amplitude sinusoidal perturbation (10 mV) was superimposed. The alternating potential frequency was swept over $10^{-3}$ to $10^{5}$ Hz, yielding the complex impedance $Z(\omega) = E(\omega)/I(\omega)$ and its phase angle φ. Where relevant, experiments were repeated over extended intervals (typically up to 24 h) to assess stability and ensure quasi–steady-state conditions.

Impedance data (Nyquist and/or Bode representations) were interpreted using equivalent-circuit models comprising resistive, capacitive, and diffusive elements connected in series and parallel. From these fits, parameters such as the solution/electrolyte resistance $R_s$, charge-transfer resistance $R_{ct}$, double-layer capacitance (or constant-phase element, $C_{dl}$/CPE), and diffusional contributions (e.g., Warburg impedance, (W)) were extracted. Compared with time-domain techniques, EIS provides frequency-resolved insight into interfacial kinetics and structure, enabling quantitative evaluation of capacitive behaviour and electron-transfer resistance in the electrode materials. The Solartron equipment employed in recording the impedance

data is shown in Figure 2.10.

**Figure 2.10.** A Solartron 1287 potentiostat coupled with a 1250 or 1255 FRA (Solartron) electrochemical impedance spectroscopy (EIS).

Electrochemical impedance spectroscopy (EIS) was employed to evaluate the interfacial charge-transport behaviour and the conductivity-related electrochemical properties of the fabricated electrode materials in PB solution and in the presence of the target antibiotic analyte. EIS measurements were conducted using the same electrochemical three-electrode configuration as used for CV and DPV. Unless otherwise stated, all experiments were performed at ambient temperature (approximately 20-25 °C). The AC perturbation amplitude was maintained within the linear response regime at 10 mV. Spectra were acquired over a broad frequency range from $1 \times 10^5$ Hz to 5 mHz. All EIS measurements were repeated using independently prepared electrodes and/or replicate runs (n=12) to assess reproducibility. For data presentation and equivalent-circuit analysis, equivalent-circuit fitting was performed using dedicated fitting software (ZView) to obtain quantitative parameters, including charge-transfer resistance, constant-phase elements, and diffusion elements. The selected circuit model was justified based on the observed spectral features and the known physicochemical characteristics of the electrode coating.

## 2.4. Surface Analytical Techniques

A variety of surface analytical techniques were employed, and these are introduced in the following sections.

### 2.4.1. Scanning Electron Microscopy (SEM)

The Scanning electron microscopy (SEM) images were recorded in Maynooth University - in person, University of Limerick - services by contract, Yeungnam University - by group colleague, and China University of Petroleum (East China) - in person. The following section shows the SEM from Maynooth University. Each material was prepared on a flat pad of carbon, and the carbon pad was affixed to a platform, secured in a slot, and then put into the SEM for image capture and EDX measurements.

SEM images a specimen by rastering a finely focused, high-energy electron beam across its surface and collecting the signals generated by beam–sample interactions. These signals comprise secondary electrons (topographic contrast), backscattered electrons (atomic-number contrast), and characteristic X-rays (elemental analysis via EDX). They are detected, amplified, and rendered to form high-resolution micrographs. To minimise gas-phase scattering and maintain beam stability, the electron source, lenses, and specimen are operated under high vacuum. SEM routinely resolves features from the micrometre (μm) down to the nanometre (nm) scale. The SEM used in this thesis is shown in Fig. 2.11.

An SEM comprises two main subsystems: (i) the electron column and (ii) the control/console electronics. The column houses the electron gun and a series of electromagnetic lenses and apertures that shape and focus the beam onto the specimen. Electron sources are commonly thermionic (e.g., heated tungsten filaments) or field-emission guns (Schottky or cold FEG), the latter affording smaller probe sizes and

enhanced brightness. Electrons are accelerated through a potential difference (typically ~0.5-30 kV) and focused by condenser and objective lenses to generate a nanometre-scale probe at the surface.

The electron de Broglie wavelength decreases with increasing accelerating voltage according to Eq. (2.4), but in SEM the practical spatial resolution is governed predominantly by probe size, lens aberrations, and the interaction volume within the specimen rather than by wavelength alone. Accordingly, optimizing accelerating voltage involves trade-offs between surface sensitivity, penetration depth, charging, and signal yield; higher voltages can increase X-ray generation and BSE contrast, whereas lower voltages can improve surface detail and mitigate charging in non-conductive samples.

$$\lambda = (\frac{1.5}{V})^{1/2} \quad \textbf{(2.4)}$$


**Figure. 2.11.** (a) Hitachi S-4800 FESEM was used in Chapters 3-5, and (b) SEM phenom world pro X was used in Chapters 6-7 of the SEM studies.

The electron–optical column is mounted to a high-vacuum specimen chamber [18]. The electron gun is located at the apex of the column, while the specimen is positioned on a stage within the chamber. As the focused primary beam impinges on the specimen, elastic scattering produces backscattered electrons (BSEs) that emerge from a pear-shaped interaction volume extending up to ~1 μm, contingent on accelerating voltage

and composition; detection of these BSEs yields the image contrast, Fig. 2.12 [19], [20].

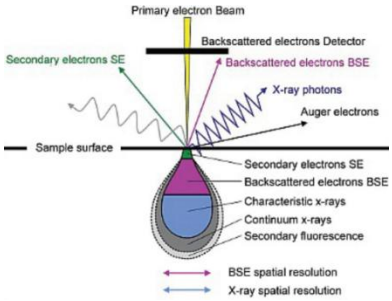


**Figure. 2.12.** Diagram of the interaction of beam-specimen in SEM [21].

In addition to elastic scattering, interactions of the primary beam with atomic electrons and nuclei give rise to inelastic processes that generate secondary electrons (SEs), characteristic X-rays, and Auger electrons. These signals furnish complementary contrast: SEs are highly surface sensitive and reveal fine topography; characteristic X-rays enable elemental analysis via energy-dispersive spectroscopy (EDS/EDX); and Auger electrons provide ultra-shallow compositional information. Collectively, they inform on surface texture, chemical composition, and aspects of crystallinity/phase distribution.

## 2.4.2. X-ray Diffraction (XRD)

X-ray diffraction (XRD) was recorded in University of Limerick, Yeungnam University, and China University of Petroleum (East China). Powder X-ray diffraction is a scientific method for determining the structure of materials. XRD is a cornerstone technique for elucidating crystalline structure and assessing phase composition and crystallinity. For sufficiently large, well-ordered crystals (e.g., many inorganic solids and macromolecular crystals), single-crystal XRD can determine the full three-dimensional arrangement of atoms. When crystals are sub-micrometre or polycrystalline, powder XRD enables phase identification, evaluation of lattice parameters and phase purity, and, with appropriate models, estimation of crystallite size

and microstrain. The method exploits the fact that X-ray wavelengths (typically 0.5-2.5 Å) are comparable to interplanar spacings in solids. Coherent elastic scattering from the periodic electron density yields constructive interference at scattering angles that satisfy Bragg's law, shown in Eq. (2.5).

$$Sin\theta = n\lambda/2d \quad \textbf{(2.5)}$$

Where λ is the X-ray wavelength, d is the spacing of lattice planes indexed, θ is the Bragg (incidence) angle, and n is an integer. Diffracted intensities recorded as a function of 2θ give peak positions that reflect d values (hence the crystal structure), while relative intensities encode the structure factors and, thus, atomic arrangements as shown in Fig. 2.13. Constructive interference produces enhanced signals at specific angles, whereas destructive interference suppresses others, allowing rigorous determination of composition and crystallographic structure.

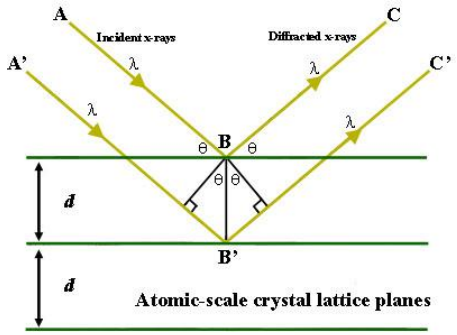


**Figure. 2.13.** Bragg's Law reflection.

The XRD analysis was carried out with a PANalytical, X'Pert-PRO MPD system, as shown in Fig. 2.14. These analyses were carried out at the Bernal Institute, University of Limerick.


**Figure. 2.14.** PANalytical, X'Pert-PRO MPD system.

## 2.5 Spectroscopy

Spectroscopy is an interdisciplinary field at the interface of physics and chemistry that interrogates the interaction of electromagnetic radiation with matter as reflected in absorption, emission, and scattering spectra. Electromagnetic radiation (light) spans a continuum of wavelengths/frequencies—the electromagnetic spectrum—including, the X-ray, ultraviolet–visible (UV–Vis), and infrared (IR) regions. Analysis of spectral responses across these domains yields insight into the structural, electronic, and dynamical properties of atoms, molecules, and condensed phases.

### 2.5.1. Energy Dispersive X-Ray Spectroscopy (EDX)

Energy-dispersive X-ray spectroscopy (EDX), operated in conjunction with SEM, was used to assess elemental composition. When the focused electron beam irradiates the specimen, inelastic interactions eject core-level electrons; relaxation of the resulting vacancies by higher-energy electrons emits characteristic X-rays whose energies are element-specific. Detection of these X-rays provides qualitative identification of constituent elements, with an information depth on the order of ~0.5–2 μm, contingent on accelerating voltage and matrix properties [22]. Quantitative analysis can, in principle, be performed by integrating peak areas and converting them to weight or atomic fractions using appropriate matrix corrections [23]. However, surface roughness and compositional inhomogeneity can compromise quantitation by altering X-ray

generation and collection efficiencies [24]. Consequently, in this thesis, EDX was employed primarily for qualitative characterisation of the modified electrodes.

## 2.5.2. Fourier-transform Infrared (FTIR) Spectroscopy

Infrared (IR) spectra were measured using a Nicolet iS50 FT-IR microscope, as shown in Fig. 2.15. Samples were prepared either as finely ground powders (mortar and pestle) or as thin deposits on flat substrates. Upon irradiation with infrared (AIR) light, photons are absorbed when the photon energy matches allowed molecular vibrational (and, in some cases, rotational) transitions, promoting populations from the ground to higher vibrational levels. These modes include bond stretching and bending motions. IR activity obeys the dipole-selection rule: a vibration is IR-active only if it entails a change in the molecular dipole moment.

IR spectra are typically collected over 4000 to 400 $cm^{-1}$ and displayed as wavenumber ($cm^{-1}$) on the abscissa versus transmittance (T%) or absorbance (A) on the ordinate. This measurement, commonly implemented as Fourier-transform infrared (FTIR) spectroscopy, provides diagnostic bands that enable the assignment of functional groups and the assessment of molecular structure. In this thesis, IR spectroscopy was employed to characterise the materials formed in Chapters 3-7.

**Figure. 2.15.** Nicolet iS50 FTIR spectrometer.

## 2.5.3. Ultraviolet-Visible Spectroscopy (UV-vis spectroscopy)

Ultraviolet–visible (UV–vis) spectroscopy is widely employed for qualitative and quantitative chemical analysis, particularly for detecting analytes at low concentrations in solution. In this technique, a sample is irradiated, and the transmitted intensity is measured to obtain the absorbance spectrum. The wavelengths and magnitudes of absorption arise from electronic transitions determined by the analyte's molecular or atomic structure and, for solutions, its concentration. Using ultraviolet-visible spectroscopy, the quantitative analysis is based on the Beer-Lambert law, as shown in Eq. (2.6).

$$A = \varepsilon bc \qquad \textbf{(2.6)}$$

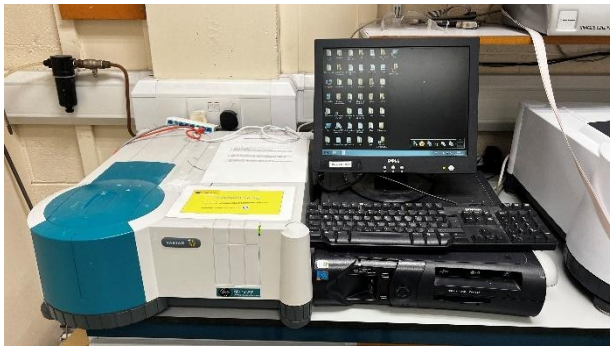

**Figure. 2.16.** A Cary 50 UV-visible spectrometer.

In this equation, A is the absorbance; ε is the molar absorptivity (extinction coefficient), which depends on the nature of the absorbing species and the incident wavelength λ; b is the optical path length (cm); and c is the analyte concentration (mol $L^{-1}$). Unless otherwise stated, spectra were acquired on a Varian Cary UV–vis spectrophotometer using 1 cm quartz cuvettes for both qualitative and quantitative measurements. In this thesis, UV–vis spectroscopy was employed to materials and drug analytical characteristics.

## 2.5.4. X-ray Photoelectron Spectroscopy (XPS)

X-ray Photoelectron Spectroscopy (XPS) was recorded in the University of Limerick and China University of Petroleum (East China). XPS works by bombarding a sample with X-rays, which ejects core-level electrons, called photoelectrons. X-rays (photons) are bombarded onto a sample, and when electrons in the sample absorb enough energy, they are ejected from the sample with a certain kinetic energy. A detector analyses the energy of those ejected electrons, and a plot of these energies and relative numbers of electrons is produced. Electrons of different energies follow different paths through the detector, allowing differentiation of the electrons and enabling the generation of the XPS spectra, as shown in Fig. 2.17 and 2.18.

**Figure. 2.17.** FiKratos AXIS ULTRA spectrometer.

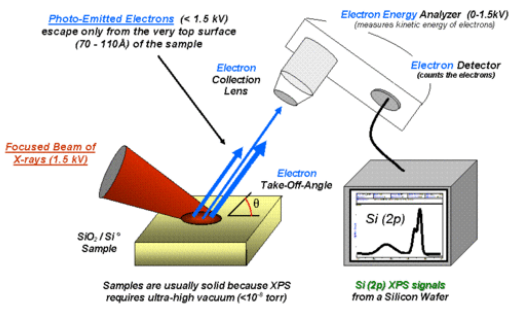


**Figure. 2.18.** Diagram depicting the instrumentation of the X-ray photoelectron spectrometer.

Atoms present in compound being tested by XPS are determined according to the Eq. (2.7).

$$E_{binding} = E_{photon} - E_{kinetic} + \phi \quad \textbf{(2.7)}$$

Here, binding energy is the energy of an electron attracted to a nucleus; photon energy is the energy of X-ray photons being used by the spectrometer, and the kinetic energy is the energy of the ejected electrons from the sample. The work function is a correction factor for the instrument and correlates to the minimum energy required to eject an electron from an atom. The work function and photon energy are known, and the detector measures the kinetic energy. As electrons are in orbitals farther from the nucleus, less energy is required to eject them, so the binding energy is lower for higher orbitals. Also, electrons in different subshells (s, p, d, etc.) have different energies.

The XPS data recorded in this thesis were carried out with a FiKratos AXIS ULTRA spectrometer, as shown in Fig. 2.17, at the Bernal Institute at the University of Limerick.

### 2.5.5. Raman Spectroscopy

Raman spectroscopy was recorded at the University of Limerick, Yeungnam University, and China University of Petroleum (East China). Raman spectroscopy is a vibrational spectroscopic technique that typically requires minimal sample preparation. In a Raman experiment, a monochromatic excitation source (near-UV, visible, or near-IR) illuminates the specimen. While most photons are elastically scattered (Rayleigh scattering), a small fraction undergoes inelastic scattering, yielding Stokes-shifted (longer wavelength) or anti-Stokes-shifted (shorter wavelength) photons. The frequency shifts correspond to molecular vibrational energies and thus constitute a "fingerprint" of the chemical composition and structure of the analyte. The Raman system used in these studies is shown in Figure 2.19, while a schematic of the technique is provided in Figure 2.20.


**Figure. 2.19.** inVia Reflex Raman Microscope (532 and 632.8 nm).

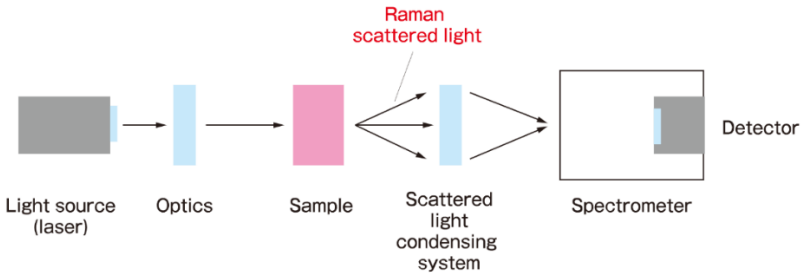


**Figure. 2.20.** Example of Raman spectroscopy configuration.

## 2.5.6. Fluorescence Spectroscopy

Fluorescence spectroscopy is a technique that analyses the light emitted by a sample after it has been excited by a light source, such as ultraviolet light. Molecules absorb photons, become electronically excited, and then release energy by emitting their own photons as fluorescence. This emitted light is then measured to determine the sample's structure or concentration, making the method highly sensitive and selective.

**Figure. 2.21.** Agilent® Cary Eclipse Fluorescence Spectrometer.

## 2.6 Data Acquisition and Statistical Analysis

All electrochemical experiments were carried out at room temperature. Each experiment was repeated at least three times, and the %RSD was computed. The recorded experimental impedance data were fitted to an equivalent circuit, with fitting errors kept below 2%. Again, all the impedance experiments were performed in triplicate.

# References

[1] N. Liu, Q. Tang, B. Huang, and Y. Wang, “Graphene Synthesis: Method, Exfoliation Mechanism and Large-Scale Production,” Jan. 01, 2022, MDPI. doi: 10.3390/cryst12010025.

[2] R. Yang et al., “Synthesis of atomically thin sheets by the intercalation-based exfoliation of layered materials,” Feb. 01, 2023, Nature Publishing Group. doi: 10.1038/s44160-022-00232-z.

[3] Y. X. Gan, A. H. Jayatissa, Z. Yu, X. Chen, and M. Li, “Hydrothermal Synthesis of Nanomaterials,” 2020, Hindawi Limited. doi: 10.1155/2020/8917013.

[4] P. T. Rimbi, N. O’Boyle, G. R. Douce, M. Pizza, R. Rosini, and A. J. Roe, “Enhancing a multi-purpose artificial urine for culture and gene expression studies of uropathogenic Escherichia coli strains,” J. Appl. Microbiol., vol. 135, no. 4, Apr. 2024, doi: 10.1093/jambio/lxae067.

[5] T. Yu, “The Detection and Removal of Pollutants in Aquatic Environments: Developing Sensitive Electrochemical Sensors and Using Magnetic Adsorbents,” 2024.

[6] R. D. O’Neill, S. C. Chang, J. P. Lowry, and C. J. McNeil, “Comparisons of platinum, gold, palladium and glassy carbon as electrode materials in the design of biosensors for glutamate,” in Biosensors and Bioelectronics, Jun. 2004, pp. 1521–1528. doi: 10.1016/j.bios.2003.12.004.

[7] A. J. . Bard and L. R. . Faulkner, Electrochemical methods : fundamentals and applications. John Wiley & Sons, Inc., 2001.

[8] “https://www.nanoscience.com/techniques/electrochemistry/.”

[9] Y. Rico, J. C. Bidegain, and C. I. Elsner, “Synthetic and natural Iron oxide characterization through microparticle voltammetry,” 2009.

[10] “https://mtxlabsglobal.com/cyclic-voltammetry/.”

[11] E. M. Espinoza, J. A. Clark, J. Soliman, J. B. Derr, M. Morales, and V. I. Vullev, “Practical Aspects of Cyclic Voltammetry: How to Estimate Reduction Potentials When Irreversibility Prevails,” J. Electrochem. Soc., vol. 166, no. 5, pp. H3175–H3187, 2019, doi: 10.1149/2.0241905jes.

[12] C. M. A. . Brett and A. M. Oliveira. Brett, Electrochemistry : principles, methods, and applications. Oxford University Press, 1993.

[13] C. M. A. Brett and A. M. O. Brett, “Electroanalysis Oxford University Press,” New York, 1998.

[14] D. Pletcher, R. Greff, R. Peat, L. M. Peter, and J. Robinson, Instrumental methods in electrochemistry. Elsevier, 2001.

[15] M. G. Trachioti, A. C. Lazanas, and M. I. Prodromidis, “Shedding light on the calculation of electrode electroactive area and heterogeneous electron transfer rate constants at graphite screen-printed electrodes,” Microchimica Acta, vol. 190, no. 7, Jul. 2023, doi: 10.1007/s00604-023-05832-w.

[16] A. N. Tufan, S. Baki, K. Güçlü, M. Özyürek, and R. Apak, “A novel differential pulse voltammetric (DPV) method for measuring the antioxidant capacity of

polyphenols-reducing cupric neocuproine complex," J. Agric. Food Chem., vol. 62, no. 29, pp. 7111–7117, Jul. 2014, doi: 10.1021/jf5017797.
[17] C. Harley, C. Breslin, and D. Rooney, "The Formation of an Electrochemical Sensor for the Selective Detection of Dopamine," 2009.
[18] G. J. Johnson, "Encyclopedia of analytical science," Reference Reviews, vol. 19, no. 8, pp. 38–39, 2005.
[19] "http//www. Jeol.co.jp."
[20] W. Zhou and Z. L. Wang, Scanning microscopy for nanotechnology: techniques and applications. Springer science & business media, 2007.
[21] R. W. Kelsall, I. W. Hamley, and M. Geoghegan, "Nanoscale Science and Technology," 2005.
[22] G. Lawes, "Scanning electron microscopy and X-ray microanalysis," 1986.
[23] J. I. Goldstein, D. E. Newbury, J. R. Michael, N. W. M. Ritchie, J. H. J. Scott, and D. C. Joy, Scanning electron microscopy and X-ray microanalysis. springer, 2017.
[24] N. Kanani, "Electroplating: Basic Principles, Processes and Practice." Technology & Engineering, Elsevier, 23 Nov 2004.

# **Chapter 3** Electrochemical Detection of Metronidazole (MTZ) with Electrodeposited $MoS_x$ and Exfoliated $MoS_2$

# 3.1. Introduction

It is well known that nitroimidazole antibiotics exhibit broad antimicrobial activity against anaerobic bacteria and protozoa, making them widely prescribed in both human and veterinary medicine worldwide [1-4], as discussed in Chapter 1. Among them, metronidazole (MTZ) remains one of the most commonly used drugs for oral, dental and respiratory tract infections and Crohn's disease, supporting its extensive consumption and environmental release [5-8]. At the same time, excessive use and incomplete removal during wastewater treatment can lead to MTZ residues remaining in aquatic environments, raising concerns due to reported genotoxic and mutagenic effects and the potential for ecological and human exposure. Consequently, sensitive and selective monitoring of MTZ in complex water matrices is an environmental and public-health priority [9-13].

A growing body of literature has explored electrochemical routes for MTZ quantification, as they enable rapid, low-cost measurements with portable instrumentation suitable for on-site analysis. Reported platforms span cobalt-reduced graphene oxide hybrids [14], electrodeposited bismuth films [15], iron-oxide [16] and manganese-oxide nanocomposites [17], among others [18], which demonstrate strong analytical promise [19]. However, despite the widespread use of $MoS_2$, we found no prior reports that directly employ $MoS_2$ itself as the active modifier for MTZ electroanalysis [20-25].

In this work, we address that gap and, in parallel, benchmark $MoS_2$ against an amorphous $MoS_x$, which is attractive for its one-step, aqueous process electrodeposition. Specifically, we compare few-layer $MoS_2$ nanosheets prepared by rapid, environmentally benign tryptophan-assisted exfoliation and drop-casting on glassy carbon (GCE/$MoS_2$) with amorphous, sulfur-rich $MoS_x$ films electrodeposited from

$(NH_4)_2MoS_4$ in near-neutral acetate electrolyte. This pairing contrasts a defect- and edge-rich 2D semiconductor with a comparable amorphous coating, while maintaining scalability and solvent-free synthesis.

In this study, a comparison is made linking material structure to sensing performance for MTZ using exfoliated $MoS_2$ sheets and electrodeposited $MoS_2$. Therefore, this study aims to (i) establish and verify each surface modifier's morphology and surface chemistry, (ii) evaluate interfacial charge-transfer and capacitive backgrounds by impedance analysis, and (iii) relate these descriptors to the analytical performance obtained by cyclic and differential-pulse voltammetry in neutral phosphate buffer. This study provides both a practical route to green preparation of $MoS_2$ modifiers and a comparison of exfoliated $MoS_2$ and electrodeposited $MoS_x$ when designing electrochemical sensors for MTZ.

## 3.2. Experimental

The cyclic voltammetry measurements, described in the Section 2.3.3.1, were carried out using a Solartron 1287 potentiostat, electrochemical impedance spectroscopy measurements were performed with a Solartron 1287 potentiostat coupled with a 1255 FRA (Solartron). While differential pulse voltammetry experiments (DPV), described in the Section 2.3.3.2, were recorded using a CHI440 CH Instruments, Inc. potentiostat. The Electrochemical Impedance Spectroscopy (EIS), described in the Section 2.3.3.3, were recorded using a solartron 1287 potentiostat coupled with a 1255 FRA (Solartron). The surface morphology was studied using scanning electron microscopy (SEM), described in the Section 2.4.1, with a Hitachi S-4800 FESEM, while energy dispersive X−ray analysis (EDX), described in the Section 2.5.1. FTIR measurements, described in the Section 2.5.2, were performed using a Nicolet iS50 FTIR spectrometer, and UV-vis spectroscopy, described in the Section 2.5.3, measurements were recorded using a Cary 50 spectrometer. The procedure for material characterisation methods and specific characterisation techniques usage is detailed in the corresponding sections of Chapter 2, Experimental and Research Methods.

### 3.2.1. Preparation of Electrodeposited $MoS_x$ and Exfoliated $MoS_2$

The amorphous $MoS_x$ was electrodeposited from a 5 mM $(NH_4)_2MoS_4$ solution dissolved in an aqueous 0.1 M $CH_3COONa$ adjusted to a pH of 7.5 by cycling between 0.2 and −1.2 V at 50 mV $s^{-1}$. This electrodeposited film was formed at both GCE and ITO electrodes. The $MoS_2$ powder was dispersed in an aqueous solution of 1.0 mM DL-tryptophan to give a 8 mg/10 mL sample. This sample was sonicated for 30 min and then centrifuged for an additional 30–min period. The supernatant was collected and 6.6 µL of this solution (shown in Table 3.1), which contains the smaller sheets, was drop cast onto the GCE electrode and dried under an infrared lamp. This process was

optimised for both reproducibility and to maximise the peak current for the reduction of MTZ by varying the drop cast volume between 2.5 and 10.0 µL. The optimum drop cast volume of 6.6 µL was applied three times to increase the density of the $MoS_2$ sheets deposited at the GCE. The electrode was dried thoroughly between each step.

**Table 3.1**: Comparison of the different volumes of the drop of the exfoliated $MoS_2$ sheets solution for the detection of 155 µM MTZ.

| Value of solution (µL) | Potential (mV) | Current (µA) | RSD (%) |
|---|---|---|---|
| 2.5 | -0.784 | 5.73 | 4.16 |
| 5.6 | --0.724 | 9.84 | 3.96 |
| 6.6 | -0.682 | 10.42 | 3.80 |
| 8.6 | -0.688 | 9.32 | 3.82 |
| 10.0 | -0.744 | 7.77 | 4.97 |

## 3.2.2. Electrochemical Protocols

The electrochemical experiments were carried out in a neutral 0.1 M phosphate buffer solution (pH of 7.0), which was deoxygenated with high-purity nitrogen gas for 30 min prior to the electrochemical measurements. The concentration of MTZ was maintained at 100 µM and the cyclic voltammetry experiments were recorded at a scan rate of 50 mV $s^{-1}$. The DPV experiments were carried out with an amplitude of 0.06 V, a pulse width of 0.05 s, a sampling width of 0.0167 s, and a pulse period of 0.5 s. The pH was varied by adding $HNO_3$ or NaOH to the 0.1 M phosphate buffer solution. The electrochemical impedance data were recorded under open-circuit conditions in the phosphate buffer in the presence of 100 µM MTZ between 3 mHz and 100 kHz following a 30-min immersion period in the solution.

# 3.3. Results and Discussion

## 3.3.1. Formation and Characterisation

The growth of the amorphous $MoS_x$ film is illustrated in Fig. 3.1 (a), where the voltammograms shown correspond to cycling of the GCE between 0.2 and −1.0 V in a near neutral acetate solution containing $(NH_4)_2MoS_4$. Peaks labelled as (I), (II) and (III) emerge with increasing cycling. The reduction wave labelled as (I) is consistent with the reduction of $MoS_4^{2-}$, Eq. (3.1), and this is in good agreement with previous studies [12]. As the GCE is initially cycled from 0.2 V in the cathodic direction, the first reduction wave, which can be attributed to Eq. (3.1), appears as a small broad wave at a relatively low potential of −1.0 V as the $MoS_2$ is deposited at the GCE surface. With subsequent cycling, the reduction of $MoS_4^{2-}$ occurs at a much higher potential of about −0.6 V, suggesting that $MoS_2$ preferentially forms on the previously deposited $MoS_2$.

$$MoS_4^{2-} + 2H_2O + 2e^- \rightarrow MoS_2 + 2HS^- + 2OH^- \quad \textbf{(3.1)}$$

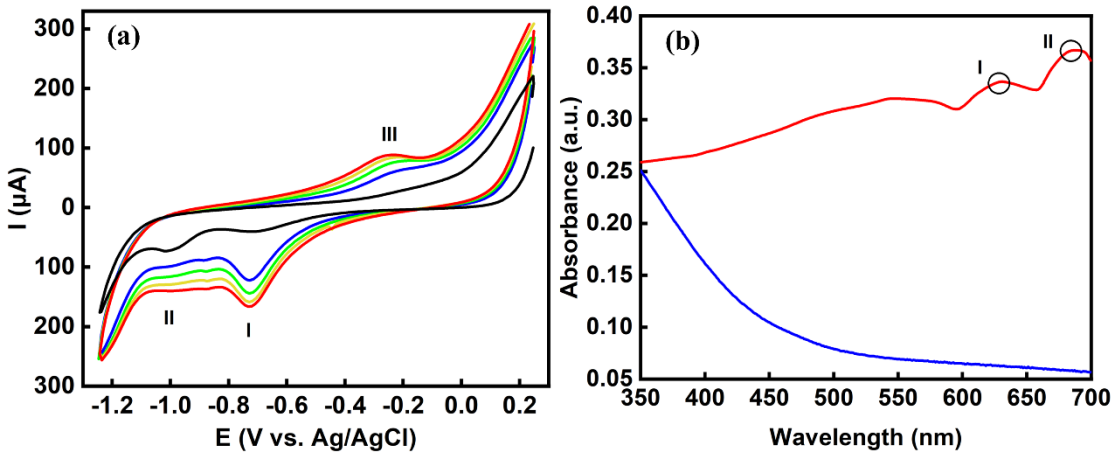


**Figure 3.1.** (a) Cyclic voltammograms recorded at 50 mV $s^{-1}$ in 5 mM $(NH_4)_2MoS_4$ and 0.1 M $CH_3COONa$ at a pH of 7.5, (b) UV-visible spectrum recorded for $MoS_2$ exfoliated for 30 min in 1.0 mM tryptophan and electrodeposited $MoS_x$.

As the p*K*a of $H_2S$ is 6.8 and the p*K*a of $HS^-$ is approximately 14.0 [38], $HS^-$ is the predominant species with a much lower concentration of $S^{2-}$ in the neutral acetate

solution. The broad oxidation wave observed at about −0.2 V (Peak III) is consistent with the oxidation of $MoS_4^{2-}$ to $MoS_3$, Eq. (3.2). The $MoS_3$ can be further reduced to give $MoS_2$ as illustrated in Eq. (3.3) and this reduction reaction appears as Peak II in Fig. 3.1(a). Considering Eqs. (3.1)-(3.3), it is likely that the deposit will not only contain $MoS_2$, but also traces of $MoS_3$ to give $MoS_x$.

$$MoS_4^{2-} \rightarrow MoS_3 + S + 2e^- \quad \textbf{(3.2)}$$

$$MoS_3 + 2e^- + H_2O \rightarrow MoS_2 + HS^- + OH^- \quad \textbf{(3.3)}$$

The UV-visible spectra of the exfoliated $MoS_2$ powders and the electrodeposited $MoS_x$ are presented in Fig. 3.1 (b). The characteristic peaks at about 632 and 683 nm, which have been attributed to the 2D $MoS_2$ sheets, are clearly evident for the exfoliated $MoS_2$ sheets [39,40]. This indicates that the tryptophan with its aromatic indole ring can disperse the hydrophobic $MoS_2$ sheets.

As expected, these peaks are absent for the amorphous $MoS_x$. In Fig. 3.2, the FTIR spectra of the $MoS_2$ sheets and electrodeposited $MoS_x$, recorded in the range of 500–4000 $cm^{-1}$, are shown. The spectra are similar, with the additional peaks in the vicinity of 500 to 1500 $cm^{-1}$ in the spectrum of the $MoS_2$ sheets indicating the presence of tryptophan. The characteristic peaks of $MoS_2$ are evident at 1423 and 1114 $cm^{-1}$ [41], and at about 900 $cm^{-1}$ [41]. In addition, the band at about 634 $cm^{-1}$ has been attributed to $MoS_2$ [42], while the band at 526 $cm^{-1}$ may be due to the S − S bond [43]. The broad band centred between 3700 and 3000 $cm^{-1}$ is consistent with O–H stretching from adsorbed water molecules. Likewise, the hydroxyl group stretching vibrations, associated with adsorbed $H_2O$ molecules [44] are seen at 1601 $cm^{-1}$.

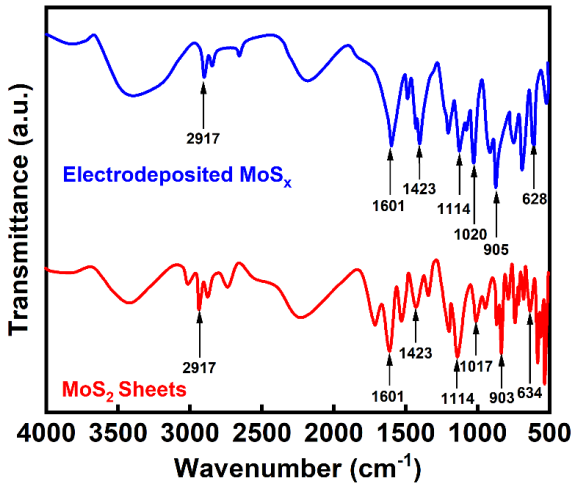


**Figer 3.2.** FTIR spectrum for the electrodeposited $MoS_x$ and the exfoliated $MoS_2$ sheets.

The surface morphologies of the electrodeposited $MoS_x$ and the GCE/$MoS_2$ are shown in Fig. 3.3. The surface of the $MoS_x$ is smooth, Fig. 3.3 (a), with some defects, as shown in the inset. The EDX spectrum in Fig. 3.3 (b) indicates the presence of both Mo and S, as evidenced by overlapping peaks with similar keV values. There is evidence of some oxygen in the EDX spectrum, which may indicate the presence of Mo−O species, such as $MoO_3$, in the electrodeposited $MoS_x$ [11]. Indeed, it is very likely that the aqueous $(NH_4)_2MoS_4$ solution will contain traces of $MoO_4^-$.The morphology of the GCE/$MoS_2$ is shown in Fig. 3.3 (c), where distinct sheets are visible. Clearly, applying three drop-cast layers results in excellent coverage of the GCE surface. The sheets range in size from approximately 0.5 to 2.5 μm, as illustrated in the inset of Fig. 3.3 (c). The EDX spectrum in the inset of Fig. 3.3 (d) closely resembles that of the electrodeposited $MoS_x$. However, the weak O signal in this case is likely due to tryptophan used during exfoliation. After applying five successive drop-cast layers, the agglomeration of the $MoS_2$ sheet becomes apparent, as shown in Fig. 3.3 (e). Subsequently, the individual sheets become less distinct (Fig. 3.3 (f)), indicating that the sheets are stacked.

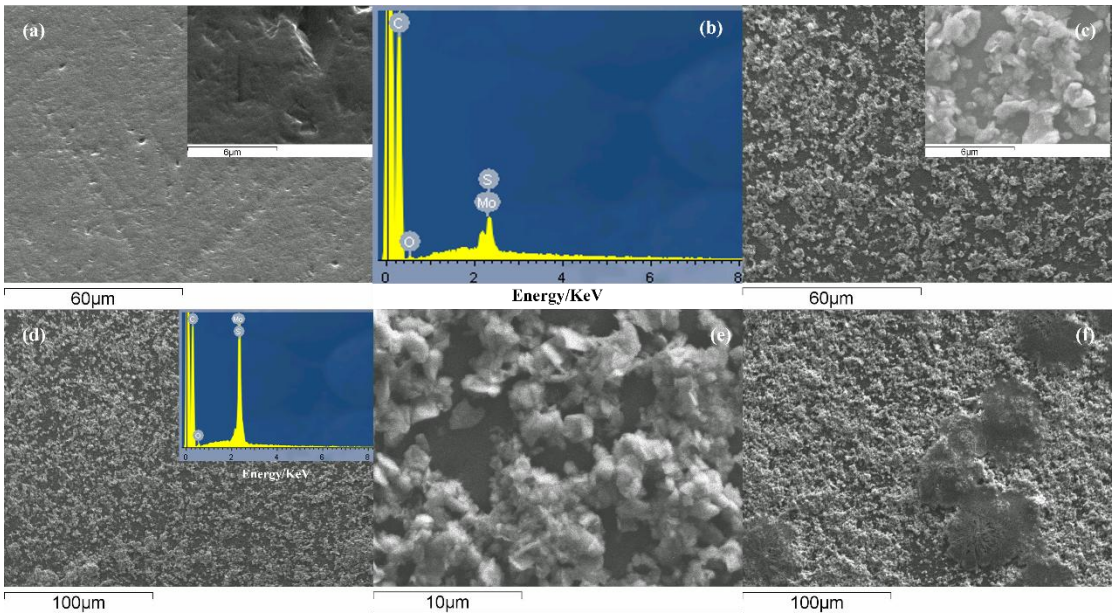


**Figure 3.3.** (a) SEM micrographs for electrodeposited $MoS_x$, (b) EDX spectrum for $MoS_x$, (c) and (d) SEM micrographs and corresponding EDX spectrum for GCE/$MoS_2$ (3 layers), (e) and (f) SEM micrographs of GCE/$MoS_2$ (5 layers).

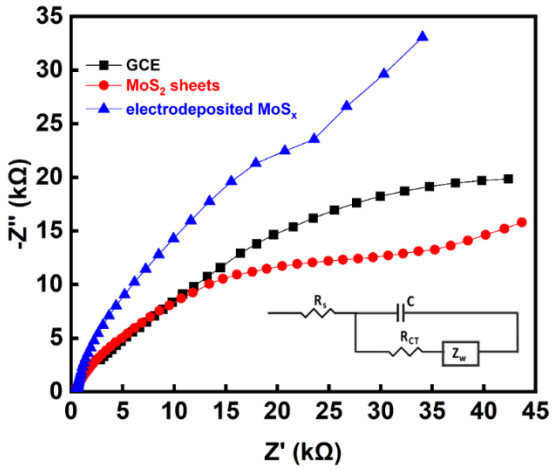


**Figure 3.4.** Electrochemical impedance data recorded for GCE, GCE/$MoS_2$ and electrodeposited $MoS_x$.

The electronic conductivity and capacitance of both the GCE/$MoS_2$ sheets and electrodeposited $MoS_x$ were evaluated using electrochemical impedance spectroscopy. Measurements were performed in 0.1 M phosphate buffer containing 100 µM MTZ under open-circuit conditions, as illustrated in Fig. 3.4. The impedance spectra were analysed with an equivalent circuit model where $R_s$ represents solution resistance, $R_{CT}$ denotes charge transfer resistance, C indicates capacitance, and $Z_w$ corresponds to a

Warburg element reflecting MTZ diffusion. Characteristic features include a semicircular response at high frequencies and a Warburg diffusion tail at lower frequencies, with electrodeposited $MoS_x$ displaying the highest overall impedance and GCE/$MoS_2$ exhibiting the lowest. Using the equivalent circuit, the $R_{CT}$ was estimated at $2.04 \pm 0.07 \times 10^4$ Ω (n=3) for the GCE/$MoS_2$ and $6.28 \pm 0.06 \times 10^5$ Ω (n=3) for the electrodeposited $MoS_x$, indicating a near 30-fold difference in $R_{CT}$ on comparing the two systems. On evaluating the capacitance, it was found that the electrodeposited $MoS_x$ exhibited the highest capacitance, at $9.7 \pm 0.3 \times 10^{-5}$ C compared to a lower value of $5.6 \pm 0.3 \times 10^{-6}$ C for the GCE/$MoS_2$. These results indicate that the GCE/$MoS_2$ provides a more promising sensor with a lower $R_{CT}$ combined with a lower capacitance. This highlights the advantage of $MoS_2$ sheets as an electrode modifier in terms of reducing the overall charge transfer resistance, ultimately resulting in improved electrochemical activity.

## 3.3.2. Electrochemical Behaviour of MTZ

The electrochemical reduction of MTZ is an irreversible process, with the transfer of $4H^+/4e^-$ to give the N–hydroxy amino compound, as illustrated in Scheme 3.1.

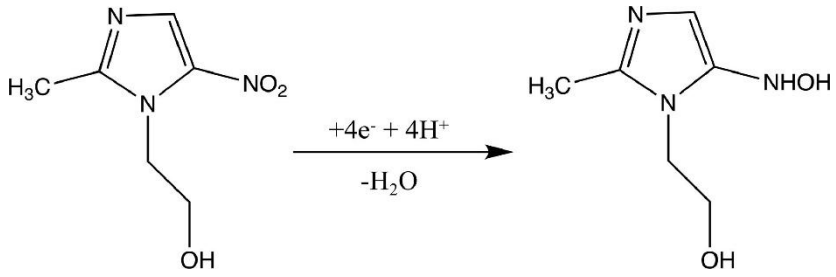


**Scheme 3.1.** Irreversible reduction of MTZ where the $NO_2$ group is converted into NHOH with the transfer of $4e^-/4H^+$.

This electron transfer step typically occurs at potentials around −0.70 to −0.80 V vs SCE for the reduction of MTZ [34]. The performance of the GCE/$MoS_2$ and electrodeposited $MoS_x$ in the electrochemical detection of MTZ is summarised in Fig.

3.5. In Fig. 3.5 (a), the cyclic voltammograms recorded in 100 µM MTZ and in the background phosphate electrolyte are shown for the GCE/$MoS_2$. The onset of MTZ reduction is observed at approximately −0.30 V, while the peak current is reached at −0.67 V.

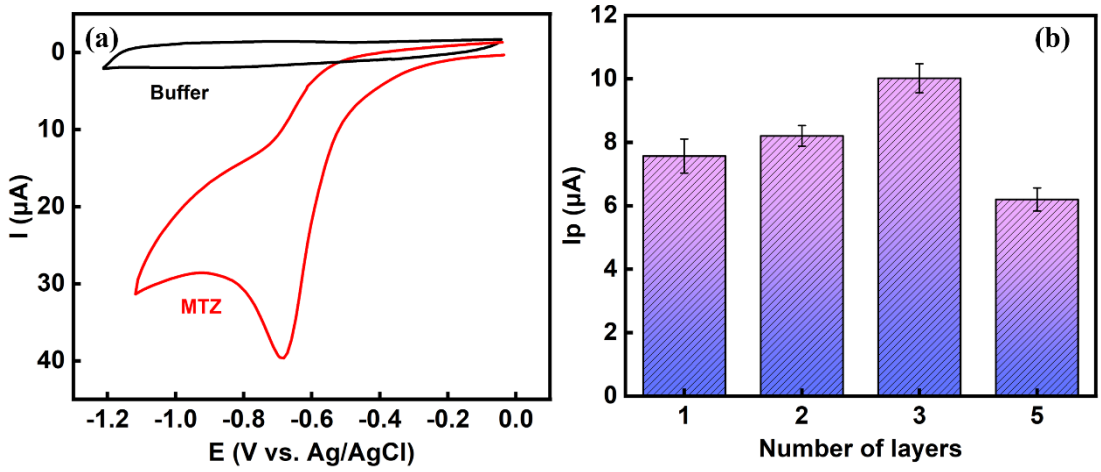


**Figure 3.5.** (a) Cyclic voltammograms recorded for GCE/$MoS_2$ in phosphate buffer and in phosphate buffer with 100 µM MTZ, (b) peak current (background corrected) for 100 µM MTZ plotted as a function of the number of $MoS_2$ layers applied to the GCE (n = 3).

With a single application of the $MoS_2$ sheets, an impressive peak current of 6.9 µA is achieved, which increases to about 9.9 µA with the application of three layers of $MoS_2$, as summarised in Fig. 3.5 (b). However, applying five layers results in a slight reduction in the peak current. This decrease may be related to the restacking of the $MoS_2$ sheets, observed when increasing the number of drop–cast $MoS_2$ layers, as confirmed by SEM micrographs, Fig. 3.3 (f).

The type of exfoliation solvent notably influenced the reduction of MTZ. Using a ratio 1:1 of ethanol/water mixture yielded a lower peak current of 3.54 µA at −0.72 V, while cyrene resulted in an even lower peak of 1.86 µA at −0.78 V. The optimal exfoliation time in the aqueous tryptophan solution was 30 min, with no significant increase in peak current observed at 120, 150, or 180 min. Cyrene effectively exfoliated bulk $MoS_2$,

but its high boiling point (227 °C) and viscosity made isolating smaller $MoS_2$ sheets and removing them during drop-casting difficult. The ethanol/water solution was also effective, and after drop-casting onto the GCE, the ethanol evaporates, leaving tryptophan evident in FTIR spectra (Fig. 3.2), which can prevent $MoS_2$ sheets from restacking. Although not shown, a low peak current of 1.79 μA at −0.74 V for the unmodified GCE suggests that GCE/$MoS_2$, especially when exfoliated with aqueous tryptophan, is highly effective for MTZ electrochemical reduction.

Similar data are shown in Fig. 3.6 (a) and (b) for the electrodeposited $MoS_x$. In this case, a broad wave is observed for the reduction of 100 μM MTZ, and a well-formed peak emerges only at a much higher concentration of 2 mM MTZ. Furthermore, this peak current appears at a lower potential of −0.74 V, and this electrodeposited film exhibits a much higher capacitive current compared with the GCE/$MoS_2$. This higher capacitance aligns with the impedance data presented in Fig. 3.4. The effect of the number of cycles employed in the electrodeposition of the film, where the GCE substrate is cycled between 0.2 V and −1.2 V, is illustrated in Fig. 3.6 (b). Initially, the peak current increases with the number of cycles; however, after approximately 18 cycles, the current stabilises and shows no further increase. This phenomenon may be associated with the electrodeposition process, which is initially efficient, evidenced by increasing currents at Peak 1 for cycles 2 to 4, as shown in Fig. 3.1 (a). Nonetheless, minimal amounts of $MoS_x$ are deposited beyond 18 cycles. Clearly, there is a considerable variation in the detection of MTZ at the GCE/$MoS_2$ and electrodeposited $MoS_x$. The peak currents are significantly lower for the electrodeposited $MoS_x$, as shown by comparing the data in Fig. 3.5 (b) and Fig. 3.6 (b). The enhanced performance of the GCE/$MoS_2$ seems to be linked to a reduced charge transfer resistance, as depicted in Fig. 3.4. Additionally, it may be associated with an increased surface area, edge effects, and potential defects in the exfoliated $MoS_2$ sheets, which facilitate and improve efficient electron transfer.

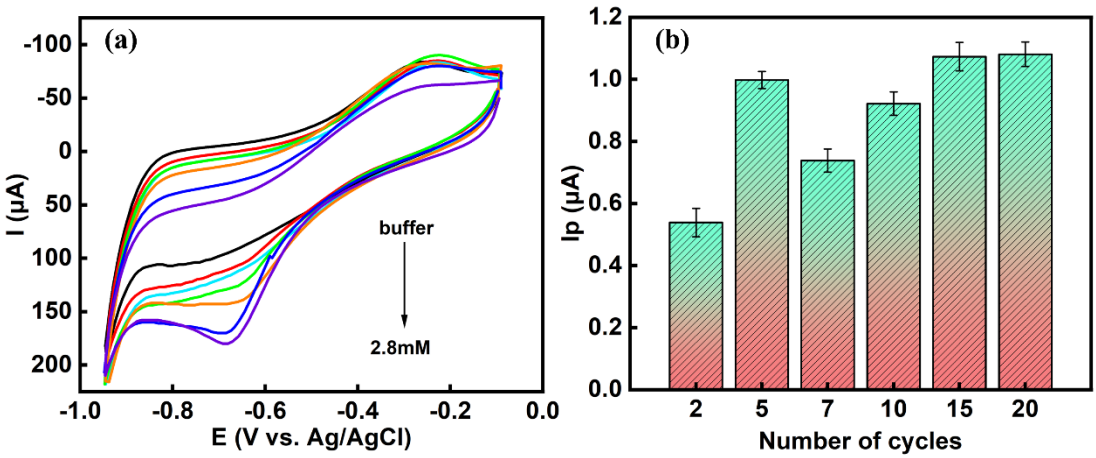


**Figure 3.6.** (a) cyclic voltammograms for the electrodeposited $MoS_x$ cycled in solutions with MTZ concentrations of 0.1, 0.3, 0.5, 1.0, 2.0, 2.8 mM, (b) peak current (background corrected) for 100 μM MTZ as a function of the number of cycles in the electrodeposition of $MoS_x$ (n = 3).

In Fig. 3.7 (a), the voltammograms recorded in the presence of the $[Fe(CN)_6]^{3-/4-}$ redox couple for both the GCE and the GCE/$MoS_2$ are presented. The GCE/$MoS_2$ displays a pair of well-defined redox peaks with a peak current ratio of 0.97 and a peak-to-peak potential separation of 125 mV. At this relatively low scan rate, the peak currents for GCE/$MoS_2$ are only marginally higher than those of the GCE. When plotting the peak current against the square root of the scan rate, linear plots were obtained for both the unmodified GCE and GCE/$MoS_2$ electrodes, indicating that the oxidation and reduction of the $[Fe(CN)_6]^{3-/4-}$ couple are governed by diffusion. Using linear regression, the relationship obtained for the GCE/$MoS_2$ was $I_p$ (μA) = 171.6 $v^{1/2}$ ($V^{1/2}$ $s^{-1/2}$) – 13.7, while a lower gradient was obtained for the GCE, with the linear equation being $I_p$ (μA) = 132.4 $v^{1/2}$ (($V^{1/2}$ $s^{-1/2}$) – 7.6. The non-zero intercepts, often seen in experimental data, suggest a deviation from the ideal Randles–Ševčík equation. However, the higher gradient is consistent with a higher surface area for the GCE/$MoS_2$, as evident in Fig. 3.3 (c) and (d). Accordingly, the active surface areas of both the unmodified GCE and GCE/$MoS_2$ were estimated using the Randles–Ševčík Equation, which is provided in Eq. (2.2). Here, C and D represent the concentration and diffusion coefficient of the $[Fe(CN)_6]^{3-/4-}$, respectively, A is the electroactive surface area, n is the number of electrons transferred and I and v are the parameters measured and varied and correspond

to the peak current and scan rate, respectively. Using the linear plots in Fig. 3.7 (b), the electroactive surface areas of the GCE and GCE/$MoS_2$ were estimated as 0.071 ± 0.002 and 0.094 ± 0.004 $cm^2$, respectively, to give a 1.3–fold increase in the area on decorating the GCE with the $MoS_2$ sheets.

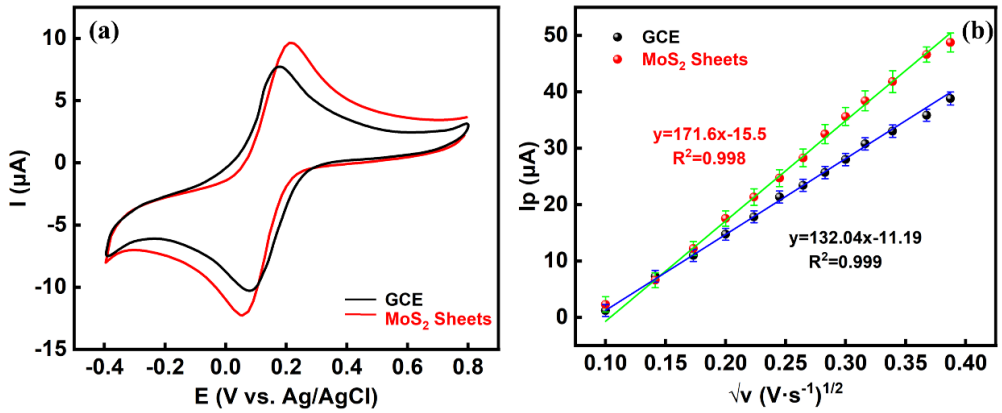


**Figure 3.7** (a) Cyclic voltammograms recorded at 50 mV $s^{-1}$ at GCE and GCE/$MoS_2$ in 2.5 mM $[Fe(CN)_6]^{3-/4-}$ (b) peak currents plotted as a function of the square root of the scan rate for GCE and GCE/$MoS_2$ in 2.5 mM $[Fe(CN)_6]^{3-/4-}$ (n = 3).

The influence of scan rate on the peak current and peak potential for the reduction of 100 µM MTZ at the GCE/$MoS_2$ is illustrated in Fig. 3.8 (a). The peak potential shifts to more negative values as the scan rate increases, characteristic of an irreversible reaction with slow electron transfer. The peak current increases with the scan rate, resulting in a linear relationship, as shown in Fig. 3.8 (b), where the peak current is plotted against the square root of the scan rate. Additionally, the reduction of MTZ is diffusion-controlled, as described by Eq. (3.4).

$$I_p = (2.99 \times 10^5)n(\alpha n')^{1/2}D^{1/2}v^{1/2}AC_o \qquad \textbf{(3.4)}$$

In this analysis, $I_p$ is the peak current, n indicates the number of electrons transferred, D denotes the diffusion coefficient, ν represents the scan rate, $C_o$ is the concentration, A represents the electroactive area, α is the charge transfer coefficient and n' is the number of electrons transferred during the rate–determining step.

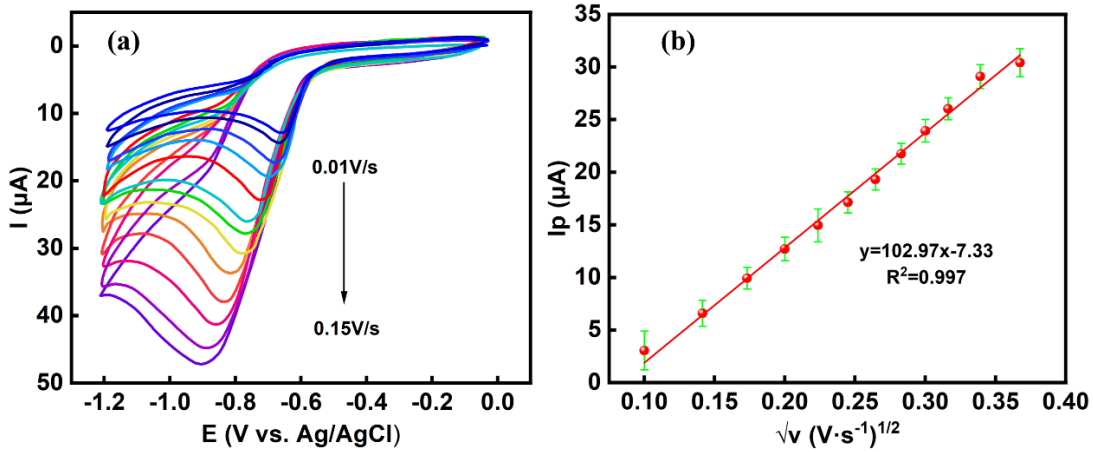


**Figure 3.8.** (a) cyclic voltammograms recorded for GCE/$MoS_2$ in 100 μM MTZ and (b) peak currents plotted as a function of the square root of the scan rate for GCE/$MoS_2$ in 100 μM MTZ (n = 3).

The αn' value can be estimated using Eq. (3.5), where $E_p$ is the peak potential and $E_{p1/2}$ is the half–wave potential. The $|E_p–E_{p1/2}|$ term, which is described as the shape factor, was computed as a function of the scan rate. An average value of 103 ± 0.67 mV was obtained for the shape factor, and the αn' was calculated to be 0.46. Setting α to 0.5, a typical value for electron transfer reactions, results in an n' value of 0.92, which is consistent with a single electron transfer rate-determining step.

$$\left|E_p - E_{p/2}\right| = 1.857\frac{RT}{F\alpha n'} \qquad \textbf{(3.5)}$$

The influence of pH on the peak potential and peak current is demonstrated in Fig. 3.9 (a) and (b), respectively. A near-linear relationship is observed when plotting the peak potential as a function of pH across the range from 3.0 to 11.0. The average gradient was determined to be 0.0462 V/pH unit, with a linear equation of $E_p$ = –0.0462 pH – 0.3905 ($R^2$ = 0.98).

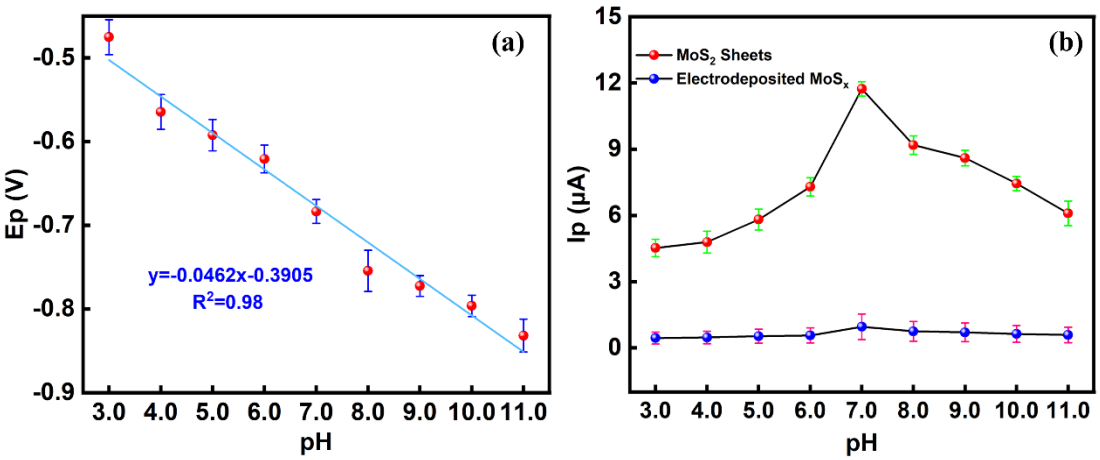


**Figure 3.9.** (a) peak potential (n = 3), (b) peak current plotted as a function of the pH of the solution with 100 μM MTZ for GCE/$MoS_2$ and electrodeposited $MoS_x$ (n = 3).

These findings are in good agreement with the Nernst equation, which predicts a theoretical slope of 0.059 m/n V/pH, where m and n denote the number of protons and electrons transferred, respectively. This observation aligns with the transfer of equal quantities of protons and electrons, as illustrated in Scheme 1. The maximum peak current was recorded at a pH of approximately 7.0, as shown in Fig. 3.9 (b), and this pH value was used in all subsequent experiments. Similar patterns were also observed with the electrodeposited $MoS_x$, as illustrated in Fig. 3.9 (b). However, the peak currents related to the reduction of MTZ are notably lower.

### 3.3.3 Analytical Characteristics

The analytical performance of the GCE/$MoS_2$ is summarised in Fig. 3.10. The DPVs recorded for the GCE/$MoS_2$ are shown in Fig. 3.10 (a), with the corresponding calibration plot in Fig. 3.10 (b). A well-defined linear response was obtained over the concentration range of 1.9 – 2000 μM, described by the regression equation, $I_p$ (μA) = 0.090 c (μM) – 3.16 ($R^2$ = 0.993). This gives a sensitivity of 0.090 μA $\mu M^{-1}$. Using the geometric surface area of 0.07 $cm^2$, the sensitivity can be computed as 1.29 μA $cm^{-2}$ $\mu M^{-1}$.

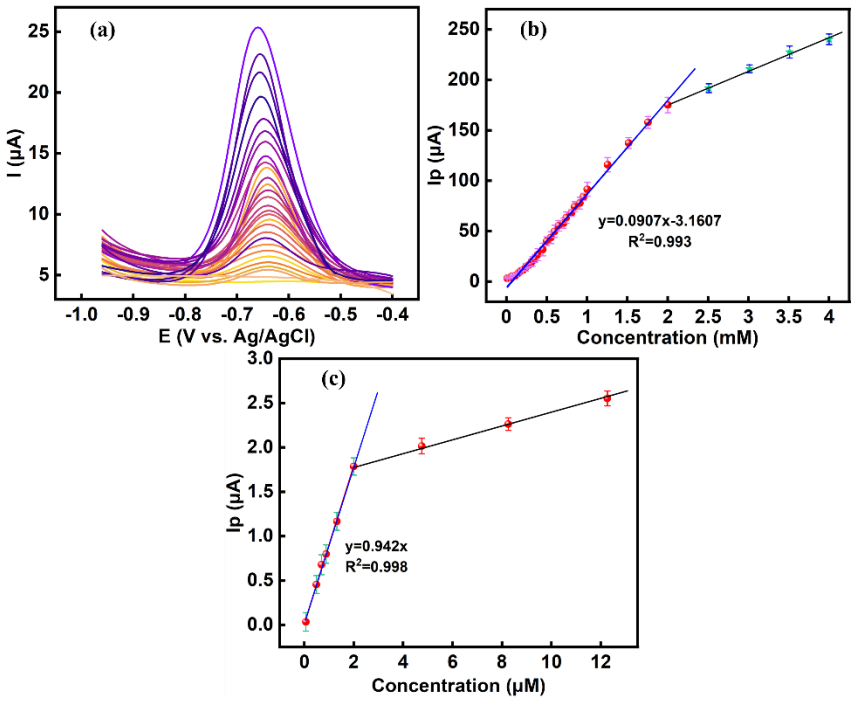


**Figure 3.10.** (a) DPV recorded between MTZ concentrations of 0.04 and 353 μM at the GCE/$MoS_2$, (b) linear calibration curves for the GCE/$MoS_2$ (n = 3), and (c) calibration curve showing the lower concentrations for GCE/$MoS_2$ (n = 3).

At lower concentrations, between 0.04 and 1.99 μM, as shown in Fig. 3.10 (c), the sensor exhibited an enhanced sensitivity of 0.943 μA $\mu M^{-1}$ (13.32 μA $\mu M^{-1}$ $cm^{-2}$). In this case, the linear regression equation is $I_p$ (μA) = 0.9426c (μM) ($R^2$ = 0.998). The limit of detection (LOD) was calculated as 4.3 nM using the sensitivity in the low-concentration range of 0.943 μA $\mu M^{-1,}$ and the standard deviation of blank DPV responses (LOD = 3σ/sensitivity). These data compare very well with some recently published reports, where LOD values of 24 nM [45], 6 nM [46] and 0.23 nM [47] were reported.

A more direct comparison with the existing literature is presented in Table 3.1 and demonstrates that the LOD of 4.3 nM achieved with the GCE/$MoS_2$ is very favourable relative to recent studies. Likewise, the GCE/$MoS_2$ shows a broad linear range extending to very high concentrations, from 1.9 to 2000 μM, which is significantly

higher than recently reported linear ranges from 5 to 120 μM [47] and surpasses many of the linear ranges listed in Table 3.2.

**Table 3.2**: Comparison of GCE/$MoS_2$ with the recently published papers in the electrochemical detection of MTZ.

| Materials | Linear range/ μM | LOD/ nM | Sensitivity μA/μM | Refs. |
|---|---|---|---|---|
| Ag electrode | 8 – 2000 | 1430 | 0.3797 | [48] |
| α-$Fe_2O_3$/CPE (carbon paste) | 0.8 – 100 | 285 | 5.621 | [49] |
| AgNP/CuMOF/Ppy–rGO | 0.08 – 160 | 24 | 0.0701 | [50] |
| C60-rGO-NF/SPE | 0.25 – 34 | 210 | 0.15 | [51] |
| O-gCN | 0.01 – 2060 | 5 | 0.038 | [52] |
| $Zn_3(VO_4)_2$ | 0.05 – 1303 | 9 | 0.0324 | [53] |
| CdS QDs | 0.1 – 203 | 53 | 0.0575 | [54] |
| Co/NC@w-$NiSO_4NiS_2$ | 3– 200<br>200 – 1000 | 9 | 0.1384<br>0.0482 | [55] |
| MnOOH/EG/GCE | 0.07 – 30 | 17 | 0.2235 | [56] |
| S–$CePO_4$@GCE | 5.0 – 3980 | 3600 | 0.0075 | [57] |
| NiO-Ni | 0.01–1.63 | 6 | 0.0272 | [58] |
| NiO | 0.8 – 4.7 | 8 | 0.0222 | [58] |
| CNF@AuNPs | 0.1 – 2000 | 24 | 0.0824 | [59] |
| RGO/$Mn_3O_4$/GCE | 0.1 – 9.5 | 37 | 13.786 | [60] |
| GR/$Fe_3O_4$NPs/GCE | 0.05–5<br>5–120 | 0.23 | 1.0423<br>0.0878 | [61] |
| $MoS_2$/GCE | 0.04 – 1.9<br>1.9 – 2000 | 4.3 | 0.943<br>0.090 | This work |

This extended concentration range is ideally suited for MTZ concentrations in the vicinity of 45 mg $L^{-1}$ (122 μM), which represent toxicity levels for algal cells, such as Chlorella pyrenoidosa, where 45.125 mg $L^{-1}$ was determined as the EC50 value [62]. Another interesting aspect of the GCE/$MoS_2$ is the high sensitivity of 13.32 μA $\mu M^{-1}$ $cm^{-2}$ in the low concentration range that extends to 1990 nM with the LOD at 4.3 nM, making the GCE/$MoS_2$ suitable for the detection of MTZ in both river sediments and

vegetables that have been reported to reach levels between 1.21 µg $kg^{-1}$ and 27.2 µg $kg^{-1}$ (0.1589 µM to 0.238 µM) [63].

The electrochemical reduction of nitroimidazoles has previously been described as an inner-sphere electron transfer reaction [64]. Accordingly, the nature of the electrode surface will play a significant role in the reduction of MTZ. At very low concentrations, MTZ molecules can be accommodated at the surface. However, as the concentration increases beyond 1990 nM, competition for surface sites becomes evident, resulting in a lower gradient for the calibration curve with two distinct linear regions (Fig. 3.10 (c)). There is no evidence for poisoning of the GCE/$MoS_2$, as the higher concentration linear region extends from 1.9 – 2000 µM, Fig. 3.10 (b), and there is only a relatively small shift in the peak potential varying from –0.65 V at 1.9 µM to –0.74 V at 2000 µM MTZ.

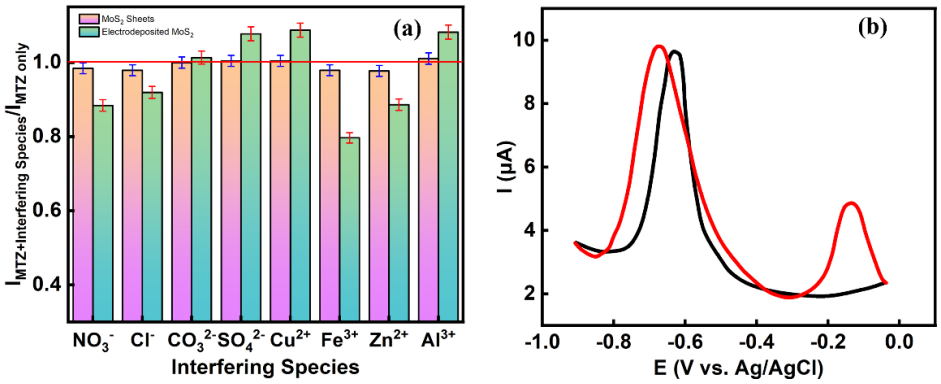


**Figure 3.11.** (a) Influence of various interferents for GCE/$MoS_2$ and GCE/electrodeposited $MoS_x$ (n = 3), (b) DPV for 100 µM MTZ in the absence (black trace(III)) and presence of 100 µM Cu(II) (red trace (I and II).

The influence of various interfering species on the peak currents recorded for the MTZ is illustrated in Fig. 3.11 (a). The figure depicts the ratio of the peak current measured for 100 µM MTZ in the presence and absence of each interferent, as a function of different anions and cations commonly encountered in aquatic environments. The concentrations of these interferents were maintained at 100 µM to accurately reflect typical water conditions contaminants (37.5 mg $L^{-1}$, 25 mg $L^{-1}$, 8 mg $L^{-1}$, 8 mg $L^{-1}$, 2.0 mg $L^{-1}$ Cu(II), 12 mg $L^{-1}$ Fe(III), 10 mg $L^{-1}$ Zn(II) and 10 mg $L^{-1}$ Al(III)). As

demonstrated, the peak current resulting from the reduction of MTZ remains relatively unaffected by the presence of interferents, yielding a ratio approximately equal to one across all tested interferent species. Many of these interferents, including Cu(II), Fe(III), and Zn(II), are capable of electrochemical reduction, as observed in Fig. 3.11 (b), which displays DPV plots for 100 μM MTZ in both the presence and absence of Cu(II). In this case, the reduction of Cu(II) to metallic copper is evident at approximately –0.18 V, and during this reduction event, it has a minimal influence on the signal from the MTZ. The peak currents are quite similar, but there is a slight shift in the peak potential, which may be due to minor pH variations or the deposition of trace amounts of copper at the GCE/$MoS_2$. Interestingly, the $MoS_x$ experiences more interference, Fig. 3.11 (a), which could be linked to the low peak currents observed with the MTZ, with the interfering species exerting more influence on the MTZ signal. Furthermore, the deposition of small amounts of copper at the electrodeposited $MoS_x$ results in a higher peak current, which may be attributed to the formation of a more conductive surface that facilitates the more efficient reduction of MTZ.

**Table 3.3**: Recovery data obtained for MTZ in tap water and real river samples.

| Sample | Added Drug (μM) | Recovery (%) |
|---|---|---|
| Tap Water | 50 | 89.9 ± 3.74 |
| | 100 | 96.2 ± 3.06 |
| | 200 | 96.8 ± 3.05 |
| Real River Water | 50 | 80.8 ± 6.45 |
| | 100 | 92.8 ± 4.80 |
| | 200 | 92.6 ± 4.42 |

The selectivity of the GCE/$MoS_2$ was further examined using tap water and water collected from a nearby river. In these experiments, the water was filtered to remove any solid particles and then buffered to a neutral pH with 0.1 M phosphate buffer. Good recoveries were obtained for all samples except at the lower concentrations of MTZ in

the river sample. This resulted in a recovery of 80.8% for a 50 µM MTZ spiked sample (n = 6), as shown in Table 3.3.

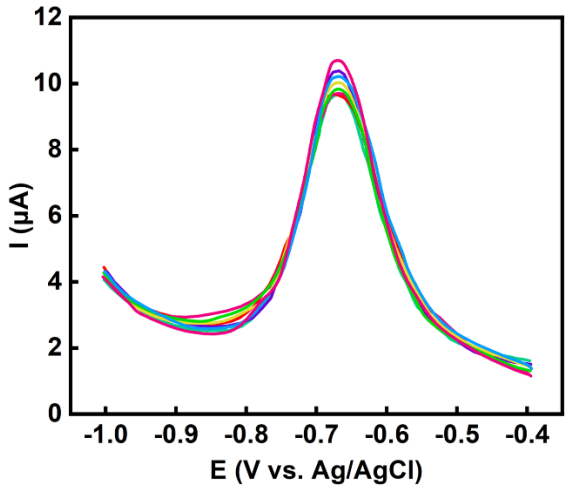


**Figure 3.12.** Repeatability showing 9 repeated traces on one electrode with the same GCE/$MoS_2$ (n = 1).

**Table 3.4**: Reproducibility for GCE/$MoS_2$ at three different MTZ concentrations.

| Concentration of MTZ (µM) | Experiment I Current (µA) | Experiment II Current (µA) | Experiment III Current (µA) | Average Current (µA) | RSD (%) |
|---|---|---|---|---|---|
| 55 | 5.62 | 5.74 | 5.64 | 5.67 | 2.17 |
| 155 | 10.17 | 10.88 | 10.22 | 10.42 | 3.80 |
| 225 | 16.03 | 16.14 | 16.02 | 16.06 | 0.41 |

Other important parameters include the repeatability, reproducibility, and stability of the sensor. Repeatability is demonstrated in Fig. 3.12, showing acceptable consistency over nine successive experiments, with a maximum peak current reduction of 11.3%, t-value of the repeatability was computed as 0.355, with the corresponding p-value > 0.05 (95% confidence level), indicating that the variation among the nine measurements was not statistically significant and confirming good repeatability and data reliability, with a relative standard deviation (RSD%) of 3.6%. Reproducibility is demonstrated in Table 3.4, where the average error, calculated over three experiments, remains

relatively low, at ≤ 3.8%. Long-term stability was examined by immersing the GCE/$MoS_2$ electrode in a 0.1 M phosphate buffer for a week. The sensor was periodically removed, and its ability to detect 100 µM MTZ was evaluated using DPV.

Additionally, the surface morphology following this week-long period was examined, and the data are presented in Fig. 3.13. In Fig. 3.13 (a), the SEM micrograph is shown after a 7-day immersion. The dispersed $MoS_2$ sheets are clearly visible, with no indication that they have been lost from the surface. The corresponding EDX analysis shows the presence of Mo, S, and O, indicating that most of the tryptophan responsible for separating the $MoS_2$ sheets remains. It is evident from Fig. 3.13 (b) that excellent stability is maintained during the first five days, with a decrease in peak current only occurring after day 7.

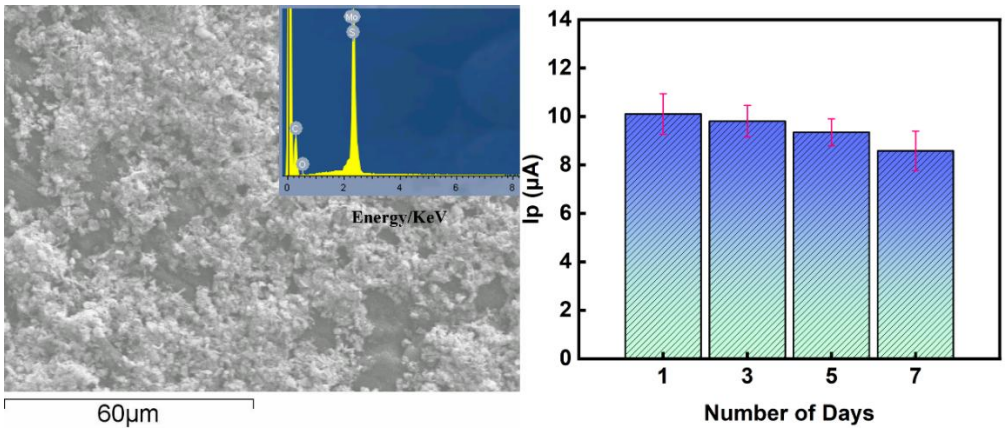


**Figure 3.13.** (a) SEM micrographs and corresponding EDX spectrum for GCE/$MoS_2$ following a 7 – day immersion period in phosphate buffer, (b) DPV voltammograms recorded in 100 µM MTZ following various immersion periods over the 7-day period (n = 3).

## 3.4 Conclusions

In this study, exfoliated $MoS_2$ sheets and electrodeposited amorphous $MoS_x$ were systematically evaluated for the electrochemical detection of metronidazole (MTZ). While both materials facilitated the reduction of MTZ, the exfoliated $MoS_2$ nanosheets (GCE/$MoS_2$) demonstrated superior performance, enabling detection over an extended concentration range with a remarkably low detection limit. The use of tryptophan-assisted exfoliation in aqueous medium—a simple, rapid (30 min), and environmentally benign process—yielded few-layer $MoS_2$ sheets with high electrocatalytic activity, excellent selectivity, and stability. This efficient exfoliation protocol not only allows straightforward sensor regeneration through a quick redeposition step but also holds promise for extending to other layered materials and applications beyond electrochemical sensing.

The principal strength of the present work is its unusually broad working domain: two well-defined linear regimes from 0.04-1.99 μM to 1.9-2000 μM. This combination of a nanomolar LOD with a linear range extending with the state-of-the-art literature, where many platforms either prioritise low LOD at the expense of dynamic range or offer wide ranges but with substantially poorer detection limits. This research addresses an identified gap by demonstrating $MoS_2$ as an effective active modifier for MTZ electroanalysis. It introduces and validates a green, tryptophan-assisted exfoliation strategy that produces electroactive $MoS_2$ nanosheets without harsh solvents, while simultaneously helping mitigate restacking and enabling reproducible electrode preparation. Collectively, these findings establish a low-cost and environmentally aligned sensing route that is competitive with current leading methods while offering an unusually wide linear range and a practical pathway for scalable deployment.

# References


[1] M. Acerce, D. Voiry, and M. Chhowalla, "Metallic 1T phase $MoS_2$ nanosheets as supercapacitor electrode materials," *Nature Nanotechnology*, vol. 10, no. 4, pp. 313–318, Mar. 2015, doi: 10.1038/nnano.2015.40.

[2] K. F. Mak, C. Lee, J. Hone, J. Shan, and T. F. Heinz, "Atomically Thin$MoS_2$: a new Direct-Gap semiconductor," *Physical Review Letters*, vol. 105, no. 13, p. 136805, Sep. 2010, doi: 10.1103/physrevlett.105.136805.

[3] A. Gupta, V. Arunachalam, and S. Vasudevan, "Liquid-Phase exfoliation of $MoS_2$ nanosheets: The critical role of trace water," *The Journal of Physical Chemistry Letters*, vol. 7, no. 23, pp. 4884–4890, Nov. 2016, doi: 10.1021/acs.jpclett.6b02405.

[4] S. Karmakar, S. Biswas, and P. Kumbhakar, "Low power continuous-wave nonlinear optical effects in $MoS_2$ nanosheets synthesized by simple bath ultrasonication," *Optical Materials*, vol. 73, pp. 585–594, Oct. 2017, doi: 10.1016/j.optmat.2017.09.020.

[5] P.Z. Li, N. Chen, A. Al-Hamry, E. Sheremet, R. Lu, Y. Yang, O. Kanoun, R.R. Baumann, R.D. Rodriguez, J.J. Chen., "Inkjet-printed $MoS_2$-based 3D-structured electrocatalysts on Cu films for ultra-efficient hydrogen evolution reaction," *Chemical Engineering Journal*, vol. 457, p. 141289, Jan. 2023, doi: 10.1016/j.cej.2023.141289.

[6] A. Jawaid, D. Nepal, K. Park, M. Jespersen, A. Qualley, P. Mirau, L.F. Drummy, and R.A. Vaia, "Mechanism for liquid phase exfoliation of $MoS_2$," *Chemistry of Materials*, vol. 28, no. 1, pp. 337–348, Dec. 2015, doi: 10.1021/acs.chemmater.5b04224.

[7] J. Liu, Z. Zeng, X. Cao, G. Lu, L.H. Wang, Q.L. Fan, W. Huang, and H. Zhang, "Preparation of $MoS_2$-Polyvinylpyrrolidone Nanocomposites for Flexible Nonvolatile Rewritable Memory Devices with Reduced Graphene Oxide Electrodes," *Small*, vol. 8, no. 22, pp. 3517–3522, Aug. 2012, doi: 10.1002/smll.201200999.

[8] Y. Yao, L. Tolentino, Z. Yang, X. Song, W. Zhang, Y. Chen, and C.P. Wong, "High-Concentration aqueous dispersions of $MOS_2$," *Advanced Functional Materials*, vol. 23, no. 28, pp. 3577–3583, Feb. 2013, doi: 10.1002/adfm.201201843.

[9] Q. Yao, J. Guo, F. Guan, M. Zhao, S. Zhang, X. Tuo, and Q. Yang, "Ultrasonic-Assisted Exfoliation Bulk-Phase of $MoS_2$ with Chitosan/Acetic Acid Solution," *JOM*, vol. 75, no. 3, pp. 701–707, Jan. 2023, doi: 10.1007/s11837-022-05666-6.

[10] S. Ravula, J. B. Essner, and G. A. Baker, "Kitchen-Inspired nanochemistry: dispersion, exfoliation, and hybridization of functional $MOS_2$ nanosheets using culinary hydrocolloids," *ChemNanoMat*, vol. 1, no. 3, pp. 167–177, Apr. 2015, doi: 10.1002/cnma.201500022.

[11] E. A. Ponomarev, M. Neumann-Spallart, G. Hodes, and C. Lévy-Clément, "Electrochemical deposition of $MoS_2$ thin films by reduction of

tetrathiomolybdate," *Thin Solid Films*, vol. 280, no. 1–2, pp. 86–89, Jul. 1996, doi: 10.1016/0040-6090(95)08204-2.

[12] H. Vrubel and X. Hu, "Growth and activation of an amorphous molybdenum sulfide hydrogen evolving catalyst," *ACS Catalysis*, vol. 3, no. 9, pp. 2002–2011, Jul. 2013, doi: 10.1021/cs400441u.

[13] M. Chhowalla and G. a. J. Amaratunga, "Thin films of fullerene-like $MoS_2$ nanoparticles with ultra-low friction and wear," *Nature*, vol. 407, no. 6801, pp. 164–167, Sep. 2000, doi: 10.1038/35025020.

[14] D. Lembke, S. Bertolazzi, and A. Kis, "Single-Layer $MOS_2$ Electronics," *Accounts of Chemical Research*, vol. 48, no. 1, pp. 100–110, Jan. 2015, doi: 10.1021/ar500274q.

[15] M.L. Tsai, S.H. Su, J.K. Chang, D.S. Tsai, C.H. Chen, C.I. Wu, L.J. Li, L.J. Chen, and J.H. He, "Monolayer $MOS_2$ heterojunction Solar cells," *ACS Nano*, vol. 8, no. 8, pp. 8317–8322, Jul. 2014, doi: 10.1021/nn502776h.

[16]R. Ganatra and Q. Zhang, "Few-Layer $MOS_2$: a promising layered semiconductor," *ACS Nano*, vol. 8, no. 5, pp. 4074–4099, Mar. 2014, doi: 10.1021/nn405938z.

[17] R. Sukanya, D. C. Da Silva Alves, and C. B. Breslin, "RevIew—Recent Developments in the applications of 2D transition metal dichalcogenides as electrocatalysts in the generation of hydrogen for renewable energy conversion," *Journal of the Electrochemical Society*, vol. 169, no. 6, p. 064504, May 2022, doi: 10.1149/1945-7111/ac7172.

[18] W. Yin, J. Yu, F. Lv, L. Yan, L.R. Zheng, Z. Gu, and Y. Zhao, "Functionalized Nano-$MoS_2$ with Peroxidase Catalytic and Near-Infrared Photothermal Activities for Safe and Synergetic Wound Antibacterial Applications," *ACS Nano*, vol. 10, no. 12, pp. 11000–11011, Nov. 2016, doi: 10.1021/acsnano.6b05810.

[19] K.-J. Huang, Y.-J. Liu, Y.-M. Liu, and L.-L. Wang, "Molybdenum disulfide nanoflower-chitosan-Au nanoparticles composites based electrochemical sensing platform for bisphenol A determination," *Journal of Hazardous Materials*, vol. 276, pp. 207–215, May 2014, doi: 10.1016/j.jhazmat.2014.05.037.

[20] T. Wang, H. Zhu, J. Zhuo, Z. Zhu, P. Papakonstantinou, G. Lubarsky, J. Lin, and M. Li, "Biosensor based on ultrasmall $MOS_2$ nanoparticles for electrochemical detection of H2O2 released by cells at the nanomolar level," *Analytical Chemistry*, vol. 85, no. 21, pp. 10289–10295, Sep. 2013, doi: 10.1021/ac402114c.

[21] L. Xing and Z. Ma, "A glassy carbon electrode modified with a nanocomposite consisting of $MoS_2$ and reduced graphene oxide for electrochemical simultaneous determination of ascorbic acid, dopamine, and uric acid," *Microchimica Acta*, vol. 183, no. 1, pp. 257–263, Sep. 2015, doi: 10.1007/s00604-015-1648-8.

[22] P. Zhao, M. Ni, Y. Xu, C. Wang, C. Chen, X. Zhang, C. Li, Y. Xie, and J. Fei, "A novel ultrasensitive electrochemical quercetin sensor based on $MoS_2$ - carbon nanotube @ graphene oxide nanoribbons / HS-cyclodextrin / graphene quantum dots composite film," *Sensors and Actuators B Chemical*, vol. 299, p. 126997, Aug. 2019, doi: 10.1016/j.snb.2019.126997.

[23] H. Sun, J. Chao, X. Zuo, S. Su, X. Liu, L. Yuwen, C. Fan, and L. Wang, "Gold nanoparticle-decorated $MoS_2$ nanosheets for simultaneous detection of ascorbic

acid, dopamine and uric acid," *RSC Advances*, vol. 4, no. 52, p. 27625, Jan. 2014, doi: 10.1039/c4ra04046e.

[24] J. Huang, Z. Dong, Y. Li, J. Li, W. Tang, H. Yang, J. Wang, Y. Bao, J. Jin, and R. Li, "$MoS_2$ nanosheet functionalized with Cu nanoparticles and its application for glucose detection," *Materials Research Bulletin*, vol. 48, no. 11, pp. 4544–4547, Aug. 2013, doi: 10.1016/j.materresbull.2013.07.060.

[25] V. Mani, M. Govindasamy, S.-M. Chen, R. Karthik, and S.-T. Huang, "Determination of dopamine using a glassy carbon electrode modified with a graphene and carbon nanotube hybrid decorated with molybdenum disulfide flowers," *Microchimica Acta*, vol. 183, no. 7, pp. 2267–2275, May 2016, doi: 10.1007/s00604-016-1864-x.

[26] F. Chekin, F. Teodorescu, Y. Coffinier, G.H. Pan, A. Barras, R. Boukherroub, and S. Szunerits, "$MoS_2$/reduced graphene oxide as active hybrid material for the electrochemical detection of folic acid in human serum," *Biosensors and Bioelectronics*, vol. 85, pp. 807–813, Jun. 2016, doi: 10.1016/j.bios.2016.05.095.

[27] M. Govindasamy, S.M. Chen, V. Mani, R. Devasenathipathy, R. Umamaheswari, K.Joseph Santhanaraj, and A. Sathiyan, "Molybdenum disulfide nanosheets coated multiwalled carbon nanotubes composite for highly sensitive determination of chloramphenicol in food samples milk, honey and powdered milk," *Journal of Colloid and Interface Science*, vol. 485, pp. 129–136, Sep. 2016, doi: 10.1016/j.jcis.2016.09.029.

[28] M. Govindasamy, "$MoS_2$ Flowers Grown on Graphene/Carbon Nanotubes: a Versatile Substrate for Electrochemical Determination of Hydrogen Peroxide," *International Journal of Electrochemical Science*, pp. 2954–2961, Apr. 2016, doi: 10.20964/110402954.

[29] H. Wang, P. Chen, F. Wen, Y. Zhu, and Y. Zhang, "Flower-like $Fe_2O_3$@$MoS_2$ nanocomposite decorated glassy carbon electrode for the determination of nitrite," *Sensors and Actuators B Chemical*, vol. 220, pp. 749–754, Jun. 2015, doi: 10.1016/j.snb.2015.06.016.

[30] L. E. Strange, S. Garg, P. Kung, M. Ashaduzzaman, G. Szulczewski, and S. Pan, "Electrodeposited transition metal dichalcogenides for use in hydrogen evolution electrocatalysts," *Journal of the Electrochemical Society*, vol. 169, no. 2, p. 026510, Jan. 2022, doi: 10.1149/1945-7111/ac4f25.

[31] T. Liang, H. Jia, Y. Zhou, J. Fan, Y. Xu, Y. Hu, L. Zhou, C. Wang, F. Chen, P. Guan, M. Ferry, and D. Chu, "A facile approach to enhance the hydrogen evolution reaction of electrodeposited $MoS_2$ in acidic solutions," *New Journal of Chemistry*, vol. 46, no. 48, pp. 23344–23350, Jan. 2022, doi: 10.1039/d2nj04547h.

[32] A.M. Teli, S.A. Beknalkar, S.M. Mane, T.S. Bhat, B.B. Kamble, S.B. Patil, S.B. Sadale, and J.C. Shin, "Electrodeposited crumpled $MoS_2$ nanoflakes for asymmetric supercapacitor," *Ceramics International*, vol. 48, no. 19, pp. 29002–29010, Apr. 2022, doi: 10.1016/j.ceramint.2022.04.208.

[33] J. Huang, Z. Qiu, J. Lin, J. Lin, F. Zhu, G. Lai, and Y. Li, "Ultrasensitive determination of metronidazole using flower-like cobalt anchored on reduced

graphene oxide nanocomposite electrochemical sensor," *Microchemical Journal*, vol. 188, p. 108444, Jan. 2023, doi: 10.1016/j.microc.2023.108444.

[34] T. Yu, L. Glennon, O. Fenelon, and C. B. Breslin, "Electrodeposition of bismuth at a graphene modified carbon electrode and its application as an easily regenerated sensor for the electrochemical determination of the antimicrobial drug metronidazole," *Talanta*, vol. 251, p. 123758, Jul. 2022, doi: 10.1016/j.talanta.2022.123758.

[35] Z. Liu, Z. Wang, and Y. Xu, "A powerful electrochemical sensor based on $Fe_2O_3$ nanoparticle-Graphene oxide nanocomposites for determination of metronidazole as an antibacterial drug," *International Journal of Electrochemical Science*, vol. 17, no. 7, p. 220731, Jun. 2022, doi: 10.20964/2022.07.11.

[36] Y. Xia, X. Ou, Y. Zhao, M. Xia, D. Chen, and W. Gao, "Facile synthesis of reduced graphene oxide-octahedral $MN_3O_4$ nanocomposites as a platform for the electrochemical determination of metronidazole and sulfamonomethoxine," *Electroanalysis*, vol. 33, no. 6, pp. 1646–1656, Apr. 2021, doi: 10.1002/elan.202100015.

[37] A. Hernández Ceruelos, L.C. Romero-Quezada, J.C. Ruvalcaba Ledezma, L. López Contreras. "Therapeutic uses of metronidazole and its side effect s: an update," *Eur. Rev. Med. Pharmacol. Sci.*, 23,2019, pp. 397-401, 10.2 6355/eurrev_201901_16788.

[38] K. Ono, T. Akaike, T. Sawa, Y. Kumagai, D.A. Wink, D.J. Tantillo, A.J. Hobbs, P. Nagy, M. Xian, J. Lin, J. Lin, and J.M. Fukuto, "Redox chemistry and chemical biology of $H_2S$, hydropersulfides, and derived species: Implications of their possible biological activity and utility," *Free Radical Biology and Medicine*, vol. 77, pp. 82–94, Sep. 2014, doi: 10.1016/j.freeradbiomed.2014.09.007.

[39] K. Dharamalingam, B. Arjun Kumar, G. Ramalingam, S. Sasi Florence, K. Raju, P. Senthil Kumar, S. Govindaraju, and E. Thangavel, "The role of sodium dodecyl sulfate mediated hydrothermal synthesis of $MoS_2$ nanosheets for photocatalytic dye degradation and dye-sensitized solar cell application," *Chemosphere*, vol. 294, p. 133725, Jan. 2022, doi: 10.1016/j.chemosphere.2022.133725.

[40] P. Sharma, M. K. Singh, and M. S. Mehata, "Sunlight-driven $MoS_2$ nanos heets mediated degradation of dye (crystal violet) for wastewater treatmen t," *Journal of Molecular Structure*, vol. 1249, p. 131651, Oct. 2021, doi: 10.1016/j.molstruc.2021.131651.

[41] W. Feng, L. Chen, M. Qin, X. Zhou, Q. Zhang, Y. Miao, K. Qiu, Y. Zhang, and C. He, "Flower-like PEGylated $MoS_2$ nanoflakes for near-infrared photothermal cancer therapy," *Scientific Reports*, vol. 5, no. 1, p. 17422, Dec. 2015, doi: 10.1038/srep17422.

[42] T. Wang, W. Liu, and J. Tian, "Preparation and characterization of gold/poly(vinyl alcohol)/$MoS_2$ intercalation nanocomposite," *J. Mater. Sci. Mater. Electron.*, vol. 15, no. 7, pp. 435–438, Jun. 2004, doi: 10.1023/b:jmse.0000031597.00716.2e.

[43] B. Fall, D.D. Sall, M. Hémadi, A.K.D. Diaw, M. Fall, H. Randriamahazaka, and S. Thomas, "Highly efficient non-enzymatic electrochemical glucose sensor based on carbon nanotubes functionalized by molybdenum disulfide and decorated with

nickel nanoparticles (GCE/CNT/$MoS_2$/NiNPs)," *Sensors and Actuators Reports*, vol. 5, p. 100136, Dec. 2022, doi: 10.1016/j.snr.2022.100136.

[44] S. Kimiagar and F. Abrinaei, "Laser-assisted hydrothermal synthesis of $MoS_2$ nanosheets under different laser energies and potential application in nonlinear optics," *Optik*, vol. 272, p. 170305, Nov. 2022, doi: 10.1016/j.ijleo.2022.170305.

[45] L. Zhang, M. Yin, J. Qiu, T. Qiu, Y. Chen, S. Qi, X. Wei, X. Tian, and D. Xu, "An electrochemical sensor based on CNF@AuNPs for metronidazole hypersensitivity detection," *Biosensors and Bioelectronics X*, vol. 10, p. 100102, Dec. 2021, doi: 10.1016/j.biosx.2021.100102.

[46] M. Darbandi, M. F. Mohajer, M. Eynollahi, and K. Asadpour-Zeynali, "Sensitive sensing platform based on NiO and NiO-Ni nanoparticles for electrochemical determination of Metronidazole," *Chemical Physics*, vol. 560, p. 111590, May 2022, doi: 10.1016/j.chemphys.2022.111590.

[47] R. Zokhtareh, M. Rahimnejad, G. Najafpour-Darzi, and H. Karimi-Maleh, "A novel sensing platform for electrochemical detection of metronidazole a ntibiotic based on green-synthesized magnetic $Fe_3O_4$ nanoparticles," *Enviro nmental Research*, vol. 216, no. Pt 3, p. 114643, Oct. 2022, doi: 10.1016/ j.envres.2022.114643.

[48] F.E. Ettadili, M. Matrouf, O.T. Alaoui, F. Laghrib, S. Saqrane, A. Farahi, M. Bakasse, S. Lahrich, and M.A. El Mhammedi, "Catalytic effect of silver in reducing metronidazole in human blood and water samples," *Case Studies in Chemical and Environmental Engineering*, vol. 5, p. 100204, Apr. 2022, doi: 10.1016/j.cscee.2022.100204.

[49] J. Zoubir, N. Bougdour, C. Radaa, A. Idlahcen, I. Bakas, and A. Assabba ne, "Elaboration of a novel nanosensor using nanoparticles of α-$Fe_2O_3$ mag netic cores for the detection of metronidazole drug. Urine human and tap water," *Sensors International*, vol. 3, p. 100160, Jan. 2022, doi: 10.1016/j. sintl.2022.100160.

[50] H. Saedi, M. R. Fat'hi, and B. Zargar, "Synthesis of AgNPs functionalized CuMOF/PPy–rGO nanocomposite and its use as an electrochemical sensor for metronidazole determination," *Journal of the Chinese Chemical Society*, vol. 68, no. 10, pp. 1954–1964, Jun. 2021, doi: 10.1002/jccs.202100081.

[51] E. M. Materón, A. Wong, T. A. Freitas, R. C. Faria, and O. N. Oliveira, "A sensitive electrochemical detection of metronidazole in synthetic serum and urine samples using low-cost screen-printed electrodes modified with reduced graphene oxide and C60," *Journal of Pharmaceutical Analysis*, vol. 11, no. 5, pp. 646–652, Mar. 2021, doi: 10.1016/j.jpha.2021.03.004.

[52] G. Kesavan, V. Vinothkumar, S.-M. Chen, and T. D. Thangadurai, "Construction of metal-free oxygen-doped graphitic carbon nitride as an electrochemical sensing platform for determination of antimicrobial drug metronidazole," *Applied Surface Science*, vol. 556, p. 149814, Apr. 2021, doi: 10.1016/j.apsusc.2021.149814.

[53] G. Kesavan and S.-M. Chen, "Sonochemical-assisted synthesis of zinc vanadate microstructure for electrochemical determination of metronidazole," Journal of

Materials Science Materials in Electronics, vol. 32, no. 7, pp. 9377–9391, Mar. 2021, doi: 10.1007/s10854-021-05601-6.

[54] P. K. Gopi, G. Kesavan, S.-M. Chen, and C. H. Ravikumar, "Cadmium sulfide quantum dots anchored on reduced graphene oxide for the electrochemical detection of metronidazole," *New Journal of Chemistry*, vol. 45, no. 6, pp. 3022–3033, Jan. 2021, doi: 10.1039/d0nj05501h.

[55] Y. Pan, D. Chen, Y. Fan, J. Zuo, Q. Yang, F. Qiu, L. Qiu, H. Song, and S. Zhang, "Highly-sensitive and anti-interferential electrochemical determination of hazardous metronidazole using w-$NiSO_4 \cdot NiS_2$ coated ZIF-67-derived cobalt/nitrogen-doped carbon," *Colloids Surf. A Physicochem. Eng. Asp.*, vol. 666, p. 131293, Mar. 2023, doi: 10.1016/j.colsurfa.2023.131293.

[56] X. Hu, Y. Zhang, T. Zeng, Q. Wan, K. Wu, and N. Yang, "A novel electrochemical sensor based on MnOOH nanorod/expanded graphite for sensitive monitoring of metronidazole," *Diamond and Related Materials*, vol. 128, p. 109303, Aug. 2022, doi: 10.1016/j.diamond.2022.109303.

[57] K. Zhu, X.-F. Chao, Y. Liu, Y.-H. Luo, and D.-E. Zhang, "Ce-MOFs derived cerium phosphate for high-efficiency electrochemical detection of metronidazole," *J. of Solid State Chemistry*, vol. 314, p. 123406, Jul. 2022, doi: 10.1016/j.jssc.2022.123406.

[58] M. Darbandi, M. F. Mohajer, M. Eynollahi, and K. Asadpour-Zeynali, "Sensitive sensing platform based on NiO and NiO-Ni nanoparticles for electrochemical determination of Metronidazole," *Chemical Physics*, vol. 560, p. 111590, May 2022, doi: 10.1016/j.chemphys.2022.111590.

[59] L. Zhang, M. Yin, J. Qiu, T. Qiu, Y. Chen, S. Qi, X. Wei, X. Tian, and D. Xu, "An electrochemical sensor based on CNF@AuNPs for metronidazole hypersensitivity detection," *Biosensors and Bioelectronics X*, vol. 10, p. 100102, Dec. 2021, doi: 10.1016/j.biosx.2021.100102.

[60] Y. Xia, X. Ou, Y. Zhao, M. Xia, D. Chen, and W. Gao, "Facile synthesi s of reduced graphene oxide-octahedral $MN_3O_4$ nanocomposites as a platfo rm for the electrochemical determination of metronidazole and sulfamonom ethoxine," *Electroanalysis*, vol. 33, no. 6, pp. 1646–1656, Apr. 2021, doi: 10.1002/elan.202100015.

[61] R. Zokhtareh, M. Rahimnejad, G. Najafpour-Darzi, and H. Karimi-Maleh, "A novel sensing platform for electrochemical detection of metronidazole a ntibiotic based on green-synthesized magnetic $Fe_3O_4$ nanoparticles," *Enviro nmental Research*, vol. 216, no. Pt 3, p. 114643, Oct. 2022, doi: 10.1016/ j.envres.2022.114643.

[62] J. Li, Y. Wang, Z. Fan, P. Tang, M. Wu, H. Xiao, and Z. Zeng, "Toxicity of Tetracycline and Metronidazole in Chlorella pyrenoidosa," *Int. J. Environ. Res. Public Health.*, vol. 20, no. 4, p. 3623, Feb. 2023, doi: 10.3390/ijerph20043623.

[63] N. Hanna, P. Sun, Q. Sun, X. Li, X. Yang, X. Ji, H. Zou, J. Ottoson, L. E. Nilsson, B. Berglund, A.J. Tamhankar, and C. Stålsby Lundborg, "Prese nce of antibiotic residues in various environmental compartments of Shand ong province in eastern China: Its potential for resistance development and

ecological and human risk," *Environment International*, vol. 114, pp. 131-142, Mar. 2018, doi: 10.1016/j.envint.2018.02.003.

[64] R. Rajakumaran, K. Balamurugan, S.-M. Chen, and R. Sukanya, "Facile synthesis of neodymium stannate nanoparticles an effective electrocatalyst for the selective detection of dimetridazole in biological samples," *Analytica Chimica Acta*, vol. 1190, p. 339234, Nov. 2021, doi: 10.1016/j.aca.2021.339234.

# **Chapter 4** Electrochemical Detection of Sulfanilamide (SFD) with Exfoliated $MoS_2$ Nanosheets combined with reduced Graphene Oxide/Graphite

# 4.1. Introduction

It is well known that sulfonamide antibiotics are widely deployed in human and veterinary medicine and can persist in aquatic systems, where they contribute to ecological risk and antimicrobial resistance [1-4]. Sulfanilamide (SFD) is of particular interest, as it frequently appears as a transformation product of other sulfonamides and dyes, making its sensitive determination in water especially relevant [5,6]. Consequently, selective monitoring of SFD in complex matrices is both environmentally and clinically important [7-10].

Electrochemical sensing has emerged as a practical route to SFD quantification as it enables rapid, low-cost measurements with portable electrochemical instrumentation [11-15]. Reported platforms span laser-induced porous graphene [16], $CO_2$-treated graphene sheets [17], reduced graphene oxide (rGO) [18], carbon black [19], multi-walled carbon nanotubes [20], pencil graphite [21], $MnO_2$-carbon paste [22], cobalt phthalocyanine-chitosan [23], and Ag-Pt-Rh core-shell nanostructures [24]. While promising, many exhibit restricted linear ranges (often 1-100 μM) and detection limits in the micromolar regime, highlighting space for materials innovation [25-28].

In this work, we address this by using few-layered $MoS_2$ sheets produced by tannic-acid-assisted exfoliation (ta-$MoS_2$) and interfaced with an electrodeposited rGO/graphite scaffold (rGO/G), yielding GCE/rGO/G/ta-$MoS_2$. The rGO/G underlayer increases the electroactive area and provides an efficient electron-transfer network, while ta-$MoS_2$ contributes abundant edge/defect sites. Together, this combination lowers the oxidation overpotential and enhances the SFD signal compared to either component alone. Optimisation of the GO to G ratio and deposition sequence further enhances performance.

Framed in this manner, this study connects structure with electrochemical detection. In particular, it (i) establishes each modifier composition and morphology (GO/graphite mixing verified by XRD/Raman), (ii) quantifies interfacial kinetics and accessible area (ferricyanide probe; impedance), and (iii) relates these parameters to the detection of SFD obtained by cyclic and differential-pulse voltammetry in phosphate buffer. The resulting sensor delivers an extended linear range of 0.1 - 566 μM with an LOD of 86 nM, good selectivity against common ions and co-occurring sulfonamides, acceptable recoveries in tap and river waters, and very good stability, providing a practical, scalable route to high-performance SFD monitoring.

# 4.2. Experimental

## 4.2.1. Formation of the GCE/rGO/ta-$MoS_2$ and GCE/rGO/G/ta-$MoS_2$ Sensors

The overall synthetic process is summarised in Scheme 4.1. Graphene oxide (GO) was prepared using the Hummers method with some slight modifications. In a typical procedure, 1.0 g of graphite flakes and 1.0 g of sodium nitrate ($NaNO_3$) were mixed with 46 mL of concentrated sulfuric acid ($H_2SO_4$), then stirred at 0 °C for 4 h. Subsequently, 6.0 g of potassium permanganate ($KMnO_4$) was added. The mixture was stirred for 2 h before deionised water was gradually introduced. The reaction temperature was then elevated to 98 °C for 15 min. Afterwards, 200 mL of warm deionised water and 40 mL of hydrogen peroxide ($H_2O_2$) were added, and the mixture was maintained at room temperature for 12 h. The resulting solid GO was collected using a centrifuge, and then thoroughly washed with a 10 % HCl solution, followed by 3 sequential ethanol and deionised water washes. The final product was dried at 50 ºC for 48 h. The GO/G composite was prepared by combining GO and the graphite flakes in a 3:2 ratio (optimised ratio), and finally electrodeposited onto the glassy carbon electrode (GCE).

The rGO and rGO/G modified GCE were prepared by initially polishing the GCE with a 1 μm particle-sized diamond suspension (Akasol), followed by brief sonication in deionised water and ethanol, and subsequently rinsed with deionised water and air-dried. The GO and GO/G were dispersed via sonication in 0.1 M $Na_2SO_4$ (1 mg/mL) at a pH of 3.2 and electrodeposited onto the GCE through cycling from −0.5 V to −1.5 V at a scan rate of 17 mV $s^{-1}$ for six cycles. The $MoS_2$ sheets were synthesised by dispersing 1.2 mg/mL of $MoS_2$ in 0.5 mM tannic acid, sonicated for 2 h, and centrifuged for 30 min. The supernatant, containing the smaller sheets, was retained and used to drop cast

the smaller-sized $MoS_2$ sheets (2.5 µL applied three times) onto the rGO or rGO/G surfaces to produce GCE/rGO/ta-$MoS_2$ and GCE/rGO/G/ta-$MoS_2$.

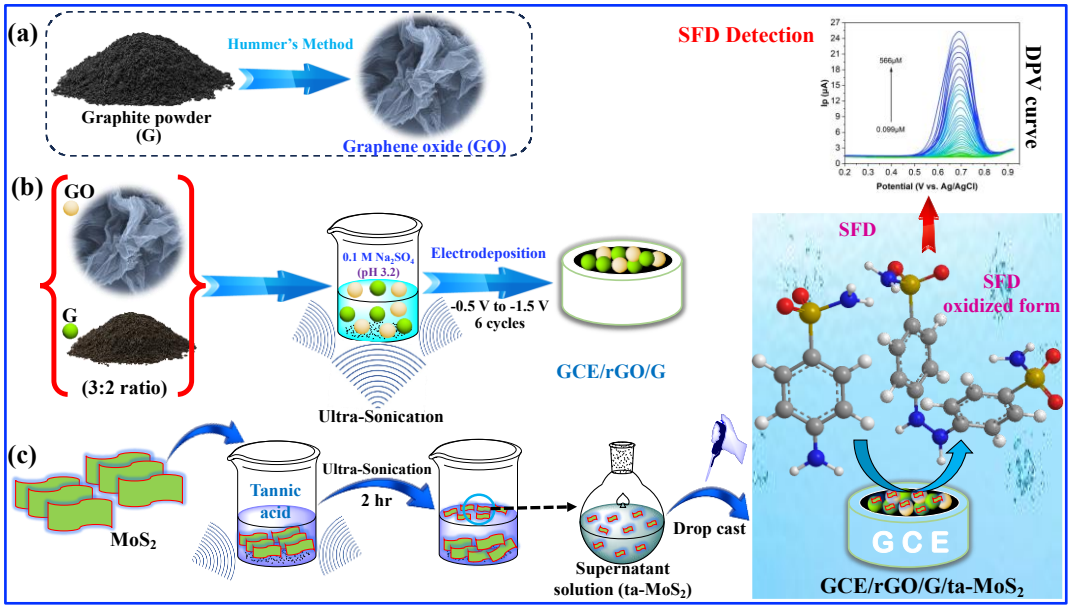


**Scheme 4.1.** Synthetic process (a) preparation of GO, (b) GO/G composite and (c) formation of ta-$MoS_2$.

## 4.2.2. Electrochemical Measurements

All electrochemical studies were performed with a high surface area Pt wire, a Ag/AgCl reference electrode and the GCE/rGO/G/ta-$MoS_2$ or GCE/rGO/ta-$MoS_2$ as the working electrode (GCE = 3 mm in diameter). A 0.05 M phosphate buffer at a pH of 8.0 was used as the supporting electrolyte. A solution of 2.5 mM $[Fe(CN)_6]^{3-/4-}$ dissolved in 0.1 M KCl was used to estimate the electroactive surface area of the GCE/rGO/G/ta-$MoS_2$. Unless otherwise stated, a 50 mV $s^{-1}$ scan rate was employed in all CV measurements. A pulse amplitude of 60 mV, a pulse width of 0.05 s, a sampling width of 0.0167 s, and a pulse period of 0.5 s were used to record the DPV experiments. Impedance data were recorded in the buffered 200 µM SFD solution at 0.74 V between 100 kHz and 5 mHz using a 10 mV perturbation following a 30 min preconditioning period to ensure steady-

state conditions. All experiments were performed at least in triplicate, and the standard errors and RSD (%) were computed.

All the electrochemical and surface analysis equipment used in this study is described in Chapter 2. This includes electrochemical techniques such as cyclic voltammetry (CV), differential pulse voltammetry (DPV), and electrochemical impedance spectroscopy (EIS) in Section 2.3.3. The surface analysis equipment, including scanning electron microscopy (SEM), powder X-ray diffraction (P-XRD), FTIR measurements, Raman spectroscopy, and UV–visible spectrometry, is described in Sections 2.4 and 2.5. The procedure for material characterisation methods and specific characterisation techniques usage is detailed in the corresponding sections of Chapter 2, Experimental and Research Methods.

## 4.3. Results and Discussion

### 4.3.1. Formation, Characterisation and Selection of the Electrocatalyst

XRD analysis was employed to gain information on the crystalline nature of the synthesised GO and GO/G. Representative data are presented in Fig. 4.1 (a). The XRD pattern for GO exhibits a sharp diffraction peak at $2\theta = 10.97°$, indicating an interlayer spacing of 0.81 nm, as calculated from Bragg's equation (Eq. (2.5)). Here $\lambda$ is the X-ray wavelength, which is 0.154 nm (CuK$\alpha$ source), d is the spacing or distance between the lattice planes, $\theta$ is the Bragg (incidence) angle, and n is an integer (n = 1 for a first-order diffraction).

The GO/G shows two diffraction peaks, with the peak at $2\theta = 10.97°$ arising from the pure GO, while the second diffraction peak at $2\theta = 25.76°$ indicates the presence of the G [29]. The interlayer spacing of the graphite was calculated to be 0.35 nm. There is no evidence of unreacted G in the synthesised GO, with the absence of any diffraction peaks in the vicinity of $2\theta = 25.76°$ that would indicate the presence of G. Furthermore, it appears that the GO/G combination remains as a simple mixture. On addition of G to GO, there is no change to the GO diffraction, either in terms of the diffraction angle or any peak broadening, as evident in Fig. 4.1 (a).

The Raman spectra for GO and GO/G are shown in Fig. 4.1 (b) and display the well-known G and D bands characteristic of graphene oxide-based materials [30]. The G band results from the in-plane vibrations of the $sp^2$ hybridised carbon atoms, while the D band relates to structural defects and edge effects. For pure GO, the D and G bands are centred at 1347 and 1594 $cm^{-1}$, respectively, with a D to G band ratio of 0.97, indicating minimal disorder. The spectrum for the GO/G sample aligns with a mixture of GO and graphite. The D band at 1347 $cm^{-1}$ is linked to GO, while the more intense band at 1596 $cm^{-1}$ originates from the G bands of both G and GO. The Raman shift at

2700 $cm^{-1}$ is associated with the graphite and corresponds to the 2D band, which is normally attributed to a double resonance process [31]. These data are in good agreement with the XRD results, suggesting that the GO/G exists as a mixture, retaining the properties of the individual components rather than forming a new hybrid material. Indeed, it is unlikely that a new hybrid would form from the simple dispersion of the GO and G powders in solution.

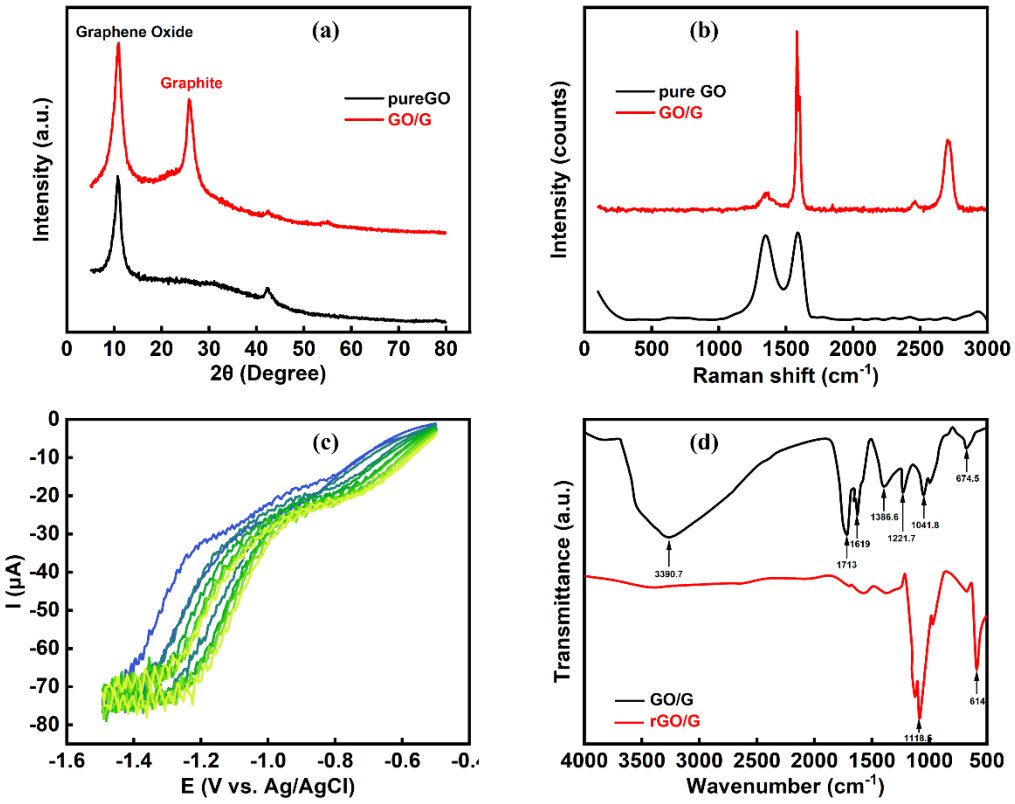


**Figure. 4.1.** (a) XRD patterns of GO and GO/G; (b) Raman spectra for GO and GO/G; (c) electrodeposition of GO/G onto GCE with 1 mg/mL of GO/G in 0.1 M $Na_2SO_4$ at a pH of 3.2 showing 6 cycles recorded at 17 mV $s^{-1}$, with continuous stirring (giving rise to noise in the signal); (d) FTIR spectra of electrodeposited rGO/G and the synthesised GO/G.

The GCE/rGO and GCE/rGO/G modified electrodes were fabricated through an electrodeposition process, which involved cycling the GCE from −0.5 to −1.5 V while

continuously stirring the solution to maintain the well-dispersed state of GO and GO/G in the solution phase. Representative CVs obtained during the electrodeposition of GO/G on the GCE are depicted in Fig. 4.1 (c). Two reduction waves are observed at −0.83 V and −1.24 V (start of the wave), corresponding to the reduction of carbon-based functional groups on the GO. Repeated cycling results in increased current, indicating the formation of more conductive rGO and the effective transformation of GO to rGO. During electrodeposition and the formation of rGO/G, the GO sheets are reduced at the GCE, leading to the removal of certain functional groups, like edge and basal epoxy groups and hydroxyl and phenolic groups. The loss of these groups, which maintain the dispersion of GO sheets in solution, facilitates their deposition onto the GCE. Similarly, graphite flakes collide with the GCE surface and may become incorporated or trapped within the depositing GO, contributing to the formation of the conductive rGO/G composite. Variations in scan rate and cycle number were implemented to optimise sensing of SFD, with the optimal parameters determined to be a scan rate of 17 mV $s^{-1}$ and six cycles in the formation of the GCE/rGO/G.

The electrodeposited rGO/G was further analysed using FTIR to monitor the electrochemical reduction processes. FTIR spectra are presented in Fig. 4.1 (d). Several peaks indicating the presence of oxygenated functional groups are observed with the GO/G. The peak in the vicinity of 1700 $cm^{-1}$ can be assigned to ketone groups, while the peak at 1619 $cm^{-1}$ indicates the presence of carbonyl groups. The peaks at lower wave numbers, such as 1040 $cm^{-1}$, indicate the presence of edge and basal epoxy groups, while the peaks at 1221 $cm^{-1}$ and 1386 $cm^{-1}$ indicate the presence of hydroxyl and phenolic groups. The broad band between 3000 and 3500 $cm^{-1}$ corresponds to the O–H vibrations [32]. The FTIR spectrum for the rGO/G is significantly different, with many of the functional groups observed in GO no longer evident or at lower intensities. Two main peaks at 1118 $cm^{-1}$ and 614 $cm^{-1}$ are seen, and these can be attributed to adsorbed sulfates [33] arising from the electrodeposition medium. This analysis clearly

shows that the electrochemical reduction process effectively decreases the concentration of oxygenated functional groups, as observed in the more complex chemical reduction of GO to rGO [34].

Before combining the $MoS_2$ with the GCE/rGO/G and GCE/rGO, the $MoS_2$ was exfoliated to produce few-layer $MoS_2$ sheets. An aqueous solution of tannic acid, a hydrophilic polyphenol, was used as the exfoliation medium, and its effect on exfoliation is illustrated in Fig. 4.2 (a), where the sonication time is varied over 4 h. The absorbance increases with longer exfoliation time. Notable absorbance peaks appear at 621 nm and 682 nm, with a maximum absorbance of 1.57 reached after 4 h. These absorbance bands are characteristic of the 2D exfoliated $MoS_2$ sheets, corresponding to the direct transition from the valence to conduction band at the Brillouin zone (B and A transitions) [35].

The high absorbance indicates a high yield of the exfoliated sheets, which can be attributed to the presence of catechol and pyrogallol functional groups on the tannic acid [36]. Interestingly, the absorbance peaks shift to lower wavelengths as sonication time increases, indicating that the size of the sheets depends on the duration of sonication, resulting in smaller $MoS_2$ sheets or fewer stacked $MoS_2$ sheets with longer sonication. Moreover, the exfoliated sheets exhibit excellent stability and can be stored for 30 days without showing any signs of agglomeration or restacking.

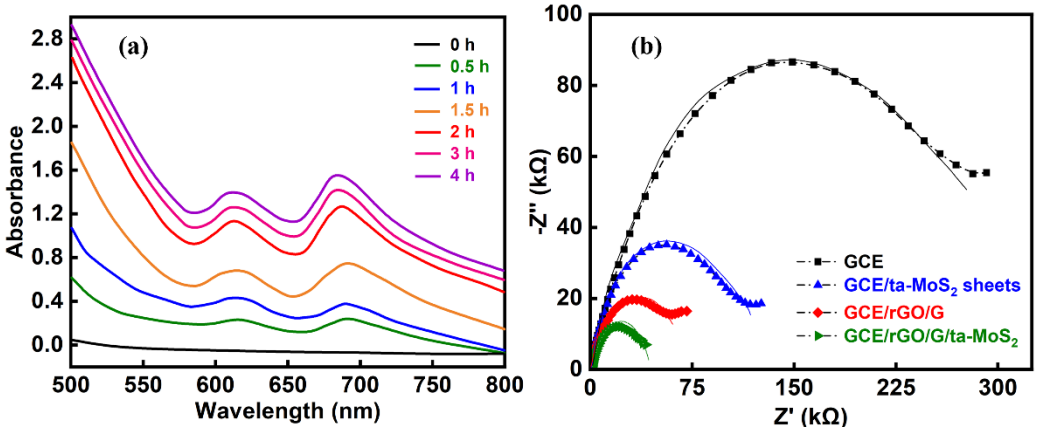


**Figure. 4.2.** (a) UV-visible spectra recorded at different exfoliation times for 1.2 mg/mL of $MoS_2$ in 0.5 mM tannic acid; (b) EIS spectra recorded for GCE, GCE/rGO/G, GCE/ta-$MoS_2$ and GCE/rGO/G/ta-$MoS_2$ at 0.74 V.

The impedance of GCE/rGO/G/ta-$MoS_2$ was recorded in the presence of SFD and compared with the individual components, GCE, GCE/rGO/G and GCE/ta-$MoS_2$. These data are presented in Fig. 4.2 (b). The experimental data are represented by symbols, whereas the simulated profile generated using the fitted equivalent circuit is depicted as continuous traces. A simple Randles cell was employed in the fitting, with a solution resistance, Rs, a constant phase element (CPE), and a charge transfer resistance ($R_{CT}$), as indicated in Eq. (4.1). Here $0 < \varphi \leq 1$ is the CPE exponent and $Q_{dl}$ is the magnitude of the CPE and corresponds to the dispersed double-layer capacitance parameter [37]. There is a clear variation between the impedance response of the four electrodes, with the GCE/rGO/G/ta-$MoS_2$ giving the lowest impedance, with the smallest semicircle.

$$Z = Rs + \frac{1}{\frac{1}{R_{CT}} + (J\omega)^{\phi} Q_{dl}} \qquad \textbf{(4.1)}$$

The $R_{CT}$ values were computed as 275 kΩ, 115 kΩ, 72 kΩ and 43 kΩ for the GCE, GCE/ta-$MoS_2$, GCE/rGO/G, and GCE/rGO/G/ta-$MoS_2$, respectively, indicating a considerable reduction in $R_{CT}$ when $MoS_2$ is combined with the rGO/G. In all cases, the

semicircles are depressed, indicating $\varphi < 1$, with CPE values of 4.8 $\mu\Omega^{-1}$ $s^{0.73}$ for GCE, of 6.3 $\mu\Omega^{-1}$ $s^{0.75}$ for GCE/ta-$MoS_2$, 9.2 $\mu\Omega^{-1}$ $s^{0.72}$ for GCE/rGO/G, and 10.2 $\mu\Omega^{-1}$ $s^{0.72}$ for GCE/rGO/G/ta-$MoS_2$, suggesting that the GCE/rGO/G/ta-$MoS_2$ has a slightly higher capacitance.

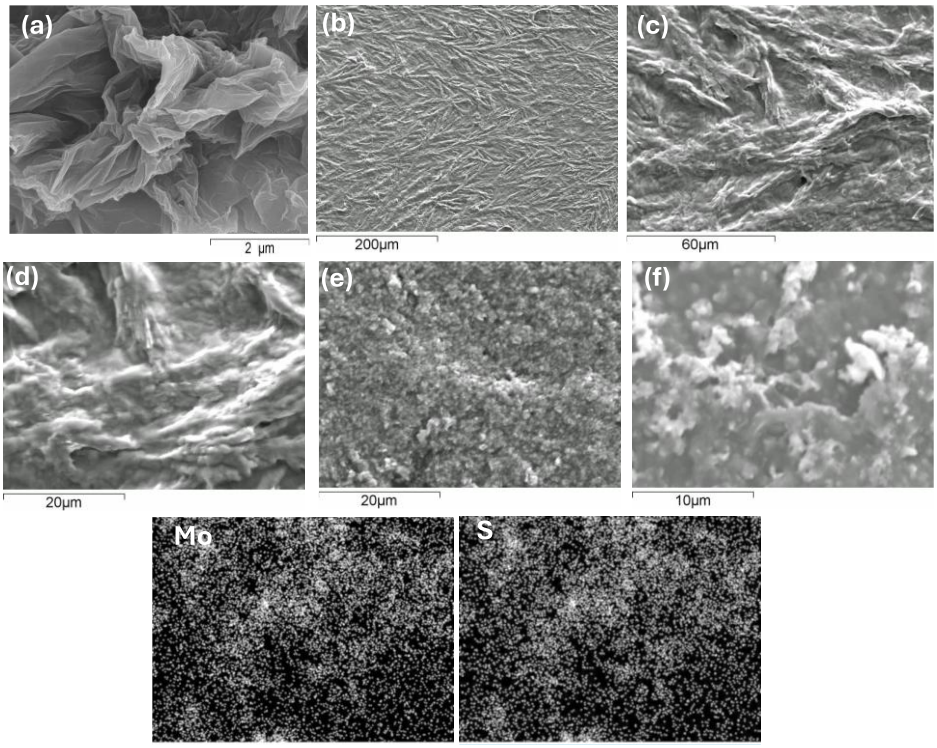


**Figure 4.3.** SEM micrographs recorded for (a) synthesised GO; electrodeposited rGO/G at the GCE at (b) low magnification and (c) and (d) higher magnifications; SEM micrographs recorded for GCE/rGO/G/ta-$MoS_2$ (e) and (f) and elemental mapping for Mo and S at the GCE/rGO/G/ta-$MoS_2$.

The morphologies of the GO and electrodeposited rGO/G and GCE/rGO/G/ta-$MoS_2$ are shown in Fig. 4.3. The micrograph recorded for GO, Fig. 4.3 (a), reveals the characteristic sheet-like structure with prominent wrinkling and folds, which has been attributed to the high amount of oxygen-containing functional groups, including hydroxyl and epoxy functional groups on the basal plane and carboxyl groups at the edges [38]. On the other hand, Fig. 4.3 (b), (c) and (d) show a somewhat different

morphology of the electrodeposited rGO/G that extends across the entire surface, where the rGO sheets are strongly interlocked with each other and with the G flakes. As shown in Fig. 4.3 (b), this wrinkled rGO/G network completely covers the GCE to give wrinkling on the micro- and macroscopic scales.

At a slightly increased magnification, the wrinkled structure becomes more discernible. This high surface area and conducting interface between the GCE and $MoS_2$ sheets has the capacity to facilitate efficient electron transfer, as demonstrated by the impedance data in Fig. 4.2 (b). The t-value of the repeatability was computed as 0.1655, with the corresponding p-value > 0.05, indicating that the variation among the nine measurements was not statistically significant and confirming good repeatability and data reliability

Upon the addition of tannic acid exfoliated $MoS_2$, the sheets are well dispersed across the wrinkled GO/G surface, as illustrated in Fig. 4.3 (e) and (f). The elemental mapping reveals that molybdenum (Mo) and sulfur (S) are thoroughly dispersed across the surface, highlighting the excellent dispersion of the $MoS_2$ sheets within the wrinkled rGO/G network.

Following the characterisation studies, the performance of the GCE/rGO/G/ta-$MoS_2$ sensor in the detection of SFD was studied. Fig. 4.4 (a) presents a comparative analysis of the cyclic voltammograms recorded in phosphate buffer and in the presence of 200 μM SFD. The voltammogram obtained in the buffer shows a low background current at potentials where the SFD is oxidised. At higher potentials, an increase in the current is observed, and this was attributed to the onset of the oxygen evolution reaction. Upon addition of SFD, a distinct oxidation wave emerges, characterised by a peak potential at 726 mV.

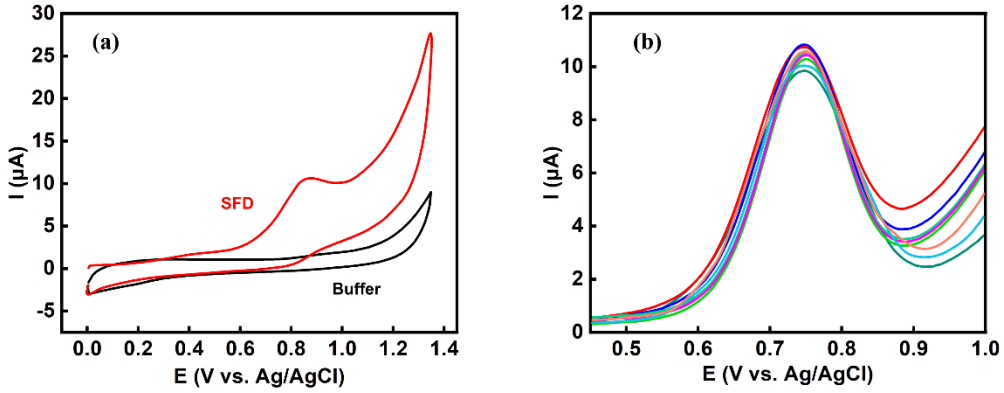


**Figure. 4.4.** (a) CVs recorded at 50 mV $s^{-1}$ for GCE/rGO/G/ta-$MoS_2$ in 0.05 M phosphate buffer with and without 200 μM SFD; (b) repeated DPVs recorded in 200 μM SFD for GCE/rGO/G/ta-$MoS_2$ (n=9).

There is no corresponding reduction wave, indicating an irreversible oxidation reaction, as illustrated in Scheme 4.2. Here, the SFD is oxidised to form a radical species through a one electron and one proton transfer reaction.

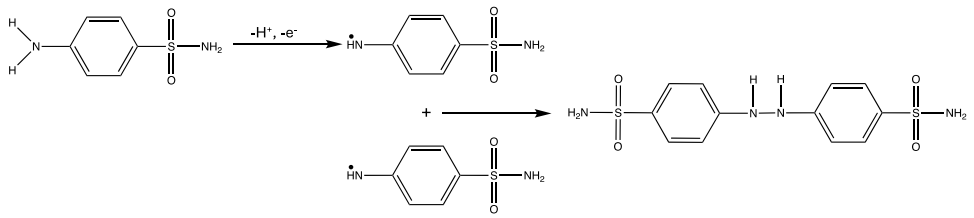


**Scheme 4.2.** Mechanism for the oxidation of SFD [39].

These radicals can then combine to generate the final product. The performances of the various modified electrodes in the electrochemical detection of 200 μM SFD, including GCE, GCE/rGO, GCE/G, GCE/rGO/G, GCE/ta-$MoS_2$, GCE/rGO/ta-$MoS_2$, GCE/rGO/G/ta-$MoS_2$ and GCE/ta-$MoS_2$/rGO/G, are summarised in Table 4.1.

The unmodified GCE and the GCE/rGO show the lowest peak currents at 4.39 and 4.00 μA, respectively, while some of the highest oxidation potentials are seen with GCE

(828 mV), GCE/ta-$MoS_2$ (862 mV) and GCE/rGO/ta-$MoS_2$ (832 mV). The addition of rGO/G to the GCE shifts the potential in the negative direction to 752 mV, indicating a more thermodynamically viable oxidation process. On modifying the GCE with ta-$MoS_2$, there is a significant increase in the peak current, reaching values of 7.25 μA, but the oxidation potential is high at 862 mV.

**Table 4.1** Summary of the peak potential and current recorded for the various modified electrodes at 50 mV $s^{-1}$ in 200 μM SFD in 0.05 M phosphate buffer at a pH of 7.0 (n=3).

| Modified electrode | Potential (mV) | Current (μA) | RSD (%) |
|---|---|---|---|
| GCE | 828 | 4.39 | 1.22 |
| GCE/rGO | 776 | 4.00 | 6.74 |
| GCE/G | 808 | 5.37 | 2.15 |
| GCE/rGO/G | 752 | 5.02 | 2.35 |
| GCE/ta-$MoS_2$ | 862 | 7.25 | 3.68 |
| GCE/rGO/ta-$MoS_2$ | 832 | 5.24 | 7.04 |
| GCE/ta-$MoS_2$/rGO/G | 740 | 7.77 | 6.32 |
| GCE/rGO/G/ta-$MoS_2$ (1:1 GO/G) | 735 | 7.55 | 3.88 |
| GCE/rGO/G/ta-$MoS_2$ (2:3 GO/G) | 740 | 7.79 | 3.71 |
| GCE/rGO/G/ta-$MoS_2$ (3:2 GO/G) | 726 | 9.59 | 2.16 |

However, when the ta-$MoS_2$ is combined with the conducting rGO/G, then the detection of SFD is observed at more favourable oxidation potentials of 726 mV and with a higher peak current of 9.59 μA. Interestingly, the sensor performs better when the rGO/G is first electrodeposited onto the GCE to create a higher surface area with a conducting interface between the GCE and ta-$MoS_2$. Slightly lower peak currents are seen when the rGO/G is electrodeposited onto the GCE/ta-$MoS_2$. Higher amounts of GO in the GO/G mixture is beneficial with the highest peak current obtained with a GO:G ratio of 3:2. It is also clear that the combination of rGO/G and ta-$MoS_2$ results in good

repeatability. This is illustrated in Fig. 4.4 (b), where the DPV plots for repeated measurements with the GCE/rGO/G/ta-$MoS_2$ are compared, with a variation in the peak current of 2.5 %.

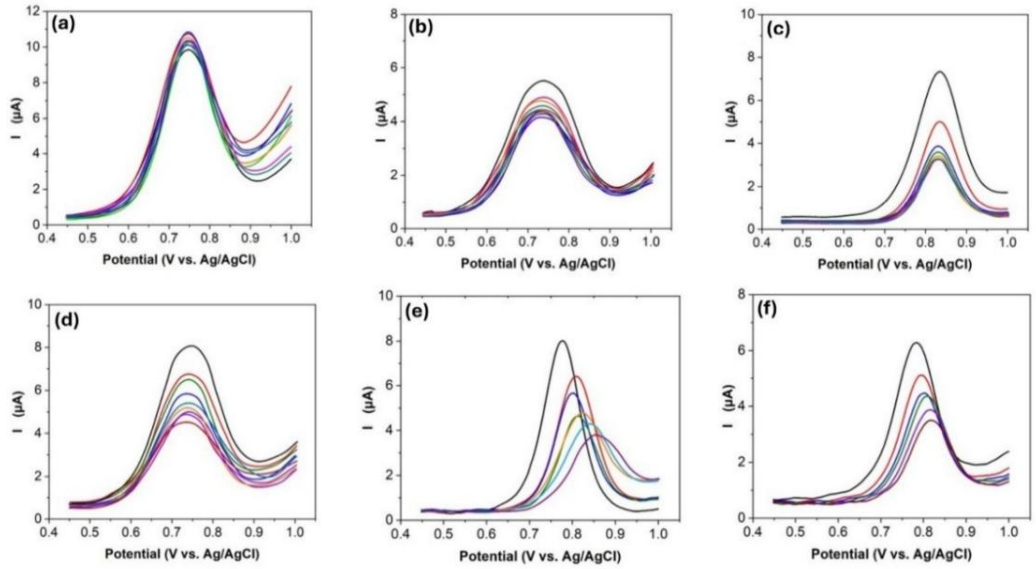


**Figure. 4.5.** Repeated DPVs stability of (a) GCE/rGO/G/ta-$MoS_2$ (n = 9); (b) GCE/rGO/G; (n = 9) (c) GCE/rGO/ta-$MoS_2$ (n = 9); (d) GCE/ta-$MoS_2$ (n = 9); (e) GCE/G (n = 6) and (f) GCE/rGO recorded in 200 μM SFD at a pH of 7.0 in 0.05 M PBS (n = 6).

On the other hand, there is a reduction in the peak currents on the repeated cycling of GCE/rGO, GCE/G, GCE/rGO/G, GCE/ta-$MoS_2$, and GCE/rGO/ta-$MoS_2$, as shown in Fig. 4.5. The reproducibility of the various sensors is highlighted in Table 4.2. On comparing the carbon-based materials, a RSD of 15.6 % is achieved when rGO and G are combined. It is also observed that the GCE/rGO/G/ta-$MoS_2$ exhibits very good reproducibility, with the lowest RSD of all the materials at 0.48% for 200 μM SFD. Therefore, this optimised GCE/rGO/G/ta-$MoS_2$ sensor was used in all further experiments.

**Table 4.2** Peak currents recorded for three different experiments (electrodes), with computed RSD%, recorded at 50 mV $s^{-1}$ in 200 µM SFD dissolved in 0.05 M phosphate buffer at a pH of 7.0 (n = 3).

| Modified electrode | Experiment I Current (µA) | Experiment II Current (µA) | Experiment III Current (µA) | Average Current (µA) | RSD (%) |
|---|---|---|---|---|---|
| GCE/G | 7.619 | 4.949 | 3.565 | 5.370 | 31.3 |
| GCE/rGO | 6.162 | 3.011 | 2.784 | 3.985 | 38.6 |
| GCE/rGO/G | 5.755 | 4.264 | 4.135 | 4.718 | 15.6 |
| GCE/ta-$MoS_2$ | 8.714 | 7.724 | 6.060 | 7.366 | 14.6 |
| GCE/rGO/G/ ta-$MoS_2$ | 9.591 | 9.533 | 9.484 | 9.536 | 0.46 |

To estimate the electroactive surface area, the $[Fe(CN)_6]^{3-/4-}$ probe was used. Typical CVs for GCE and GCE/rGO/G/ta-$MoS_2$ recorded in the $[Fe(CN)_6]^{3-/4-}$ solution are shown in Fig. 4.6 (a), with the peak currents plotted against the square root of the scan rate in Fig. 4.6 (b). These data were fitted to the Randles-Sevick equation (Eq. (2.2)), with linear regression equations, $I_p$ (µA) = 208.72 $v^{1/2}$ (V $s^{-1})^{1/2}$ −18.95 for GCE/rGO/G/ta-$MoS_2$ and $I_p$ (µA) = 130.8 $v^{1/2}$ (V $s^{-1})^{1/2}$ −10.86 for GCE, giving electroactive surface areas of 0.070 and 0.113 $cm^2$, respectively, reflecting a 1.6–fold increase for the modified electrode. Fig. 4.6 (a) shows that GCE/rGO/G/ta-$MoS_2$ enhances electron transfer efficiency, with a peak-to-peak separation of 85 ± 0.37 mV, which is relatively close to the ideal value of 57 mV, compared with a value of 186 ± 0.66 mV for the GCE.

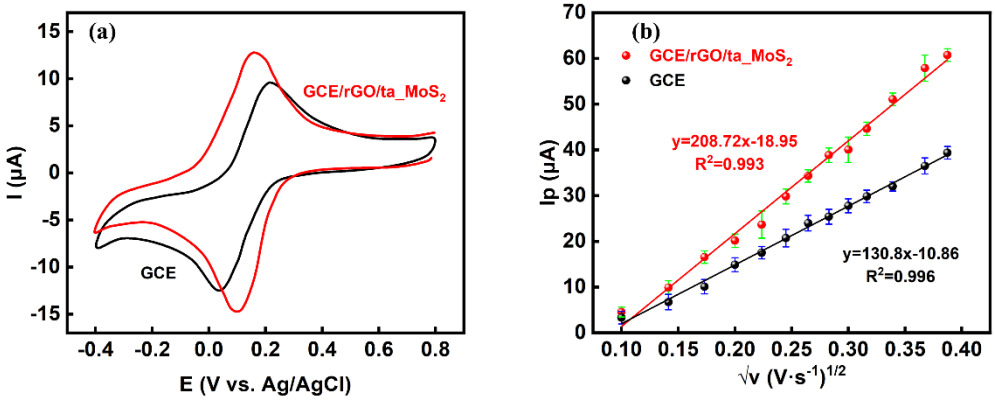


**Figure. 4.6.** (a) CVs recorded and (b) peak current (Ip) plotted against the square root of scan rate for GCE/rGO/G/ta-$MoS_2$ and GCE in 2.5 mM $[Fe(CN)_6]^{3-/4-}$ dissolved in 0.1 M KCl, (n = 3).

## 4.3.2. Influence of pH and Role of Adsorption and Diffusion in Sensing

Since the mechanism for SFD oxidation involves proton transfer, the effect of solution pH on SFD detection was examined. The pH was adjusted from 2.0 to 11.0, and the resulting DPVs are displayed in Fig. 4.7 (a). A gradual shift of the peak potential towards lower values is observed with increasing pH, as shown in Fig. 4.7 (b), which demonstrates a linear relationship between pH and peak potential. The gradient of the plot, at 0.053 V/pH, aligns well with the Nernst equation for an electron transfer reaction involving equal transfer of electrons and protons. This is consistent with Scheme 4.2, which consists of the transfer of one electron and one proton. The peak current increases with increasing pH, reaching a current of 18 µA at a pH of 11.0, as shown in Fig. 4.7 (a). There is a more significant increase in the peak current in these alkaline solutions, compared with a more gradual change at pH values < 6.0. This appears to be related to the deprotonation of SFD, as shown in Scheme 4.3, with p$K_a$ values of 5.9 and 12.6 for SFD [40].

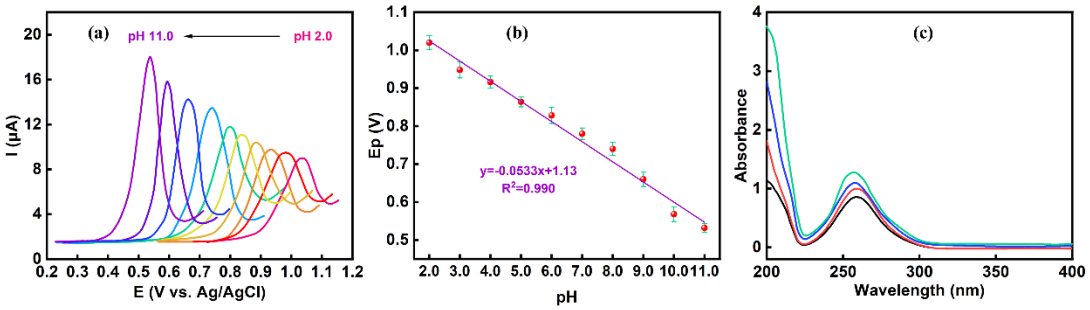


**Figure. 4.7.** (a) DPVs recorded for 200 μM SFD at pH values of 2.0, 3.0, 4.0, 5.0, 6.0, 7.0, 8.0, 9.0, 10.0 and 11.0 at GCE/rGO/G/ta-$MoS_2$; (b) plot of peak potential, $E_p$, as a function of pH (n = 3) and (c) UV-visible spectra recorded for a 200 μM SFD at pH values of 4, 7, 8 and 10.

Given the p$K_a$ value of 12.6, the SFD will be more soluble in water at pH values near 12.6, due to its anionic nature, and this is consistent with the higher currents observed in alkaline solutions. This was further corroborated using UV–vis spectroscopy, where the concentration was maintained fixed and the pH was increased. An increase in absorbance was observed (Fig. 4.7(c)), indicating greater solubility in the more alkaline solutions.

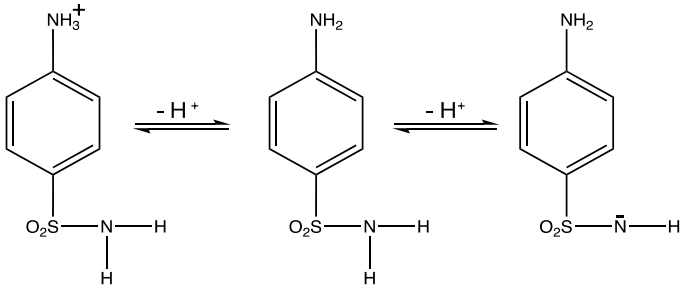


**Scheme 4.3.** Influence of pH on the nature of SFD.

The relationship between the scan rate and peak currents was studied to determine if the oxidation of SFD was under adsorption or diffusion control. Typical CVs recorded at scan rates from 10 to 100 mV $s^{-1}$ are shown in Fig. 4.8 (a). The peak current increases and the peak potential shifts to slightly higher potentials with increasing scan rate.

When the peak current was plotted against the scan rate, a linear relationship was observed, consistent with adsorption control, as illustrated in Fig. 4.8 (b).

The regression equation was deduced as, $I_p$ (μA) = 228.5 v (V $s^{-1}$) + 0.679. To further evaluate the extent of this adsorption control, the logarithm of the peak current was plotted as a function of the logarithm of the scan rate to give a linear plot with a slope of 0.87, indicating that the oxidation of SFD is largely an adsorption-controlled process at GCE/rGO/G/ta-$MoS_2$.

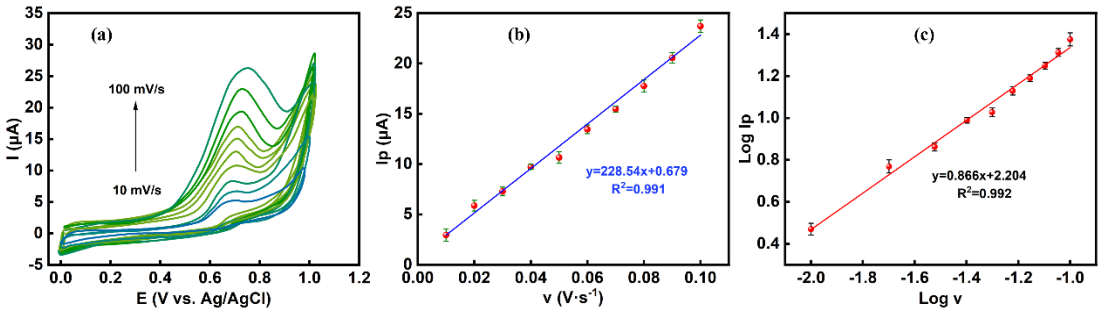


**Figure 4.8.** (a) CVs recorded at different scan rates from 10 to 100 mV $s^{-1}$ in 200 μM SFD solution (n = 3); (b) peak current, $I_p$, plotted as a function of scan rate (n = 3), and (c) logarithm of the peak current plotted as a function of the logarithm of the scan rate for 200 μM SFD solution (n = 3).

## 4.3.3. Analytical Performance of the GCE/rGO/G/ta-$MoS_2$

The analytical performance of the GCE/rGO/G/ta-$MoS_2$ was evaluated through a series of assessments, including calibration curves to determine the linear range, sensitivity, and limit of detection (LOD). Additionally, selectivity studies, as well as spiking and recovery tests with tap and river water samples, were conducted to validate accuracy and applicability. The DPV profiles recorded at different concentrations, ranging from 0.1 to 566 μM, are shown in Fig. 4.9 (a) and clearly demonstrate an increase in the peak current as the concentration increases.

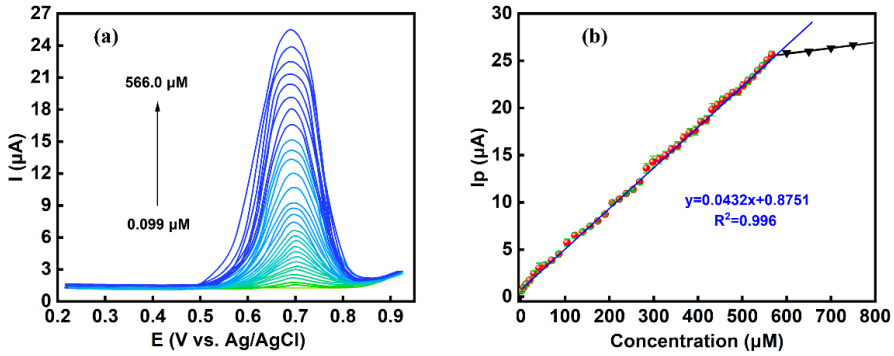


**Figure. 4.9.** (a) DPVs recorded for SFD concentrations ranging from 0.1 to 566 µM at GCE/rGO/G/ta-$MoS_2$; (b) corresponding calibration curve plotted with the DPV peak currents against the SFD concentration (n = 3).

The peak current was plotted as a function of the concentration, and this calibration plot is presented in Fig. 4.9 (b) with an extended linear range, from 0.1 to 566 µM. Good linearity with a $R^2$ of 0.996 was achieved together with a linear regression equation of $I_p$ (µA) = 0.0432 c (µM) + 0.875. A sensitivity of 0.0432 µA $\mu M^{-1}$ was computed, and when expressed in terms of the geometric surface area of the GCE (3 mm diameter), the sensitivity was 0.61 µA $\mu M^{-1}$ $cm^{-2}$ and using the estimated surface area of 0.113 $cm^2$, the sensitivity was computed as 0.38 µA $\mu M^{-1}$ $cm^{-2}$. Using the expression for the LOD (LOD = 3σ/sensitivity), the LOD was computed as 86 nM.

The analytical performance is compared with other sensors that have been developed for SFD in Table 4.3, where it is clear that the GCE/rGO/G/ta-$MoS_2$ compares very favourably. A more extensive linear range is achieved, while the LOD of 86 nM is considerably lower than that of many of the existing sensors. Likewise, the RSD at 0.48 % is lower than that of the previously reported sensors.

The selectivity of the GCE/rGO/G/ta-$MoS_2$ was assessed in the presence of various salts found in aquatic environments, including $NO_3^-$, $SO_4^{2-}$, $Cl^-$, $CO_3^{2-}$ anions and $Al^{3+}$,

$Co^{2+}$, $Cu^{2+}$, $Fe^{3+}$, $Zn^{2+}$ cations. Structurally related drugs from the sulfonamide family were also employed, and this involved Sulfamerazine (SRZ) and Sulfapyridine (SAD). The SFD concentration was set at 200 μM, and the interferent concentration was maintained at 2 mM, giving a 10-fold excess of the interferent. These experiments are summarised in Fig. 4.10 (a), where the ratio of the peak current obtained in the presence of the interferent is compared to the current obtained in its absence. In this analysis, a value of unity indicates no interference. It can be seen from Fig. 4.10 (a) that little interference is seen, with ratios close to unity even with the structurally related SRZ and SAD. This indicates that the GCE/rGO/G/ta-$MoS_2$ possesses good selectivity for SFD.

**Table 4.3** Comparison of GCE/rGO/G/ta-$MoS_2$ with recently reported sensors for SFD, showing Linear range, LOD, RSD (computed in buffer solutions), and recovery range obtained in real samples. (a, water samples; b, honey; c, fish/shrimp; d, pharmaceutical; e, biological; f, pork samples.)

| Materials | Linear range (μM) | LOD (μM) | %RSD | Recovery Range (%) | Refs. |
|---|---|---|---|---|---|
| Graphene sheets (GS) | 1–90 | 0.23 | 44.5 | – | [17] |
| $CO_2$-GS | 1–90 | 0.11 | 6.8 | 94–119[a] | [17] |
| Carbon black/polylactic acid | 1–10 | 0.26 | 2.1 | 85–120[b] | [22] |
| Pencil graphite | 24–120 | 2.37 | 4.2 | 92–97[b] | [20] |
| Laser-induced porous graphene | 2–100 | 0.17 | 6.44 | 96–105[c] | [16] |
| $MnO_2$ nanorod–carbon paste electrode | 0.07–100 | 0.01 | – | 97–104[a] | [21] |

| | | | | | |
|---|---|---|---|---|---|
| Ag@Pt–Rh core–shell nanostructures | 2.6–320 | 0.27 | 2.0 | 98–105[a] | [24] |
| Cobalt phthalocyanine chitosan | 1–53 | 0.27 | – | 99–102[d] | [23] |
| rGO | 10–50 | 2.3 | 5.6 | 83–109[e] | [18] |
| Silsesquioxane/nickel(II) phthalocyanine | 35–301 | 12 | 2.0 | – | [41] |
| Carboxyl MWCNTs | 1–100 | 0.5 | – | 95–103[f] | [19] |
| GCE/rGO/G/ta-$MoS_2$ | 0.1–566 | 0.086 | 0.48 | 83–99 | This work |

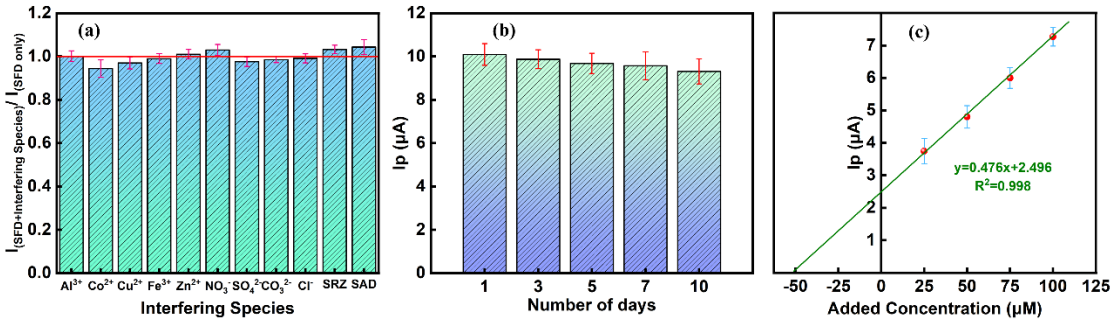


**Figure 4.10.** (a) selectivity with the ratio of the peak current with and without the interferent with a 200 µM SFD solution and 2 mM interferent, plotted against the nature of the interferent (n = 3); (b) stability showing the peak current as a function of days stored in solution (n = 3), and (c) Standard addition experiment with the addition of aliquots of 25 µM SFD to a river water sample initially spiked with 50 µM SFD (n=3).

Nevertheless, the GCE/rGO/G/ta-$MoS_2$ is capable of detecting both SRZ and SAD, as illustrated in Fig. 4.11, where the DPV profiles of SFD, SRZ, and SAD are compared at an equimolar concentration of 200 µM. Clearly, the good selectivity achieved in the detection of SFD in the presence of SFD and SAD is due to the more

thermodynamically favourable oxidation potential of SFD at GCE/rGO/G/ta-$MoS_2$, compared to the higher oxidation potentials of 0.96 V for SFX and 0.92 V for SAD.

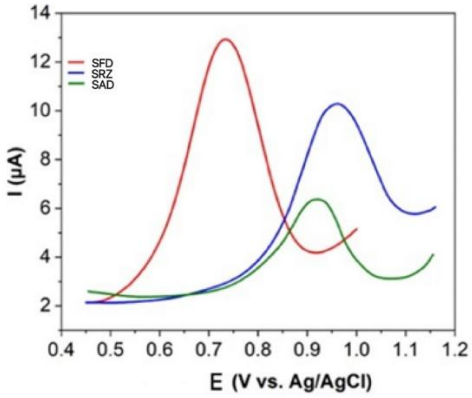


**Figure 4.11.** DPVs recorded for 200 μM SFD, 200 μM SRZ and 200 μM SAD at GCE/rGO/G/ta-$MoS_2$ at a pH of 7.0 in 0.05 M PBS.

Another important parameter is the overall stability of the sensor and this was evaluated over a 10-day period where the sensor was stored at room temperature in the phosphate buffer and then transferred to a buffered 200 μM SFD solution and the DPVs were recorded at regular intervals. It is evident from Fig. 4.10 (b) that the GCE/rGO/G/ta-$MoS_2$ exhibits good stability. There is only a slight reduction of 8.3 ± 0.136 % in the peak signal over the 10-day period.

Finally, a water spiking and recovery experiment was performed, where both tap water and river water were spiked with a known amount of SFD and the recovery was followed. These experiments were carried out over a week-long period to examine both the inter-day and intra-day recoveries in the river samples. All samples were filtered, and then sufficient phosphate was added to give the 0.05 M phosphate-buffered solution. The results from these experiments are provided in Table 4.4 and show acceptable recovery.

**Table 4.4** Recovery studies performed with tap and river water.

| Sample | Added Drug (μM) | Recovery (%) | RSD (%) |
|---|---|---|---|
| Tap Water | 50 | 90.4 | 4.3 |
| | 100 | 94.8 | 3.5 |
| | 150 | 96.7 | 2.4 |
| | 200 | 98.6 | 1.0 |
| | 400 | 98.9 | 0.8 |
| Real River Water | 50 | 83.5 | 7.0 |
| | 100 | 89.6 | 7.0 |
| | 150 | 93.3 | 6.5 |
| | 200 | 94.3 | 4.7 |
| | 400 | 94.4 | 2.5 |

The recovery of tap water varies from 90.4 to 98.9 %, while the recovery in the river water is somewhat lower, with values ranging from 83.5 to 94.4 %. There was no significant variation between the inter-day and intra-day recoveries in the river samples, with the average recovery at 84 % for a 50 μM spike of SFD, and the RSD at this lower concentration was 7.0 % for both sets of experiments. These measurements compare reasonably well with the recoveries listed in Table 4.3, especially with the water systems, where the recoveries range from 94 to 119 % [17].

To further explore this recovery and possible matrix effects, a standard addition experiment was employed. In these experiments, the river samples were initially spiked with 50 μM SFD, and this sample was then studied using the standard addition method. A typical plot is shown in Fig. 4.10 (c), where aliquots of 25 μM SFD were added. On analysis of the linear plot, the concentration of SFD was determined as 52.4 μM SFD, giving an acceptable error of 4.8 %, and a recovery of 105 %.

## 4.5. Conclusions

In this study a sensor for SFD was developed by coupling rGO and graphite with tannic acid exfoliated $MoS_2$ sheets. Normally, rGO is considered to be an excellent material in sensing applications. However, in this study it was found that a mixture of rGO and graphite flakes coupled with $MoS_2$ provides a highly stable, robust and reproducible sensor that was superior to the corresponding sensor fabricated with rGO and $MoS_2$, with a peak current for 200 µM SFD of 9.59 µA for GCE/rGO/G/ta-$MoS_2$ compared to a lower current of 5.24 µA for GCE/rGO/ta-$MoS_2$. On adding the $MoS_2$ sheets to the GCE/rGO/G, the peak current increased from 5.02 to 9.59 µA in a 200 µM SFD solution. The sensor provided an impressive linear region extending from 0.1 to 566 µM, with a LOD of 86 nM. Furthermore, good recovery ranging from 83.5 to 94.4 % in canal water was achieved on spiking the collected samples with various SFD concentrations from 50 to 400 µM. Moreover, tannic acid, a sustainable and environmentally acceptable biomolecule was found to be very effective in the exfoliation of $MoS_2$, giving a high yield of few-layered $MoS_2$ sheets that were especially effective in the development of the SFD sensor. These approaches, combining rGO with G and forming conducting $MoS_2$ sheets with tannic acid, has the potential to be used in formulating other sensing materials for various analytes. Another strong outcome is the reliability of the sensor response. The GCE/rGO/G/ta-$MoS_2$ shows excellent repeatability and reproducibility, good selectivity against common ions and related sulfonamides, and acceptable recoveries in real water. The sensor also retains a stable response over time, with only a modest signal decrease over 10 days. These results demonstrate that the platform is not only sensitive but also robust under realistic conditions. Overall, this work advances the state of the art by delivering a sensor at low LOD, using materials choices and processing steps that are simple, scalable, and environmentally acceptable.

# References

[1] M. Qiao, G.-G. Ying, A. C. Singer, and Y.-G. Zhu, "Review of antibiotic resistance in China and its environment," *Environment International*, vol. 110, pp. 160–172, Oct. 2017, doi: 10.1016/j.envint.2017.10.016.

[2] G. Dhillon et al., "Triclosan: current status, occurrence, environmental risks and bioaccumulation potential," *Int. J. Environ. Res. Public Health*, vol. 12, no. 5, pp. 5657–5684, May 2015, doi: 10.3390/ijerph120505657.

[3] L. Kergoat et al., "Environmental concentrations of sulfonamides can alter bacterial structure and induce diatom deformities in freshwater biofilm communities," *Frontiers in Microbiology*, vol. 12, p. 643719, May 2021, doi: 10.3389/fmicb.2021.643719.

[4] P. M. C. Huijbers, H. Blaak, M. C. M. De Jong, E. a. M. Graat, C. M. J. E. Vandenbroucke-Grauls, and A. M. De Roda Husman, "Role of the environment in the transmission of antimicrobial resistance to humans: a review," *Environmental Science & Technology*, vol. 49, no. 20, pp. 11993–12004, Sep. 2015, doi: 10.1021/acs.est.5b02566.

[5] A. K. Sarmah, M. T. Meyer, and A. B. A. Boxall, "A global perspective on the use, sales, exposure pathways, occurrence, fate and effects of veterinary antibiotics (VAs) in the environment," *Chemosphere*, vol. 65, no. 5, pp. 725–759, May 2006, doi: 10.1016/j.chemosphere.2006.03.026.

[6] R. P. Lopes, É. E. De Freitas Passos, J. F. De Alkimim Filho, E. A. Vargas, D. V. Augusti, and R. Augusti, "Development and validation of a method for the determination of sulfonamides in animal feed by modified QuEChERS and LC–MS/MS analysis," *Food Control*, vol. 28, no. 1, pp. 192–198, May 2012, doi: 10.1016/j.foodcont.2012.04.026.

[7] A. Adenaya, M. Berger, T. Brinkhoff, M. Ribas-Ribas, and O. Wurl, "Usage of antibiotics in aquaculture and the impact on coastal waters," *Marine Pollution Bulletin*, vol. 188, p. 114645, Jan. 2023, doi: 10.1016/j.marpolbul.2023.114645.

[8] S. G. Dmitrienko, E. V. Kochuk, V. V. Apyari, V. V. Tolmacheva, and Y. A. Zolotov, "Recent advances in sample preparation techniques and methods of sulfonamides detection – A review," *Analytica Chimica Acta*, vol. 850, pp. 6–25, Aug. 2014, doi: 10.1016/j.aca.2014.08.023.

[9] A. A. Lahcen, S. A. Errayess, and A. Amine, "Voltammetric determination of sulfonamides using paste electrodes based on various carbon nanomaterials," *Microchimica Acta*, vol. 183, no. 7, pp. 2169–2176, Apr. 2016, doi: 10.1007/s00604-016-1850-3.

[10] A. Joshi and K.-H. Kim, "Recent advances in nanomaterial-based electrochemical detection of antibiotics: Challenges and future perspectives," Biosensors and Bioelectronics, vol. 153, p. 112046, Jan. 2020, doi: 10.1016/j.bios.2020.112046.

[11] Q. Cai and J. Hu, "Decomposition of sulfamethoxazole and trimethoprim by continuous UVA/LED/$TiO_2$ photocatalysis: Decomposition pathways, residual

antibacterial activity and toxicity," *Journal of Hazardous Materials*, vol. 323, no. Pt A, pp. 527–536, Jun. 2016, doi: 10.1016/j.jhazmat.2016.06.006.

[12] Hamed, F. M, Hassan, B. A, and Abdulridha, M. M, "The Antitumor Activity of Sulfonamides Derivatives." *Int. J. Pharm.*, Res 2020, 12, 2512–2519. doi: 10.31838/ijpr/2020.SP1.390

[13] M. Mackeviciute et al., "Synthesis and characterization of sulphanilamide and benzimidazole pharmacophores containing γ-amino acid derivatives as dual antimicrobial and anticancer agents," *ARKIVOC*, vol. 2023, no. 7, Jun. 2023, doi: 10.24820/ark.5550190.p012.015.

[14] S.-J. Zhang, H.-Q. Yu, and Q.-R. Li, "Radiolytic degradation of Acid Orange 7: A mechanistic study," *Chemosphere*, vol. 61, no. 7, pp. 1003–1011, May 2005, doi: 10.1016/j.chemosphere.2005.03.008.

[15] H. Liu, G. Li, J. Qu, and H. Liu, "Degradation of azo dye Acid Orange 7 in water by Fe0/granular activated carbon system in the presence of ultrasound," *Journal of Hazardous Materials*, vol. 144, no. 1–2, pp. 180–186, Oct. 2006, doi: 10.1016/j.jhazmat.2006.10.009.

[16] D. Qiu et al., "A Low-Cost wireless intelligent portable sensor based on disposable Laser-Induced porous graphene flexible electrode decorated by gold nanoshells for rapid detection of sulfonamides in aquatic products," *Food Analytical Methods*, vol. 15, no. 6, pp. 1471–1481, Jan. 2022, doi: 10.1007/s12161-021-02198-8.

[17] J. F. S. Pereira et al., "$CO_2$-plasma surface treatment of graphite sheet electrodes for detection of chloramphenicol, ciprofloxacin and sulphanilamide," *Microchimica Acta*, vol. 190, no. 10, p. 379, Sep. 2023, doi: 10.1007/s00604-023-05953-2.

[18] L. V. De Faria et al., "Use of reduced graphene oxide for sensitive determination of sulfanilamide in synthetic biological fluids and environmental samples by batch injection analysis," *Journal of Electroanalytical Chemistry*, vol. 892, p. 115298, Apr. 2021, doi: 10.1016/j.jelechem.2021.115298.

[19] R. G. Rocha, L. V. De Faria, V. F. Silva, R. a. A. Muñoz, and E. M. Richter, "Carbon Black integrated polylactic acid electrodes obtained by fused deposition modeling: a powerful tool for sensing of sulfanilamide residues in honey samples," *Journal of Agricultural and Food Chemistry*, vol. 71, no. 6, pp. 3060–3067, Jan. 2023, doi: 10.1021/acs.jafc.2c07814.

[20] B. He and W. Chen, "Carboxyl Multiwalled Carbon Nanotubes through Ul trasonic Dispersing in Dimethylfomamide Modified Electrode as a Sensitive Amperometric Sensor for Detection of Sulfonamide," *International Journa l of Electrochemical Science*, vol. 10, no. 5, pp. 4335–4345, May 2015, d oi: 10.1016/s1452-3981(23)06626-9.

[21] T. P. Lisboa, B. De Cássia Moreira, C. C. De Souza, W. B. V. De Oliveira, M. A. C. Matos, and R. C. Matos, "A pencil graphite-based disposable device for electrochemical monitoring of sulfanilamide in honey and water samples,"

*Analytical Methods*, vol. 14, no. 39, pp. 3867–3874, Jan. 2022, doi: 10.1039/d2ay01137a.

[22] H. Beitollahi, S. Tajik, and A. Di Bartolomeo, "Application of $MNO_2$ NanoRoD–Ionic liquid modified carbon paste electrode for the voltammetric determination of sulfanilamide," *Micromachines*, vol. 13, no. 4, p. 598, Apr. 2022, doi: 10.3390/mi13040598.

[23] F. G. De Moura Junior, W. B. Veloso, J. A. De Oliveira Junior, H.-B. Kraatz, I. S. Da Silva, and L. M. F. Dantas, "Voltammetric determination of sulfanilamide using a cobalt phthalocyanine chitosan composite," *Monatshefte Für Chemie - Chemical Monthly*, vol. 152, no. 8, pp. 895–902, Aug. 2021, doi: 10.1007/s00706-021-02812-9.

[24] Y. Zhang, Y. Lv, Y. Chen, Y. Li, Y. Wang, and H. Zhao, "Trimetallic Ag@Pt-Rh core-shell nanocubes modified anode for voltammetric sensing of dopamine and sulfanilamide," *Chemical Engineering Science*, vol. 249, p. 117326, Dec. 2021, doi: 10.1016/j.ces.2021.117326.

[25] R. Sukanya, D. C. Da Silva Alves, and C. B. Breslin, "RevIew—Recent Developments in the applications of 2D transition metal dichalcogenides as electrocatalysts in the generation of hydrogen for renewable energy conversion," *Journal of the Electrochemical Society*, p. 064504, 2022.

[26] Md. Ahmaruzzaman and V. Gadore, "$MoS_2$ based nanocomposites: An excellent material for energy and environmental applications," *Journal of Environmental Chemical Engineering*, vol. 9, no. 5, p. 105836, Jun. 2021, doi: 10.1016/j.jece.2021.105836.

[27] Y. Luo, T. N. Barwa, K. Herdman, E. Dempsey, and C. B. Breslin, "Elec troanalysis of metronidazole using exfoliated $MoS_2$ sheets and electrodeposi ted amorphous MoSx," *Electrochimica Acta*, vol. 462, p. 142778, Jun. 202 3, doi: 10.1016/j.electacta.2023.142778.

[28] P. K. Kannan, D. J. Late, H. Morgan, and Chandra Sekhar Rout, "Recent developments in 2D layered inorganic nanomaterials for sensing," 2021. Available online: https://www.rsc.org/nanoscale

[29] K. Krishnamoorthy, M. Veerapandian, K. Yun, and S. -j. Kim, "The chemical and structural analysis of graphene oxide with different degrees of oxidation," *Carbon*, vol. 53, pp. 38–49, Oct. 2012, doi: 10.1016/j.carbon.2012.10.013.

[30] R. Karthik, P. R. Chavan, R. Sukanya, G. Dhakal, J.-J. Shim, and C. B. Breslin, "Flower-like strontium molybdate anchored on 3D N-rich reduced graphene oxide aerogel composite: An efficient catalyst for the detection of lethal pollutant nitrobenzene in water samples," *Composites Part B Engineering*, vol. 256, p. 110649, Feb. 2023, doi: 10.1016/j.compositesb.2023.110649.

[31] V. Zo´ Lyomi 1, J. Koltai, J. Ku ¨ rti, "Resonance Raman spectroscopy of graphite and graphene," *physica status solidi WILEY-VCH Verlag GmbH & Co. KGaA*, Weinheim, journal-article, Sep. 2011. doi:10.1002/pssb.201100295.

[32] B. D. Ossonon and D. Bélanger, "Synthesis and characterization of sulfophenyl-functionalized reduced graphene oxide sheets," *RSC Advances*, vol. 7, no. 44, pp. 27224–27234, Jan. 2017, doi: 10.1039/c6ra28311j.

[33] G. Das, N. Kakati, S. H. Lee, N. Karak, and Y. S. Yoon, "Water soluble sodium sulfate nanorods as a versatile template for the designing of copper sulfide nanotubes," *Journal of Nanoscience and Nanotechnology*, vol. 14, no. 6, pp. 4455–4461, Feb. 2014, doi: 10.1166/jnn.2014.8282.

[34] Z. Lin, Y. Yao, Z. Li, Y. Liu, Z. Li, and C.-P. Wong, "Solvent-Assisted thermal reduction of graphite oxide," *The Journal of Physical Chemistry C*, vol. 114, no. 35, pp. 14819–14825, Aug. 2010, doi: 10.1021/jp1049843.

[35] D. Wang et al., "Anomalous nano-barrier effects of the ultrathin molybdenum disulfide nanosheets for improving flame retardance of polymer nanocomposites," *Journal of Materials Chemistry A*, May 2015.

[36] H. Peng, D. Wang, and S. Fu, "Tannic acid-assisted green exfoliation and functionalization of $MoS_2$ nanosheets: Significantly improve the mechanical and flame-retardant properties of polyacrylonitrile composite fibers," *Chemi cal Engineering Journal*, vol. 384, p. 123288, Nov. 2019, doi: 10.1016/j.ce j.2019.123288.

[37] A. Lasia, "The origin of the constant phase element," *The Journal of Phy sical Chemistry Letters*, vol. 13, no. 2, pp. 580–589, Jan. 2022, doi: 10.10 21/acs.jpclett.1c03782.

[38] X. Shen, X. Lin, N. Yousefi, J. Jia, and J.-K. Kim, "Wrinkling in graphene sheets and graphene oxide papers," *Carbon*, vol. 66, pp. 84–92, Sep. 2013, doi: 10.1016/j.carbon.2013.08.046.

[39] B. R. L. Ferraz, T. Guimarães, D. Profeti, and L. P. R. Profeti, "Electrooxidation of sulfanilamide and its voltammetric determination in pharmaceutical formulation, human urine and serum on glassy carbon electrode," *Journal of Pharmaceutical Analysis*, vol. 8, no. 1, pp. 55–59, Oct. 2017, doi: 10.1016/j.jpha.2017.10.004.

[40] P. Cysewski, "Apparent basicities of the surfaces characterizing the dominant crystal habits of distinct polymorphic forms of 4-aminosulfonamide," *Journal of Molecular Modeling*, vol. 20, no. 7, p. 2276, Jun. 2014, doi: 10.1007/s00894-014-2276-7.

[41] C. R. Vanoni, J. P. Winiarski, G. R. Nagurniak, H. A. Magosso, and C. L. Jost, "A novel electrochemical sensor based on Silsesquioxane/Nickel (II) phthalocyanine for the determination of sulfanilamide in clinical and drug samples," *Electroanalysis*, vol. 31, no. 5, pp. 867–875, Feb. 2019, doi: 10.1002/elan.201800832.

# **Chapter 5** Electrochemical Detection of Flutamide (FLD) with Carbon Particles (CPs) and $WS_2$ Platelets

# 5.1. Introduction

It is well established that carbon-based nanostructures, ranging from carbon dots and nanoparticles to graphene, carbon fibres, carbon black, and carbon nanotubes, offer high surface areas, abundant surface functional groups, and excellent charge transport, making them versatile supports for electroanalytical sensing platforms [1-7]. Their propensity to form composites with complementary materials, such as semiconductors, further enables synergistic interactions that are beneficial in sensing applications [8-12]. Among such companions, layered transition-metal dichalcogenides (TMDs, $MX_2$) provide chemically robust, van der Waals–stacked architectures with tunable electronic properties [13-16]. $MoS_2$ has been widely explored, and $WS_2$, though less represented, has demonstrated suitable conductivity for sensing and successful integration with carbonaceous hosts [17-19].

Flutamide (FLD), a non-steroidal antiandrogen used clinically for prostate cancer and in certain endocrine indications, is increasingly scrutinised due to its occurrence in aquatic systems and potential ecotoxicological impacts [20-23]. Electrochemical determination of FLD has been reported using a wide range of diverse oxide and graphene-based materials, including Ni-, Mo-, and Co-oxide composites and reduced-graphene-oxide hybrids [24-27]. However, to the best of our knowledge, $WS_2$ or $WS_2$-carbon composites have not yet been applied directly to the electroanalysis of FLD. This absence suggests an opportunity to develop a valuable conductive, high-surface-area $WS_2$-carbon interface tailored for FLD detection [28-30].

Accordingly, in this work, we address this limitation by engineering a size-matched composite comprising micron-scale carbon particles (CPs), prepared via a green hydrothermal route, and $WS_2$ platelets. This approach yields a stable CPs-$WS_2$ hybrid with the CPs anchored onto the $WS_2$ surfaces. The composite is drop-cast onto glassy

carbon (GCE/CPs-$WS_2$) to furnish an electrochemical sensor for FLD. We (i) establish morphology and phase/composition by SEM, XRD, Raman, and spectroscopic analyses, (ii) quantify electroactive area and interfacial kinetics using the $[Fe(CN)_6]^{3-/4-}$ probe and impedance spectroscopy, and (iii) evaluate analytical performance toward FLD via cyclic voltammetry and differential-pulse voltammetry in phosphate buffer, including optimization of modifier loading and pH, assessment of diffusion/adsorption contributions, and benchmarking of sensitivity, selectivity, precision, and operational stability. Finally, applicability is demonstrated in spiked environmental (tap/canal) waters and artificial urine for more biological applications.

The data show that the CPs-$WS_2$ interface delivers enhanced charge transfer and well-resolved reduction waves for FLD ($-NO_2 \rightarrow -NHOH$, $4e^-/4H^+$), enabling nanomolar-level detection with excellent repeatability and robust recoveries in complex matrices, thereby positioning $WS_2$-carbon hybrids as practical candidates for FLD monitoring.

Due to solubility limitations, the solubility of FLD in water was experimentally determined to be approximately 110 μM. Therefore, the maximum concentration selected for different drug concentrations in the experiment was set at 104 μM. Consequently, this work focuses more on detecting lower concentrations.

## 5.2. Experimental

### 5.2.1. Synthesis of Carbon Particles (CPs)

To prepare CPs from A. *deliciosa* (Kiwifruit), the methodology developed for the preparation of carbon nanostructures using sustainable approaches was adapted [31]. The fruit (fresh fruit, used on the day it was purchased from the supermarket) was first washed with deionised water, dried, and peeled. The peeled fruit was cut into small pieces and blended using a laboratory blender. The resulting puree was then squeezed through cheesecloth to obtain the concentrated juice. The juice, 40 mL, was transferred to a hydrothermal autoclave (100 mL) and heated to 180 °C for 24 h, as shown in Scheme 5.1. The hydrothermal product was collected, filtered at least three times to remove the larger carbon structures, and finally centrifuged to obtain a clear solution of the CPs. The collected solution containing the CPs was refrigerated at 4 °C for future use. Two additional samples were prepared by combining the blended puree with either water or ethanol in a 3:1 ratio prior to the hydrothermal reaction. The resulting CPs were labelled as CPs (concentrated juice), CPs-DI (juice diluted with deionised water (DI), and CPs-EtOH (juice diluted with ethanol (EtOH)).

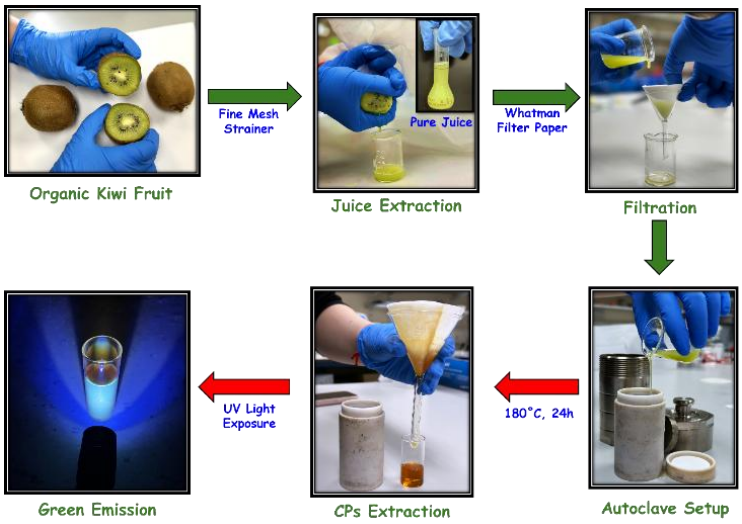


**Scheme 5.1.** Synthetic Method Used to Prepare the CPs.

## 5.2.2. Synthesis of CPs-$WS_2$

To prepare the composites comprising the CPs and $WS_2$, 1 g of $WS_2$ powder (commercial) was mixed with 10 mL of each of the CPs prepared by using the method in Section 5.2.1 and obtained from the A. *deliciosa* juice, CPs, CPs-DI, and CPs-EtOH. The mixture was thoroughly homogenised and centrifuged for 20 min at 2000 rpm. This process was repeated five times, with each round of centrifugation being followed by washing of the composite with DI. The composite was then dried overnight at 60 °C to eliminate any residual moisture. By combining $WS_2$ with the different types of CPs, three distinct composite materials were obtained, namely, the CPs combined with the concentrated juice, CPs-$WS_2$, CPs-DI-$WS_2$, and CPs-EtOH-$WS_2$, with all the materials adopting silver/black metallic-like colours.

## 5.2.3. Preparation and Use of the GCE/CPs-$WS_2$ Sensor

The FLD sensor was fabricated using the prepared CPs-$WS_2$ composites. First, a GCE (3 mm) was polished and cleaned as shown in Section 2.3.2.4. The GCE was then rinsed with DI and dried in an air stream. The CPs-$WS_2$ composites were sonicated in DI (1 mg/1 mL) for 30 min. Next, 5 µL of this dispersion was drop-cast onto the GCE and dried at room temperature, resulting in the formation of a modified GCE with the CPs-$WS_2$ composite material. A standard three-electrode cell was utilised for the electrochemical measurements, consisting of the GCE/CPs-$WS_2$, Ag/AgCl reference electrode, and a high surface area platinum wire serving as the counter electrode. All solutions were deoxygenated with nitrogen for 30 min before conducting the electrochemical tests.

The optimised sensor was applied in the sensing of FLD in both real water samples and artificial human urine. Water samples were collected from the local canal in Maynooth.

The samples were filtered promptly to eliminate debris and stored at 4 $^{o}$C until analysis, with all tests conducted within four hours. For these water measurements, both the GCE and carbon screen-printed electrodes (SPE), obtained from Metrohm, were utilised to support the CPs-$WS_2$ composite.

The electrochemical and surface analysis instrumentation utilised in this study is detailed in Chapter 2. Electrochemical techniques, including cyclic voltammetry (CV), differential pulse voltammetry (DPV), and electrochemical impedance spectroscopy (EIS), are discussed in Section 2.3.3. Surface analysis methods, such as scanning electron microscopy (SEM), X-ray diffraction (XRD), Fourier-transform infrared (FTIR) spectroscopy, Raman spectroscopy, and Fluorescence spectroscopy and UV–visible spectroscopy, are described in Sections 2.4 and 2.5. The procedure for material characterisation methods and specific characterisation techniques usage is detailed in the corresponding sections of Chapter 2, Experimental and Research Methods.

# 5.3. Results and discussion

## 5.3.1. Characterization of CPs and the CPs-$WS_2$ Composite

Once the CPs were synthesised, they were characterised using a combination of UV–visible, FTIR, and HR-SEM, and the relevant data are presented in Fig. 5.1, 5.2 and 5.3. In Fig. 5.1 (a) and (b), the UV–visible and FTIR spectra are shown for the three CPs, and the nature of the extracted juice clearly influences the spectra. The CPs show strong absorption in the ultraviolet region with two prominent peaks for all three CPs in the vicinity of 200 and 280 nm. These can be attributed to the higher energy π–π* transition of the C═C bonds and the lower energy n–π* transition of the C═O bonds [32]. There are no absorbance bands from approximately 350–600 nm, nor is there any evidence of polymer chains that typically absorb at these longer wavelengths. Regarding the higher energy absorption peak, the $\lambda_{max}$ values range from 222 to 197 nm, suggesting variations in the nature or concentration of the surface groups.

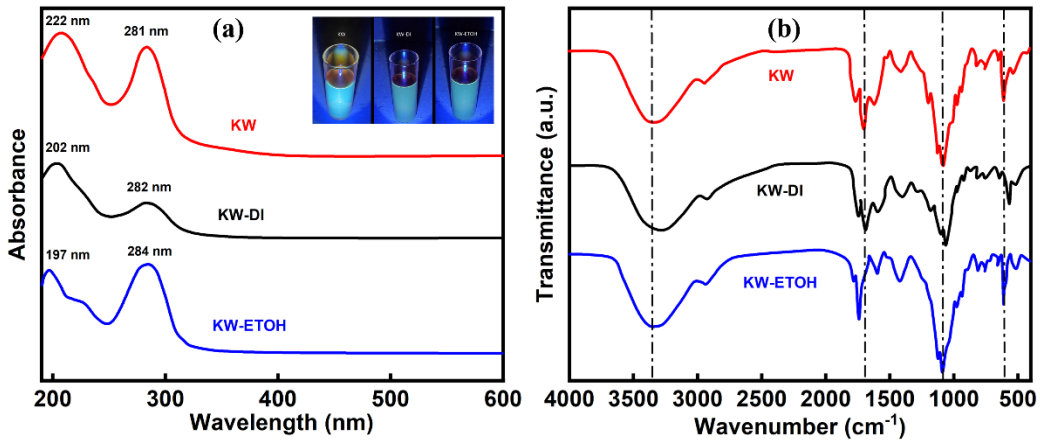


**Figure 5.1.** (a) UV–vis absorption spectra recorded for CPs, CPs-DI, and CPs-EtOH, and (b) FTIR spectra recorded for CPs, CPs-DI, and CPs-EtOH.

The FTIR spectra, depicted in Fig. 5.1 (b), show four main peaks. The broad peak at about 3350 $cm^{-1}$ indicates the presence of O–H. Strong peaks are evident at 1640 and 1023 $cm^{-1}$, and these can be attributed to the presence of C═O and C–O groups, while

the peak at about 600 $cm^{-1}$ may indicate the presence of C–H groups. This is consistent with the presence of O–H, C═O, and C–H moieties at the surface of the CPs. There is also a peak at 1405 $cm^{-1}$, which is indicative of C═C, and suggests that the CPs possess a graphitic structure, which is very relevant in terms of electrochemical-based sensing.

As shown in the inset in Fig. 5.1 (a) and in Fig. 5.2 (a), the fluorescence evident in the image is consistent with the presence of CQDs that are small and surface-functionalised. In this analysis, the sample was excited at various wavelengths ranging from 320 nm to 400 nm. The observed emission peaks for all excitation wavelengths are centred in the visible region, with the highest intensity recorded upon excitation at 320 nm. As the excitation wavelength increases, a gradual decrease in intensity is evident, accompanied by a slight redshift and broadening of the emission maxima. This is probably due to the presence of CQDs of varying sizes. Specifically, the observed redshift and broadening of emission with increasing excitation wavelength align with a heterogeneous size distribution of the CQDs, where the smaller dots emit at shorter wavelengths and the larger dots at longer wavelengths. [33,34]

Regrettably, although fluorescence phenomena were observed during the initial preparation of CPs-EtOH, these CQDs proved unstable. After a short period of time, SEM and fluorescence analysis revealed that the CQDs aggregated, exceeding nanoscale dimensions. Consequently, when utilising this material as a sensor, it no longer comprised CQDs but had transformed into macroscopic CPs.

The Raman spectrum of the CPs is presented in Fig. 5.2 (b) and exhibits the D and G bands, characteristic of carbon-based materials. The D band at about 1350 $cm^{-1}$ is linked to carbon defects, while the G-band is related to the $sp^2$-hybridised carbon network. The $I_D/I_G$ ratio was computed as 0.75 ± 0.037 (n = 3), indicating some defects in the CPs.

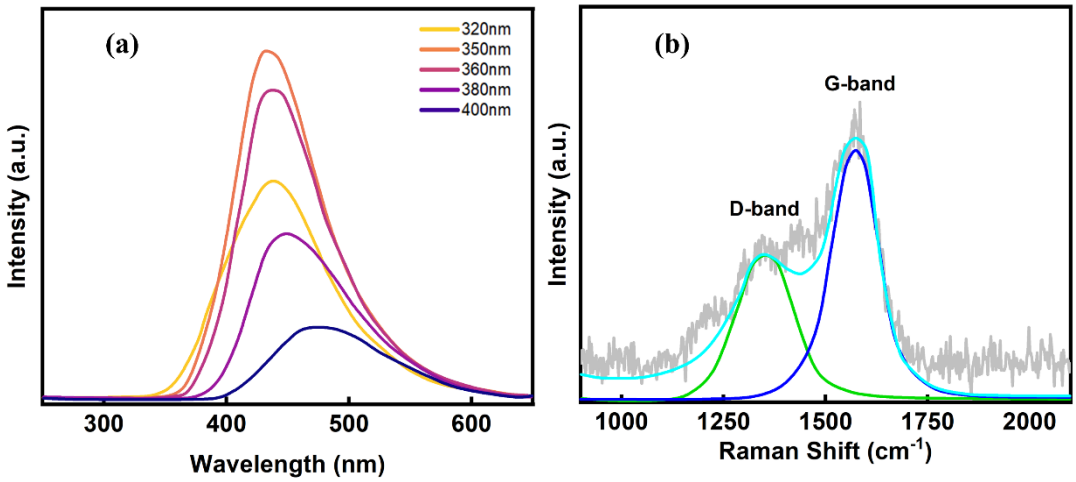


**Figure 5.2.** (a) Fluorescence evident of CQDs-EtOH under UV illumination, and (b) Raman spectrum recorded for CPs.

The size and morphology of the CPs were studied using HR-SEM in Maynooth University, and representative micrographs are presented in Fig. 5.3. The size distribution histogram indicates that the CPs vary from approximately 0.2–1.5 μm in diameter, with the highest population ranging in size from about 0.4–0.6 μm, Fig. 5.3 (b). The surface morphology of the CPs is more evident in Fig. 5.3 (e) and (f). The larger CPs appear to be composed of much smaller CPs, or CQDs, assembled and connected. The variation in size of the CPs, Fig. 5.3 (b), may indicate a progressive-like nucleation and growth of the particles and is also consistent with the fluorescence seen in Fig. 1(c). It appears that the CQDs are initially formed, consistent with Fig. 5.3 (c), but then proceed to evolve through an Ostwald ripening mechanism whereby they redeposit onto the larger forming CPs. Indeed, Ostwald ripening has previously been observed during the vapour phase growth of carbon spheres. [35]

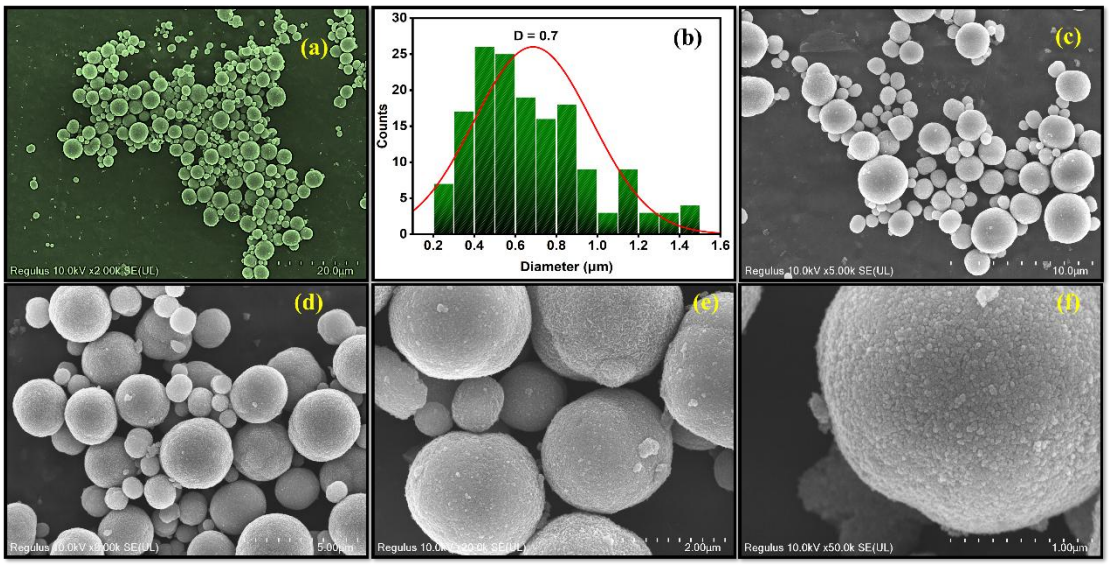


**Figure 5.3.** (a) SEM micrographs recorded for CPs at low resolution; (b) size summary of CPs from (a); SEM micrographs recorded for the CPs at different magnifications with scales at (c) 10; (d) 5; (e) 2; (f) 1 μm.

In Fig. 5.4, SEM micrographs are provided for the $WS_2$ and the CPs-$WS_2$ composite. These offer a morphological overview and particle size evolution for the synthesised composite. The $WS_2$ appears as platelets of different sizes, ranging from 0.2 to 1.5 μm, as shown in Figure 5.4 (a), with some as large as 2 μm, making them ideal supports for the CPs, which have diameters between 0.4 and 0.8 μm. In Fig. 54 (b), the $WS_2$ flakes are highlighted (yellow/orange dashed outline), displaying the characteristic layered morphology typical of transition metal dichalcogenides. The CPs (yellow/green dashed outline) exhibit smaller, nearly spherical particles distributed closely to $WS_2$, indicating successful loading of the CPs onto the $WS_2$ surface. This composite exhibits a significantly different morphology compared to either the CPs (Fig. 5.3) or the $WS_2$ (Fig. 5.4 (a)), offering a high surface area that is appealing for the development of electrochemical-based sensors.

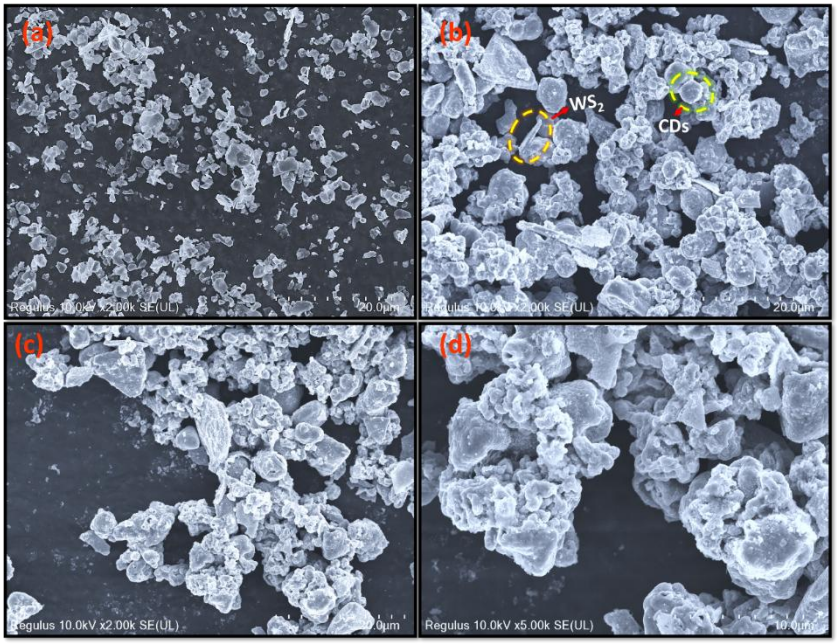


**Figure. 5.4.** SEM images for (a) bulk $WS_2$; (b) CPs-$WS_2$; (c) CPs-$WS_2$ and (d) CPs-$WS_2$.

Clear evidence for the formation of this CPs-$WS_2$ composite is seen on comparing the XRD and Raman spectra recorded for $WS_2$ and CPs-$WS_2$. In Fig. 5.5 (a), the XRD pattern of $WS_2$, with diffraction angles at 14.3, 28.9, 32.8, 33.5, 35.8, 39.5, 43.9, 49.7, 58.5, 59.8, 60.4, 62.6, 66.5, 69.1, 72.8, 75.8, and 77.2° corresponding to the (002), (004), (100), (101), (102), (103), (006), (105), (106), (008), (102), (122), (114), (102), (200), (203), and (116) planes, are evident. These are in good agreement with previous publications [36]. When the CPs-$WS_2$ composite is formed, the diffraction pattern changes, with the diffraction peaks associated with the $WS_2$ becoming somewhat broader. In addition, a broad peak corresponding to the (002) plane of the CPs is evident, indicating that the CPs are slightly amorphous in nature due to the presence of the functional groups [32].

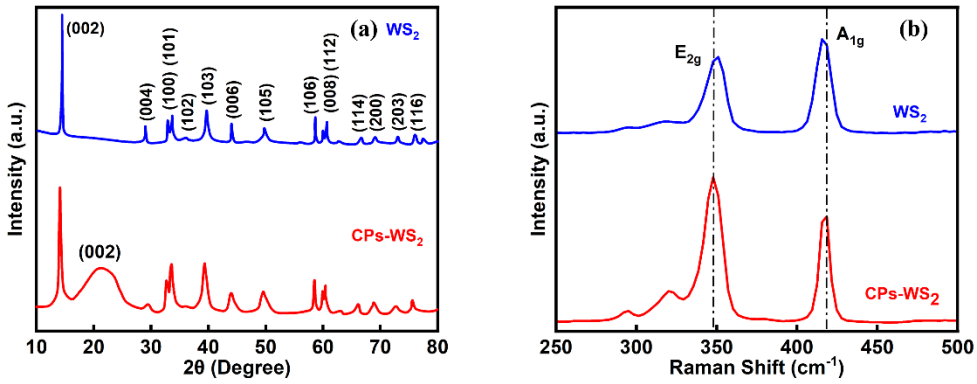


**Figure 5.5.** (a) XRD patterns for $WS_2$ and CPs-$WS_2$, and (b) Raman spectra for $WS_2$ and CPs-$WS_2$.

Similarly, the Raman data show changes in the $WS_2$ spectrum on adding the CPs. The plot recorded for the $WS_2$ is in good agreement with previous reports [37]. However, on forming the composite, a different spectrum was observed, as shown in Fig. 5.5 (b). The ratio of the $E_{2g}/A_{1g}$ peak heights varies from 0.83 for pure $WS_2$ to 1.83 for the CPs-$WS_2$ composite. Furthermore, the position of the $E_{2g}$ peak shifts from 350.9 to 347.5 $cm^{-1}$, while $A_{1g}$ changes from 415.5 to 418.5 $cm^{-1}$ when combined with the CPs. These data clearly show the formation of a new composite that is distinct from the individual components when the CPs and $WS_2$ are combined.

## 5.3.2. Electrochemical Properties and Detection of FLD at GCE/CPs-$WS_2$

Initially, the electrochemical characteristics of the CPs, CPs-DI, and CPs-EtOH combined with the $WS_2$ to give the composites, CPs-$WS_2$, CPs-DI-$WS_2$, and CPs-EtOH-$WS_2$, were monitored in the electrochemical reduction of 100 µM FLD. Peak currents of 8.242, 6.864, and 7.520 µA with peak potentials of −680, −702, and −762 mV were obtained for CPs-$WS_2$, CPs-DI-$WS_2$, and CPs-EtOH-$WS_2$, respectively, using CV measurements. This analysis shows that the CPs-$WS_2$ composite provides not only

the highest peak current but also the most thermodynamically favourable reduction potential. Therefore, CPs-$WS_2$ was selected for all further studies and named as GCE/CPs-$WS_2$ when drop-cast onto the GCE. The drop-casting method was further studied to determine the optimum drop-casting volume and the number of layers of the drop-casting solution. The drop-casting volume was varied from 1 to 10 µL, and the corresponding sensor was evaluated in the electrochemical reduction of 100 µM FLD using CV. The influence of volume is observed in Fig. 5.6 (a), where it is evident that a volume of 5 µL provides optimal coverage of the GCE. This 5 µL volume was subsequently applied repeatedly to the GCE, with drying at room temperature between applications. The summarised data are presented in Fig. 5.6 (b), indicating that a single layer yields the most effective detection of FLD. Consequently, a single application of 5 µL of the CPs-$WS_2$ dispersion was employed throughout all studies.

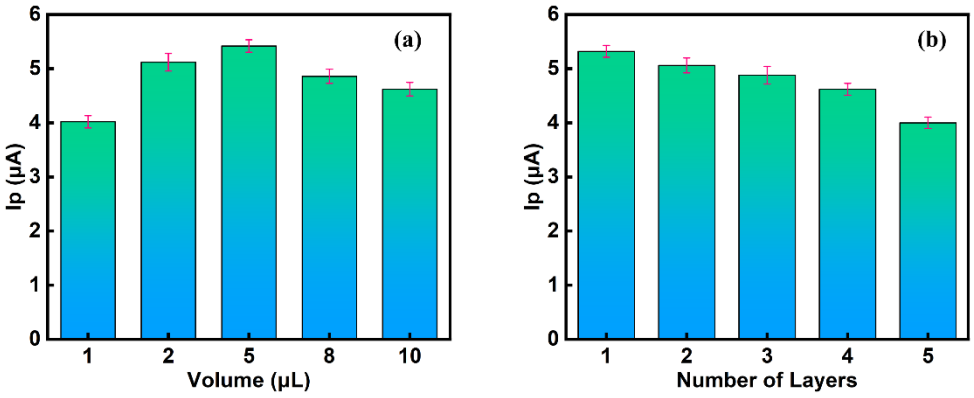


**Figure 5.6.** (a) Influence of the drop casting volume of the CPs-$WS_2$ dispersion, and (b) the number of 5 µL layers applied on the peak current recorded during the reduction of 100 µM FLD.

## 5.3.3. Electrochemical Characteristics

The electrochemical reduction of FLD at the GCE/CPs-$WS_2$-modified sensor was initially studied using CV, and a representative CV recorded at 50 mV $s^{-1}$ is illustrated

in Fig. 5.7 (a). In the absence of the FLD, a low background capacitive current is observed with no evidence of any redox reactions which was deoxygenated with high-purity nitrogen gas for 30 min prior to the electrochemical measurements. On adding 100 µM FLD, a clear reduction wave at −0.68 V, corresponding to the reduction reaction highlighted in Scheme 5.2, occurs, indicating that GCE/CPs-$WS_2$ facilitates the irreversible electrochemical reduction of FLD. These observed peak potential and peak current values provide evidence for the feasibility of FLD detection at the GCE/CPs-$WS_2$.

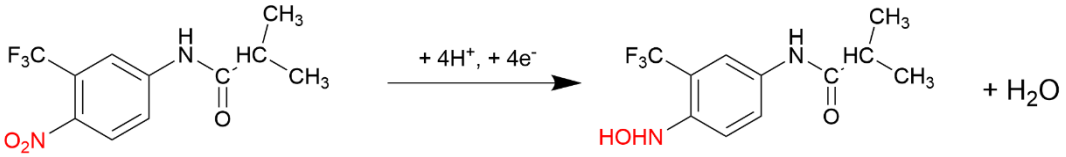


**Scheme 5.2.** Irreversible reduction of FLD, with the reduction of the –$NO_2$ to the –NHOH group with the transfer of $4e^-/4H^+$.

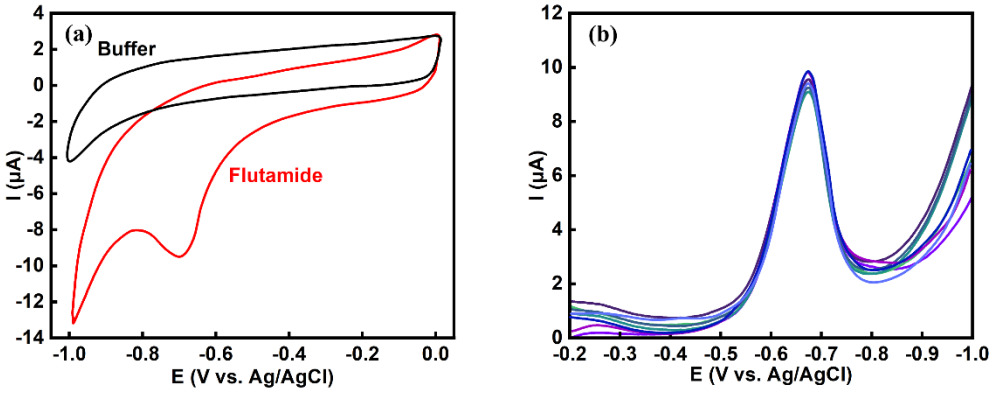


**Figure 5.7.** For typical example recorded by (a) CVs for GCE/CPs-$WS_2$ at pH 7.0 in phosphate buffer in the presence and absence of 100 µM FLD; (b) DPVs for nine repeated experiments by using the same electrode for GCE/CPs-$WS_2$ in 100 µM FLD in phosphate buffer.

The capacitive characteristics of GCE/CPs-$WS_2$ are clearly evident in Fig. 5.7 (a), with the relatively high background capacitive currents for buffer and the FLD in the phosphate buffer. This is consistent with the high surface area morphology of CPs-$WS_2$,

Fig. 5.4. Therefore, in an attempt to reduce the contribution of the background current, DPV was employed as the technique. Representative DPVs, recorded in 100 μM FLD are shown in Fig. 5.7 (b), where the DPV experiments were repeated nine times. More prominent and well-defined peaks are evident, making this a more effective technique in the detection of FLD. The repeatability of the GCE/CPs-$WS_2$ sensor was further examined using DPV, and the reproducibility is displayed in the data in Fig. 5.7 (b). An average peak current of 8.13 μA, with a maximum current of 8.27 μA, was recorded, and the RSD was calculated as 0.90%, indicating very good repeatability. This shows excellent electrode repeatability, which is important in terms of the sensor stability and suggests it could be employed for repeated use.

To determine the independent roles of the CPs and $WS_2$ components of the sensor, the performance of the GCE/CPs-$WS_2$-modified sensor is compared with that of GCE/CPs and GCE/$WS_2$ in Table 5.1. Here, the peak current recorded in 100 μM FLD and the corresponding reproducibility are summarised. While the GCE gives relatively good reproducibility, the peak current is low at 4.1 μA. When the GCE was modified with exfoliated $WS_2$ sheets, where the exfoliation was performed with sonication for 30 min in 0.5 mM tannic acid, a higher peak current was achieved, but the reproducibility was low. Likewise, poor reproducibility with an RSD of 22.48% was achieved with the CPs, possibly due to their agglomeration when exposed to the aqueous solution.

However, when the CPs-$WS_2$ composites were employed, improved reproducibility was seen, and higher peak currents were achieved. It is also evident that the ratio of $WS_2$ to CPs impacts the detection of FLD, with the best detection, in terms of enhanced intra-electrode reproducibility (RSD of 0.90%) and peak current (8.24 μA for 100 μM FLD), was obtained when higher amounts of $WS_2$ were used. The data in Table 1 also show that excellent precision is achieved for GCE/CPs-$WS_2$, with the RSD at 0.90% for three sensors, fabricated on different days. These studies are consistent with a clear interaction between the CPs and the $WS_2$, and they also show that the optimal detection and reproducibility are achieved with the GCE/CPs-$WS_2$ with a loading of 1.0 g $WS_2$

with 10 mL of the CPs.

**Table 5.1** Peak current recorded at 50 mV $s^{-1}$ for 100 μM FLD in 0.1 M PBS with a pH of 7.0 for the various modified electrodes (n = 3).

| Modified electrode | Experiment I current (μA) | Experiment II current (μA) | Experiment III current (μA) | Average current (μA) | RSD (%) |
|---|---|---|---|---|---|
| GCE | 4.109 | 4.096 | 4.116 | 4.107 | 0.25 |
| GCE/ta-$WS_2$ | 6.162 | 5.711 | 5.487 | 5.786 | 5.94 |
| GCE/CPs | 4.755 | 4.304 | 3.012 | 4.023 | 22.48 |
| GCE/CPs-$WS_2$ (0.5 g $WS_2$/ 10 mL CPs) | 7.714 | 7.204 | 6.941 | 7.286 | 5.39 |
| GCE/CPs-$WS_2$ (1.0 g $WS_2$/ 10 mL CPs) | 8.286 | 8.154 | 8.279 | 8.240 | 0.90 |

As shown in Fig. 5.4, the CPs-$WS_2$ provides a high surface area morphology, and accordingly, the surface area of the GCE/CPs-$WS_2$ was estimated using the well-known $[Fe(CN)_6]^{3-/4-}$ probe. CVs were recorded at different scan rates in a 0.1 M NaCl solution with 2.5 mM $[Fe(CN)_6]^{3-/4-}$. Typical CVs recorded for GCE and GCE/CPs-$WS_2$ are shown in Fig. 5.8 (a), where more reversible-like behaviour and higher peak currents are seen with GCE/CPs-$WS_2$ compared with the unmodified GCE.

The peak-to-peak separation was computed as 71 mV for GCE/CPs-$WS_2$ compared to a much higher value of 184 mV for the GCE. This indicates a more efficient electron transfer step in the electrochemical conversion between the $[Fe(CN)_6]^{3-}$ and $[Fe(CN)_6]^{4-}$ ions at GCE/CPs-$WS_2$. The peak currents for the oxidation waves are plotted in Fig. 5.8 (b) as a function of the square root of the scan rate. Good linearity is

achieved, with the linear regression equations deduced as $I_p$ (μA) = 242.06 $v^{1/2}$ ($V^{1/2}$ $s^{-1/2}$) – 19.92, ($R^2$ = 0.9951) for the GCE/CPs-$WS_2$ and $I_p$ (μA) = 128.52 $v^{1/2}$ ($V^{1/2}$ $s^{-1/2}$) – 10.86 ($R^2$ = 0.9964) for the GCE. The Randles–Sevick equation, Eq. 2.2, was employed to estimate the A values. Here, *I*p is the peak current, C represents the concentration of the $[Fe(CN)_6]^{3-/4-}$ probe, D is the diffusion coefficient of the probe, n corresponds to the number of electrons transferred, v gives the scan rate, and A is the electroactive surface area. Using this approach, the A values were estimated as 0.069 ± 0.002 $cm^2$ and 0.130 ± 0.003 $cm^2$ for the GCE and GCE/CPs-$WS_2$, respectively, corresponding to a 1.6-fold increase in the electroactive area on forming the modified GCE/CPs-$WS_2$ electrode.

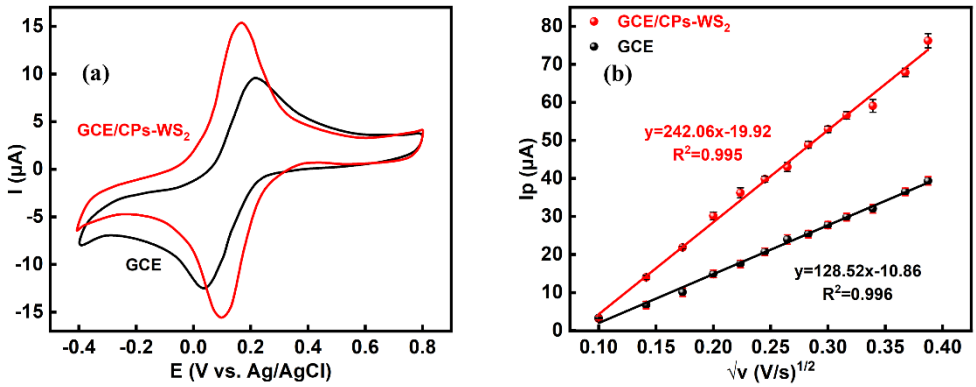


**Figure 5.8.** (a) CVs recorded and (b) peak current plotted vs square root of scan rate for GCE/CPs-$WS_2$ and GCE in 2.5 mM $[Fe(CN)_6]^{3-/4-}$ dissolved in 0.1 M NaCl.

To gain information on the conducting properties of GCE/CPs-$WS_2$ in the presence of FLD, EIS was employed and compared with the GCE. These data were recorded between 100 kHz and 7 mHz using a perturbation potential of 10 mV and are displayed in Fig. 5.9 (a). The plots are characterised by a semicircle at the higher frequencies, with evidence of a diffusional process emerging at 7 mHz. Clearly, GCE/CPs-$WS_2$ has a lower impedance with a smaller semicircle and presents a more conducting interface. In these plots, the symbols indicate the experimental data, while continuous traces represent the simulated profiles. For GCE/CPs-$WS_2$, a simple Randles cell proved

suitable in the fitting of the experimental data. In this case, the circuit consists of a solution resistance term, Rs, in series with a constant phase element, ($Q_{dl}$), and charge transfer resistance ($R_{CT}$), in parallel, Eq. (4.1).

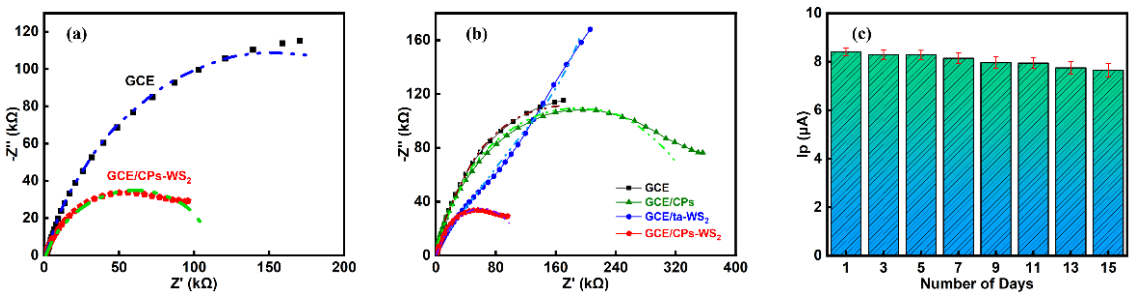


**Figure 5.9.** (a) EIS spectra for GCE and GCE/CPs-$WS_2$ at −0.68 V in buffered 100 μM FLD; (b) EIS spectra recorded for GCE, GCE/CPs, GCE/$WS_2$ and GCE/CPs-$WS_2$ at −0.68 V in 100 μM FLD in phosphate buffer. A Warburg diffusional element was added to the Randles Cell circuit for GCE/ta-$WS_2$. The GCE, GCE/CPs, GCE/CPs-$WS_2$ were all modelled with the Randles Cell, and (c) stability of GCE/CPs-$WS_2$ over 15 days with peak current in 100 μM FLD in phosphate buffer plotted as a function of immersion period in phosphate buffer.

The $R_{CT}$ values were computed as 293 ± 3.0 (n = 3) and 120 ± 6.0 kΩ (n = 3) for the GCE and GCE/CP-$WS_2$, respectively, indicating a more conducting GCE/CPs-$WS_2$. The impedance data recorded for GCE/CPs and GCE/$WS_2$ are shown in Fig. 5.9 (b), where the individual components of the composite have a higher $R_{CT}$, with larger diameters for the depressed semicircles. Indeed, the $R_{CT}$ was determined as 313 ± 10 kΩ (n = 3) for GC/CPs, while GC/$WS_2$ exhibited a clear diffusional term with a Warburg resistance of 505 ± 6 kΩ (n = 3). The enhanced conducting properties of the CPs-$WS_2$ composite are clear from this analysis.

In Fig. 5.9 (c), the overall stability of GCE/CPs-$WS_2$ is summarised. These data were recorded by storing the GCE/CPs-$WS_2$ electrodes in the phosphate buffer at room temperature over a 15-day storage period. The electrodes were removed at different intervals, and the DPVs were recorded in the presence of 100 μM FLD. As shown in

the figure, good long-term stability is achieved. The peak current decreased only slightly from 8.24 to 8.02 μA over the 15-day period, indicating a loss of only 0.95% in the peak current over the 15 days. A similar analysis was performed with 10, 30, and 50 μM FLD, and these data are summarised in Table 5.2. Again, good stability is seen with the RSD over the 15 days computed as 1.38, 1.87, and 5.64% for the 50, 30, and 10 μM FLD, respectively.

**Table 5.2** Peak currents recorded for different concentrations of FLD in 0.1 M phosphate buffer over 15 days (n = 3).

| FLD Concentration (μM) | First Day Average Current (μA) | After 10 days Average Current (μA) | After 15 days Average Current (μA) | %RSD |
|---|---|---|---|---|
| 10 | 2.86 | 2.83 | 2.47 | 5.64 |
| 30 | 4.07 | 4.03 | 3.87 | 1.87 |
| 50 | 5.24 | 5.12 | 5.04 | 1.38 |
| 100 | 8.24 | 8.12 | 8.02 | 0.95 |

## 5.3.4. Influence of the pH and Surface and Diffusional-Controlled Processes

The influence of pH on the electrochemical reduction of FLD is summarised in Fig. 5.10 (a) and (b). The DPV plots show that both the peak current and peak potential are dependent on the pH of the solution. The peak potentials shift from −0.50 to −0.84 V as the pH of the solution is increased from 3.0 to 9.0. It is also evident from Fig. 5.10 (a) that the maximum peak current is seen at a pH of 7.0. The peak current decreases as the pH of the solutions is increased from 7.0 to 9.0 and lowered from 7.0 to 3.0. On plotting the peak potential as a function of pH, a linear plot was achieved with a slope of 0.0541 ± 0.0147 V $pH^{-1}$, which is close to the value predicted from the Nernst

equation at 298 K of 0.0591 V $pH^{-1}$. This is consistent with the reduction mechanism detailed in Scheme 5.2, indicating the transfer of equal numbers of electrons and hydrogen ions. Clearly, the highest peak current is seen at a pH of 7.0, and this was chosen for all the electroanalytical studies, including sensitivity and selectivity studies.

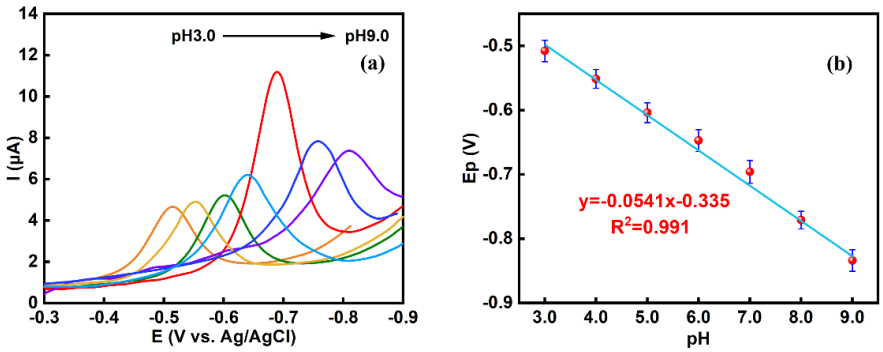


**Figure 5.10.** (a) DPVs for 100 μM FLD at pH values of 3.0, 4.0, 5.0, 6.0, 7.0, 8.0, and 9.0; (b) plot of peak potential, Ep, as a function of pH.

Another important parameter in the reduction of FLD at the GCE/CPs-$WS_2$ is the way the FLD reaches and interacts with the electrode surface. Therefore, to determine if the reduction of FLD was under diffusion or adsorption control, scan rate studies were performed, and the resulting CV curves are shown in Fig. 5.11 (a). The capacitive behaviour of the GCE/CPs-$WS_2$ is evident in these CVs. As the scan rate is increased, the peak current increases. There is no indication that the peak potential shifts to lower potentials with increasing scan rates, which is indicative of sluggish electron transfer reactions. Instead, the peak potentials remain relatively constant. In Fig. 5.11 (b), the peak current is shown plotted against the square root of the scan rate, consistent with Eq. (3.4), corresponding to a diffusion-controlled process for an irreversible process.

Here nα is the number of electrons transferred prior to and including the rate-determining step. A linear plot was obtained with a regression equation, $I_p$ (μA) = 44.29 $v^{1/2}$ ($V^{1/2}$ $s^{-1/2}$) – 1.808 ($R^2$ = 0.9922), which is consistent with a diffusion-controlled reduction of FLD. However, a linear plot $I_p$ (μA) = 100.3 $v$ (V $s^{-1}$) + 2.61, ($R^2$ = 0.9894)

was also obtained when the peak current was plotted as a function of scan rate, consistent with adsorption control, Eq. (5.1). In this adsorption relationship, F, R, and T have their usual meanings, α is the charge transfer coefficient, A represents the surface area, and τ* corresponds to the surface-bound redox couple.

$$I_p = \frac{F}{RT}\frac{\alpha F A \tau^*}{2.718} v \qquad \textbf{(5.1)}$$

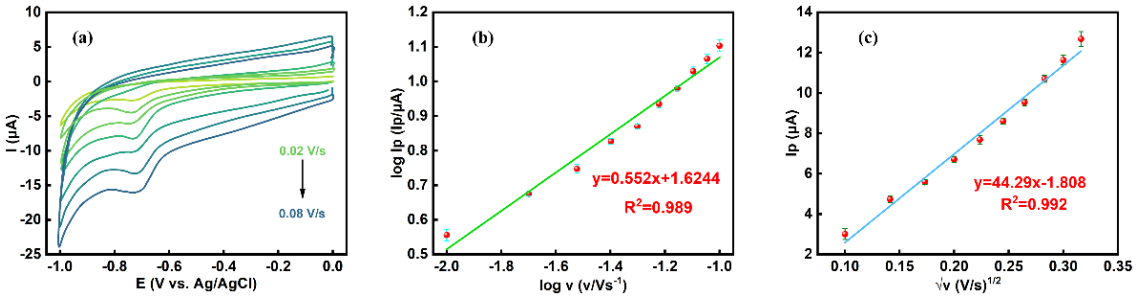


**Figure 5.11.** (a) CV curves at different scan rates in a 100 μM FLD solution, pH of 7.0; (b) logarithm of the peak current plotted as a function of the logarithm of the scan rate for 100 μM FLD in phosphate buffer, and (c) peak current, $I_p$, plotted as a function of the square root of the scan rate ($v$).

To clearly distinguish between these two processes, the logarithm of the peak current was plotted against the logarithm of the scan rate. A linear equation of log $I_p$ ($I_p$/μA) = 0.552 log $v$ ($v$/V $s^{-1}$) + 1.624, ($R^2$ = 0.9894) was obtained. The slope of this plot at approximately 0.5 clearly indicates a diffusion-controlled reduction reaction.

## 5.3.5. Sensing Performance

The performance of GCE/CPs-$WS_2$ in the sensing of FLD was evaluated using a combination of sensitivity, selectivity, and real sample analyses. In Fig. 5.12 (a), the DPVs recorded as a function of the concentration of FLD in phosphate buffer are shown, while the DPVs obtained in 1, 5, 10, 20, and 30 nM FLD are provided in Fig. 5.12 (b).

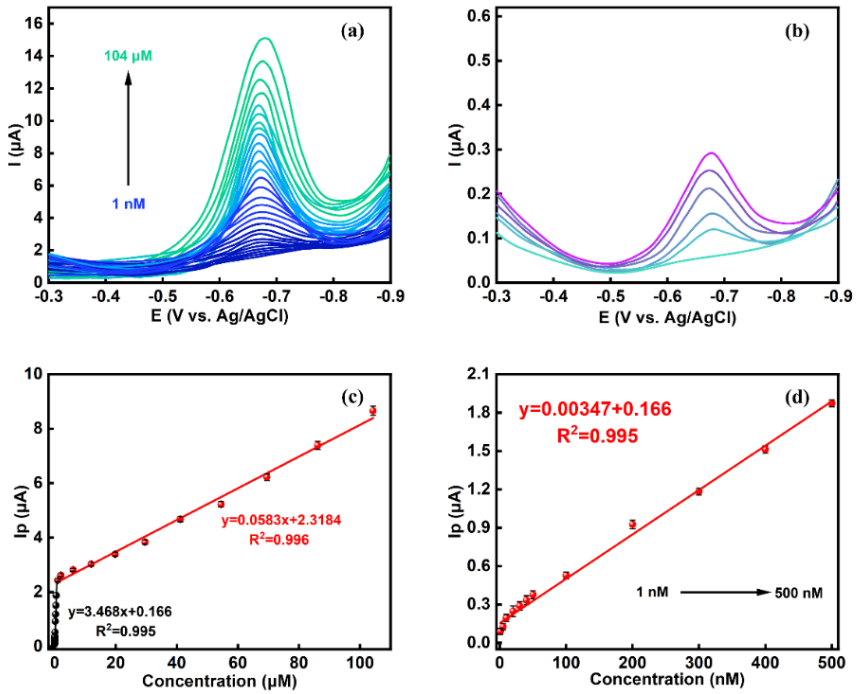


**Figure 5.12.** (a) DPVs for concentrations from 1 nM to 104 µM, (b) DPVs recorded for FLD concentrations of 1 nM, 5 nM, 10 nM, 20 nM and 30 nM (blue trace without a peak is the background electrolyte); (c) calibration curve with the DPV peak current shown against the FLD concentration, and (d) Calibration curve plotted with the DPV peak currents against the FLD concentration from 1 nM to 500 nM (n = 3).

As the FLD has a limited solubility in water, the highest concentration employed in this analysis was 104 µM. As shown in Fig. 5.12 (a), the peak current increases with increasing FLD concentrations. The peak potential shifts slightly to more negative values from −674 mV at 20 nM FLD to −688 mV for 104 µA. However, the most significant aspect of this composite is the well-defined reduction wave obtained at a FLD concentration of 1 nM, Fig. 5.12 (b), making this sensor suitable for the sensing of nM concentrations of FLD.

The peak currents from the DPVs were plotted as a function of the concentration of the FLD to give the calibration curve, as depicted in Fig. 5.12 (c). Two linear regions are

seen. The linear calibration curve equation, $I_p$ (μA) = 0.0583 C (μM) + 2.3184 ($R^2$ = 0.9960), was obtained for concentrations ranging from 1 to 104 μM. For lower concentrations extending from 1 to 500 nM, shown in the inset and in Fig. 5.12 (d), the linear regression equation, $I_p$ (μA) = 3.468 C (μM) + 0.166 ($R^2$ = 0.9950), was achieved. Using the well-known expression for the limit of detection (LOD), where the LOD = 3σ/sensitivity, the LOD was calculated as 0.74 nM, using the lower concentration linear range.

This agrees well with the distinct peak response observed for 1.0 ± 0.531 nM (n = 9) FLD in Fig. 5.12(b). In both cases, the peak is clearly separated from the background and remains well shaped, which confirms that FLD can be detected with good definition at this low concentration. The sensitivity was computed as 26.7 μA $\mu M^{-1}$ $cm^{-2}$ using the estimated electroactive surface area of 0.130 $cm^2$ for the GCE/CPs-$WS_2$ and the lower concentration range from 1 to 500 nM. These analytical characteristics are compared with some of the recently reported sensors for FLD in Table 5.3.

The linear range is similar to many of these previously reported sensors. However, the LOD is considerably lower than many of these reports, while the high sensitivity of 26.7 ± 0.7 μA $\mu M^{-1}$ $cm^{-2}$ is a clear benefit in the detection of the lower nM concentrations. Furthermore, the well-defined reduction wave observed for a 1 nM concentration, Fig. 5.12 (b), is an obvious advantage of this GCE/CPs-$WS_2$ material in the detection of low concentrations of FLD.

**Table 5.3** Comparison of GCE/CPs-$WS_2$ with Recently Reported Sensors for FLD.

| Sensor | Method | Linear range (μA) | LOD (nM) | Sensitivity (μA $\mu M^{-1}$ $cm^{-2}$) | Refs. |
|---|---|---|---|---|---|
| GCE/CPs-$WS_2$ | DPV | 0.001–104 | 0.74 | 26.7 | this work |
| GCE/$CaMoO_4$/$MoO_3$ | *I–t* | 0.0449– | 1.6 | 53.34 | [25] |

| | | | | | |
|---|---|---|---|---|---|
| | | 1184 | | | |
| MoW–P/RGO | DPV | 0.3–1152 | 9 | 0.50 | [38] |
| $BiVO_4$rGO/CE-BN/GCE | DPV | 0.04–102 | 11 | 3.80 | [39] |
| Sr@FeNi–S/GnRbs | | 0.020–0.450 | 20 | | [40] |
| ZnO–$Co_3O_4$@$C_3N_4$ | DPV | 0.01–98.6 | 3.7 | 5.33 | [27] |
| Sn–ZnO/rGO | DPV | 0.01–170 | 7.3 | 14.10 | [41] |
| AuNP@rGO/PPyNT | DPV | 0.01–1214 | 2.5 | 50.06 | [42] |
| GOS/$CaTiO_3$ | *I–t* | 0.015–1184 | 5.7 | 1.073 | [30] |
| β-$Cu_2V_2O_7$/PC | *I–t* | 0.01–2.11 | 0.62 | 24.33 | [43] |
| $MoS_2$–CeZrO | DPV | 0.019–668 | 5 | 0.353 | [44] |

The selectivity of GCE/CPs-$WS_2$ was studied using ions that are commonly found in real water samples. For these studies, 1 mM of the interferent was added to 100 μM FLD to give a 10-fold interferent concentration. The ratio of the peak current obtained for the pure 100 μM FLD to the 100 μM FLD with 1 mM interferent was calculated, and these data are summarized in Fig. 5.13 (a). The addition of these ions has little effect on the detection of FLD, with the ratio of the peak currents, remaining very close to unity. The selectivity of the GCE/CPs-$WS_2$ sensor was probed further using real water samples, collected from the local canal in Maynooth, and artificial urine samples. The results from these studies are summarized in Table 5.4. The recovery varies from 90.2 to 98.8% for tap water, 88.5 to 95.0% for canal water, and 89.5 to 96.8% for the artificial urine samples. The highest RSD values were 3.70% for tap water, 5.27% for canal water, and 5.70% for the artificial urine at the lower concentrations of 10 μM FLD. These data show acceptable recovery in all the real samples.

**Table 5.4** Comparison Table of Different Analysis Samples for Flutamide.

| Samples | | Added drug FLD (μM) | Recovery (%) |
|---|---|---|---|
| Water analysis | Tap water | 10 | 90.2 |
| | | 30 | 94.6 |
| | | 50 | 97.3 |
| | | 100 | 98.8 |
| | Canal/River water | 10 | 88.5 |
| | | 30 | 91.1 |
| | | 50 | 94.5 |
| | | 100 | 95.0 |
| Biological analysis | Artificial urine | 10 | 89.5 |
| | | 30 | 92.7 |
| | | 50 | 95.4 |
| | | 100 | 96.8 |

To explore further the versatility of the CPs-$WS_2$ dispersions, SPE were modified with these dispersions, and a standard addition method was used with both tap water and the canal/river water samples. The CPs-$WS_2$ dispersions were applied to the SPE and processed using the optimized method developed for the GCE. The water sample was initially spiked with 10 μM FLD to form the FLD sample. Further additions of FLD were then added, and the DPVs were recorded to determine the peak currents. These data are shown in Fig. 5.13 (b). The linear regression equations were determined as $I_p$ (μA) = 0.116 C (μM) + 1.24 ($R^2$ = 0.9978) for the tap water and $I_p$ (μA) = 0.094 C (μM) + 1.27 ($R^2$ = 0.9984) for the canal water samples.

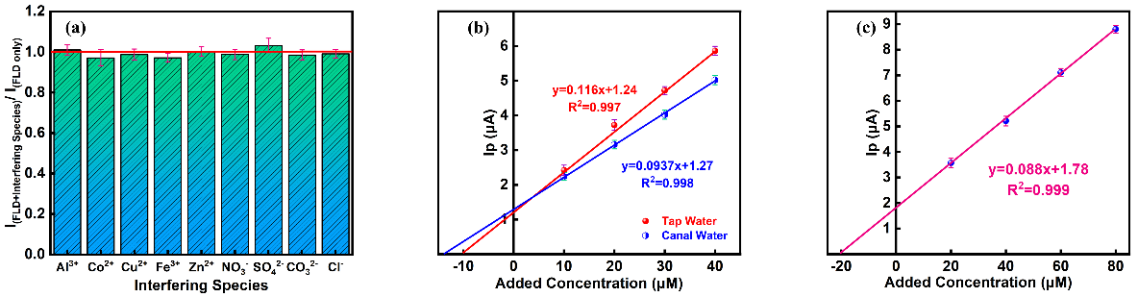


**Figure 5.13.** (a) ratio of peak current with and without the interferent for 100 μM FLD and 1 mM interferent; (b) standard addition method for the analysis of tap and river water samples spiked with FLD using screen-printed electrodes (SPE/CPs-$WS_2$), and (c) Standard addition method using deionised water, illustrating the accuracy of the GCE/CPs-$WS_2$ sensor, with 20 μM FLD added before the standard additions were made.

The concentration of the initial FLD sample was determined as 10.6 μM, giving an error of 6%, for the tap water sample, indicating acceptable detection in this aquatic system. However, the FLD was computed at a concentration of 13.5 μM for the canal water sample, indicating that the presence of contaminants, such as microbiological matters, nutrients, suspended solids, sediment-associated pollutants and organic pollution, in the real water sample may contribute to making the detection of FLD more complex. This can also be seen in the linear plots, with the gradients varying from 0.116 μA $\mu M^{-1}$ for the tap water to 0.094 μA $\mu M^{-1}$ for the canal water samples.

The accuracy of the GCE/CPs-$WS_2$ sensor was evaluated using the standard addition method with deionised water as the aqueous component. A known concentration of FLD was added to the sample, standard additions were made, and the computed concentration from the linear plot was compared with the known concentration added. A typical plot is shown in Fig. 5.13 (c), where the known concentration of FLD was 20 μM. Using the linear plot, the concentration was computed as 20.2 μM, corresponding to a 1% error, indicating very good accuracy.

## 5.4 Conclusions

In this study, GCE/CPs-$WS_2$ can serve as a highly sensitive and selective sensor for the electrochemical analysis of FLD. The key novelty lies in (i) the first direct application of a CPs-$WS_2$ composite to FLD electroanalysis, and (ii) a clear synergetic effect is seen between the $WS_2$ and CPs as their sizes and dimensions facilitate these interactions, and this results in a high surface area and conducting material, suitable for electrochemical-based applications. The CPs-$WS_2$ formation is corroborated by SEM, XRD and Raman signatures, alongside electrochemical evidence of enhanced interfacial kinetics.

While prior FLD sensors primarily rely on metal-oxide or graphene-derived platforms, the CPs-$WS_2$ interface achieves a competitive nanomolar detection capability with a clearly defined peak at 1 nM FLD, a calculated LOD of 0.74 nM, and high sensitivity normalised by electroactive area. The composite outperforms CPs or $WS_2$ only modifiers by combining improved charge transfer with an increased electroactive surface area. Importantly, the platform maintains operational stability over 15 days and delivers acceptable recoveries in tap water, canal water, and artificial urine, demonstrating practical robustness beyond idealised buffer conditions. Transferability to screen-printed electrodes further supports deployment-oriented potential.

This work answers whether a rationally engineered $WS_2$ carbon materials composite interface can generate synergistic conductivity and accessible active area sufficient to enable reliable nanomolar FLD detection. The results confirm that the size-matched CPs-$WS_2$ hybrid provides the required synergy, yielding well-resolved FLD reduction responses with impressive stability, very good selectivity, sensitivity, and acceptable recovery in complex canal water and artificial urine samples.

# References

[1] A. Molla and J. H. Youk, “Recent progress on electroanalytical sensing of small molecules and biomolecules using carbon dots: A review,” *Journal of Industrial and Engineering Chemistry*, vol. 127, pp. 62–81, Jul. 2023, doi: 10.1016/j.jiec.2023.07.037.

[2] E. Asadian, M. Ghalkhani, and S. Shahrokhian, “Electrochemical sensing based on carbon nanoparticles: A review,” *Sensors and Actuators B Chemical*, vol. 293, pp. 183–209, Apr. 2019, doi: 10.1016/j.snb.2019.04.075.

[3] Y. Yan, J. Gong, J. Chen, Z. Zeng, W. Huang, K. Pu, J. Liu, and P. Chen et al., “Recent advances on graphene quantum dots: From chemistry and physics to applications,” *Advanced Materials*, vol. 31, no. 21, p. e1808283, Mar. 2019, doi: 10.1002/adma.201808283.

[4] S. K. Krishnan, E. Singh, P. Singh, M. Meyyappan, and H. S. Nalwa, “A review on graphene-based nanocomposites for electrochemical and fluorescent biosensors,” *RSC Advances*, vol. 9, no. 16, pp. 8778–8881, Jan. 2019, doi: 10.1039/c8ra09577a.

[5] V. Schroeder, S. Savagatrup, M. He, S. Lin, and T. M. Swager, “Carbon Nanotube Chemical sensors,” *Chemical Reviews*, vol. 119, no. 1, pp. 599–663, Sep. 2018, doi: 10.1021/acs.chemrev.8b00340.

[6] C. B. Breslin, D. Branagan, and L. M. Garry, “Electrochemical detection of Cr(VI) with carbon nanotubes decorated with gold nanoparticles,” *Journal of Applied Electrochemistry*, vol. 49, no. 2, pp. 195–205, Oct. 2018, doi: 10.1007/s10800-018-1259-2.

[7] D. Branagan and C. B. Breslin, “Electrochemical detection of glucose at physiological pH using gold nanoparticles deposited on carbon nanotubes,” *Sensors and Actuators B Chemical*, vol. 282, pp. 490–499, Nov. 2018, doi: 10.1016/j.snb.2018.11.089.

[8] G. Collins, P. R. Kasturi, R. Karthik, J.-J. Shim, R. Sukanya, and C. B. Breslin, “Mesoporous carbon-based materials and their applications as non-precious metal electrocatalysts in the oxygen reduction reaction,” *Electrochimica Acta*, vol. 439, p. 141678, Dec. 2022, doi: 10.1016/j.electacta.2022.141678.

[9] T. Gao, W. Luo, Y. Yang, Y. Zhou, J. Xu, N. Li, J. Li, and Z. Liu, “Engineering hierarchically porous carbon nanorods electrode materials for high performance zinc ion hybrid supercapacitors,” *Colloids and Surfaces a Physicochemical and Engineering Aspects*, vol. 684, p. 133057, Dec. 2023, doi: 10.1016/j.colsurfa.2023.133057.

[10] H. Qi, M. Teng, M. Liu, S. Liu, J. Li, H. Yu, C. Teng, Z. Huang, H. Liu, Q. Shao, A. Umar, and T. Ding, “Biomass-derived nitrogen-doped carbon quantum dots: highly selective fluorescent probe for detecting Fe3+ ions and tetracyclines,” *Journal of Colloid and Interface Science*, vol. 539, pp. 332–341, Dec. 2018, doi: 10.1016/j.jcis.2018.12.047.

[11] A. Padmapriya, P. Thiyagarajan, M. Devendiran, R. A. Kalaivani, and A. M. Shanmugharaj, “Electrochemical sensor based on N,P–doped carbon quantum

dots derived from the banana flower bract (Musa acuminata) biomass extract for selective and picomolar detection of dopamine," *Journal of Electroanalytical Chemistry*, vol. 943, p. 117609, Jun. 2023, doi: 10.1016/j.jelechem.2023.117609.

[12] E. Blanco, L. Hristova, R. Martínez-Moro, L. Vázquez, G. J. Ellis, L. Sánchez, M. del Pozo, M. D. Petit-Domínguez, E. Casero and, C. Quintana, "A 2D tungsten disulphide/diamond nanoparticles hybrid for an electrochemical sensor development towards the simultaneous determination of sunset yellow and quinoline yellow," *Sensors and Actuators B Chemical*, vol. 324, p. 128731, Aug. 2020, doi: 10.1016/j.snb.2020.128731.

[13] R. Sukanya, D. C. Da Silva Alves, and C. B. Breslin, "RevIew—Recent Developments in the applications of 2D transition metal dichalcogenides as electrocatalysts in the generation of hydrogen for renewable energy conversion," *Journal of the Electrochemical Society*, vol. 169, no. 6, p. 064504, May 2022, doi: 10.1149/1945-7111/ac7172.

[14] D. Alves, P. R. Kasturi, G. Collins, T. N. Barwa, S. Ramaraj, R. Karthik, and C. B. Breslin, "2D layered double hydroxides and transition metal dichalcogenides for applications in the electrochemical production of renewable hydrogen," *Materials Advances*, vol. 4, no. 24, pp. 6478–6497, Jan. 2023, doi: 10.1039/d3ma00685a.

[15] Y. Luo, T. N. Barwa, K. Herdman, E. Dempsey, and C. B. Breslin, "Elect roanalysis of metronidazole using exfoliated MoS2 sheets and electrodeposi ted amorphous $MoS_x$," *Electrochimica Acta*, vol. 462, p. 142778, Jun. 202 3, doi: 10.1016/j.electacta.2023.142778.

[16] Y. Luo, T. N. Barwa, E. Dempsey, R. Karthik, J. J. Shim, R. Sukanya, and C. B. Breslin, "Electrochemical detection of sulfanilamide using tannic acid exfoliated MoS2 nanosheets combined with reduced graphene oxide/graphite," *Environmental Research*, vol. 248, p. 118391, Feb. 2024, doi: 10.1016/j.envres.2024.118391.

[17] K. Abid, D. Iannazzo, C. Celesti, A. Khaskhoussi, A. Foti, R. Maalej, P. G. Gucciardi, and G. Neri, "A novel 2D-GO@$WS_2$ electrochemical platform for the determination of thiram fungicide," *Journal of Environmental Sciences*, vol. 136, pp. 226–236, Dec. 2022, doi: 10.1016/j.jes.2022.11.018.

[18] F. Mashkoor, R. Mashkoor, M. Shoeb, A. H. Anwer, H. Jeong, and C. Jeong, "Freestanding WS2-MWCNT Nanocomposite for Electrochemical Detection of Contaminants of Emerging Concern─Perfluorooctanoic Acid 'A Forever Chemical' and Supercapacitor applications," *ACS Sustainable Chemistry & Engineering*, vol. 11, no. 36, pp. 13306–13319, Aug. 2023, doi: 10.1021/acssuschemeng.3c02376.

[19] G. Jeevanandham, G. P. Kuppuswamy, D. C. Sesu, and K. Vediappan, "Screen printed carbon electrode modified with $WS_2$ nanosheet incorporated with cobalt oxide for non-enzymatic detection of lactic acid," *Surfaces and Interfaces*, vol. 40, p. 103097, Jun. 2023, doi: 10.1016/j.surfin.2023.103097.

[20] E. D. Crawford, P. F. Schellhammer, D. G. McLeod, J. W. Moul, C. S. Higano, N. Shore, L. Denis, P. Iversen, M. A. Eisenberger, and F. Labrie, "Androgen Receptor Targeted Treatments of Prostate Cancer: 35 Years of Progress with Antiandrogens,"

*The Journal of Urology*, vol. 200, no. 5, pp. 956–966, May 2018, doi: 10.1016/j.juro.2018.04.083.

[21] N. F. Goodman, R. H. Cobin, W. Futterweit, J. S. Glueck, R. S. Legro, and E. Carmina, "American Association of Clinical Endocrinologists, American College of Endocrinology, and Androgen Excess and PCOS Society Disease State Clinical Review: Guide to the Best Practices in the Evaluation and Treatment of Polycystic Ovary Syndrome - Part 1," *Endocrine Practice*, vol. 21, no. 11, pp. 1291–1300, Oct. 2015, doi: 10.4158/ep15748.dsc.

[22] T. I. A. Gouveia, I. H. Mota, A. M. T. Silva, A. Alves, and M. S. F. Sa ntos, "Are cytostatic drugs in surface waters a potential threat?," *The Scie nce of the Total Environment*, vol. 853, p. 158559, Sep. 2022, doi: 10.101 6/j.scitotenv.2022.158559.

[23] H. Bhatia, A. Kumar, Y. Ogino, J. Du, A. Gregg, J. Chapman, M. J. Mclaughlin, and T. Iguchi, "Effects of the commercial antiandrogen flutamide on the biomarkers of reproduction in male Murray rainbowfish (Melanotaenia fluviatilis)," *Environmental Toxicology and Chemistry*, vol. 33, no. 5, pp. 1098–1107, Jan. 2014, doi: 10.1002/etc.2524.

[24] Z. Fathi, S. Jahani, and M. M. Foroughi, "Electrode material fabricated by doping holmium in nickel oxide and its application in electrochemical sensor for flutamide determination as a prostate cancer drug," *Monatshefte Für Chemie - Chemical Monthly*, vol. 152, no. 7, pp. 757–766, Jul. 2021, doi: 10.1007/s00706-021-02794-8.

[25] N. Nataraj, T.-W. Chen, S.-M. Chen, T. Kokulnathan, F. Ahmed, T. Alshahrani, and N. Arshi, "Electrochemical detection of anti-cancer drug flutamide in biological fluids with calcium molybdate/molybdenum oxide as an effective electrocatalyst," *Journal of the Taiwan Institute of Chemical Engineers*, vol. 156, p. 105348, Jan. 2024, doi: 10.1016/j.jtice.2024.105348.

[26] R. K. Devi, G. Muthusankar, S.-M. Chen, and G. Gopalakrishnan, "In situ formation of $Co_3O_4$ nanoparticles embedded N-doped porous carbon nanocomposite: a robust material for electrocatalytic detection of anticancer drug flutamide and supercapacitor application," *Microchimica Acta*, vol. 188, no. 6, p. 196, May 2021, doi: 10.1007/s00604-021-04860-8.

[27] N. Umesh, J. Antolin Jesila, S.-F. Wang, M. Govindasamy, R. A. Alshgari, M. Ouladsmane, and I. V. Asharani, "Fabrication of highly sensitive anticancer drug sensor based on heterostructured ZnO-$Co_3O_4$ capped on carbon nitride nanomaterials," *Microchemical Journal*, vol. 167, p. 106244, Apr. 2021, doi: 10.1016/j.microc.2021.106244.

[28] L. Durai, A. Gopalakrishnan, and S. Badhulika, "A low-cost and facile electrochemical sensor for the trace-level recognition of flutamide in biofluids using large-area bimetallic NiCo2O4 micro flowers," *New Journal of Chemistry*, vol. 46, no. 7, pp. 3383–3391, Jan. 2022, doi: 10.1039/d1nj05246b.

[29] T. Ravele, N. W. Hlongwa, T. T. I. Nkambule, N. N. Gumbi, and K. E. Sekhosana, "Electrochemical Sensors Based on Manganese and Cobalt Oxide Nanostructures for the Detection of Flutamide and its Derivatives in Real Water Samples," *Journal*

*of Cluster Science*, vol. 35, no. 1, pp. 285–297, Jul. 2023, doi: 10.1007/s10876-023-02474-z.

[30] T.-W. Tseng, U. Rajaji, T.-W. Chen, S.-M. Chen, Y.-C. Huang, V. Mani, and A. Irudaya Jothi, "Sonochemical synthesis and fabrication of perovskite type calcium titanate interfacial nanostructure supported on graphene oxide sheets as a highly efficient electrocatalyst for electrochemical detection of chemotherapeutic drug," *Ultrasonics Sonochemistry*, vol. 69, p. 105242, Jul. 2020, doi: 10.1016/j.ultsonch.2020.105242.

[31] R. Atchudan, T. N. J. I. Edison, S. Perumal, R. Vinodh, A. K. Sundramoorthy, R. S. Babu, and Y. R. Lee, "Leftover kiwi fruit Peel-Derived carbon dots as a highly selective fluorescent sensor for detection of ferric ion," *Chemosensors*, vol. 9, no. 7, p. 166, Jul. 2021, doi: 10.3390/chemosensors9070166.

[32] N. Murugan, M. Prakash, M. Jayakumar, A. Sundaramurthy, and A. K. Sundramoorthy, "Green synthesis of fluorescent carbon quantum dots from Eleusine coracana and their application as a fluorescence 'turn-off' sensor probe for selective detection of $Cu^{2+}$," *Applied Surface Science*, vol. 476, pp. 468–480, Jan. 2019, doi: 10.1016/j.apsusc.2019.01.090.

[33] M. Chakraborty, I. Mitra, K. Sarkar, M. Bardhan, S. Paul, S. Basu, and T. Ganguly, "Fluorescence enhancement via aggregation effect due to microenvironmental alterations in human hemoglobin protein in presence of carbon quantum dots (CQD): Comparative spectroscopic approach," *Spectrochimica Acta Part a Molecular and Biomolecular Spectroscopy*, vol. 215, pp. 313–326, Feb. 2019, doi: 10.1016/j.saa.2019.02.108.

[34] N. Murugan, M. Prakash, M. Jayakumar, A. Sundaramurthy, and A. K. Sundramoorthy, "Green synthesis of fluorescent carbon quantum dots from Eleusine coracana and their application as a fluorescence 'turn-off' sensor probe for selective detection of $Cu^{2+}$," *Applied Surface Science*, vol. 476, pp. 468–480, Jan. 2019, doi: 10.1016/j.apsusc.2019.01.090.

[35] H. Ham, N.-H. Park, S. S. Kim, and H. W. Kim, "Evidence of Ostwald ripening during evolution of micro-scale solid carbon spheres," *Scientific Reports*, vol. 4, no. 1, p. 3579, Jan. 2014, doi: 10.1038/srep03579.

[36] A. Verma, A. Singh, P. Chaudhary, R. K. Tripathi, B. C. Yadav, P. Chauhan, and D. Kumar, "Photocurrent conversion capability of a 2D $WS_2$-polyvinyl alcohol matrix and its DFT-based charge carrier dynamics analysis," *Materials Advances*, vol. 4, no. 4, pp. 1062–1074, Jan. 2023, doi: 10.1039/d2ma00962e.

[37] J. P. Hughes, F. D. Blanco, C. E. Banks, and S. J. Rowley-Neale, "Mass-producible 2D-$WS_2$ bulk modified screen printed electrodes towards the hydrogen evolution reaction," *RSC Advances*, vol. 9, no. 43, pp. 25003–25011, Jan. 2019, doi: 10.1039/c9ra05342e.

[38] N. Karuppusamy, S. Subburaj, S. M. Chen, P. Veerakumar, K.-Y. Lin, and S. Meenakshi, "Determination of flutamide toward a real-time electrochemical sensor based on ultrathin reduced graphene oxide-covered MoW-P," *New Journal of Chemistry*, vol. 47, no. 40, pp. 18671–18681, Jan. 2023, doi: 10.1039/d3nj02800c.

[39] C. Bhuvaneswari, K. Palpandi, B. Amritha, P. Paunkumar, R. Lakshmi Priya, N. Raman, S. Ganesh Babu, "Conniving for the first time of $BiVO_4$ – rGO/CE-BN and its potential as enhanced electrochemical sensing of non-steroidal anti-androgen drug," *Microchemical Journal*, vol. 184, p. 108174, Nov. 2022, doi: 10.1016/j.microc.2022.108174.

[40] A. S. Santhosh, K. M. Sahana, S. Sandeep, P. N. Prashanth Kumar, N. S. Alsaiari, K. M. Katubi, K. M. Abualnaja, and J. R. Rajabathar, "Synthesis and application of a 0D/2D nanocomposite for the nanomolar level detection of an antiandrogen drug," *New Journal of Chemistry*, vol. 46, no. 33, pp. 16068–16077, Jan. 2022, doi: 10.1039/d2nj01967a.

[41] K.-Y. Hwa, A. Santhan, and S. K. S. Tata, "Fabrication of Sn-doped ZnO hexagonal micro discs anchored on rGO for electrochemical detection of anti-androgen drug flutamide in water and biological samples," *Microchemical Journal*, vol. 160, p. 105689, Nov. 2020, doi: 10.1016/j.microc.2020.105689.

[42] A. Sangili, V. Vinothkumar, S.-M. Chen, P. Veerakumar, and K.-C. Lin, "Gold Nanoparticle Embedded on a Reduced Graphene Oxide/polypyrrole Nanocomposite: Voltammetric Sensing of Furazolidone and Flutamide," *Langmuir*, vol. 36, no. 46, pp. 13949–13962, Nov. 2020, doi: 10.1021/acs.langmuir.0c02448.

[43] S. M. Babulal, J. Anupriya, and S. M. Chen, "Self assembled three dimensional β-$Cu_2V_2O_7$ hierarchical flower decorated porous carbon: An efficient electrocatalyst for flutamide detection in biological and environmental samples," *Chemosphere*, vol. 303, no. Pt 3, p. 135203, Jun. 2022, doi: 10.1016/j.chemosphere.2022.135203.

[44] S. V. Selvi, N. Nataraj, T.-W. Chen, S. M. Chen, S. Nagarajan, C. S. Ko, T.-W. Tseng, and C.-C. Huang, "In-situ formation of 2H phase $MoS_2$/cerium-zirconium oxide nanohybrid for potential electrochemical detection of an anticancer drug flutamide," *Materials Today Chemistry*, vol. 23, p. 100749, Jan. 2022, doi: 10.1016/j.mtchem.2021.100749.

# **Chapter 6** Electrochemical Detection of Sulfamerazine (SRZ) with $WS_2$ sheets and $ZnMn_2O_4$ spinel spheres decorated with $CeO_2$ nano-powders

# 6.1. Introduction

Metal-oxide-based electrochemical sensors are attractive for such tasks owing to their stability, accessible active sites and favourable charge-transport characteristics [1-4]. Within this class, the spinel $ZnMn_2O_4$ (ZMO) couples abundant redox-active centres with semiconductor behaviour and high surface area [5-8], while cerium oxide ($CeO_2$) contributes redox buffering and antifouling attributes relevant to environmental sensing [4,6,9-11]. Two-dimensional $WS_2$, a layered transition-metal dichalcogenide, offers edge-rich sheets that enable interfacial electron transfer and integrate effectively with oxide scaffolds [12-14]. For SRZ, a representative sulfonamide, is routinely administered in veterinary and agricultural settings and is increasingly detected in natural waters, underscoring the need for sensitive on-site electroanalysis in complex matrices [15-17]. Yet, despite progress with ZMO composites in energy and sensing, a ZMO-$CeO_2$ framework augmented by exfoliated $WS_2$ has not, to our knowledge, been applied to sulfamerazine (SRZ) electroanalysis.

This chapter reports a hierarchical $CeO_2$-ZMO/$WS_2$ composite as an electrocatalytic interface for SRZ determination with glassy carbon (GCE) and screen-printed carbon electrodes (SPE) as supports. $CeO_2$ and ZMO are synthesised separately, combined to form a uniformly $CeO_2$ coating over ZMO spheres, and subsequently decorated with size-matched $WS_2$ sheets obtained by surfactant-assisted exfoliation. We establish morphology and composition by SEM/EDX, FTIR and XPS, quantify electroactive area and interfacial kinetics with the $[Fe(CN)_6]^{3-/4-}$ probe and electrochemical impedance spectroscopy, and then optimise operational parameters (supporting electrolyte, pH, and pre-accumulation conditions) to maximise the SRZ response.

Analytical evaluation employs cyclic voltammetry and differential-pulse voltammetry in phosphate buffer near neutral pH, with attention to adsorption-controlled kinetics,

peak-potential/pH relationships, and calibration behaviour over low- and mid-μM ranges. Selectivity is assessed against common inorganic ions and structurally related drugs, and practical performance is demonstrated by recoveries in spiked tap and canal water as well as artificial urine. In parallel, we compare GCE and SPE substrates to highlight portability and fabrication versatility. The resulting architecture is designed to merge (i) ZMO-mediated catalytic activity, (ii) $CeO_2$-enabled stability and resistance to biofouling, and (iii) $WS_2$ edge sites that accelerate charge transfer at the electrolyte–electrode boundary. Collectively, the $CeO_2$-ZMO/$WS_2$ interface provides a stable, high-area and fast-transfer platform tailored to SRZ, offering a pragmatic pathway for sensitive monitoring of SRZ in environmental and biological samples.

## 6.2. Experimental

### 6.2.1. Preparation of the GCE/$CeO_2$-ZMO/$WS_2$ Sensor

The $CeO_2$ and ZMO were synthesised separately and then combined, while commercial $WS_2$ powders, obtained from Sigma Aldrich, were exfoliated and combined with the $CeO_2$-ZMO to give the final composite, $CeO_2$-ZMO/$WS_2$. All chemicals used were of analytical reagent grades and are listed in Chapter 2, Section 2.2.1.

#### 6.2.1.1. Synthesis of $CeO_2$

To prepare the $CeO_2$, 50 mL of 0.5 M $Ce(NO_3)_3$ was prepared and adjusted to a pH of 12.0 using a small volume of 1.0 M KOH. This solution was stirred for 2 h and then transferred to a hydrothermal autoclave (100 mL) and heated in an oven at 180 °C for 14 h. After this period, the reactor was allowed to cool to room temperature naturally. Then the product was removed and washed five times with ethanol and three times with deionised water (DI-water), with the collection of the product using centrifugation steps between rinsings. Finally, the $CeO_2$ were dried in an oven at 60 °C for 12 h.

#### 6.2.1.2. Synthesis of ZMO

Zinc acetate was used as the source of Zn, while manganese acetate provided the Mn. Initially, four solutions were prepared, each dissolved in 10 mL of ethylene glycol. The compositions of the solutions were 0.5 g of $Zn(CH_3CO_2)_2$ (A), 1.0 g of $Mn(CH_3CO_2)_2$ (B), 1.5 g of urea (C), and 1.0 g of K-carrageenan (D). Solutions A, B, C, and D were stirred at 60 °C for 30 min. They were then combined into a single solution, resulting in a total volume of 40 mL, and mixed for an additional hour. The mixture was transferred to a Teflon-lined stainless-steel autoclave and heated at 180 °C for 18 h. (shown in Scheme 6.1) After cooling, the product was washed five times with ethanol and three times with DI-water, then dried in an oven at 60 °C for 12 h. Finally, the dried product was calcined in a muffle furnace at 400 °C for 5 h in an air atmosphere.

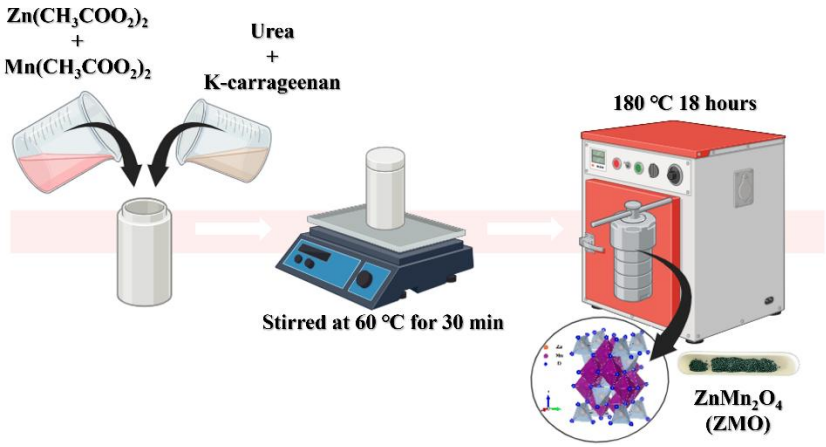


**Scheme 6.1.** Synthesis of ZMO.

### 6.2.1.3. Synthesis of the $CeO_2$-ZMO Composite

To prepare the composites comprising the $CeO_2$ and $ZnMn_2O_4$ (ZMO), the collected $CeO_2$ and ZMO were combined in 1:3 ratio (optimised ratio) in DI-water (2 mg $CeO_2$ and 6 mg ZMO in 3 mL DI-water). This mixture was stirred for 30 min and sonicated for 1 h in a bath sonicator. The composite was collected using centrifugation and dried at 60 °C for 12 h. Prior to forming the sensor, the $CeO_2$-ZMO powders were sonicated in DI-water for 30 min. The glassy carbon electrode (3 mm) was polished on a microcloth with a 1 µm sized diamond suspension, thoroughly rinsed with DI water, sonicated for 2 min and dried under an air stream. Then 5 µL of the $CeO_2$-ZMO dispersion was drop-cast onto the clean and polished GCE or onto a carbon screen printed electrode (Metrohm) to give the GCE/$CeO_2$-ZMO and SPE/$CeO_2$-ZMO.

### 6.2.1.4. Dispersion of the $WS_2$ sheets and Formation of GCE/$CeO_2$-ZMO/$WS_2$

To prepare the $WS_2$ sheets, 1 g of $WS_2$ powder was mixed with 10 mL of 0.1 M sodium cholate and stirred for 12 h. This solution was then centrifuged at 2500 rpm for 20 min, and the supernatant was discarded. The solid was redispersed in the cholate, stirred for 6 h and then centrifuged again. The supernatant (containing the smaller nanosheets) was collected, centrifuged, and the collected powder was then dried at 60 °C for 12 h.

To prepare the sensor, 2 mg of this powder was combined with 1 mL of DI-water and sonicated for 30 min. Then 5 μL of this $WS_2$ dispersion was drop-cast onto the surface of the GCE/$CeO_2$-ZMO to give the GCE/$CeO_2$-ZMO/$WS_2$. Similarly, the $WS_2$ sheets were drop-cast onto the SPE/$CeO_2$-ZMO.

All the electrochemical and surface analysis equipment that have been used in this study are described in Chapter 2. These include electrochemical equipment such as cyclic voltammetry (CV), differential pulse voltammetry (DPV), and electrochemical impedance spectroscopy (EIS) as outlined in Section 2.3.3; surface analysis equipment encompassing scanning electron microscopy (SEM), energy dispersive X-ray analysis (EDX), Fourier-transform infrared (FTIR) measurements, and X-ray photoelectron spectroscopy (XPS) detailed in Sections 2.4 and 2.5. The procedures for material characterisation methods and the use of specific characterisation techniques are detailed in the corresponding sections of Chapter 2, Experimental and Research Methods.

# 6.3. Results and discussion

## 6.3.1. Characterisation of the $CeO_2$ and the ZMO

The surface morphologies of the synthesised $CeO_2$ and the ZMO components are shown in the SEM micrographs depicted in Fig. 6.1. The $CeO_2$ appears as irregularly shaped solid stone-like deposits, with sizes reaching up to 1 μm, Fig. 6.1 (a) and (b). Conversely, the ZMO exhibits sphere-like morphologies, as illustrated in Fig. 6.1 (c). The dispersion in size of these spheres is depicted in the histogram shown in Fig. 6.1 (d). The majority of the spheres possess diameters ranging from 0.4 to 1.0 μm, with an average size of 0.8 μm. The EDX spectrum and mapping images are presented in Fig. 6.2 for ZMO, confirming the presence of Zn, Mn, and O. These elements are well dispersed across the surface, suggesting a uniform composition and the absence of other elements, thereby indicating the formation of ZMO without impurities.

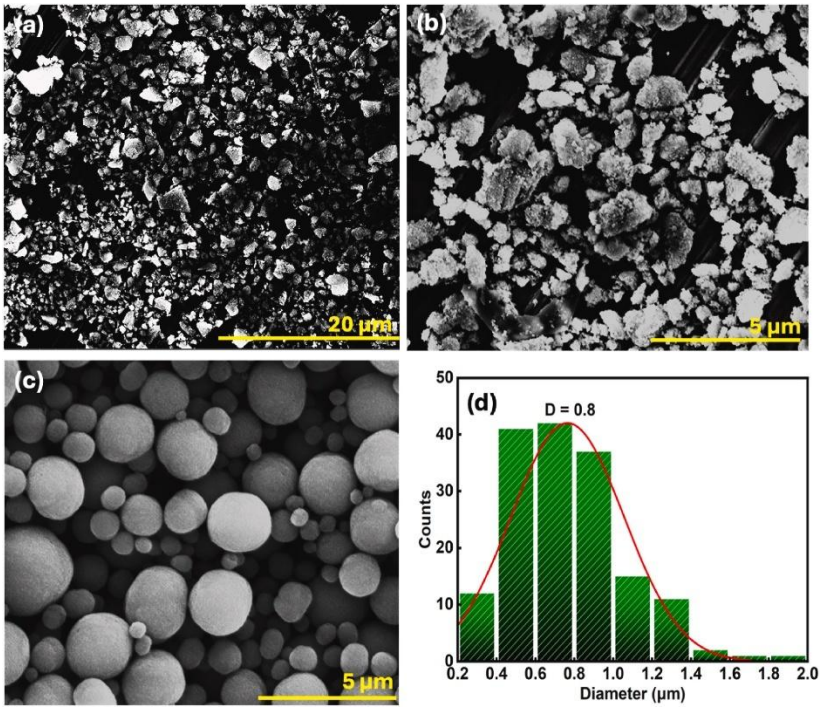


**Figure. 6.1.** SEM micrographs for $CeO_2$ at (a) low and (b) high magnification, and (c) for ZMO at high magnification and (d) size distribution histogram of the ZMO particles.

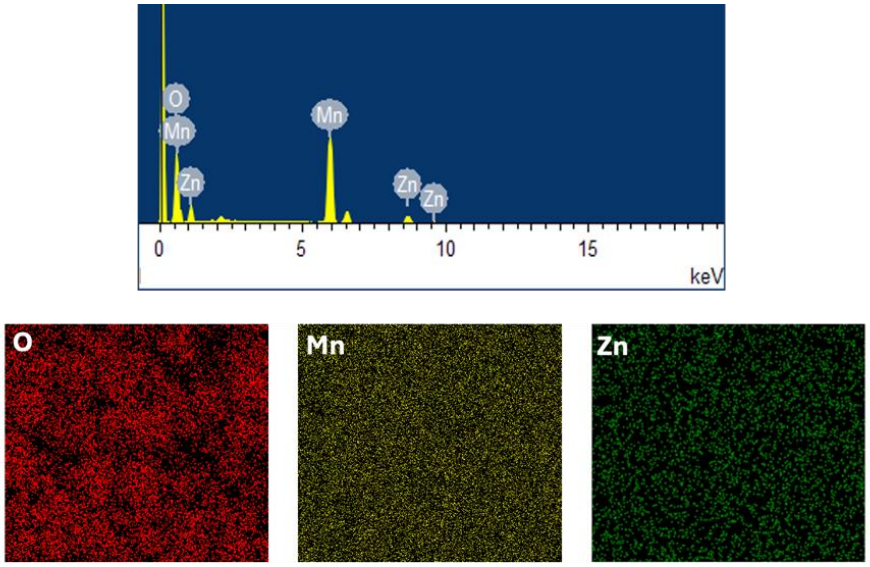


**Figure 6.2.** EDX spectrum and mapping plots recorded for ZMO.

When the ZMO spheres and $CeO_2$ stone-like particles were combined and subjected to sonication for 1 h, a distinct morphology emerged. The $CeO_2$ stones were transformed into smaller-sized powder particles, which gave a sprinkled-like $CeO_2$ coating over the ZMO spheres, Fig. 6.3 (a) and (b). The morphology of the exfoliated $WS_2$ sheets is evident in Fig. 6.3 (c). The sheets range in size from about 0.2 to 1.0 μm and match well with the size of the ZMOs. While the $WS_2$ sheets are generally well dispersed across the surface, there is evidence of some bundling of the sheets. Clearly, the three components have different morphologies, but when combined to give the final sensor, $CeO_2$-ZMO/$WS_2$, electron transfer is facilitated across the three closely connected components. As the exfoliated $WS_2$ sheets were simply drop-cast onto the $CeO_2$-ZMO, the formation of a heterostructure between the $WS_2$ and $CeO_2$-ZMO is highly unlikely. Similarly, the low-energy sonication of $CeO_2$ with ZMO, while leading to the excellent dispersion of $CeO_2$, is unlikely to give rise to the formation of a new heterostructure. Instead, it appears that the sizes of the three components facilitate communication as the ZMO is partially covered by a fine dusting of $CeO_2$ that is sandwiched between the ZMO and $WS_2$.

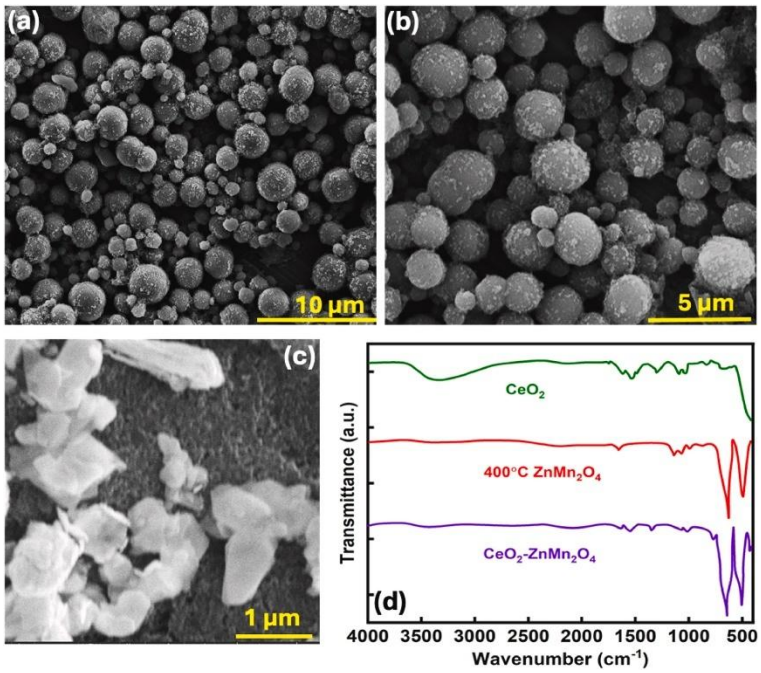


**Figure 6.3.** SEM micrographs for $CeO_2$-ZMO at low (a) and (b) higher magnification, (c) SEM of dispersed $WS_2$ sheets, and (d) FTIR of $CeO_2$, ZMO and $CeO_2$-ZMO.

As described in the experimental section, the hydrothermally formed spinel product was calcined at 400 °C for 5 h to produce ZMO, and this calcined product was subsequently combined with $CeO_2$. In Fig. 6.3 (d), FTIR spectra are shown for $CeO_2$, calcined ZMO, and the $CeO_2$-ZMO composite. The broad absorption band observed between 3500 and 3000 $cm^{-1}$ is attributed to the vibration of surface-adsorbed hydroxyl groups, which is more prominent for $CeO_2$ since the ZMO was calcined to remove these surface groups. The FTIR spectrum for $CeO_2$ features an absorption peak at 550 $cm^{-1}$, attributable to Ce-O vibration [18]. Two distinct absorption bands are evident for the ZMO within the spectral range from 700 to 500 $cm^{-1}$, and this is characteristic of ZMO spinels and has been attributed to metal-oxygen stretching vibrations in the tetrahedral and octahedral sites [19]. In particular, the absorption bands centred at 615.6 and 504.4 $cm^{-1}$ are consistent with the presence of M-O, and M-O-M, where M represents Zn and Mn [20]. The band at 504.4 $cm^{-1}$ is attributed to the octahedral sites, while the vibration at 615.6 $cm^{-1}$ is assigned to the vibrations in the tetrahedral sites [19]. On comparing the spectra, it is evident that the final composite, $CeO_2$-ZMO, exhibits the vibrations of the individual components.

To further characterise the surface of the synthesised ZMO and $CeO_2$, XPS spectra were recorded, and the spectra are provided in Fig. 6.4. The survey spectrum of ZMO, Fig. 6.4 (a), confirms the presence of oxygen, as the O 1s, manganese as the Mn 2p, and zinc as the Zn 2p. The O 1s spectrum, shown in Fig. 6.4 (b), can be deconvoluted into two peaks at 528.5 eV and 529.7 eV. The peak at 528.5 eV can be attributed to chemisorbed $O^{2-}$, while the peak observed at 529.7 eV indicates the presence of surface oxygen species, such as $O_2^{2-}$, $O^-$, and $OH^-$. These peaks are consistent with oxygen species on the ZMO surface [21]. The XPS analysis of the Zn 2p, displayed in Fig. 6.4 (c), indicates two distinct peaks with binding energies of 1019.9 and 1043 eV, corresponding to the Zn $2p_{3/2}$ and Zn $2p_{1/2}$ states. This confirms the presence of $Zn^{2+}$ ions in the ZMO and is in good agreement with previous studies [19,20].

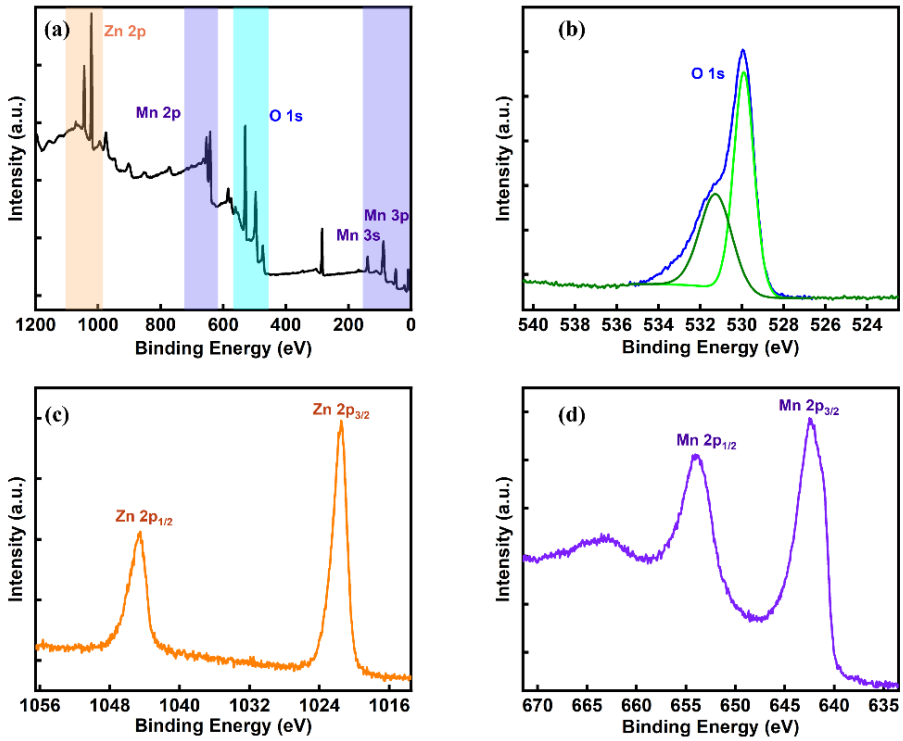


**Figure 6.4.** XPS spectra of (a) ZMO, (b) O 1s, (c) Zn 2p and (d) Mn 2p.

In addition, the binding energy gap of 23.1 eV between the Zn $2p_{3/2}$ and Zn $2p_{1/2}$ agrees well with previous reports and is further evidence for the presence of $Zn^{2+}$ in the ZMO

[19]. The Mn 2p spectrum shows the presence of two main peaks at binding energies of 642.3 and 655.7 eV. These peaks corresponding to the Mn $2p_{3/2}$ and $2p_{1/2}$ orbitals have a binding energy difference of 11.8 eV, indicating the presence of $Mn^{3+}$ in the ZMO. Furthermore, the ratio of Zn to Mn at the surface was 1.1:2.0, which is close to the expected ratio of 1:2 for Zn and Mn in the $ZnMn_2O_4$ stoichiometry.

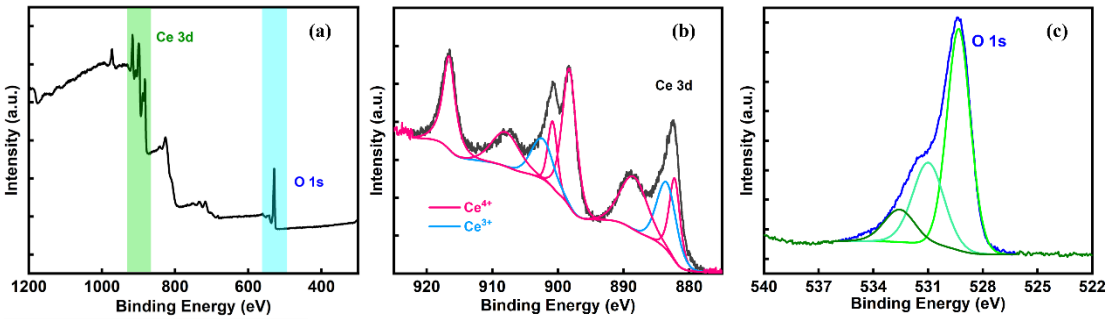


**Figure 6.5.** XPS spectra, (a) survey spectrum of $CeO_2$ (b) deconvoluted spectra for Ce 3d and (c) O 1s.

The XPS survey spectrum for the synthesised $CeO_2$ and the Ce 3d and O 1s XPS spectra are all provided in Fig. 6.5. The Ce 3d level consists of two series of peaks, corresponding to the $3d_{5/2}$ and $3d_{3/2}$. The peaks at 880.66 and 890.00 eV have previously been assigned to the mixing of the Ce 3 $d^9$ $4f^2$ $Ln^{-2}$ and Ce 3 $d^9$ $4f^1$ $Ln^{-1}$ Ce(IV) states, and indicate the presence of Ce(IV) [22], while the peaks at 916.36, 908.20, 900.22, 898.22, 888.26 and 882.23 eV are also consistent with Ce(IV). On the other hand, the peaks observed at 902.60 and 883.24 eV, indicate the presence of Ce(III). This suggests that the $CeO_2$ contains both Ce(III) and Ce(IV), in good agreement with other studies [23]. The presence of Ce(III) in $CeO_2$ has been linked to the existence of oxygen vacancies within $CeO_2$ [24]. Based on the XPS peak areas attributed to Ce(III) and Ce(IV), it was estimated that Ce(III) accounted for 22.95 % of the total peak area and Ce(IV) accounted for 77.05 % to give a Ce(III):Ce(IV) ratio of 1.0:3.4, indicating a relatively high level of Ce(III) and possibly oxygen vacancies. The corresponding O1s spectrum, depicted in Fig. 6.5 (c), can be attributed to the lattice oxygen in the $CeO_2$ and surface oxygen species.

The results of the characterisation studies confirm the successful synthesis of ZMO and indicate that the $CeO_2$ phase is of high purity, though it exhibits approximately 22% Ce(III) at the surface. Upon combination with ZMO, $CeO_2$ forms a coating resembling a fine powder distributed over the ZMO surface. Furthermore, commercial $WS_2$ can be efficiently exfoliated in the presence of sodium cholate, enabling its uniform dispersion across the $CeO_2$-ZMO composite to yield the final $CeO_2$-ZMO/$WS_2$ material.

## 6.3.2. Selection and electrochemical analysis of the materials

To elucidate the contribution of each constituent within the GCE/$CeO_2$-ZMO/$WS_2$ composite, the GCE was systematically modified with both individual and combined components. The resulting electrochemical responses are summarised in Table 6.1, with current measurements acquired using DPV to minimise capacitive background effects. Triplicate cycles were performed for each electrode configuration to provide an initial assessment of sensor stability and repeatability under repeated measurement conditions. The unmodified GCE exhibited consistently low current responses, accompanied by a pronounced decline in peak current across successive cycles, thereby demonstrating poor repeatability.

Similarly, the $WS_2$-modified electrode displayed limited repeatability. In contrast, the ZMO-modified electrode initially exhibited a high peak current in the first cycle. However, this response declined rapidly in subsequent cycles, leading to a significantly higher RSD, as summarised in Table 6.1. Notably, the $CeO_2$-modified electrodes exhibited excellent repeatability, with a low RSD of 0.30%. Furthermore, when ZMO was combined with $CeO_2$, the repeatability of the ZMO-based sensor was substantially enhanced, as evidenced by the reduced RSD. It should be noted, however, that this improvement was accompanied by a moderate reduction in peak current relative to the initial cycle observed with the ZMO alone.

**Table 6.1** Peak current recorded for 100 μM SRZ in 0.1 M PBS at a pH of 7.0 using DPV for various modified electrodes following a 15 min immersion period in the solution.

| Modified electrode | Cycle I Current (μA) | Cycle II Current (μA) | Cycle III Current (μA) | Average Current (μA) | RSD (%) |
|---|---|---|---|---|---|
| GCE | 5.524 | 5.218 | 4.976 | 5.239 | 5.24 |
| GCE/$WS_2$ | 8.282 | 8.038 | 7.742 | 8.021 | 3.37 |
| GCE/$CeO_2$ | 3.175 | 3.163 | 3.182 | 3.173 | 0.30 |
| GCE/ZMO | 15.86 | 2.747 | 2.686 | 7.098 | 106.9 |
| GCE/$CeO_2$-ZMO | 14.28 | 14.06 | 14.08 | 14.14 | 0.86 |
| GCE/$CeO_2$-ZMO/$WS_2$ | 19.07 | 19.02 | 18.96 | 19.02 | 0.29 |

Clearly, the integration of the three components results in elevated peak currents. The ZMO and $WS_2$ serve as effective materials for electron transfer, whereas $CeO_2$ substantially enhances the stability of the sensor. As illustrated in Fig. 6.6, the DPV profiles exhibit broad oxidation signals for the bare GCE, GCE/$WS_2$, and GCE/$CeO_2$ electrodes (Fig. 6.6 (a)), signifying sluggish electron transfer kinetics. While the GCE/$CeO_2$ system produces a lower peak potential, indicating a more thermodynamically favourable oxidation process, the corresponding peak current remains low and the wave is notably broadened. In contrast, the GCE/$CeO_2$-ZMO/$WS_2$ configuration demonstrates a distinctively sharper and more symmetric peak, accompanied by a substantially higher peak current. Collectively, these findings confirm that GCE/$CeO_2$-ZMO/$WS_2$ operates as a more efficient electrode for the electrochemical oxidation of SRZ.

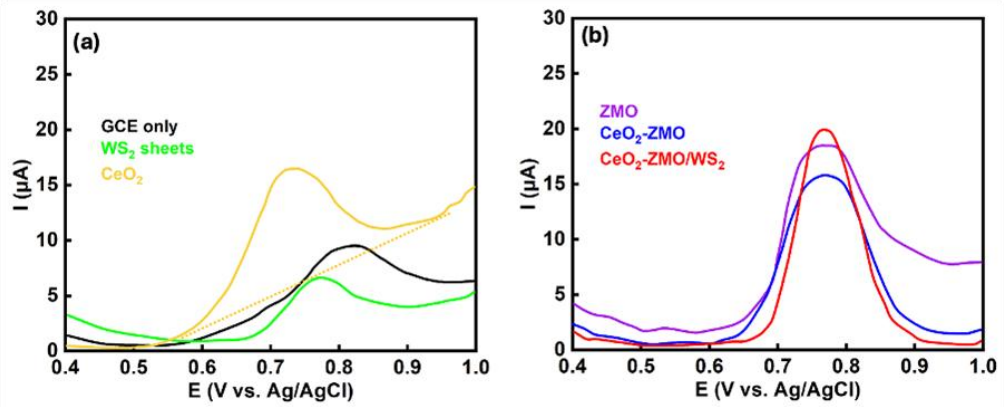


**Figure 6.6.** DPV voltammograms recorded in 100 μM SRZ at a pH of 7.0 for (a) bare GCE, GCE/$WS_2$ and GCE/$CeO_2$ and (b) GCE/ZMO, GCE/$CeO_2$-ZMO and GCE/$CeO_2$-ZMO/$WS_2$. (Note: the peak currents are computed using the background current as illustrated for $CeO_2$).

The performance of the GCE/$CeO_2$-ZMO/$WS_2$ sensor in the electrochemical oxidation of SRZ was studied initially using CV, and a typical plot is shown in Fig. 6.7 (a). For comparative analysis, the voltammograms recorded in the absence of the drug and for the GCE electrode are also shown. The oxidation of SRZ is evident with a pronounced oxidation wave extending from 0.78 to 0.85 V with a peak potential of 0.82 V (at a scan rate of 80 mV $s^{-1}$) corresponding to the oxidation of SRZ. On the other hand, the GCE gives a much lower peak current, and the oxidation wave is shifted to higher potentials. The observed oxidation peak potential (0.82 V vs Ag/AgCl) compares very favourably with the peak potential reported with a MIP/$MoS_2$/GCE sensor, where the peak potentials were between 1.0 and 1.05 V vs SCE [25]. Clearly, the oxidation of SRZ is an irreversible reaction, as depicted in Scheme 6.2. The oxidation reaction is accompanied by the loss of two electrons from the $NH_2$ group, with the conversion of this group to the NHOH group.

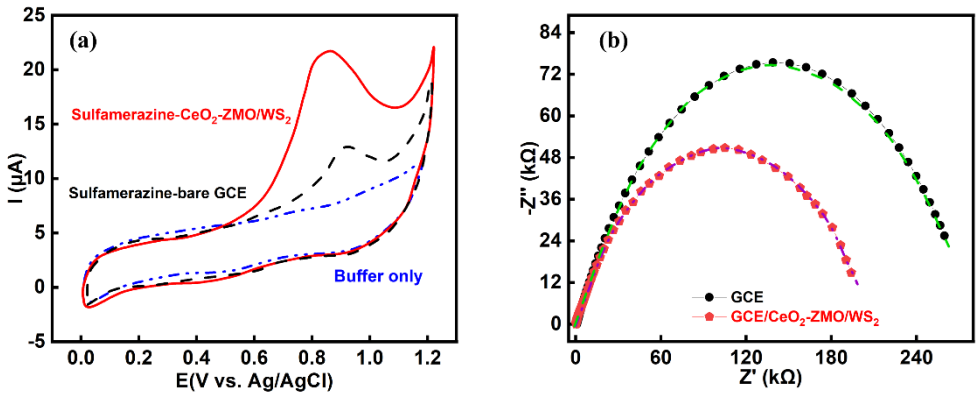


**Figure 6.7.** (a) CVs at 80 mV $s^{-1}$ of bare GCE and GCE/$CeO_2$-ZMO/$WS_2$ recorded in the presence and absence of 100 µM SRZ in 0.1 M PBS at a pH of 7.0, and (b) Nyquist plots for GCE and GCE/$CeO_2$-ZMO/$WS_2$ recorded at 0.82 V in 100 µM SRZ, pH of 7.0.

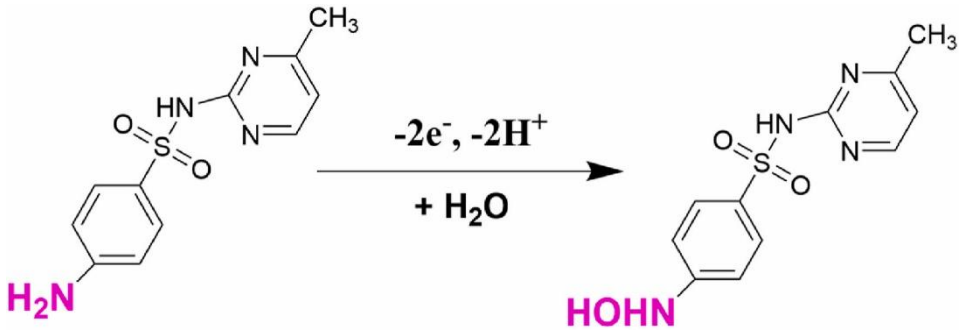


**Scheme 6.2.** Electrochemical oxidation of SRZ, with the reduction of the $–NH_2$ to the –NHOH group with the transfer of $2e^-/2H^+$.

The conducting characteristics of the GCE/$CeO_2$-ZMO/$WS_2$ and GCE substrates were analysed through electrochemical impedance spectroscopy, with a representative Nyquist plot illustrated in Fig. 6.7 (b). The data were acquired in a 100 µM SRZ solution, maintained at a pH of 7.0, and conducted at a constant potential of 0.82 V, corresponding to the oxidation potential of SRZ. The frequency was varied from 100 kHz to 7 mHz, and a perturbation potential of 10 mV was employed. Depressed semicircles are evident in both cases. However, the GCE/$CeO_2$-ZMO/$WS_2$ exhibits a smaller diameter, indicating a lower charge transfer resistance, $R_{CT}$. An equivalent circuit was utilised to further analyse the data. Good agreement between the experimental and simulated data was achieved with a simple Randles cell, comprising

a solution resistance, $R_s$ in series with a parallel RC couple, where R and C represent the $R_{CT}$ and constant phase element, CPE, respectively. The $R_{CT}$ values were determined as 279 ± 13.7 kΩ (n = 3) and 203 ± 6.3 kΩ (n = 3) for the GCE and GCE/$CeO_2$-ZMO/$WS_2$, respectively, indicating more efficient electron transfer for the GCE/$CeO_2$-ZMO/$WS_2$. Values of 10.9 ± 0.25 $\mu\Omega^{-1}$ $s^{0.63}$ for GCE and 10.3 ± 0.22 $\mu\Omega^{-1}$ $s^{0.64}$ for GCE/$CeO_2$-ZMO/$WS_2$, were obtained for the CPEs. The exponent values of 0.63 and 0.64 indicate considerable deviation from an ideal capacitor.

Information on the estimated surface area of the GCE/$CeO_2$-ZMO/$WS_2$ was obtained using an electrochemical probe and cyclic voltammetry. Both the modified and unmodified electrodes were cycled in 2.5 mM $K_3Fe(CN)_6$. The resulting voltammograms are depicted in Fig. 6.8 (a), where it is evident that the GCE/$CeO_2$-ZMO/$WS_2$ gives quasi-reversible characteristics. Higher peak currents combined with lower peak separations are evident with the GCE/$CeO_2$-ZMO/$WS_2$. Indeed, the peak separation, $\Delta E_p$, was computed at 318 mV for the GCE and 109 mV for the GCE/$CeO_2$-ZMO/$WS_2$, indicating a considerable reduction in $\Delta E_p$ on modifying the GCE. These studies were carried out at different scan rates. The peak current $I_p$ was plotted against the square root of the scan rate, as illustrated in Fig. 6.8 (b). Linear plots were obtained for both the GCE and the GCE/$CeO_2$-ZMO/$WS_2$, indicating that the oxidation and reduction of the probe molecules are dominated by diffusion control. The linear regression equations were computed as $I_p$ (μA) = 313.1 $\upsilon^{1/2}$ ($V^{1/2}$ $s^{-1/2}$) + 5.6 for GCE/$CeO_2$-ZMO/$WS_2$ and $I_p$ (μA) = 136.6 $\upsilon^{1/2}$ ($V^{1/2}$ $s^{-1/2}$) + 8.3 for the GCE. Using the Randles Sevcik equation, Eq. (6.1), and the diffusion coefficient of the $[Fe(CN)_6]^{3-}$ probe, the surface areas were estimated as 0.073 ± 0.004 $cm^2$ (n = 3) for GCE and 0.168 ± 0.003 $cm^2$ (n = 3) for the GCE/$CeO_2$-ZMO/$WS_2$.

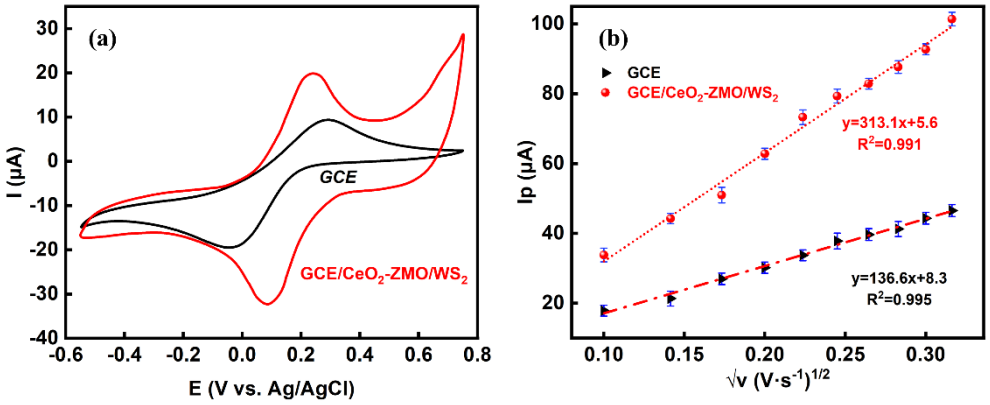


**Figure 6.8.** (a) CVs for GCE and GCE/$CeO_2$-ZMO/$WS_2$ recorded in 2.5 mM $K_3Fe(CN)_6$ in 0.1 M KCl and (b) oxidation peak currents recorded in 2.5 mM $K_3Fe(CN)_6$ plotted against the square root of the scan rate (n=3).

In Eq. (3.4), the peak current is represented as $I_p$, and the scan rate is indicated by $v$. The additional parameters are n (number of electrons transferred), $D$ (diffusion coefficient of the $[Fe(CN)_6]^{3-}$ probe, taken as $7.6 \times 10^{-6}$ $cm^2$ $s^{-1}$), A (surface area of the electrode) and C is the concentration of $[Fe(CN)_6]^{3-}$ (2.5 mM). This analysis indicates that the modified electrode has a 2.3-fold higher surface area compared with the unmodified GCE.

## 6.3.3. Influence of pH and kinetic processes

Prior to studying the analytical performance of the GCE/$CeO_2$-ZMO/$WS_2$ in the electrochemical detection of SRZ, the optimum pH was selected, and the role of diffusion and/or adsorption in the detection of SRZ was evaluated. The influence of pH was studied using DPV, and representative plots are shown in Fig. 6.9 (a). Clearly, a pH of 7.0 gives the optimum detection with a high peak current of 19.12 μA for a 100 μM SRZ solution. Much lower currents are observed as the pH is increased or decreased. Furthermore, the peaks become broader in the acidic and alkaline media, indicating a slower rate of electron transfer. This may be related to the speciation of SRZ as the pH changes. Under acidic conditions, the $NH_2$ group is protonated, while it will adopt an

overall neutral charge at pH values in the vicinity of 7.0, which seems to favour the adsorption of SRZ onto the GCE/$CeO_2$-ZMO/$WS_2$ surface.

It is also evident from Fig. 6.9 (a) that the peak potentials shift with pH, and this relationship is summarised in Fig. 6.9 (b). A linear plot is obtained with a linear regression equation of $E_p$ (V) = −0.0571 pH + 1.19. The gradient of this linear plot is in good agreement with the Nernst equation that predicts a slope of 0.0591 m/n V/pH, where m and n correspond to the number of hydrogen ions and electrons, respectively, which are transferred during the oxidation event. The computed slope indicates the transfer of equal numbers of protons and electrons (m = n) during the oxidation reaction, and this is in very good agreement with Scheme 6.2.

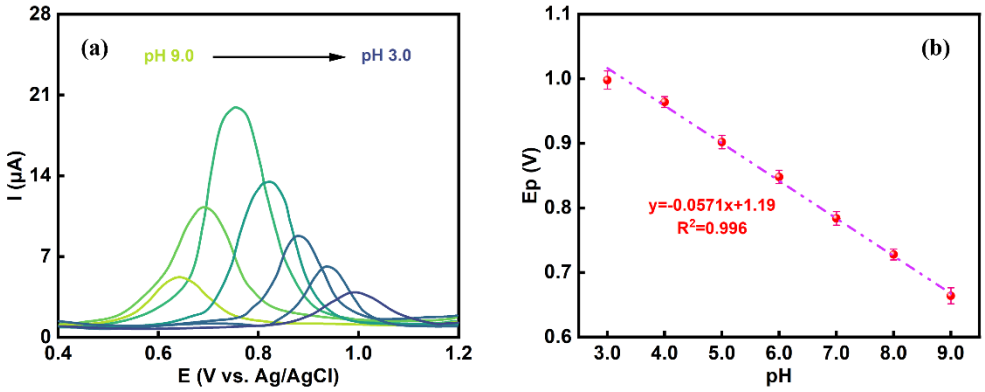


**Figure 6.9.** (a) DPVs of GCE/$CeO_2$-ZMO/$WS_2$ recorded at different pH values in the presence of 100 μM SRZ, and (b) oxidation peak currents plotted versus the pH of the solution (n=3).

The influence of scan rate on the peak current and peak potential was monitored using cyclic voltammetry. Typical voltammograms are presented in Fig. 6.10 (a) at scan rates from 10 to 90 mV $s^{-1}$. Higher currents are observed as the scan rate increases. When plotting the peak currents against the scan rate, a linear relationship was obtained, as shown in Fig. 6.10 (b). The linear equation was deduced as $I_p$ (μA) = 166.23 $\upsilon$ (V $s^{-1}$)

+ 0.44 ($R^2$ = 0.997). This linear plot indicates that the oxidation of SRZ is dominated by an adsorption-controlled process.

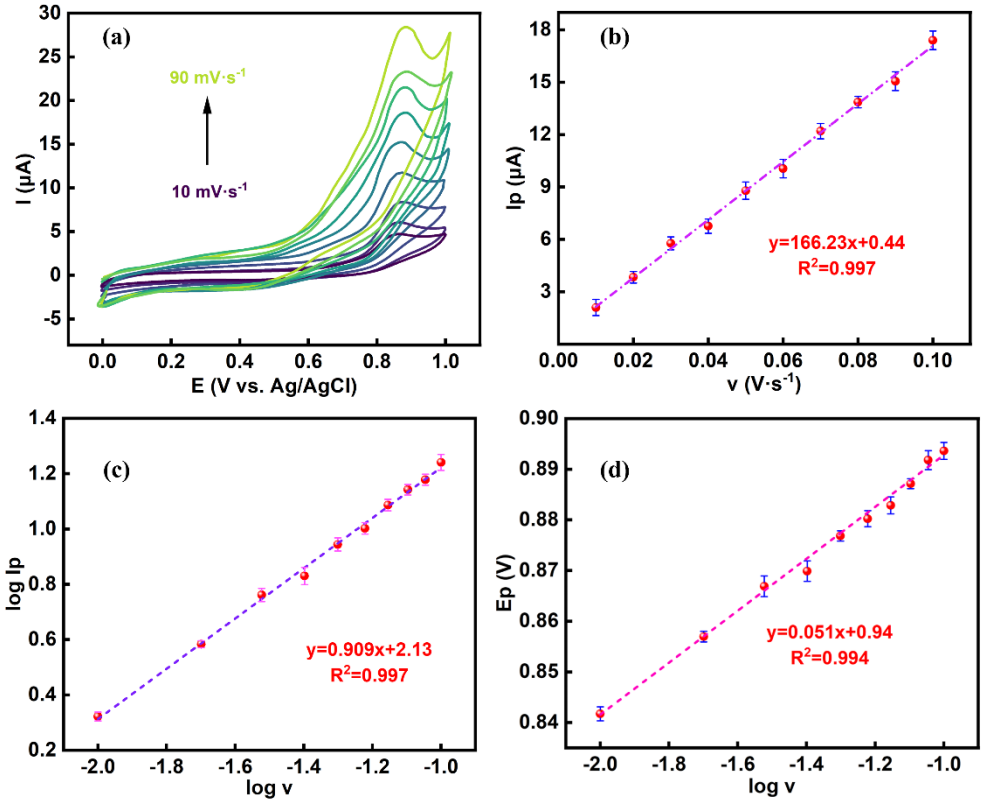


**Figure 6.10.** (a) CVs of GCE/$CeO_2$-ZMO/$WS_2$ recorded in 100 µM SRZ in 0.1 M PBS at a pH of 7.0; (b) peak current plotted as a function of the scan rate in the presence of GCE/$CeO_2$-ZMO/$WS_2$ at 100 µM SRZ, pH of 7.0. All data recorded following 15 min immersion in the SRZ solution (n=3); (c) logarithm of the peak current plotted as a function of the logarithm of the scan rate (V $s^{-1}$) (n=3), and (d) plot of the peak potential, Ep, as a function of the logarithm of the scan rate (scan rate in units of V $s^{-1}$) (n=3).

To further confirm this analysis, the logarithm of the peak current was plotted against the scan rate, and this plot is shown in Fig. 6.10 (c). Once again, a linear relationship was observed, and the slope of 0.91 is consistent with this adsorption-controlled process. The surface concentration of SRZ adsorbed onto the GCE/$CeO_2$-ZMO/$WS_2$ surface was estimated using Eq. (6.1), where r represents the surface concentration of adsorbed SRZ

molecules, and the other parameters have their usual meanings. Using this approach, the adsorbed surface concentration was computed as $6.25 \times 10^{-10}$ mol cm$^{-2}$.

$$I_p = \frac{n^2F^2rAv}{4RT} \quad \textbf{(6.1)}$$

The relationship between the peak potential and the logarithm of the scan rate is depicted in Fig. 6.10 (d), demonstrating excellent linearity. Utilising Eq. (6.2) and the linear regression equation derived from the $E_p$/log $v$ plot, expressed as $E_p = 0.051 \log v + 0.94$ with $R^2 = 0.994$, the $(1 - \alpha)n$ parameter was calculated as 1.16. Assuming n as 2.0, according to Scheme 6.2, the $(1 - \alpha)$ value was determined to be 0.58, resulting in an α value of 0.42, which aligns reasonably well with the broadly accepted value of 0.5.

$$\frac{E_p}{log\ v} = 2.303\frac{RT}{(1-\alpha)nF} \quad \textbf{(6.2)}$$

In addition, Eq. (6.3) was used to provide an estimation of the heterogeneous rate constant, $k^0$ [26]. In this analysis, n, F, A, and C represent the number of electrons transferred, the Faraday constant, surface area, and concentration of SRZ, respectively, while $E^0$ is the formal electrode potential, which was estimated as 790 mV by extrapolating $v$ to 0 mV s$^{-1}$.

$$I_p = 0.227nFACk^0exp\left[\frac{(1-\alpha)nF}{RT}(E_p - E^0)\right] \quad \textbf{(6.3)}$$

This was achieved by plotting the peak potential as a function of the logarithm of the scan rate. A plot of the logarithm of $I_p$ as a function of $E_p$-$E^0$ is shown in Fig. 6.11. The corresponding linear regression equation was deduced as ln $I$ ($I$ (A)) = 40.66 ($E_p$-$E^0$) (V) − 15.167 ($R^2 = 0.996$). By employing the intercept of this linear relationship and Eq. (6.3), the rate constant, $k^0$, was determined as $3.52 \times 10^{-4}$ cm s$^{-1}$. Using the gradient

of the plot, 40.66 $V^{-1}$, (1 – α) was estimated at 0.52, which is in relatively good agreement with the value of 0.58 calculated using Eq. (6.2).

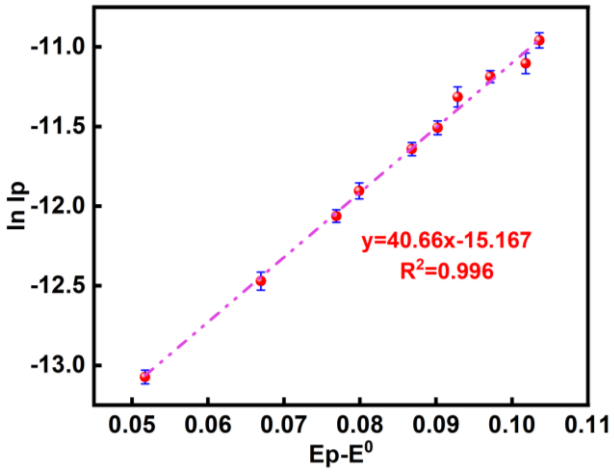


**Figure 6.11.** Plot of the logarithm of the peak current (in units of A) as a function of $E_p$-$E^0$ (in units of V) (n=3).

## 6.3.4. Optimisation of adsorption and sensing performance

The adsorption-driven detection of SRZ required systematic optimisation. Specifically, the interaction time between the GCE/$CeO_2$-ZMO/$WS_2$ electrode and a 100 µM SRZ buffer solution was systematically varied under open-circuit conditions to determine the optimal adsorption duration. Additionally, the influence of electrochemical preconditioning was investigated by applying a range of potentials from −0.1 V to 0.4 V, designed to enhance the adsorption of SRZ before subsequent sensing measurements. The corresponding experimental parameters and outcomes are detailed and summarised in Table 6.2.

In addition to measuring the peak current, the stability of the sensor was monitored over three cycles, and the data are represented as Cycle 1, II and III. It is evident from this analysis that the optimal accumulation potential is 0.4 V, giving a relatively high current which is stable over the three cycles. However, higher currents were obtained on simple

immersion of the GCE/$CeO_2$-ZMO/$WS_2$ sensor in the presence of SRZ. This is illustrated in Fig. 6.12, where the optimal immersion time is 15 min. In addition, the influence of the supporting electrolyte was investigated, and these studies are summarised in Table 6.3, where the phosphate buffer provides the highest peak current. Therefore, a phosphate buffer at a pH of 7.0 and an immersion period of 15 min was employed in all the sensing studies.

**Table 6.2** DPV currents recorded following a 15 min preconditioning period at different applied potentials to facilitate adsorption of SRZ in 100 μM SRZ.

| Accumulation potentials (V) | Cycle I Current (μA) | Cycle II Current (μA) | Cycle III Current (μA) | Average Current (μA) | RSD (%) |
|---|---|---|---|---|---|
| –0.1 | 3.79 | 1.857 | 0.713 | 2.121 | 73.4 |
| 0.0 | 5.25 | 1.988 | 1.733 | 2.992 | 65.6 |
| 0.1 | 4.85 | 2.731 | 2.416 | 3.335 | 39.8 |
| 0.2 | 6.402 | 2.268 | 2.246 | 3.639 | 65.8 |
| 0.3 | 4.204 | 3.977 | 3.928 | 4.036 | 3.6 |
| 0.4 | 11.34 | 10.96 | 10.47 | 10.92 | 4.0 |

The analytical characteristics of the GCE/$CeO_2$-ZMO/$WS_2$ sensor were systematically evaluated through assessments of sensitivity, limit of detection (LOD), selectivity, operational stability, and applicability in real water analyses. Both GCE and SPE substrates were employed for comparison. As illustrated in Fig. 6.13 (a), DPVs were recorded for various concentrations of SRZ using the GCE-based sensor. Before analyte addition, the GCE/$CeO_2$-ZMO/$WS_2$ electrode was electrochemically cycled in buffer solution to stabilise the background current. Sequential aliquots of SRZ were then introduced to achieve concentrations ranging from 18 nM to 285 μM in the buffer solution. The observed increase in peak current with rising SRZ concentrations demonstrates the ability of the GCE/$CeO_2$-ZMO/$WS_2$ sensor to detect and respond to

changes in analyte concentration quantitatively. A comparison of experimental results obtained after 10- and 15-min immersion periods yielded a t-value of 0.00238. The corresponding p-value was less than 0.05 at the 95% confidence level, indicating a statistically significant difference between the two experiments. Consequently, this suggests that the sensing response depends on immersion time, with 15 min yielding greater drug adsorption.

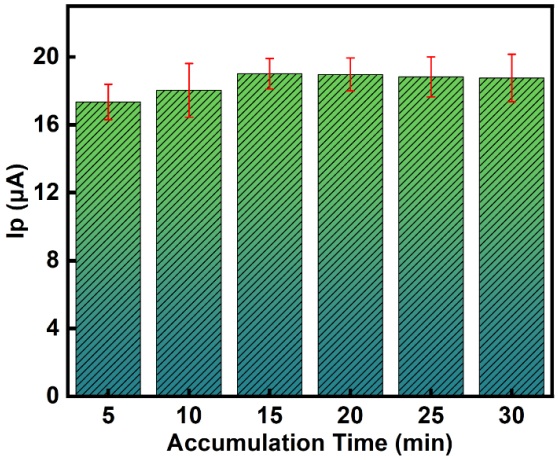


**Figure 6.12.** The influence of different accumulation times under open-circuit conditions in the detection of 100 μM SRZ (n=3).

**Table 6.3** DPV currents recorded in 100 μM SRZ with different supporting electrolytes.

| Supporting Electrolyte | Cycle I Current (μA) | Cycle II Current (μA) | Cycle III Current (μA) | Average Current (μA) | RSD (%) |
|---|---|---|---|---|---|
| 0.1 M chloride solution, at pH 6.5 | 1.86 | 1.28 | 0.79 | 1.31 | 40.9 |
| 0.1 M Acetate buffer at pH 7.0 | 4.32 | 2.79 | 2.57 | 3.23 | 29.5 |
| 0.1 M Phosphate buffer, at pH 7.0 | 19.07 | 19.02 | 18.96 | 19.02 | 0.3 |

When these peak currents were plotted as a function of the SRZ concentration, linear plots were obtained, as illustrated in Fig. 6.13 (b). At the lower concentrations, extending from 18 nM to 1.2 µM, a linear relationship was obtained with the equation, $I_p$ (µA) = 4.86 C (µM) + 1.13 ($R^2$ = 0.995). A lower gradient was achieved with concentrations between 1.2 and 300 µM, with a linear regression equation, $I_p$ (µA) = 0.132 C (µM) + 6.5 ($R^2$ = 0.997). Using the estimated surface area of 0.168 ± 0.0054 $cm^2$ for the GCE/$CeO_2$-ZMO/$WS_2$, and the lower concentrations, the sensitivity was determined as 28.9 µA $µM^{-1}$ $cm^{-2}$.

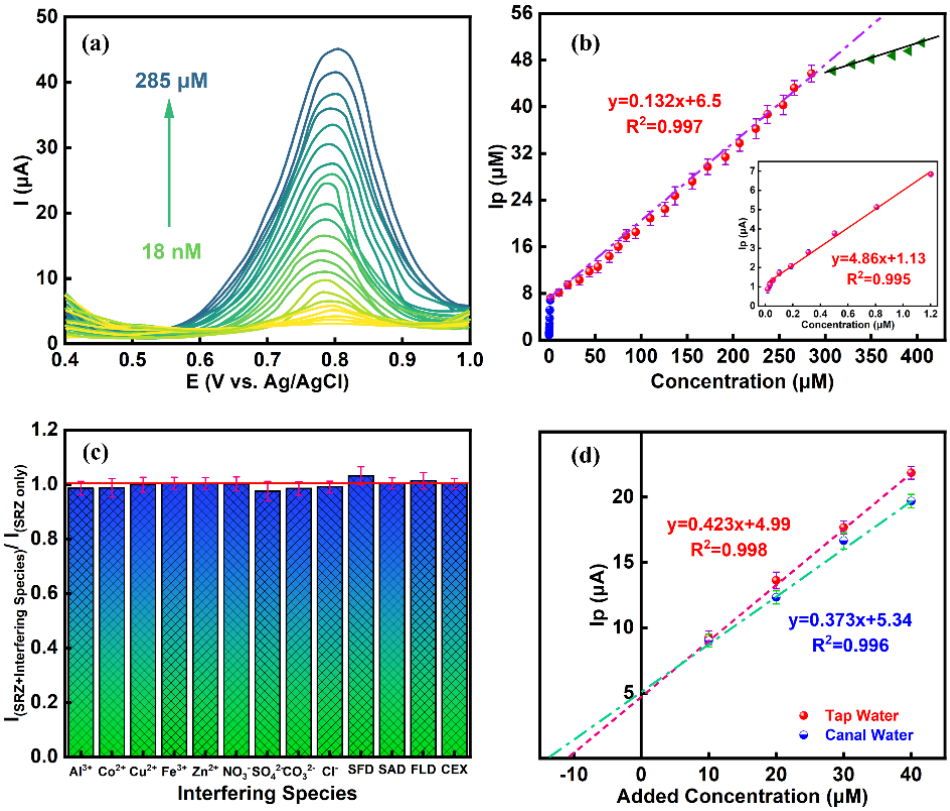


**Figure 6.13.** Data for GCE/$CeO_2$-ZMO/$WS_2$ (a) DPVs recorded at various concentrations of SRZ; (b) oxidation peak currents plotted versus the concentration of SRZ (n=3); (c) interference study in the presence of inorganic ions and other drug molecules (n=3), and (d) standard addition plot with tap water and river/canal water (n=3).

The corresponding data recorded with the screen-printed electrode as the substrate is shown in Fig. 6.14. The same linear calibration curves were obtained, with the lower concentration range extending from 18 nM to 2.3 μM. The linear regression equation obtained, $I_p$ (μA) = 4.14 C (μM) + 0.85 ($R^2$ = 0.998), is similar, but with a somewhat lower gradient compared to the GCE. Likewise, a linear relationship between the peak current and concentration was achieved between the concentration range of 2.3 and 285 μM ($I_p$ (μA) = 0.162 C (μM) + 12.2 ($R^2$ = 0.997). These analytical parameters compare very well with the sensors previously fabricated for the detection of SRZ and sulfamethazine, which is structurally related to SRZ, as illustrated in Table 6.4. Indeed, the GCE/$CeO_2$-ZMO/$WS_2$ sensor has a lower LOD, and a higher sensitivity compared to the previously reported sensors for the electrochemical detection of SRZ. Moreover, the LOD is lower than a recently reported fluorescence (FL) sensor for SRZ [27].

**Table 6.4** Comparison of the GCE/$CeO_2$-ZMO/$WS_2$ sensor with previously reported sensors for the electrochemical detection of SRZ.

| Sensor | Technique | Linear Range (μM) | LOD (nM) | Sensitivity | Refs. |
|---|---|---|---|---|---|
| GCE/$CeO_2$-ZMO/$WS_2$ | DPV | 0.018–285 | 13.8 | 28.9 μA $\mu M^{-1}$ $cm^{-2}$ (0.018–1.2 μM) | This work |
| CPE | SWV | 1–10 | 600 | 0.021 μA $\mu M^{-1}$ | [28] |
| MIP/$MoS_2$/$NH_2$-MWCNT@COF/GCE | DPV | 0.3–200 | 110 | – | [25] |
| MIPSMR/$Ni_2P$/GCE | DPV | 0.05–20 | 19 | – | [29] |
| MIP@GC@ZnO@AuNP | DPV | 0.05–40 | 46 | 0.24 μA $\mu M^{-1}$ | [30] |
| Europium-doped | FL | 0–500 | 45 | – | [27] |

| | | | | | |
|---|---|---|---|---|---|
| Porphyrin-based MOFs $Cu_2Y_2O_5$/g-$C_3N_4$/GCE (Sulfamethazine) | i-t | 2–276 | 23 | 8.86 μA $\mu M^{-1}$ $cm^{-2}$ | [31] |
| $SrWO_4$/g-$C_3N_4$ (Sulfamethazine) | i-t | 0.02–8 | 8.8 | 8.174 μA $\mu M^{-1}$ $cm^{-2}$ | [32] |

Another important parameter in the development of sensors is selectivity and this was studied by adding various interfering compounds to the buffered SRZ solution, and by testing the performance of the sensor in real water samples. The influence of the added interferents is summarised in Fig. 6.13 (c), using the GCE as the substrate. Here, various inorganic ions commonly found in aquatic environments, and antimicrobial drugs, such as sulfanilamide (SFD), which are related structurally to SRZ were employed as interferents. Other antimicrobial drugs including sulfapyridine (SAD), flutamide (FLD), and cefadroxil (CEX) were used. The SRZ was maintained at a concentration of 100 μM, while the interferents were added to give a 2-fold higher concentration (100 μM SRZ + 200 μM FLD). Very little interference was observed. The most significant interference was seen with the sulfonamide SFD. Still, on comparing the currents obtained for SRZ and for SRZ with the added SFD the RSD is relatively low at 3.6 %, indicating little inference even with a drug that is structurally related to SRZ. The same interference study using the SPE as the substrate is presented in Fig. 6.14 (c), and again, excellent selectivity is achieved with very similar results to those seen with the GCE substrate.

Finally, a classical standard addition experiment was performed with tap and real water samples. The samples were initially spiked with 10 μM SRZ and then standard additions were made. A typical plot for the GCE/$CeO_2$-ZMO/$WS_2$ is shown in Fig. 6.13 (d), while the corresponding plot for the SPE/$CeO_2$-ZMO/$WS_2$ is presented in Fig. 6.14 (d). The

analysis with the tap water agrees well with the initial 10 µM SRZ water sample. For example, the concentration for the SPE/$CeO_2$-ZMO/$WS_2$ is computed as 10.7 µM SRZ giving an error of 7 %. On the other hand, much higher concentrations of SRZ were calculated for the real water samples, indicating a more complex matrix in these real water samples or the presence of low levels of other components that contribute to the observed current. Overall, good selectivity and recovery were achieved with both the GCE/$CeO_2$-ZMO/$WS_2$ and SPE/$CeO_2$-ZMO/$WS_2$ in the real water samples.

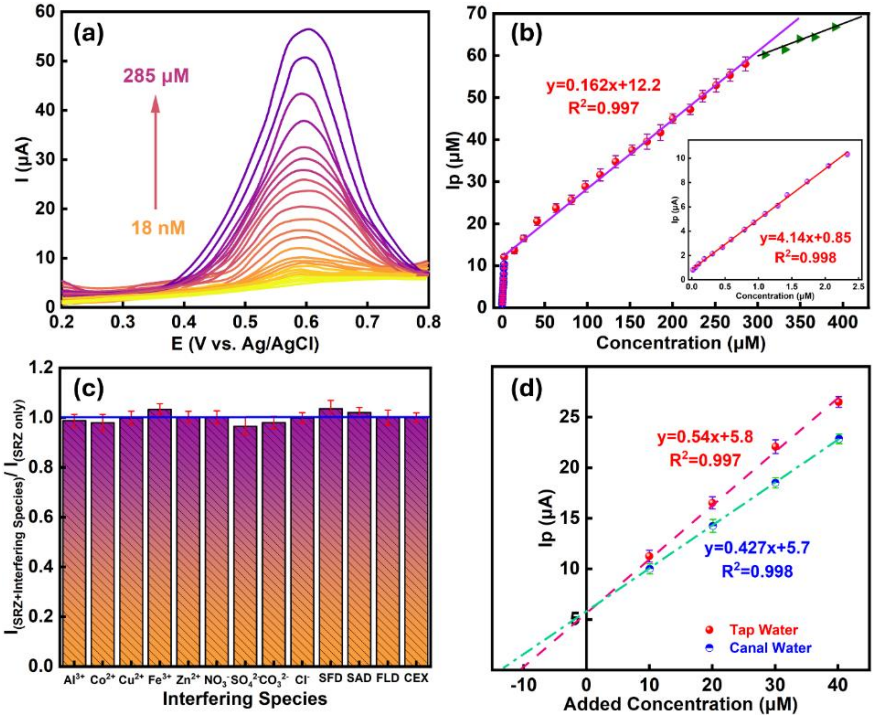


**Figure 6.14.** Data for **SPE**/$CeO_2$-MZO/$WS_2$ (a) DPVs recorded at various concentrations of SRZ; (b) oxidation peak currents plotted versus the concentration of SRZ (n=3); (c) interference study in the presence of inorganic ions and drug molecules (n=3), and (d) standard addition plot with tap water and canal/river water (n=3).

The stability of the GCE/$CeO_2$-ZMO/$WS_2$ in 100 µM SRZ is demonstrated in Fig. 6.15 (a). In these experiments, the sensor was subjected to continuous immersion in the SRZ solution, and at various intervals, the peak current was measured using DPV. All traces exhibit a pronounced and highly symmetrical oxidation peak characteristic of a well-

defined redox process. The minimal fluctuation among these voltammograms indicates excellent stability. Moreover, the baseline currents remain low and stable, supporting negligible background interference, which is critical for reliable quantification. This is further analysed in Fig. 6.15 (b), where the peak currents are plotted as a function of the days of immersion in a lower concentration of 50 µM SRZ. Each bar is accompanied by a standard error, which remains small, indicating the low day-to-day variability. Excellent stability is seen over a period of two days, after which the peak current decreases slightly during days three and four until it stabilises at a constant current of 18 µA, which is maintained over days six and seven. Overall, excellent stability is observed in the presence of the SRZ. This indicates that the sensor retains its electrochemical activity and integrity throughout the week. These results corroborate the suitability of the GCE/$CeO_2$-ZMO/$WS_2$ for repeated and prolonged use in analytical measurements, implying resistance to degradation or fouling.

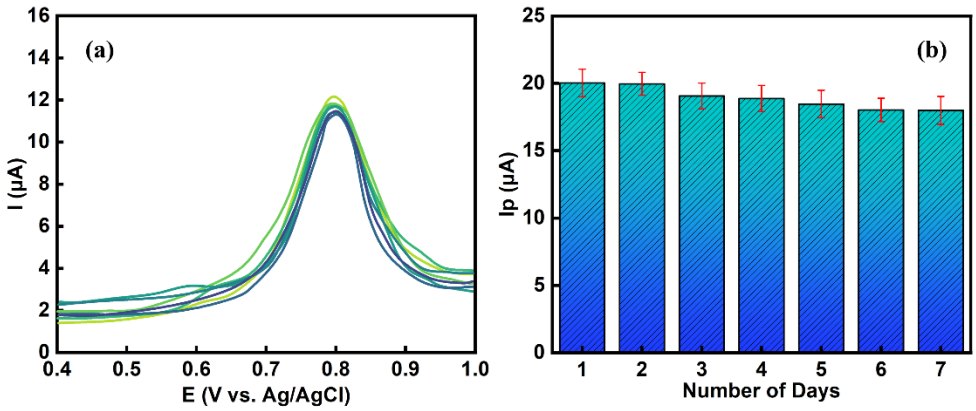


**Figure 6.15.** (a) A typical example for stability with the peak current for the oxidation of 100 µM SRZ, at pH of 7.0, over a 7-day immersion period in the SRZ by the same electrode, (b) repeatability with 10 repeated DPVs in 50 µM SRZ (n=3).

In addition to this approach, a standard addition experiment was employed with both tap water and water collected from a nearby canal. This real water sample was filtered to remove debris and then spiked with a known concentration of SRZ. Assuming that the original real water sample did not contain any SRZ, the recovery was calculated.

The results obtained from these experiments are collected in Table 6.5 with both the GCE and SPE as the substrates.

**Table 6.5** Comparison table of different analysis samples for SRZ.

| **Samples** | | | **Added Drug SRZ (μM)** | **Recovery (%)** | **%RSD** |
|---|---|---|---|---|---|
| Water Analysis | Tap water | GCE substrate | 20 | 92.2 | 2.6 |
| | | | 50 | 94.1 | 1.7 |
| | | | 100 | 98.7 | 1.0 |
| | | SPE substrate | 20 | 90.3 | 4.4 |
| | | | 50 | 93.5 | 3.8 |
| | | | 100 | 98.7 | 1.3 |
| | Canal/River Water | GCE substrate | 20 | 91.4 | 4.0 |
| | | | 50 | 93.9 | 3.6 |
| | | | 100 | 96.2 | 1.5 |
| | | SPE substrate | 20 | 89.5 | 5.7 |
| | | | 50 | 93.4 | 3.7 |
| | | | 100 | 94.7 | 1.8 |
| Biological Analysis | Artificial Urine | GCE substrate | 20 | 93.7 | 3.8 |
| | | | 50 | 95.8 | 2.5 |
| | | | 100 | 96.7 | 1.3 |
| | | SPE substrate | 20 | 92.7 | 4.7 |
| | | | 50 | 95.4 | 2.8 |
| | | | 100 | 96.8 | 1.5 |

For all the water samples the recoveries range from about 90% to 99%, providing acceptable recoveries. The sensors perform equally well in the biological samples, with good recoveries ranging from 92.7% to 96.8%. As a comparison, UV–visible

spectroscopy was employed in the analysis of tap and canal water, and the recovery data are summarised in Table 6.6. It is clear from a comparison of Table 6.5 and Table 6.6, that the GCE/$CeO_2$-ZMO/$WS_2$ and SPE/$CeO_2$-ZMO/$WS_2$ compare very well with UV–Visible spectroscopy, giving rise to similar recoveries.

**Table 6.6** Recovery data obtained using UV-Visible spectroscopy as the analytical technique.

| **Samples** | | **Added Drug SRZ (µM)** | **Recovery (%)** | **%RSD** |
|---|---|---|---|---|
| Water Analysis | Tap water | 20 | 87.8 | 1.4 |
| | | 50 | 89.3 | 1.1 |
| | | 100 | 91.9 | 0.9 |
| | Canal/River Water | 20 | 85.6 | 2.9 |
| | | 50 | 86.4 | 1.5 |
| | | 100 | 89.2 | 1.0 |

## 6.4. Conclusions

In this study, $ZnMn_2O_4$ (ZMO) was decorated with $CeO_2$ and $WS_2$ to give the sensitive and selective detection of sulfamerazine on both glassy carbon electrodes (GCE) and screen-printed carbon electrodes (SPE).

The material is formed by (i) synthesising ZMO spinel spheres, (ii) creating a finely dispersed $CeO_2$ "dusting" that coats the ZMO surface, and (iii) decorating the composite with exfoliated $WS_2$ sheets. This increases the electroactive area and accelerates charge transfer while maintaining signal stability under repeated measurements.

The work introduces $CeO_2$-ZMO/$WS_2$ sensing for SRZ and, to the best of our knowledge, this material has not previously been applied to SRZ electroanalysis. The novelty is not only compositional but also structural: $CeO_2$ stabilises the ZMO response, while $WS_2$ supplies edge-rich pathways that sharpen and amplify the SRZ oxidation peak.

Compared with reported SRZ sensors, the $CeO_2$-ZMO/$WS_2$ interface delivers nanomolar detection with a low LOD of 13.8 nM, strong low-range sensitivity, and broad working ranges. Importantly, the same sensing concept is successfully transferred from GCE to a portable SPE electrode, and its performance is validated by selectivity studies and recoveries in tap water, canal water, and artificial urine, demonstrating sensor stability beyond ideal buffer conditions. This work answers whether a $CeO_2$-stabilised spinel oxide with exfoliated $WS_2$, can provide a high-area and fast-transfer interface capable of reliable SRZ quantification in complex real samples, including on disposable, deployable electrodes.

# References


[1] K. Balamurugan, R. Karthik, S.-M. Chen, R. Sukanya, B. Thasma Subramanian, V.M.N. Biju, J.-J. Shim, C.B. Breslin, "Heterostructures of mixed metal oxides ($ZnMnO_3$/ZnO) synthesized by a wet-chemical approach and their application for the electrochemical detection of the drug chlorpromazine," *Composites Part B Engineering*, vol. 236, p. 109822, Mar. 2022, doi: 10.1016/j.compositesb.2022.109822.

[2] R. Rajakumaran, R. Sukanya, S. M. Chen, R. Karthik, C. B. Breslin, and P. M. Shafi, "Synthesis and characterization of Pyrochlore-Type praseodymium stannate nanoparticles: An effective electrocatalyst for detection of nitrofurazone drug in biological samples," *Inorganic Chemistry*, vol. 60, no. 4, pp. 2464–2476, Feb. 2021, doi: 10.1021/acs.inorgchem.0c03377.

[3] D. Hernández-Ramírez, L. H. Mendoza-Huizar, C. A. Galán-Vidal, G. Y. Aguilar-Lira, and G. A. Álvarez-Romero, "Review—Trends on the Development of Non-Enzymatic Electrochemical Sensors Modified with Metal-Oxide Nanostructures for the Quantification of Uric Acid," *Journal of the Electrochemical Society*, vol. 168, no. 5, p. 057522, Apr. 2021, doi: 10.1149/1945-7111/abf8d5.

[4] A.A. Ansari, R. Lv, S. Gai, A.K. Parchur, P.R. Solanki, Archana, Z.A. Ansari, M. Dhayal, P. Yang, M.K. Nazeeruddin, M.K. Nazeeruddin, and M.M. Tavakoli, "ZnO nanostructures – Future frontiers in photocatalysis, solar cells, sensing, supercapacitor, fingerprint technologies, toxicity, and clinical diagnostics," *Coordination Chemistry Reviews*, vol. 515, p. 215942, May 2024, doi: 10.1016/j.ccr.2024.215942.

[5] B. Karuppaiah, J. Anupriya, S. M. Chen, and S. J. Park, "An emergent electrochemical sensor based on spinel zinc manganese oxide decorated on amine-functionalized boron nitride for enhanced electrochemical determination of herbicide mesotrione," *Process Safety and Environmental Protection*, vol. 176, pp. 292–303, Jun. 2023, doi: 10.1016/j.psep.2023.06.008.

[6] Z. K. Heiba, M. B. Mohamed, A. M. El-Naggar, and Y. Altowairqi, "Structure and dielectric properties of $ZnMn_2O_4$/$NiFe_2O_4$ nanocomposite," *Applied Physics A*, vol. 127, no. 8, Jul. 2021, doi: 10.1007/s00339-021-04731-2.

[7] Z.K. Heiba, A.A. Shaltout, S.I. Ahmed, E. Alzahrani, H.H. Wahba, M.A. Deyab, and M.B. Mohamed, "Functional properties of quaternary metals $(1-x)ZnMn_2O_4/(x)MgFe_2O_4$ as supercapacitor electrode," *Applied Physics A*, vol. 127, no. 1, Jan. 2021, doi: 10.1007/s00339-020-04194-x.

[8] Z. K. Heiba, M. A. Deyab, A. M. El-Naggar, and M. B. Mohamed, "Elec trochemical performance of quaternary $(1-x)ZnMn_2O_4/(x)MgFe_2O_4$ solid solu tion as supercapacitor electrode," *Ceramics International*, vol. 47, no. 6, p p. 7475–7486, Nov. 2020, doi: 10.1016/j.ceramint.2020.11.088.

[9] Z. K. Heiba, M. B. Mohamed, and A. Badawi, "Structural and optical properties of $(1-x)ZnMn_2O_4$/xPbS nanocomposites," *Journal of Materials Science Materials in Electronics*, vol. 33, no. 14, pp. 11354–11364, Mar. 2022, doi: 10.1007/s10854-022-08108-w.

[10] Z. K. Heiba, M. B. Mohamed, and A. Badawi, "Structure and optical properties of nano-$ZnMn_2O_4$/CuS solid solution heterostructure," *Journal of Sol-Gel Science and Technology*, vol. 101, no. 3, pp. 637–648, Mar. 2022, doi: 10.1007/s10971-022-05752-w.

[11] Z. K. Heiba, M. B. Mohamed, and S. I. Ahmed, "Modifying the structure and optical characteristics of $ZnMn_2O_4$ by alloying with CdS to form heterostructure nanocomposite," *Applied Physics A*, vol. 127, no. 11, Nov. 2021, doi: 10.1007/s00339-021-05021-7.

[12] R. Sukanya, D. C. Da Silva Alves, and C. B. Breslin, "RevIew—Recent Developments in the applications of 2D transition metal dichalcogenides as electrocatalysts in the generation of hydrogen for renewable energy conversion," *Journal of the Electrochemical Society*, vol. 169, no. 6, p. 064504, May 2022, doi: 10.1149/1945-7111/ac7172.

[13] D. Alves, P.R. Kasturi, G. Collins, T.N. Barwa, S. Ramaraj, R. Karthik, and C.B. Breslin, "2D layered double hydroxides and transition metal dichalcogenides for applications in the electrochemical production of renewable hydrogen," *Materials Advances*, vol. 4, no. 24, pp. 6478–6497, Jan. 2023, doi: 10.1039/d3ma00685a.

[14] Y. Luo, T.N. Barwa, E. Dempsey, R. Karthik, J.J. Shim, R. Sukanya, and C.B. Breslin, "Electrochemical detection of sulfanilamide using tannic acid exfoliated $MoS_2$ nanosheets combined with reduced graphene oxide/graphit e," *Environmental Research*, vol. 248, p. 118391, Feb. 2024, doi: 10.1016/ j.envres.2024.118391.

[15] G. Zhang, X. Liu, S. Lu, J. Zhang, and W. Wang, "Occurrence of typical antibiotics in Nansi Lake's inflowing rivers and antibiotic source contributi on to Nansi Lake based on principal component analysis-multiple linear re gression model," *Chemosphere*, vol. 242, p. 125269, Nov. 2019, doi: 10.10 16/j.chemosphere.2019.125269.

[16] J. Wu, J. Liu, Z. Pan, B. Wang, and D. Zhang, "Spatiotemporal distributions and ecological risk assessment of pharmaceuticals and personal care products in groundwater in North China," *Hydrology Research*, vol. 51, no. 5, pp. 911–924, Apr. 2020, doi: 10.2166/nh.2020.001.

[17] S. Xiao, J. Wan, Y. Wang, Z. Yan, Y. Ma, J. Sun, M. Tang, J. Cao, and J. Chen, "Distribution, Sources, and Risk Assessment of Emerging Contaminants in the Effluents from Large-Scale Wastewater Treatment Plants in Guangzhou Central Districts, South China," *Water Air & Soil Pollution*, vol. 234, no. 7, Jul. 2023, doi: 10.1007/s11270-023-06410-9.

[18] N. Fauzia, M. A. Khan, M. Chaman, and A. Azam, "Antibacterial and sunlight-driven photocatalytic activity of graphene oxide conjugated $CeO_2$ nanoparticles," *Scientific Reports*, vol. 14, no. 1, p. 6606, Mar. 2024, doi: 10.1038/s41598-024-54905-0.

[19] Z. K. Heiba, M. B. Mohamed, and S. I. Ahmed, "Modifying the structure and optical characteristics of $ZnMn_2O_4$ by alloying with CdS to form heterostructure nanocomposite," *Applied Physics A*, vol. 127, no. 11, Nov. 2021, doi: 10.1007/s00339-021-05021-7.

[20] S. Aouini, A. Bardaoui, A. Ferraria, D. Santos, and R. Chtourou, "$ZnMn_2O_4$ nanopyramids fabrication by hydrothermal route: Effect of reaction time on the structural, morphological, and electrochemical properties," *Energies*, vol. 15, no. 24, p. 9352, Dec. 2022, doi: 10.3390/en15249352.

[21] S. Raj, R. Manna, and A. N. Samanta, "Spinel $ZnMn_2O_4$ nanosphere for the efficient Sulfamethazine degradation under visible light irradiation and photoelectrochemical study," *Journal of Environmental Chemical Engineering*, vol. 12, no. 2, p. 112277, Feb. 2024, doi: 10.1016/j.jece.2024.112277.

[22] C. Ho, J. C. Yu, T. Kwong, A. C. Mak, and S. Lai, "Morphology-Controllable synthesis of mesoporous $CeO_2$ nano- and microstructures," *Chemistry of Materials*, vol. 17, no. 17, pp. 4514–4522, Jul. 2005, doi: 10.1021/cm0507967.

[23] D. Zheng, X. Yue, Z. Wang, S. Fan, Z. Zhang, W. Dai, and X. Fu, "Investigation into the photothermal catalytic $CO_2$ decomposition over $CeO_2$ with different morphologies: Behaviors of oxygen vacancies," *Separation and Purification Technology*, vol. 350, p. 127973, May 2024, doi: 10.1016/j.seppur.2024.127973.

[24] Y. Zheng, K. Li, H. Wang, D. Tian, Y. Wang, X. Zhu, Y. Wei, M. Zheng, and Y. Luo, "Designed oxygen carriers from macroporous $LaFeO_3$ supported $CeO_2$ for chemical-looping reforming of methane," *Applied Catalysis B: Environmental*, vol. 202, pp. 51–63, Aug. 2016, doi: 10.1016/j.apcatb.2016.08.024.

[25] Y. Sun, L. Xu, G. I. N. Waterhouse, M. Wang, X. Qiao, and Z. Xu, "Novel three-dimensional electrochemical sensor with dual signal amplification based on $MoS_2$ nanosheets and high-conductive NH2-MWCNT@COF for sulfamerazine determination," *Sensors and Actuators B Chemical*, vol. 281, pp. 107–114, Oct. 2018, doi: 10.1016/j.snb.2018.10.055.

[26] R. Karthik, K. Balamurugan, S.-M. Chen, R. Sukanya, P.R. Chavan, V.Q. Nguyen, J.-J. Shim, and C.B. Breslin, "Investigation of the electrocatalytic activity of bismuth-substituted pyrochlore $Y_2Sn_2O_7$ for the voltammetry determination of the antipsychotic drug," *Materials Today Chemistry*, vol. 26, p. 101117, Aug. 2022, doi: 10.1016/j.mtchem.2022.101117.

[27] M. Jie, S. Lan, B. Zhu, A. Zhu, X. Yue, Q. Xiang, and Y. Bai, "Europiu m functionalized porphyrin-based metal-organic framework heterostructure a nd hydrogel for visual ratiometric fluorescence sensing of sulfonamides in foods," *Food Chemistry*, vol. 458, p. 140304, Jul. 2024, doi: 10.1016/j.foo dchem.2024.140304.

[28] A. A. Lahcen, S. A. Errayess, and A. Amine, "Voltammetric determination of sulfonamides using paste electrodes based on various carbon nanomateri als," *Microchimica Acta*, vol. 183, no. 7, pp. 2169–2176, Apr. 2016, doi: 10.1007/s00604-016-1850-3.

[29] M. Zhao, M. Sun, Q. Kang, X. Ma, and D. Shen, "A differential strategy to enhance the anti-interference ability of electrochemical molecularly impri nted polymers sensors for the determination of sulfamerazine and 4-acetami dophenol," *Sensors and Actuators B Chemical*, vol. 366, p. 131977, May 2022, doi: 10.1016/j.snb.2022.131977.

[30] İ. Koçak, "ZnO and Au nanoparticles supported highly sensitive and selective electrochemical sensor based on molecularly imprinted polymer for sulfaguanidine and sulfamerazine detection," *Journal of Pharmaceutical and Biomedical Analysis*, vol. 234, p. 115518, Jun. 2023, doi: 10.1016/j.jpba.2023.115518.

[31] R. Surya, S. Sakthinathan, G. A. Meenakshi, C.-L. Yu, and T.-W. Chiu, "Construction of $Cu_2Y_2O_5$/G-$C_3N_4$ novel composite for the sensitive and selective Trace-Level electrochemical detection of sulfamethazine in food and water samples," *Sensors*, vol. 24, no. 17, p. 5844, Sep. 2024, doi: 10.3390/s24175844.

[32] M. Govindaraj, J. Rajendran, U. G. P. K, M. K. Muthukumaran, B. Jayaraman, and A. S. J, "Graphitic Carbon Nitride Nanosheets Decorated with Strontium Tungstate Nanospheres as an Electrochemical Transducer for Sulfamethazine Sensing," *ACS Applied Nano Materials*, vol. 6, no. 2, pp. 930–945, Jan. 2023, doi: 10.1021/acsanm.2c04322.

# **Chapter 7** Electrochemical Detection of Sparfloxacin (SPAR) with the functionalised CNFs combined with $CeFe_2O_4$-$CeO_2$

# 7.1. Introduction

Fluoroquinolones are increasingly reported in aquatic systems, and sparfloxacin (SPAR), a third-generation member of this class, is routinely detected at μg $L^{-1}$ levels in surface waters [1,2] and wastewaters [3,4], motivating sensitive [5,6], portable measurements in complex matrices [7,8]. While chromatographic and fluorescence methods remain effective, their cost and infrastructure demands constrain routine field deployment [9-12]. This chapter develops an electrochemical route tailored to SPAR that couples a mixed-oxide/spinel transducer with a conductive carbon scaffold, and, in parallel, explores a high-surface-area carbon-cloth format for enhanced sensitivity and practical sample handling.

Specifically, a cerium–iron mixed-oxide composite ($CeFe_2O_4$-$CeO_2$, hereafter CFO) is synthesised by co-precipitation and calcination, then integrated with non-covalently dispersed carbon nanofibres (CNFs) to yield a uniform CFO-CNFs modifier for glassy carbon electrodes (GCE/CFO-CNFs). Structure and surface chemistry are established by SEM/EDX, XRD and FTIR, while XPS confirms $Ce^{3+}/Ce^{4+}$ and $Fe^{2+}/Fe^{3+}$ redox couples consistent with oxygen-vacancy-rich CFO.

Electrochemical characterisation with $Ru(NH_3)_6^{3+}$ and impedance spectroscopy evidences a substantial increase in electroactive area and a marked decrease in charge-transfer resistance relative to bare GCE, attributable to intimate oxide–carbon interfacing and CNF-enabled percolation. To benchmark scalability, a complementary carbon-cloth architecture (CC/CFO- $CeO_2$) is fabricated by immobilising CFO with $CeO_2$ and binder onto pre-treated carbon cloth, affording a porous, mechanically robust platform suited to low-level SPAR analysis.

Analytical studies employ cyclic and differential-pulse voltammetry in near-neutral phosphate buffer. Peak potential shifts with pH (≈ 0.0567 V $pH^{-1}$) indicate coupled proton–electron transfer during the irreversible oxidation of SPAR; scan-rate analyses reveal adsorption-controlled kinetics, guiding a short pre-accumulation step (15 min) that maximises response. The GCE/CFO-CNFs sensor exhibits wide linearity (0.06-240 μM), a sensitivity of 0.524 μA $\mu M^{-1}$ $cm^{-2}$ and a detection limit of 49 nM, with excellent repeatability and device-to-device reproducibility.

The CC/CFO-$CeO_2$ format further lowers the detection limit to 14 nM and delivers high sensitivities over dual dynamic ranges (10 nM-5 μM; 6-240 μM). Selectivity against common ions and co-occurring drugs is demonstrated, and recoveries are validated in spiked tap water, canal water and artificial urine. Collectively, the CFO-CNFs and CC/CFO-$CeO_2$ interfaces provide robust, scalable sensors for SPAR monitoring, balancing catalytic activity, fast electron transfer and adsorption-assisted preconcentration within practical, low-cost architectures.

## 7.2. Experimental

### 7.2.1. Synthesis of $CeFe_2O_4$-$CeO_2$ (CFO)

A co-precipitation method was employed to form CFO, as shown in Scheme 7.1. In a typical synthesis, cerium chloride heptahydrate ($CeCl_3 \cdot 7H_2O$) and iron chloride tetrahydrate ($FeCl_2 \cdot 4H_2O$) were dissolved in 100 mL of deionised water (DI water) to give concentrations of 0.1 M Ce(III) and Fe(II). This solution was stirred continuously for 30 min. An ammonium carbonate ($(NH_4)_2CO_3$) solution was prepared in 100 mL of DI water to give a final concentration of 0.1 M, with continuous magnetic stirring for 30 min. Then the two solutions were mixed and maintained at a constant temperature of 60 °C and a pH of 7-8, with continuous stirring for 6.5 h. On completion of the reaction, the solid was collected and washed with ethanol (5 times) and DI water (3 times) and then dried at 60 °C in an oven for 12 h. The $CeFe_2O_4$-$CeO_2$ (CFO) was then calcinated in air at 550 °C for 3 h.

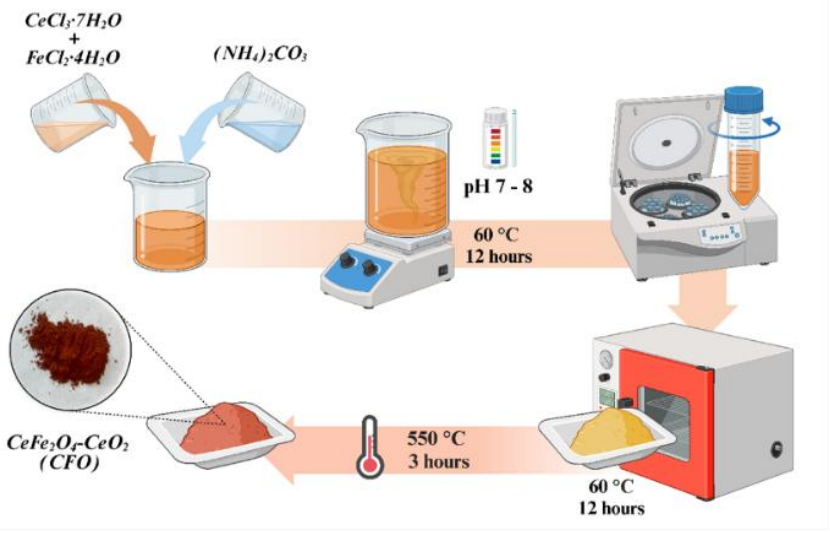


**Scheme 7.1.** Schematic representation of the fabrication of synthetic GCE/CFO-CNFs sensor for SPAR.

## 7.2.2. Dispersion of carbon nanofibers (CNFs)

For the good dispersion of the CNFs, our previously reported method using tannic acid was employed [13,14], as shown in Scheme 7.2. Typically, 50 mg of pristine carbon nanofibers were combined with 50 mL of 1 mM tannic acid to give a CNF concentration of 1 mg $mL^{-1}$. This mixture was sonicated for 30 min, stirred overnight and then probe sonicated for 60 min (18-20 °C) to give the non-covalent functionalisation of the CNFs. Afterwards, the functionalised fibres were recovered from the solution using a centrifuge, washed twice with ethanol, and dried overnight in an oven at 60 °C.

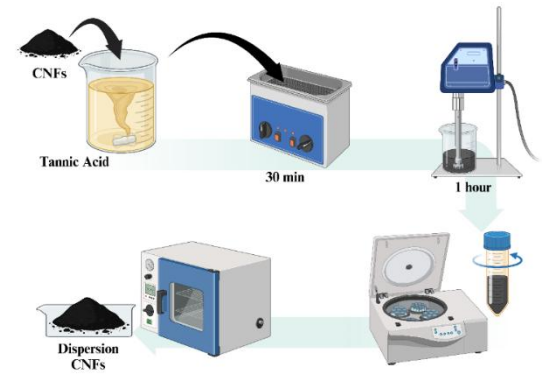


**Scheme 7.2.** Dispersion of carbon nanofibers (CNFs).

## 7.2.3. Formation of the GCE/CFO-CNFs composite sensor

For the preparation of the SPAR sensor, the CFO was combined with the functionalised CNFs to give a CFO-CNFs composite, as shown in Scheme 7.3. A glassy carbon electrode (GCE, 3 mm in diameter) was polished on a microcloth with a 1 μm diamond particle suspension, thoroughly rinsed in DI water and dried under a stream of air. The CFO-CNFs composite was sonicated in 10 mL of DI water with ethanol (1:1 ratio by volume) with 4 mg CFO and 5 mg CNFs for 30 min (optimised composition). Then 5 μL of this dispersion was drop-cast onto the prepared GCE to form GCE/CFO-CNFs, which were then dried. The GCE/CFO-CNFs was polarised at the required potential for

a 30-min period to ensure steady-state conditions prior to the impedance analysis. A 10 mV perturbation was used, while the frequency range was varied from 10 kHz to 5 mHz.

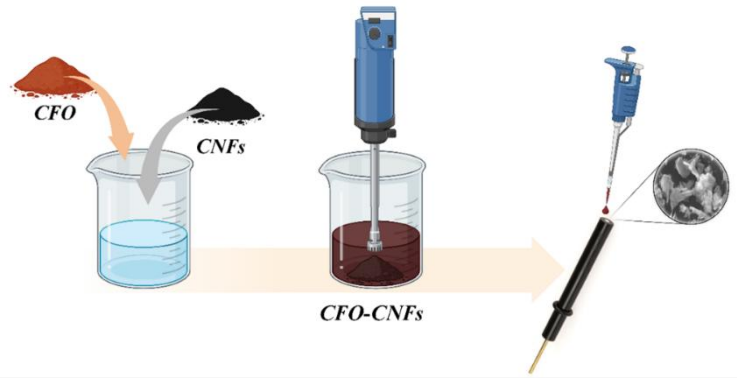


**Scheme 7.3.** The GCE/CFO-CNFs composite sensor.

## 7.2.4. Preparation of the carbon cloth and formation of CC/CFO-$CeO_2$

The carbon cloth (CC) was immersed in 1.0 M HCl solution and sonicated for 20 min. The treated CC was thoroughly washed using DI water followed by absolute ethanol to ensure its surface was clean and free from any HCl. The CC was then dried in an oven at 50 °C.

In the synthesis of $CeO_2$, 50 mL of 0.5 M $Ce(NO_3)_3$ was taken and adjusted to a pH of 12.0 using a small volume of 1.0 M KOH. The solution was stirred for 2 h and then heated at 180 °C for 14 h in a 100 mL hydrothermal autoclave. After the reactor reached room temperature, the product and washed with ethanol (5 times) and DI water (3 times). The purified $CeO_2$ product was collected using centrifugation and dried for 12 h in an oven at 60 °C.

The cleaned CC was then coated with the CFO and synthesised $CeO_2$. In a typical experiment, 40 mg of CFO and 20 mg of $CeO_2$ were mixed with 3.6 mg of polyvinylidene fluoride (PVDF), which served as a binder. This powder was placed in

a mortar and 3 drops of N-Methyl-2-pyrrolidone (NMP) were added. Using a pestle, the mixture was ground for 20 min to give a completely mixed puree-like blend. This was spread carefully and evenly over the pre-treated CC, and then thoroughly dried for 12 h at 50 °C to give CC/CFO-$CeO_2$, as shown in Scheme 7.4.

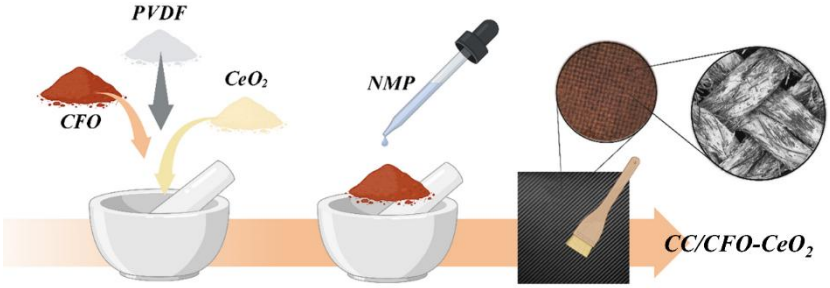


**Scheme 7.4.** The CC/CFO-$CeO_2$ composite sensor.

All the electrochemical and surface analysis equipment used in this study is described in Chapter 2. Those include electrochemical equipment: cyclic voltammetry (CV), differential pulse voltammetry experiments (DPV) and electrochemical impedance spectroscopy (EIS) in Section 2.3.3; surface analysis equipment: scanning electron microscopy (SEM), X-ray diffraction (XRD), energy dispersive X-ray analysis (EDX), FTIR measurements and X-ray photoelectron spectroscopy (XPS) in Section 2.4 and 2.5. The procedure for material characterisation methods and specific characterisation techniques usage is detailed in the corresponding sections of Chapter 2, Experimental and Research Methods.

## 7.3. Results and discussion

### 7.3.1. Characterisation of CFO, CFO-CNFs and CC/CFO-$CeO_2$

The synthesis of CFO and its application in the electrochemical detection of SPAR are summarised in Schemes 7.1 and 7.3. For the sensing studies, the CFO was combined with the CNFs (GCE/CFO-CNFs). For studies on carbon cloth (CC), the CFO was combined with $CeO_2$ and PVPD, which served as a binder, while CC served as a support to provide a high-surface-area catalyst (CC/CFO-$CeO_2$). The CC/CFO-$CeO_2$ was also successfully employed in the sensing studies, as shown in Scheme 7.4.

The morphology of CFO, CFO-CNFs, and CC/CFO-$CeO_2$ was systematically investigated using SEM. As shown in Fig. 7.1 (a), CFO exhibits a distinct flake-like morphology, accompanied by dispersed particles. The flakes and particles range in size from approximately 33 nm for the smallest particles to 0.6 μm for the largest flakes, with some degree of agglomeration observed. Upon incorporation of CFO with CNFs, depicted in Fig. 7.1 (b) and (c), the CNFs remain well dispersed, although some bundling is apparent. The CFO flakes and particles are predominantly distributed on the surface of CNFs, as indicated in Fig. 7.1 (c), while a fraction remains unattached, contributing to an increased surface area favourable for electrochemical sensing applications.

The surface morphology of the CC/CFO-$CeO_2$ composite is presented in Fig. 7.1 (d–f). The low-resolution image reveals a uniform coating of the CC substrate by the CFO-$CeO_2$, with a characteristic brown/orange colouration attributed to the presence of iron in the CFO. Higher resolution SEM images, presented in Fig. 7.1 (e) and (f), provide a more detailed view of the individual CC strands, which are well covered by CFO-$CeO_2$. Additionally, some CFO-$CeO_2$ is also captured between the strands.

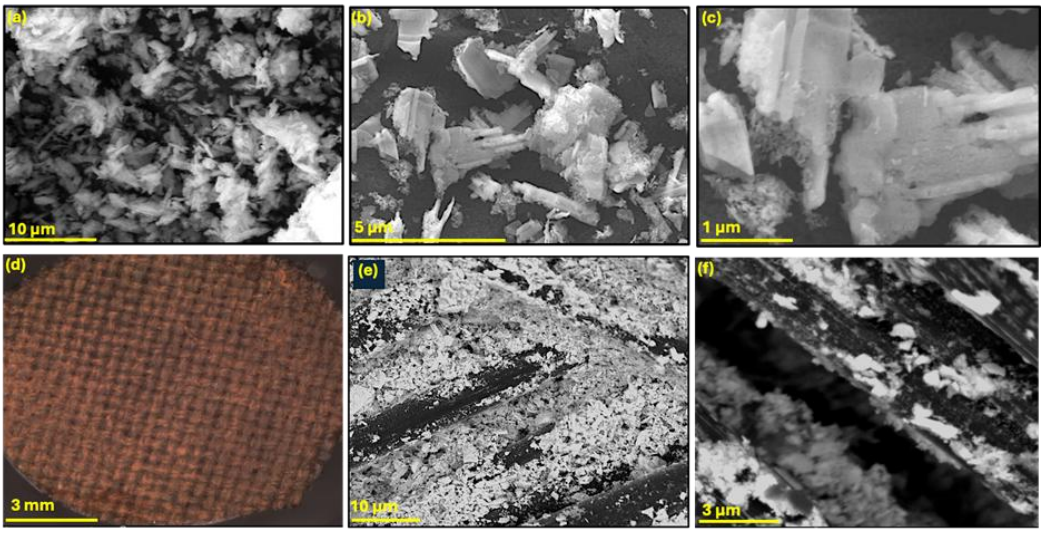


**Figure 7.1.** SEM micrographs of (a) CFO powder, (b,c) CFO combined with CNFs, (d) low-resolution image of CC/CFO-$CeO_2$ and (e,f) higher resolution images of CC/CFO-$CeO_2$.

The XPS survey spectrum of CFO is shown in Fig. 7.2 (a). It indicates the presence of Fe, Ce and O. The high-resolution Ce 3d spectrum is shown in Fig. 7.2 (b), with further deconvolution into eight envelopes, indicating the presence of both $Ce^{3+}$ and $Ce^{4+}$ at the surface. In particular, the peaks centred at 904.3 and 886.1 eV can be attributed to $Ce^{3+}$, while those at 917.0, 907.9, 900.6, 898.8, 892.1 and 882.2 eV are indicative of $Ce^{4+}$. These assignments are in good agreement with a recently reported study where a $CeFe_2O_4$ spinel was combined with graphene oxide [15]. The ratio of $Ce^{3+}$ to $Ce^{4+}$ was computed as 4:3. This indicates the presence of nearly equal levels of $Ce^{3+}$ and $Ce^{4+}$ in the CFO ($CeO_2$ and $CeFe_2O_4$ spinel), as typically seen with $CeO_2$ [16]. Also, the presence of $Ce^{3+}$ in $CeO_2$ has been attributed to oxygen vacancies [17]. The O 1s was deconvoluted into three peaks at 533.1, 531.2 and 529.5 eV, as shown in Fig. 7.2 (c). These peaks can be attributed to the oxygen in the spinel, lattice oxygen in the $CeO_2$ and surface oxygen species. The Fe 2p, Fig. 7.2 (d), is composed of 2 $p_{3/2}$ centred at 711.5 eV and 2 $p_{1/2}$ at 725.3 eV, consistent with the presence of both $Fe^{2+}$ and $Fe^{3+}$. Additionally, the satellite peaks at 718.6 and 733.4 eV confirm the presence of both $Fe^{2+}$ and $Fe^{3+}$ ions. This shows that iron provides both the divalent and trivalent cations in the CFO-based spinel.

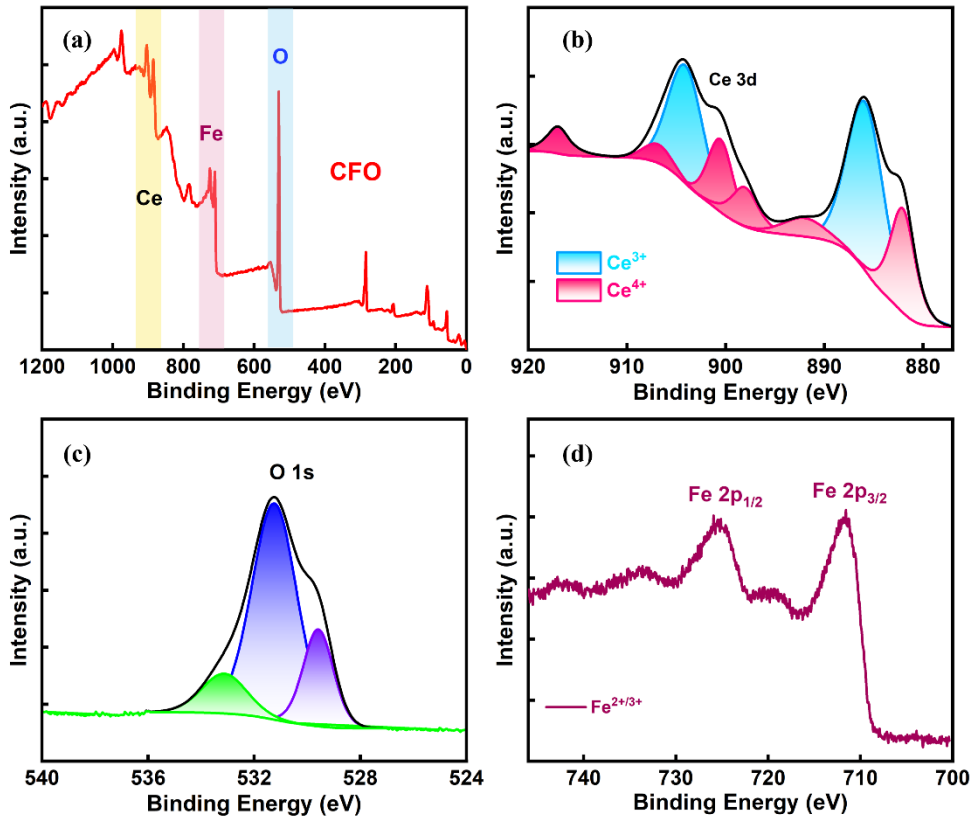


**Figure 7.2.** (a) XPS survey spectrum of CFO, indicating the presence of Ce, Fe and O, (b) XPS of Ce 3d, (c) XPS of O 1s, and (d) XPS of Fe 2p.

The XPS analysis of the tannic acid-functionalised CNFs is shown in Fig. 7.3 (b). The C 1s data are presented for the pristine and tannic acid-modified CNFs. Clearly, the nature of the oxygenated groups changes following non-covalent functionalisation. This indicates the adsorption of tannic acid at the CNFs as seen in Fig. 7.3, with the peaks at 286.5 and 288.9 eV arising from the C–O and C=O groups of the tannic acid molecule [18]. This adsorption process arises through π–π interactions between the hydrophobic aromatic rings of tannic acid and the hydrophobic carbon fibres. In contrast, the tannic acid oxygen-containing groups facilitate the good dispersion of the modified CNFs in water, as discussed in our recent work [14].

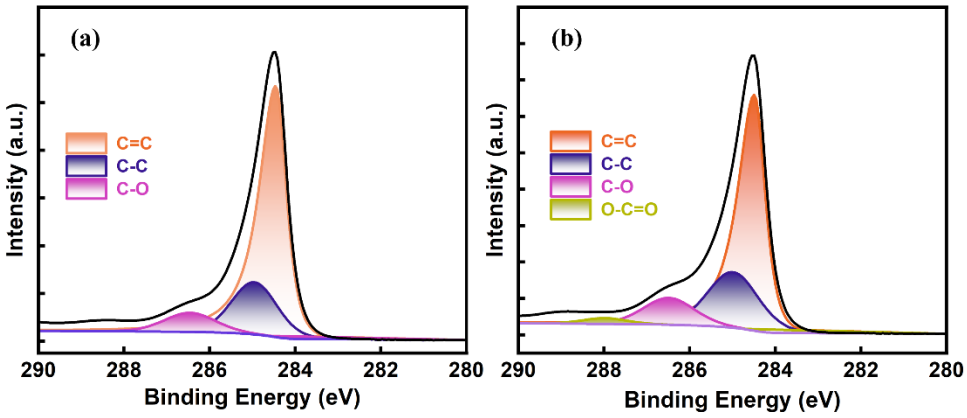


**Figure 7.3.** XPS data, C 1s, recorded for (a) pristine and (b) tannic acid modified CNFs.

The XRD spectra of the CFO and CFO-CNFs are shown in Fig. 7.4 (a). Both spectra are compared with the standard cards for $CeO_2$ (ICDD 04-016-6171) [19], $Fe_2O_3$ (ICDD 01-089-0596) [20] and $Ce_{0.9}Fe_{0.1}O_2$ (ICDD 01-090-3053) [21] in Fig. 7.4 (b, c). While the spectra in Fig. 7.4 (a) show well-defined peaks, the crystallinity is somewhat lower than might be expected for high-purity ferrite spinels, and this may be related to the nature of the composite. It contains not only ferrite spinel but also $CeO_2$. The peaks at 28.62, 33.18, 47.52, 56.52 and 68.46° can be assigned to the (220), (311), (331), (422), and (511) lattice planes of the spinel, indicating a clearly defined spinel phase, which is in good agreement with previously reported ferrite spinels [22,23]. The peak at 28.62° may also be assigned to the $CeO_2$ oxide (ICDD 04-016-6171), Fig. 7.4 (b), while some of the other peaks are also in good agreement with $CeO_2$ [19], indicating its presence in the CFO. The additional peak at 26.43°, seen with the CFO-CNFs, is connected with the CNFs, and this is characteristic of graphitic-based materials [24]. However, this peak is somewhat lower in intensity due to the surface modification of the CNFs with the tannic acid molecules, which become adsorbed onto the surface of the CNFs, as seen in our previous work [14]. Interestingly, there is no evidence of any shifts in the position of the peaks on adding the CNFs. This implies that the CNFs primarily act as a support for the CFO without altering its intrinsic crystalline nature.

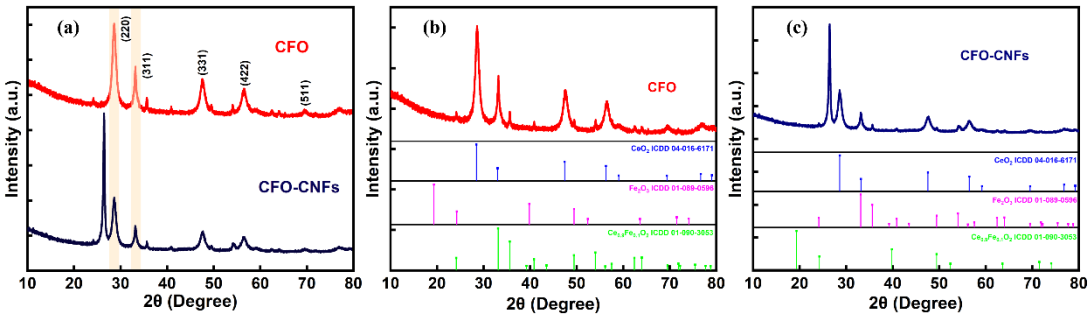


**Figure 7.4.** XRD of (a) CFO and CFO-CNFs; (b) CFO and (c) CFO/CNFs compared to $CeO_2$ (ICDD 04-016-6171), $Fe_2O_3$ (ICDD 01-089-0596) and $CeFeO_2$ (ICDD 01-090-3053).

The FTIR spectra recorded for the CFO before and after calcination are shown in Fig. 7.5, and are clearly very different. Prior to calcination, the spectrum is dominated by adsorbed water molecules (3154 $cm^{-1}$), Ce-O and Fe-O oxides/hydroxides between 600 and 900 $cm^{-1}$, and impurities. Following calcination, distinct metal-oxygen stretching vibrations become evident at 535 and 470 $cm^{-1}$, characteristic of spinel oxides [25], in which the cations are arranged in tetrahedral and octahedral sites. The peak at 470 $cm^{-1}$ is assigned to the cations in the octahedral sites, while the stretch at 535 $cm^{-1}$ represents the tetrahedral sites [26].

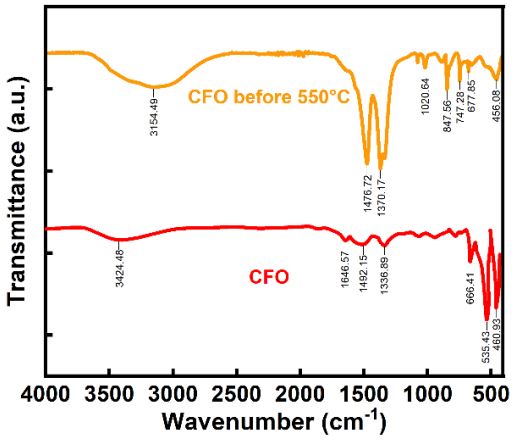


**Figure 7.5.** FTIR of CFO prior to and following calcination at 550 °C.

As the CFO contains $Fe^{2+}$, $Fe^{3+}$ and $Ce^{3+}$ cations, as shown in the XPS analysis, both the $Ce^{3+}$ and $Fe^{3+}$ will provide the trivalent ions. Therefore, some of the larger $Ce^{3+}$ ions

can replace $Fe^{3+}$ ions in the tetrahedral sites, introducing strain within the CFO. This, in turn, may enhance the electrochemical activity of the CFO. The additional absorption bands at 1336, 1492, 1646 and 3434 $cm^{-1}$ were assigned to $CeO_2$ [27], while the peak at 666 $cm^{-1}$ is consistent with the Fe-O bond, indicating the presence of iron oxides [28], which is in good agreement with the XPS data, Fig. 7.2 (d) and Fig. 7.4.

## 7.3.2. Optimisation and electrochemical characterisation studies

The electrochemical analysis of SPAR was initially studied using cyclic voltammetry, with representative CVs presented in Fig. 7.6. In this analysis, the irreversible oxidation of SPAR was examined at both the GCE and the GCE/CFO-CNFs. For comparison purposes, the CV recorded for the GCE/CFO-CNFs in buffer solution is included. As anticipated, no oxidation peaks are observed within the buffer solution. However, a comparatively high capacitive current is evident, which can be ascribed to the presence of CNFs and the inherent properties of the GCE substrate. It is apparent that the peak current for the oxidation of SPAR at the GCE/CFO-CNFs surpasses that of the bare GCE, and also occurs at a slightly lower potential, indicating a more thermodynamically favoured oxidation reaction.

The conducting properties of the GCE/CFO-CNFs and GCE were compared using electrochemical impedance spectroscopy. The data were recorded at a pH of 7.0 in 100 μM SPAR, at a potential corresponding to the peak for the oxidation of SPAR. The recorded data are presented as Nyquist plots for the GCE substrate and the GCE/CFO-CNFs in Fig. 7.6 (b), showing a considerably higher impedance for the bare GCE compared to the GCE/CFO-CNFs. The data were fitted to a simple Randles cell, incorporating a solution resistance term, $R_s$ and a parallel RC couple, where R indicates the charge transfer resistance, $R_{ct}$, and C represents a constant phase element. The $R_{ct}$ and C were deduced as 132 ± 3.55 Ω and 25.7 ± 0.62 $\mu\Omega^{-1}$ $s^{0.65}$ for GCE/CFO-CNFs, indicating a low $R_{ct}$ value combined with a relatively high C value with the exponent at

0.65, deviating considerably from an ideal capacitor. A much higher $R_{ct}$ at 775 ± 16.21 Ω and lower C of 4.286 ± 0.12 $\mu\Omega^{-1}$ $s^{0.85}$ were seen with the GCE. These results show that modifying GCE with CFO-CNFs increases its conductivity, thereby enhancing its performance as an electrochemical sensor.

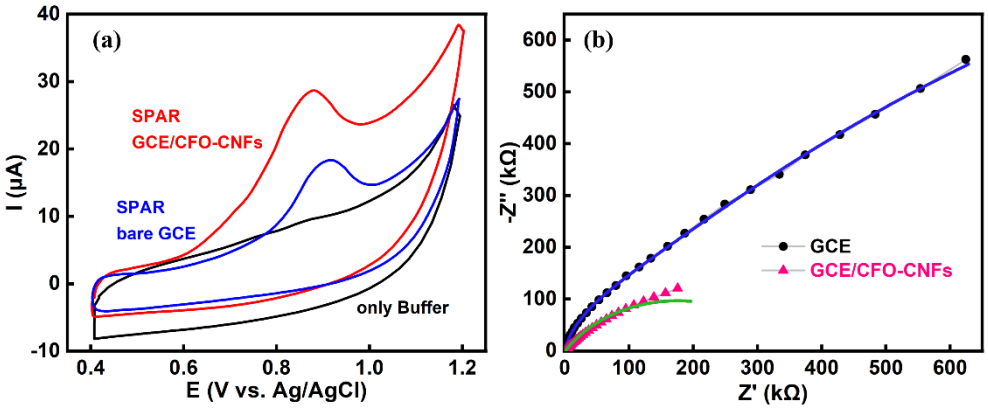


**Figure 7.6.** (a) CVs recorded in 100 μM SPAR for GCE and GCE/CFO-CNFs and in the buffer for GCE/CFO-CNFs; (b) impedance data recorded in 100 μM SPAR, at a pH of 7.0 for GCE and GCE/CFO-CNFs.

The influence of the individual components of the GCE/CFO-CNFs composite was examined by studying $CeFe_2O_4$, $CeO_2$ and CNFs in the electrochemical analysis of SPAR. This analysis was carried out using DPV to minimise the capacitive background currents seen in the CVs. The corresponding data are summarised in Table 7.1. A comparison of GCE/$CeO_2$ and GCE/CNF shows that the CNFs contribute to a higher peak current compared to both the bare GCE and the GCE/$CeO_2$. However, the current decreases after the second and third cycles. Conversely, the GCE/$CeO_2$ demonstrates greater stability over the three cycles, although its peak current is relatively low. When the CNFs and $CeO_2$ are combined with $CeFe_2O_4$ to create the optimised sensor, GCE/CFO-CNFs, both high peak currents and good stability are observed, with an RSD of 0.62% across the three cycles. This indicates that the CFO (which contains $CeO_2$) provides good stability over the three repeated cycles, while the well-dispersed CNFs facilitate the transfer of electrons giving rise to higher peak currents, Table 7.1. The GCE/CFO-CNFs composite also exhibits an electrocatalytic effect, with the peak

potential of the GCE at 812 mV, while the peak potential is significantly lower at 772 mV for the GCE/CFO-CNFs.

**Table 7.1** Peak currents recorded for 100 μM SPAR in 0.1 M PB solution at a pH of 7.0 using DPV for the various modified GCE substrates.

| Modified electrode | Cycle I Current (μA) | Cycle II Current (μA) | Cycle III Current (μA) | Average Current (μA) | RSD (%) |
|---|---|---|---|---|---|
| GCE | 5.484 | 5.051 | 4.921 | 5.152 | 5.72 |
| GCE/CFO | 3.465 | 3.095 | 2.802 | 3.121 | 10.65 |
| GCE/$CeO_2$ | 2.494 | 2.057 | 1.949 | 2.167 | 13.32 |
| GCE/CNFs | 7.057 | 4.920 | 4.695 | 5.557 | 23.46 |
| GCE/CFO-CNFs | 11.82 | 11.70 | 11.69 | 11.74 | 0.62 |

It is clear from the SEM micrographs in Fig. 7.1 that the modification of GCE with the CNFs and CFO gives rise to an increase in the surface area. To probe the extent of this surface area increase, the $Ru(NH_3)_6Cl_3$ electrochemical probe dissolved in 0.1 M KCl was employed. The well-known anionic $K_3Fe(CN)_6/K_4Fe(CN)_6$ system was not chosen due to its potential electrostatic repulsion with the oxygenated species at the surface of the CFO, as seen in the XPS analysis in Fig. 7.2.

The CVs were recorded between −0.45 V and 0.0 V vs Ag/AgCl and the peak currents were recorded as a function of the scan rate. Typical CVs are shown in Fig. 7.7 (a) for the cycling of GCE/CFO-CNFs in this $Ru(NH_3)_6Cl_3$ solution. Good reversibility was achieved with a peak-peak separation of 65.8 mV, whereas a much higher separation of 117.8 mV was observed with the GCE.

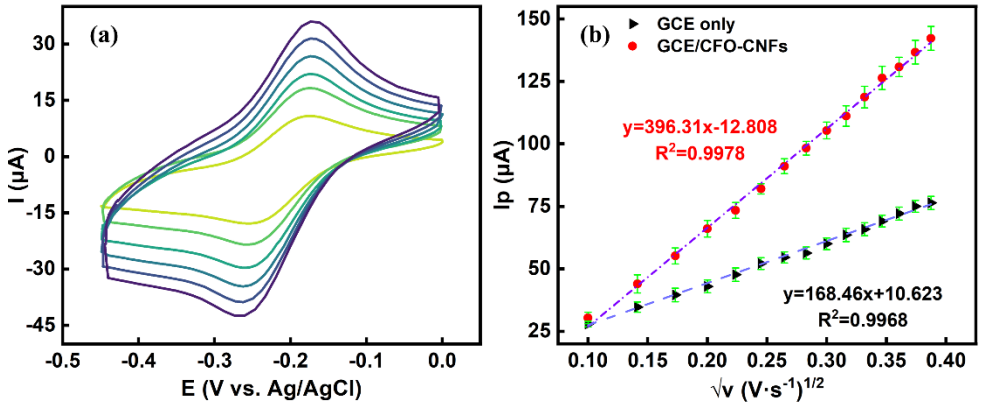


**Figure 7.7.** (a) CVs recorded for GCE/CFO-CNFs in 2.5 mM $Ru(NH_3)_6^{3+}$ in 0.1 M KCl, and (b) peak current plotted against the square root of the scan rate in 2.5 mM $Ru(NH_3)_6^{3+}$ in 0.1 M KCl for GCE/CFO-CNF and GCE (n=3).

The peak currents in Fig. 7.7 were plotted as a function of the square root of the scan rate according to the Randles-Sevcik relationship, Eq. (7.1), where D corresponds to the diffusion coefficient of the $Ru(NH_3)_6^{3+}$, which was taken as $9.0 \times 10^{-6}$ cm$^2$ s$^{-1}$ [29], A indicates the electrochemical active surface area, and the concentration (C) of the probe was set at 2.5 mM. Linear plots were obtained, as illustrated in Fig. 7.7 (b), suggesting that this redox reaction is diffusion-controlled. The equations of the linear regions were obtained as $I_p$ (μA) = 396.31 $\upsilon^{1/2}$ (V$^{1/2}$ s$^{-1/2}$) − 12.8 for GCE/CFO-CNFs and $I_p$ (μA) = 168.4 $\upsilon^{1/2}$ (V$^{1/2}$ s$^{-1/2}$) + 10.6 for the GCE. Using Eq. (2.2), the surface areas were estimated as 0.080 cm$^2$ for GCE and 0.195 cm$^2$ for the GCE/CFO-CNFs. This shows that the surface area increases by approximately a factor of 2.5, on decorating the GCE with the CFO-CNFs.

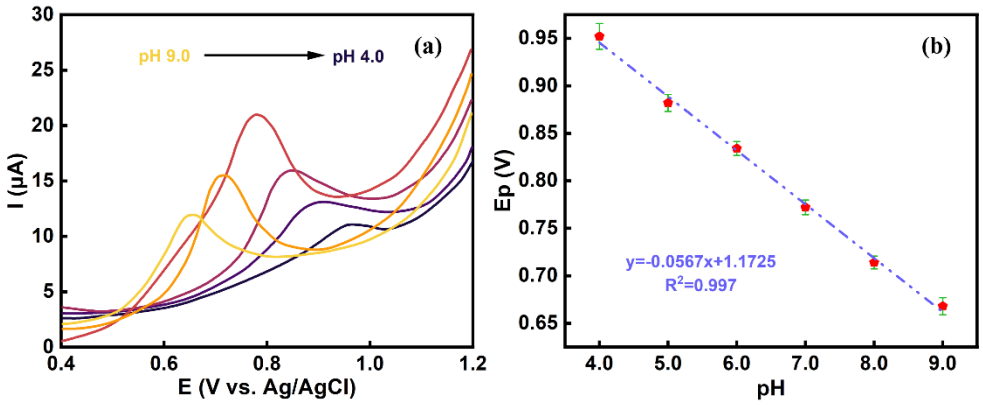


**Figure 7.8.** (a) DPVs recorded at pH values of 9.0, 8.0, 7.0, 6.0, 5.0 and 4.0, with 100 μM SPAR, (b) $E_p$, plotted as a function of the pH in 100 μM SPAR solution (n=3).

The optimal pH for the detection of SPAR at GCE/CFO-CNFs was investigated by DPV, and typical DPV data recorded over pH 4.0-9.0 are presented in Fig. 7.8 (a). The peak potential varies with the pH, and this is more clearly shown in Fig. 7.8 (b). A linear plot is achieved, with a gradient of 0.0567 V/pH. This aligns well with the Nernst equation, indicating that an equal number of electrons and protons are transferred during the oxidation of SPAR, as illustrated in Scheme 7.5. The peak current varies significantly with the pH of the solution, Fig. 7.8 (a), and this seems to be connected to the nature of the electrostatic interactions between SPAR and the GCE/CFO-CNFs. The SPAR molecule, with both an amine and a carboxylic group, has $pK_a$ values of 6.3 and 8.8. Accordingly, the SPAR will adopt a predominantly positive charge at pH values below 6.3, a neutral charge between pH values of 6.3 and 8.8, and a negative charge when the pH is greater than 8.8 [30]. The surface charge of the GCE/CFO-CNFs also depends on pH [31]. At low pH values, the surface of ferrite spinels becomes dominated by an excess positive charge due to protonation of the hydroxyl groups, and this will result in repulsive interactions with the cationic SPAR. This is consistent with the very low peak current observed at a pH of 4.0. At higher pH values, the surface of the GCE/CFO-CNFs becomes more negatively charged due to the deprotonation of hydroxyl groups. Again, this will repel the anionic SPAR, to give lower currents at pH values of 8.0 and 9.0. The optimum pH is clearly near 7.0, where these unfavourable electrostatic

interactions are minimised and the SPAR acquires an overall neutral charge. Accordingly, a pH of 7.0 was selected for all the analytical studies.

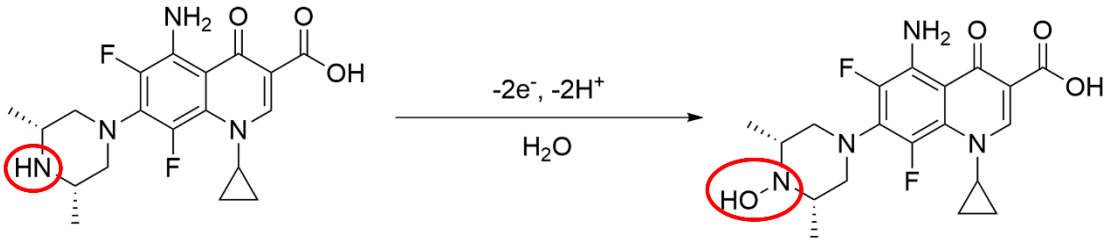


**Scheme 7.5.** Electrochemical oxidation of SPAR.

## 7.3.3. Optimisation and analytical parameters

Prior to studying the analytical parameters, the role of SPAR diffusion and adsorption was investigated at the optimal pH of 7.0. Scan rate studies were performed to gain insight into the role of diffusion and adsorption during the oxidation of SPAR. The CVs recorded as a function of scan rate are depicted in Fig. 7.9 (a), where it is seen that the peak current increases with increasing scan rate. There is also a shift in the peak potential to higher values as the scan rate increases. This suggests a sluggish oxidation of SPAR. On plotting the peak current as a function of the square root of the scan rate (diffusion control) and the scan rate (adsorption control), the data fitted the adsorption control. A linear plot was achieved with a linear regression equation of $I_p$ (μA) = 201.6 υ (V $s^{-1}$) + 1.03 ($R^2$ = 0.995), as indicated in Fig. 7.9 (b). Indeed, on plotting the logarithm of the peak current as a function of the logarithm of the scan rate, a linear plot was obtained with a slope of 0.84, which is close to unity. The corresponding plot is shown in Fig. 7.9 (c), with the linear equation deduced as, log $I_p$ ($I_p$/μA) = 0.84 log υ (υ/V $s^{-1}$) + 2.15 ($R^2$ = 0.991), confirming adsorption control.

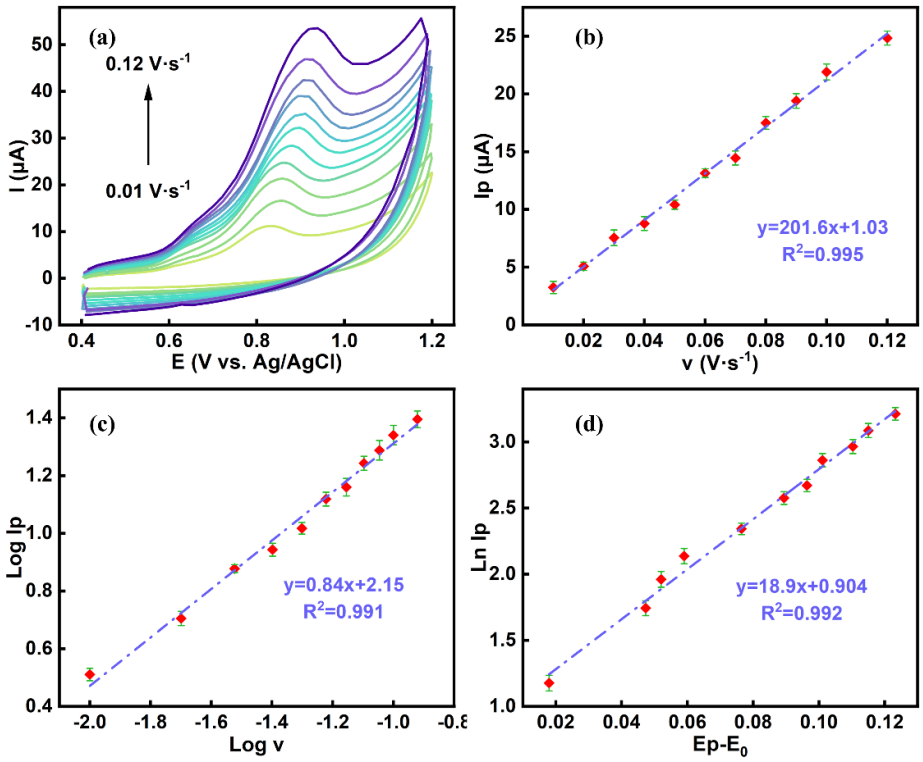


**Figure 7.9.** (a) CVs recorded at various scan rates; (b) corresponding plot of peak current as a function of scan rate for GCE/CFO-CNFs in 100 µM SPAR at a pH of 7.0 (n=3); (c) plot of the logarithm of the peak current as a function of the logarithm of the scan rate for the GCE/CFO-CNFs in 100 µM SPAR, at a pH of 7.0 (n=3), and (d) plot of the logarithm of the peak current as a function of $E_p$-$E^0$ for GCE/CFO-CNFs in 100 µM SPAR, at a pH of 7.0 (n=3).

The concentration of adsorbed SPAR molecules at the GCE/CFO-CNFs was estimated using the expression in Eq. (6.1). Here, r gives the surface concentration of the adsorbed SPAR. The physical constants R and F have their usual meanings, while n corresponds to the number of electrons transferred. For fluoroquinolones, such as SPAR, this is 2 electrons [32], as illustrated in Scheme 7.5. Using the data presented in Fig. 7.9 (b), an approximate adsorbed concentration of $2.92 \times 10^{-10}$ mol $cm^{-2}$ was obtained. The rate constant for the oxidation of the adsorbed SPAR was estimated using Eq. (6.3), where $k^0$ represents the standard rate constant, C is the concentration of SPAR, and $E^0$ is the standard or formal oxidation potential of SPAR [33]. For this analysis, the logarithm of

$I_p$ was plotted as a function of ($E_p$-$E^0$) and a representative plot is provided in Fig. 7.9 (d). The linear regression equation was, ln $I_p$ (I(μA)) = 18.9 (Ep-$E^0$)(V) + 0.90 ($R^2$ = 0.995), indicating the applicability of Eq. (6.3) in the estimation of $k^0$. The n term was taken as 2.0, Scheme 7.5, and $E^0$ was estimated as 0.807 V from the extrapolation of $E_p$ to ν at 0 mV $s^{-1}$, by plotting $E_p$ as a function of the logarithm of ν. Using Eq. (6.3) and the intercept of Fig. 7.9 (d) (adjusted as the current is in units of μA), $k^0$, was estimated as $3.1 \times 10^{-3}$ cm $s^{-1}$.

As the oxidation of SPAR is clearly under adsorption control, SPAR was accumulated under open-circuit conditions and at a range of applied potentials from 0 to 0.4 V vs Ag/AgCl in the buffer containing added SPAR. The role of the accumulation period under open-circuit potentials is illustrated in Fig. 7.10, where it is evident that the optimal accumulation period is 15 min in a solution containing 100 μM SPAR. The data recorded at different applied potentials are summarised in Table 7.2 and show that SPAR adsorption is more efficient at 0.4 V than at lower potentials. Nevertheless, higher peak currents combined with good stability were achieved by enabling the accumulation of SPAR for 15 min under open-circuit conditions, and this method was used in all electrochemical sensing experiments.

**Table 7.2** Influence of the adsorption potential on the peak current recorded for the oxidation of SPAR in 100 μM SPAR at a pH of 7.0. Cycles 1, 2 and 3 indicate repeated cycles, with 0.4 V having the best stability.

| Accumulation potentials (V) | Cycle I Current (μA) | Cycle II Current (μA) | Cycle III Current (μA) | Average Current (μA) | RSD (%) |
|---|---|---|---|---|---|
| 0 | 5.503 | 5.843 | 2.642 | 4.662 | 37.7 |
| 0.1 | 7.771 | 6.644 | 4.246 | 6.220 | 28.9 |
| 0.2 | 6.402 | 5.584 | 5.533 | 5.839 | 8.35 |
| 0.3 | 8.552 | 8.142 | 8.020 | 8.238 | 3.38 |
| 0.4 | 9.762 | 9.643 | 9.602 | 9.669 | 0.86 |

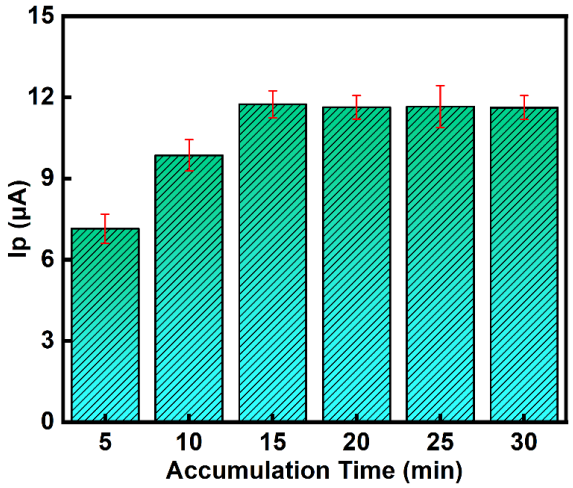


**Figure 7.10.** Influence of the accumulation time under open-circuit conditions on the peak current recorded in 100 μM SPAR at a pH of 7.0 (n=3).

The initial set of experiments focused on determining the analytical parameters, specifically the sensitivity and the limit of detection (LOD). All the data were recorded using DPV. Initially, the GCE/CFO-CNFs was cycled between 0.40 V and 1.0 V vs Ag/AgCl in the neutral buffer until a steady state current was achieved. Subsequently, aliquots of SPAR were added, and the current was recorded. A representative DPV study is summarised in Fig. 7.11 (a), which illustrates the electrode response to SPAR concentrations ranging from 50 nM to 240 μM. These data were then plotted in Fig. 7.11 (b), showing the peak current as a function of SPAR concentration. Good linearity is evident over 60 nM to 240 μM, with a linear regression equation: $I_p$ (μA) = 0.102 C (μM) + 1.55 ($R^2$ = 0.998). Using the gradient of this plot, the sensitivity was calculated as 0.102 μA $\mu M^{-1,}$ and with an estimated surface area of 0.195 $cm^2$, a sensitivity of 0.524 μA $\mu M^{-1}$ $cm^{-2}$ was achieved. The LOD was computed as 49.0 nM (3σ/sensitivity). Interestingly, when a carbon cloth substrate was used, it provided an even lower LOD of 14.0 nM and a higher sensitivity of 3.74 ± 0.23 μA $\mu M^{-1}$.

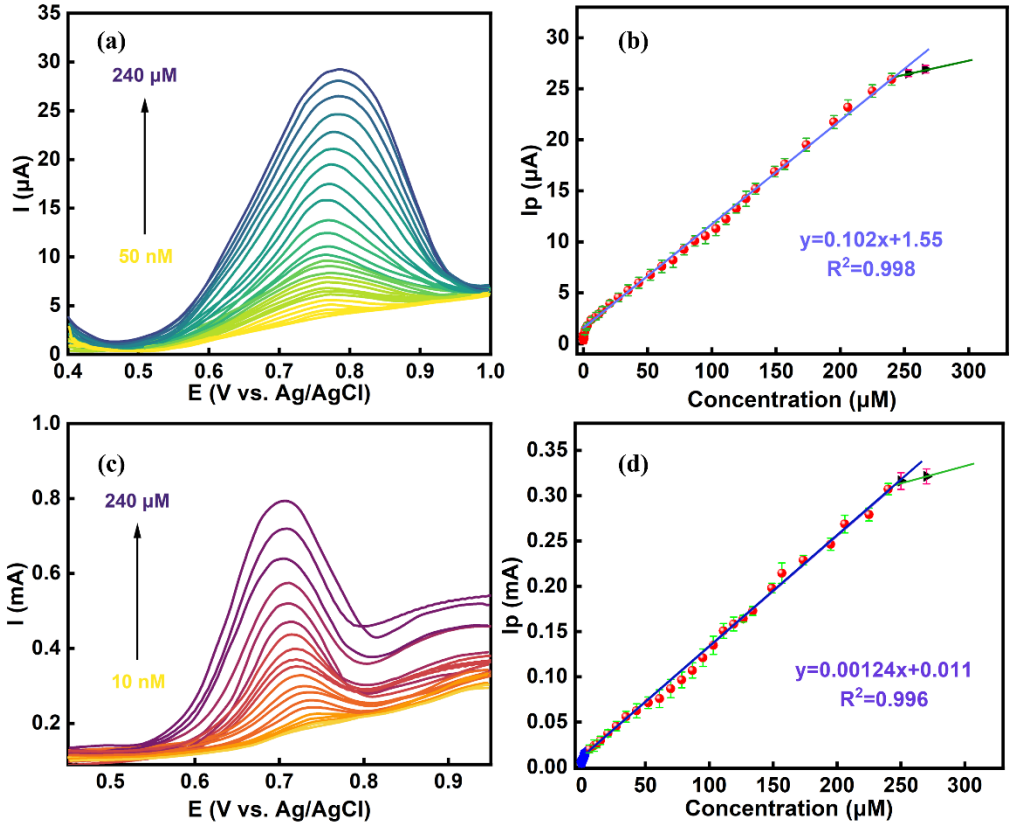


**Figure 7.11.** (a) DPVs recorded at pH 7.0 with various concentrations of SPAR from 50 nM to 240 µM; (b) corresponding linear calibration curve (n=3); (c) DPVs recorded at different concentrations ranging from 10 nM to 240 mM of SPAR using carbon cloth as the substrate with dimensions of 1.0 × 0.5 cm, and (d) corresponding calibration curve with the peak current plotted as a function of the concentration (n=3).

This can be related to the higher surface area of the carbon cloth substrate. The DPVs and the corresponding linear calibration curve are shown in Fig. 7.11. For concentrations between 6 and 240 µM, the linear regression equation was deduced as $I_p$ (mA) = 0.00124 C (µM) + 0.011 ($R^2$ = 0.996), while between 10 nM and 5 µM, the equation was $I_p$ (mA) = 0.00374 C (µM) + 0.00502 ($R^2$ = 0.981). These analytical parameters compare very favourably with those reported for the electrochemical sensors developed for SPAR (Table 7.3). In particular, a broader linear region combined with higher sensitivity is achieved with the GCE/CFO-CNFs, while the CC/CFO-$CeO_2$ exhibits even greater sensitivity due to the larger surface area of the CC. Furthermore, it has the lowest LOD reported in the literature for the detection of SPAR.

**Table 7.3** Comparison of the GCE/CFO-CNFs and the CC/CFO-$CeO_2$ sensors with previously reported sensors for the electrochemical detection of SPAR.

| Sensor | Technique | Linear Range (μM) | LOD (nM) | Sensitivity | Refs. |
|---|---|---|---|---|---|
| GCE/CFO-CNFs | DPV | 0.06–240 | 49.0 | 0.524 μA $\mu M^{-1}$ $cm^{-2}$ | This work |
| CC/CFO-$CeO_2$ | DPV | 0.01–5<br>6–240 | 14.0 | 3.74 μA $\mu M^{-1}$ | This work |
| Au/CPE/SDS | It | 0.1–3.3 | 28.7 | 0.385 μA $\mu M^{-1}$ $cm^{-2}$ | Attia et al. (2016) |
| Cyclodextrin/GPE | DPV | 0.04–60 | 40 | – | Reddy et al. (2003) |
| CPE | DPV | 0.2–60 | 70 | – | El Ries et al. (2005) |

The selectivity of the GCE/CFO-CNFs was studied using a variety of inorganic ions that are commonly found in water systems, such as rivers and lakes, including $Cu^{2+}$, $Fe^{3+}$, $Zn^{2+}$, $Al^{3+}$, $Co^{2+}$, $NO_3^-$, $CO_3^{2-}$, $Cl^-$ and $SO_4^{2-}$ and a selection of other antimicrobial drugs such as sulfanilamide (SFD), sulfapyridine (SAD), flutamide (FLD), and cefadroxil (CEX). To determine the selectivity, the interferants at a concentration of 200 μM, were added to a 100 μM SPAR solution, to give a 2-fold concentration excess. The peak currents were measured in the presence and absence of the interferents, and the ratio of these currents was taken. This analysis is summarised in Fig. 7.12 (a), where unity corresponds to identical peak currents for the pure SPAR solution and the SPAR-containing electrolyte with an excess of the interferent. As evident from this analysis, excellent selectivity is achieved, indicating that the GCE/CFO-CNFs possesses excellent selectivity in the analysis of SPAR.

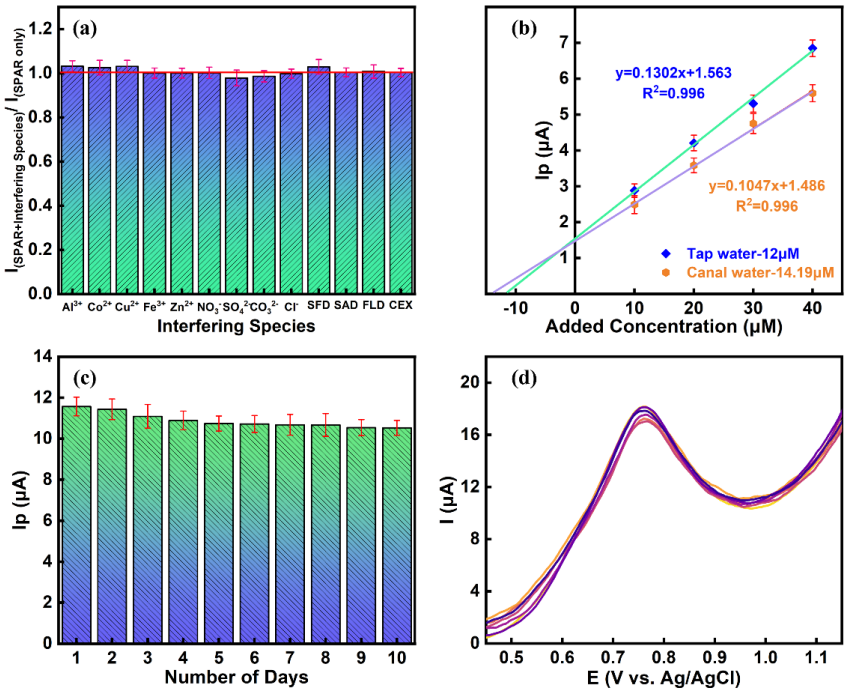


**Figure 7.12.** (a) Selectivity in the presence of ions and other drug molecules where unity represents no interference; (b) standard addition experiment recorded in tap water and canal/river water where the water samples were originally spiked with 10 μM SPAR (n=3); (c) stability of the sensor with continuous immersion in SPAR over a 10-day period (n=3), and (d) stability study with the DPVs recorded over 10 days for the GCE/CFO/CNFs continuously immersed in 100 μM SPAR, at a pH of 7.0.

Assuming that these samples did not contain any SPAR, a sufficient amount of SPAR was added to give a real sample with a concentration of 10 μM SPAR. Then standard aliquots of SPAR were added, and the peak currents were measured and plotted as a function of the concentration and extrapolated to determine the original concentration of SPAR in the solution. This analysis is shown in Fig. 7.12 (b), where the concentration of SPAR in the tap water was determined as 12.0 ± 0.08 μM, but a higher concentration of 14.0 ± 0.16 μM was measured for the canal/river water samples. On comparing these computed levels with the original 10 μM SPAR spike, an error of 20 % for the tap water and an even higher error of 40 % for the real canal/river water sample is seen. This highlights the complex nature of these real water samples, suggesting that the

consecutive additions of SPAR to the real water samples lead to interactions between the added SPAR and some of the constituents, such as microbiological matter, nutrients, suspended solids, sediment-associated species, and organic load of the water samples.

The stability of the sensor was monitored by immersing the GCE/CFO-CNFs in 100 μM SPAR. The ability of the GCE/CFO-CNFs to detect SPAR was monitored daily. The data obtained are presented in Fig. 7.12 (c), while the corresponding DPVs are shown in Fig. 7.12 (d). There is a slight decrease in the peak current over the first four days, but very good stability is seen for the remaining six days. The RSD between the first and tenth day is 8.0 %, indicating acceptable overall stability. The reproducibility of the sensor was evaluated in 100 μM SPAR using ten freshly prepared sensors. The average peak current was 11.46 μA, with the RSD at 2.17 %, indicating excellent reproducibility.

**Table 7.4** Comparison table of different analysis samples for SPAR.

| **Samples** | | **Added Drug SPAR (μM)** | **Recovery (%)** | **%RSD** |
|---|---|---|---|---|
| Water analysis | Tap water | 30 | 92.5 | 4.4 |
| | | 50 | 95.7 | 2.8 |
| | | 100 | 98.8 | 1.4 |
| | Canal/River water | 30 | 90.4 | 8.1 |
| | | 50 | 94.5 | 4.9 |
| | | 100 | 96.2 | 2.3 |
| Biological analysis | Artificial Urine | 30 | 91.4 | 5.8 |
| | | 50 | 95.6 | 3.0 |
| | | 100 | 96.8 | 1.8 |

Clearly, the GCE/CFO-CNFs composite has an impressive sensitivity and LOD, as shown in Table 7.4, for the electrochemical detection of SPAR, at the optimal conditions

of a near neutral pH followed by a short accumulation period of 15 min, where the SPAR molecules are adsorbed onto the sensor. Under these conditions, electrostatic interactions between the GCE/CFO-CNFs and SPAR are optimal, favouring the adsorption and oxidation of SPAR. Moreover, these electrostatic interactions coupled with the adsorption of SPAR are beneficial in the selectivity studies, ensuring that the SPAR can be detected with little interference from other ions or molecules.

## 7.4. Conclusions

This chapter establishes two low-cost electrochemical sensors for SPAR. The first is based on CFO via a co-precipitation method, where CFO and CNFs form a uniform GCE/CFO-CNFs. Another carbon cloth was fabricated by CFO with $CeO_2$ and a binder on a porous substrate.

The novelty is twofold: (i) the CFO-CNFs hybrid interface Ce/Fe redox couples together with CNFs to detect lower concentration of SPAR, and (ii) the work demonstrates a high-surface-area carbon-cloth format as a practical alternative to conventional electrodes for antibiotic sensing. Electrochemical characterisation confirms a substantial conductivity improvement and a large increase in electroactive area relative to bare GCE.

Under near-neutral pH, GCE/CFO-CNFs achieves wide linearity with an LOD of 49 nM, while CC/CFO-$CeO_2$ further reduces the LOD to 14 nM and delivers high sensitivities across dual dynamic ranges. These analytical figures compare very favourably with prior SPAR sensors, with the CC format providing the lowest LOD reported. Selectivity is retained against common ions and different drugs, and satisfactory recoveries are achieved in tap water, canal water, and artificial urine.

This work answers whether coupling a CFO with CNFs or $CeO_2$ on GCE or CC can produce a method capable of sensitive and transferable SPAR detection in complex real matrices using simple methods. This combination of materials, involving the elements Fe, Ce, and C, and a simple synthesis, is not only environmentally acceptable and sustainable but also cost-effective. This study also highlights that carbon cloth can serve as a substrate for electrochemical sensing.

# References

[1] R. Hill, G. D. Stentiford, D. I. Walker, C. Baker-Austin, G. Ward, B. H. Maskrey, R. van Aerle, D. Verner-Jeffreys, E. Peeler, and D. Bass, "Realising a global One Health disease surveillance approach: insights from wastewater and beyond," *Nature Communications*, vol. 15, no. 1, p. 5324, Jun. 2024, doi: 10.1038/s41467-024-49417-4.

[2] A. Shahat, Md. R. Awual, Md. A. Khaleque, Md. Z. Alam, Mu. Naushad, and A. M. S. Chowdhury, "Large-pore diameter nano-adsorbent and its application for rapid lead(II) detection and removal from aqueous media," *Chemical Engineering Journal*, vol. 273, pp. 286–295, Apr. 2015, doi: 10.1016/j.cej.2015.03.073.

[3] Md. R. Awual, Md. M. Hasan, M. M. Rahman, and A. M. Asiri, "Novel composite material for selective copper(II) detection and removal from aqueous media," *Journal of Molecular Liquids*, vol. 283, pp. 772–780, Mar. 2019, doi: 10.1016/j.molliq.2019.03.141.

[4] K. T. Kubra, Md. S. Salman, H. Znad, and Md. N. Hasan, "Efficient encapsulation of toxic dye from wastewater using biodegradable polymeric adsorbent," *Journal of Molecular Liquids*, vol. 329, p. 115541, Feb. 2021, doi: 10.1016/j.molliq.2021.115541.

[5] M. A. Makary, K. Kaczmarski, and K. Nachman, "A call for doctors to recommend antibiotic-free foods: agricultural antibiotics and the public health crisis of antimicrobial resistance," *The Journal of Antibiotics*, vol. 71, no. 8, pp. 685–687, May 2018, doi: 10.1038/s41429-018-0062-y.

[6] A. Sengar and A. Vijayanandan, "Human health and ecological risk assessment of 98 pharmaceuticals and personal care products (PPCPs) detected in Indian surface and wastewaters," *The Science of the Total Environment*, vol. 807, no. Pt 1, p. 150677, Sep. 2021, doi: 10.1016/j.scitotenv.2021.150677.

[7] N. Ranjan, P. K. Singh, and N. S. Maurya, "Pharmaceuticals in water as emerging pollutants for river health: A critical review under Indian conditions," *Ecotoxicology and Environmental Safety*, vol. 247, p. 114220, Nov. 2022, doi: 10.1016/j.ecoenv.2022.114220.

[8] X. Zhou, G. J. P. Cuasquer, Z. Li, H. P. Mang, and Y. Lv, "Occurrence of typical antibiotics, representative antibiotic-resistant bacteria, and genes in fresh and stored source-separated human urine," *Environment International*, vol. 146, p. 106280, Dec. 2020, doi: 10.1016/j.envint.2020.106280.

[9] M. Ashfaq, K. N. Khan, M. S. U. Rehman, G. Mustafa, M. F. Nazar, Q. Sun, J. Iqbal, S. I. Mulla, and C.-P. Yu, "Ecological risk assessment of pharmaceuticals in the receiving environment of pharmaceutical wastewater in Pakistan," *Ecotoxicology and Environmental Safety*, vol. 136, pp. 31–39, Nov. 2016, doi: 10.1016/j.ecoenv.2016.10.029.

[10] Y. Xiao, H. Chang, A. Jia, and J. Hu, "Trace analysis of quinolone and fluoroquinolone antibiotics from wastewaters by liquid chromatography–electrospray tandem mass spectrometry," *Journal of Chromatography A*, vol. 1214, no. 1–2, pp. 100–108, Nov. 2008, doi: 10.1016/j.chroma.2008.10.090.

[11] S. Sa-Nguanprang, A. Phuruangrat, and O. Bunkoed, “Fluorescent probe of quantum dots and zinc oxide in a highly selective polymer simultaneously determined florfenicol and sparfloxacin,” *Microchimica Acta*, vol. 190, no. 4, p. 129, Mar. 2023, doi: 10.1007/s00604-023-05704-3.

[12] N. Chansud, R. Kaewnok, P. Nurerk, F. Davis, and O. Bunkoed, “Ultrasensitive and highly selective fluorescence probe of nitrogen-doped graphene quantum dots and zinc oxide decorated carbon foam incorporated molecularly imprinted polymer for trace sparfloxacin determination,” *Materials Today Communications*, vol. 35, p. 105687, Feb. 2023, doi: 10.1016/j.mtcomm.2023.105687.

[13] G. Collins, T. N. Barwa, L. Glennon, P. R. Kasturi, and C. B. Breslin, “Corrosion of nickel foam electrodes during hydrothermal reactions: The influence of a simple protective carbon black coating,” *Electrochemistry Communications*, vol. 169, p. 107835, Nov. 2024, doi: 10.1016/j.elecom.2024.107835.

[14] T. N. Barwa, L. Glennon, D. Alves, Y. Lou, E. Dempsey, and C. B. Bres lin, “Simple dispersion of carbon nanofibers in a naturally occurring polyp henol in water and their electrochemical characteristics,” *Electrochemistry Communications*, vol. 163, p. 107727, Apr. 2024, doi: 10.1016/j.elecom.202 4.107727.

[15] Y. Guo, X. Chen, W. Ma, and X. Zhao, “$CeFe_2O_4$ Nanoparticle/Graphene Oxide Composites with Synergistic Superhydrophobicity and Microwave Absorption,” *ACS Applied Nano Materials*, vol. 5, no. 5, pp. 6513–6522, Apr. 2022, doi: 10.1021/acsanm.2c00546.

[16] D. Zheng, X. Yue, Z. Wang, S. Fan, Z. Zhang, W. Dai, and X. Fu, “Investigation into the photothermal catalytic $CO_2$ decomposition over $CeO_2$ with different morphologies: Behaviors of oxygen vacancies,” *Separation and Purification Technology*, vol. 350, p. 127973, May 2024, doi: 10.1016/j.seppur.2024.127973.

[17] Y. Zheng, K. Li, H. Wang, D. Tian, Y. Wang, X. Zhu, Y. Wei, M. Zheng, and Y. Luo, “Designed oxygen carriers from macroporous $LaFeO_3$ supported $CeO_2$ for chemical-looping reforming of methane,” *Applied Catalysis B: Environmental*, vol. 202, pp. 51–63, Aug. 2016, doi: 10.1016/j.apcatb.2016.08.024.

[18] C. Zhang, S. Wei, Y. Hu, H. Tang, J. Gao, Z. Yin, and Q. Guan, “Selective adsorption of tannic acid on calcite and implications for separation of fluorite minerals,” *Journal of Colloid and Interface Science*, vol. 512, pp. 55–63, Oct. 2017, doi: 10.1016/j.jcis.2017.10.043.

[19] E. Yu. Pikalova, V. I. Maragou, A. N. Demina, A. K. Demin, and P. E. Tsiakaras, “The effect of co-dopant addition on the properties of $Ln_{0.2}Ce_{0.8}O_2{-}\delta$ (Ln=Gd, Sm, La) solid-state electrolyte,” *Journal of Power Sources*, vol. 181, no. 2, pp. 199–206, Feb. 2008, doi: 10.1016/j.jpowsour.2008.02.003.

[20] V. A. Sadykov, L. A. Isupova, S. V. Tsybulya, S. V. Cherepanova, G. S. Litvak, E. B. Burgina, G. N. Kustova, V. N. Kolomiichuk, V. P. Ivanov, E. A. Paukshtis, A. V Golovin, and E. G. Avvakumov, “Effect of Mechanical Activation on the Real Structure and Reactivity of Iron (III) Oxide with Corundum-Type Structure,” *Journal of Solid State Chemistry*, vol. 123, no. 2, pp. 191–202, May 1996, doi: 10.1006/jssc.1996.0168.

[21] Y. Ma, Y. Ma, G. Giuli, H. Euchner, A. Groß, G. O. Lepore, F. d'Acapito, D. Geiger, J. Biskupek, and U. Kaiser, "Introducing highly Redox-Active atomic centers into Insertion-Type electrodes for Lithium-Ion batteries," *Advanced Energy Materials*, 2020, doi: 10.1002/aenm.202000783.

[22] N. Zulhadjri, Y. E. Putri, N. Mufti, V. Saraswaty, and S. Sufian, "La3+ doped ZnFe2O4 synthesized via green chemistry approach using Uncaria gambir Roxb: A study on structural, optical, magnetic, and photocatalytic properties," Journal of *Photochemistry and Photobiology a Chemistry*, vol. 461, p. 116168, Nov. 2024, doi: 10.1016/j.jphotochem.2024.116168.

[23] M. Akhter, Md. K. Amin, P. K. Dhar, S. K. Dey, M. S. Hossain, and S. K. Dutta, "Fabrication of rare-earth cerium-doped nickel–copper ferrite as a promising photo-catalyst for congo red-containing wastewater treatment," *RSC Advances*, vol. 14, no. 40, pp. 29083–29098, Jan. 2024, doi: 10.1039/d4ra04334k.

[24] Y. Luo, T. N. Barwa, E. Dempsey, R. Karthik, J. J. Shim, R. Sukanya, and C. B. Breslin, "Electrochemical detection of sulfanilamide using tannic acid exfoliated MoS2 nanosheets combined with reduced graphene oxide/graphite," *Environmental Research*, vol. 248, p. 118391, Feb. 2024, doi: 10.1016/j.envres.2024.118391.

[25] H. Guo, X. Wang, H. Li, M. Liu, L. Xing, and H. Zhai, "$AFe_2O_4$ (A=Cu, Ni, Co, Mg, Ce, Mn) Catalysts for Hydrogen-Rich Syngas Production from Corn Straw Pyrolysis-Catalytic Steam Reforming," *Energy Technology*, vol. 13, no. 1, Oct. 2024, doi: 10.1002/ente.202401302.

[26] Z. K. Heiba, M. B. Mohamed, and S. I. Ahmed, "Modifying the structure and optical characteristics of $ZnMn_2O_4$ by alloying with CdS to form heterostructure nanocomposite," *Applied Physics A*, vol. 127, no. 11, Nov. 2021, doi: 10.1007/s00339-021-05021-7.

[27] K. Madi, F. Agueniou, D. Chebli, H. Tahraoui, A. Bouguettoucha, J. Zhan g, and A. Amrane, "Polyaniline-modified iron and copper Co-doped cerium oxide nanocomposites for enhanced photocatalytic degradation of methylen e blue: Synthesis, and characterization," *Colloids and Surfaces a Physicoch emical and Engineering Aspects*, vol. 712, p. 136469, Feb. 2025, doi: 10.1 016/j.colsurfa.2025.136469.

[28] M. Rajabinezhad, M. S. Abbasi, F. H. Laybidi, M. SharifianJazi, M. Khodaei, and A. Bahrami, "Structural, mechanical and biomedical properties of 3D-printed Cu-doped $Fe_3O_4$/58S bioactive glass/polycaprolactone composite scaffold for bone tissue regeneration," *Bioprinting*, vol. 47, p. e00400, Feb. 2025, doi: 10.1016/j.bprint.2025.e00400.

[29] M. G. Trachioti, A. Ch. Lazanas, and M. I. Prodromidis, "Shedding light on the calculation of electrode electroactive area and heterogeneous electron transfer rate constants at graphite screen-printed electrodes," *Microchimica Acta*, vol. 190, no. 7, p. 251, Jun. 2023, doi: 10.1007/s00604-023-05832-w.

[30] Y. Zhou, S. Cao, C. Xi, X. Li, L. Zhang, G. Wang, and Z. Chen, "A no vel $Fe_3O_4$/graphene oxide/citrus peel-derived bio-char based nanocomposite with enhanced adsorption affinity and sensitivity of ciprofloxacin and sparf

loxacin," *Bioresource Technology*, vol. 292, p. 121951, Aug. 2019, doi: 10.1016/j.biortech.2019.121951.

[31] A. Ivanets, V. Prozorovich, M. Roshchina, T. Kouznetsova, N. Budeiko, L. Kulbitskaya, A. Hosseini-Bandegharaei, V. Masindi, and V. Pankov, "A comparative study on the synthesis of magnesium ferrite for the adsorption of metal ions: Insights into the essential role of crystallite size and surface hydroxyl groups," *Chemical Engineering Journal*, vol. 411, p. 128523, Jan. 2021, doi: 10.1016/j.cej.2021.128523.

[32] K. Rudnicki, K. Sipa, M. Brycht, P. Borgul, S. Skrzypek, and L. Poltorak, "Electrochemical sensing of fluoroquinolone antibiotics," *TrAC Trends in Analytical Chemistry*, vol. 128, p. 115907, May 2020, doi: 10.1016/j.trac.2020.115907.

[33] R. Karthik, K. Balamurugan, S.-M. Chen, R. Sukanya, P. R. Chavan, V. Q. Nguyen, J.-J. Shim, and C. B. Breslin, "Investigation of the electrocatalytic activity of bismuth-substituted pyrochlore $Y_2Sn_2O_7$ for the voltammetry determination of the antipsychotic drug," *Materials Today Chemistry*, vol. 26, p. 101117, Aug. 2022, doi: 10.1016/j.mtchem.2022.101117.

# Chapter 8 Conclusions and Future Work

## 8.1. General Conclusions

Electrochemical sensors based on TMDs, carbon materials, spinel-like oxides, and combinations of these materials were fabricated. The materials were characterised in detail using a combination of electrochemical and surface analytical techniques. Parameters such as the electrochemical surface area of the fabricated sensor and the impedance response for conductivity analysis were measured. In addition, scan rate studies were performed to determine whether the analyte detection was under diffusion or adsorption control. In the electroanalytical studies, the limit of detection (LOD), sensitivity, and selectivity were evaluated, while the performance of the sensor was further studied in real water samples, using spiking and recovery studies.

In ***Chapter 3***, the electrochemical detection of Metronidazole (MTZ) is described by comparing exfoliated $MoS_2$ sheets and electrodeposited amorphous $MoS_x$. While the MTZ was reduced at both modified surfaces, the GCE/$MoS_2$ was superior, and this was attributed to a higher surface area, a lower charge-transfer resistance and to the presence of edges, and defects in the sheets that facilitate the electron-transfer reaction. Using differential pulse voltammetry, impressive linear calibration curves were obtained for GCE/$MoS_2$ extending from 1.9 to 2000 μM and from 40 to 1990 nM at the lower concentrations. A high sensitivity of 13.32 μA $\mu M^{-1}$ $cm^{-2}$ and a LOD value of 4.3 nM were obtained using the lower concentration linear range. Good selectivity was achieved in the presence of interferents typically found in aquatic environments, with acceptable repeatability, good stability over a 7-day period, and good recovery (88.7 ± 3.9%) in water samples taken from a river.

In ***Chapter 4***, the electrochemical detection of Sulfonamide (SFD) using tannic acid exfoliated $MoS_2$ nanosheets combined with reduced graphene oxide/graphite is reported. A mixture of rGO/G was superior to pure rGO in formulating the sensor. The

fabricated sensor exhibited an extended linear range from 0.1 to 566 μM, with a LOD of 86 nM, with good selectivity in the presence of various salts found in water and structurally related drugs from the sulfonamide family. The sensor showed very good reproducibility with the RSD at 0.48 %, repeatability and acceptable long term stability over a 10-day period. Good recovery from both tap and river water was achieved, with recovery ranging from 90.4 to 98.9 % for tap water and from 83.5 to 94.4 % for real river water samples.

In ***Chapter 5***, the detection of Flutamide (FLD) using a composite comprising green synthesis carbon particles (CPs) from kiwi fruit and the $WS_2$ platelets is described. The CPs had an average diameter of 500 nm and contained surface hydroxyl and carbonyl groups. These groups may help anchor the CPs onto the $WS_2$ platelets, resulting in the formation of a CPs-$WS_2$ nanocomposite with a high surface area and a conducting network, enabling electron transfer. Using the CPs-$WS_2$ composite supported at a glassy carbon electrode, a linear concentration range extending from 1 nM to 104 μM, a limit of detection of 0.74 nM, and a sensitivity of 26.9 ± 0.7 μA $\mu M^{-1}$ $cm^{-2}$ were obtained in the detection of flutamide in a phosphate buffer. The sensor showed good recovery, ranging from 88.47 to 95.02%, in river water samples, and exhibited very good selectivity in the presence of inorganic ions, including $Al^{3+}$, $Co^{2+}$, $Cu^{2+}$, $Fe^{3+}$, $Zn^{2+}$, $NO^{3-}$, $SO_4^{2-}$, $CO_3^{2-}$, and $Cl^-$.

In ***Chapter 6***, the $WS_2$ sheets were exfoliated in sodium cholate and dispersed onto the $CeO_2$-coated ZMO to enhance its conducting properties. When ZMO combines with $CeO_2$, the $CeO_2$ appears to be sprinkled over the sphere-like morphology ZMO surface, forming a powdery coating. This highly effective material was then employed to detect Sulfamerazine (SRZ). Linear concentration plots were obtained extending from 18 nM to 1.2 μM, and between 1.2 and 300 μM, with a linear regression equation, $I_p$ (μA) = 4.86 C (μM) + 1.13, for the lower sulfamerazine concentrations. Using the estimated surface area of 0.168 $cm^2$, the sensitivity at the lower concentrations was determined as 28.9 μA $\mu M^{-1}$ $cm^{-2}$, with an LOD of 13.8 nM. Very good selectivity was achieved in

the presence of other antimicrobial drugs and inorganic ions, commonly found in water. On spiking real water samples, good recoveries were seen, varying from 89.5 to 98.7 %.

In ***Chapter 7***, a $CeFe_2O_4$ spinel was combined with $CeO_2$ to give a new composite material (CFO), the CFO was synthesis by using co-precipitation method, which was then supported by carbon nanofibers (CNFs). This CFO-CNFs composite facilitated the selective and sensitive electrochemical detection of sparfloxacin, a third-generation fluoroquinolone. A linear concentration range extending from 0.06 to 240 μM with a limit of detection of 49.0 nM and a sensitivity of 0.524 μA $\mu M^{-1}$ $cm^{-2}$ were observed. Excellent selectivity in the presence of various inorganic ions, commonly found in aquatic systems, was achieved, while good recovery (90.4-96.2 %) from real water samples was also evident. Interestingly, this immobilised catalyst at carbon cloth also facilitated the electrochemical detection of sparfloxacin, with an impressive LOD of 14.0 nM.

In this thesis, these findings advance the state of the art not only through competitive analytical figures of merit, but also through a coherent structure–interface–performance design framework, the use of simplified and partially sustainable material-processing routes, and successful translation to deployable electrode platforms. CPs-$WS_2$ composites (Chapter 5) give the best result targeted FLD, and $CeO_2$-stabilised $ZnMn_2O_4/WS_2$ (Chapter 6), and $CeFe_2O_4$-based composite on both GCE and carbon cloth (Chapter 7) show great improvements in sensitivity, selectivity, stability for SRZ and SPAR determination. But for exfoliated $MoS_2$ (Chapter 3), tannic-acid-exfoliated $MoS_2$ integrated with an rGO/graphite scaffold (Chapter 4), I hope to have the opportunity to conduct more in-depth research and analysis in future studies and experiments, to gather more data and achieve better results.

## 8.2. Future Work

As detailed above in Section 8.1, electrochemical sensors have been developed for five waterborne antibiotics, demonstrating impressive stability, selectivity, and sensitivity. The next step is to test these sensors with other analytes and in more complex media, such as wastewater and seawater. Such studies would reveal the full potential of 2D TMDs, spinel oxides, and carbon-based materials employed. Real water systems contain many more inorganic and organic species. It is therefore essential to examine competitive and synergistic effects between 2D TMDs and/or spinels-based composites combined with carbon, and their interactions with diverse pollutants in natural aquatic environments.

Morphology is likely to be a key factor. The type of carbon, such as graphene, whether flakes, graphene oxide, reduced graphene oxide, or graphene quantum dots, may significantly influence performance and warrants a systematic study. Additionally, it would be interesting to combine the 2D TMDs and spinel composites with other non-carbon-based 2D materials, such as 2D borophene sheets and borophene dots. This would enable a more detailed investigation of the composite morphology.

For real-time sensing, carbon cloth electrodes and other printed formats, such as screen-printed electrodes, are practical choices for on-site water analysis. Carbon cloth was introduced in Chapter 7. While sensors are promising for detecting antibiotic residues, meeting drinking-water standards will need additional progress: (1) develop sensor materials that remain stable and highly sensitive in complex matrices and (2) create catalytic materials that can adsorb and degrade pollutants, including antibiotics and heavy metals, through advanced oxidation processes (AOP). Electrochemical sensing technology is particularly valuable for monitoring antibiotic contamination in environmental waters. However, a significant advancement would be the integration of drug detection with in situ removal capabilities, allowing targeted antibiotics to be both

identified and eliminated from aquatic environments during sensing operations.

While electrochemical sensing has real value for environmental monitoring of antibiotic pollution in water systems, combining sensing with drug removal would significantly advance this field. This would mean that the targeted drugs could not only be detected but also removed from the aquatic environment when found.

# List of Publication

## *Publications related to this thesis:*

[1] ***Y. Luo***, T. N. Barwa, K. Herdman, E. Dempsey, and C. B. Breslin, "Electroanalysis of metronidazole using exfoliated $MoS_2$ sheets and electrodeposited amorphous $MoS_x$," Electrochim Acta, vol. 462, p. 142778, Sep. 2023, doi: 10.1016/j.electacta.2023.142778.

[2] ***Y. Luo***, T. N. Barwa, E. Dempsey, R. Karthik, J. J. Shim, R. Sukanya, and C. B. Breslin, "Electrochemical detection of sulfanilamide using tannic acid exfoliated $MoS_2$ nanosheets combined with reduced graphene oxide/graphite," Environ Res, vol. 248, p. 118391, 2024, doi:10.1016/j.envres.2024.118391.

[3] ***Y. Luo***, P. R. Kasturi, T. N. Barwa, E. Dempsey, and C. B. Breslin, "Amplifying Flutamide Sensing through the Synergetic Combination of Actinidia-Derived Carbon Particles and $WS_2$ Platelets," ACS Omega, vol. 9, no. 27, pp. 29598–29608, Jun. 2024, doi: 10.1021/acsomega.4c02795.

[4] ***Y. Luo***, P. R. Kasturi, D. Alves, T. N. Barwa, E. Dempsey, and C. B. Breslin, "Electrochemical detection of sulfamerazine with $ZnMn_2O_4$ spinel spheres decorated with $CeO_2$ nano powders and $WS_2$ sheets," Mater Today Chem, vol. 44, p. 102554, 2025, doi:10.1016/j.mtchem.2025.102554.

[5] ***Y. Luo***, D. Alves, T. N. Barwa, E. Dempsey, and C. B. Breslin, "A $CeFe_2O_4$-$CeO_2$ composite for the electrochemical detection and advanced oxidation of the antibiotic Sparfloxacin," J Environ Manage, vol. 380, p. 125167, Apr. 2025, doi: 10.1016/j.jenvman.2025.125167.

## *Collaborative publications:*

[6] R. Sukanya, T. Barwa, ***Y. Luo***, E. Dempsey, and C. B. Breslin, "Emerging Layered Materials and Their Applications in the Corrosion Protection of Metals and Alloys," Sustainability, vol. 14, no. 7, p. 4079, Mar. 2022, doi: 10.3390/su14074079.

[7] P. R. Kasturi, ***Y. Luo***, T. Barwa, D. Alves, and C. B. Breslin, "Carbon dots–A deep dive into their electrochemical applications," Comprehensive Analytical Chemistry 108, 136-160, 2024.

[8] T. Barwa, D. Alves, ***Y. Luo***, E. Dempsey, and C. B. Breslin, "A $WS_2$/CNF Nanocomposite for Electrochemical Sensing Applications," ECS Transactions 113 (12), 11, 2024.

[9] T. Barwa, L. Glennon, D. Alves, ***Y. Luo***, E. Dempsey, and C. B. Breslin, "Simple dispersion of carbon nanofibers in a naturally occurring polyphenol in water and their electrochemical characteristics," Electrochem commun, vol. 163, p. 107727, Jun. 2024, doi: 10.1016/j.elecom.2024.107727.

[10] T. Barwa, R. Sukanya, T. Kanagaraj, G. Collins, ***Y. Luo***, E. Dempsey, and C. B. Breslin, "A Nickel Telluride Electrochemical Sensor for the Detection of the Antibiotic Ronidazole," ACS Appl Nano Mater, Oct. 2025, doi: 10.1021/acsanm.5c03794.

[11] T. Barwa, D. Alves, ***Y. Luo***, E. Dempsey, R. Sukanya, R. Karthik and C. B. Breslin, "Enhanced electroanalysis of ornidazole with a CNF/$WO_3$/$WS_2$ multi functional composite," Electrochim Acta, 4:147722, 2025 Nov. doi: 10.1016/j.electacta.2025.147722.

# List of Conferences

1. The 73rd Universities Chemistry Research Colloquium (15th-16th June, 2022, University College Dublin)
2. The Chemistry Research Day 2022 (21st September, 2022, Maynooth University)
3. RSC / ISE Early Career Researcher Symposium on Electrochemistry (04th Nov, 2022, Queen's University Belfast)
4. The 74th Universities Chemistry Research Colloquium (14th-15th June, 2023, University of Galway)
5. RCS Electrochem 2023 (10th-12th September, 2023, University of Bristol)
6. The Chemistry Research Day 2023 (24th September, 2023, Maynooth University)
7. The 75th Universities Chemistry Research Colloquium (17th-18th June, 2024, Trinity College Dublin)
8. The 9th EuChemS Chemistry Congress (ECC9) (7th-11th July, 2024, the Convention Centre Dublin)
9. RCS Electrochem 2024 (11st-13rd September, 2024, Manchester Metropolitan University)
10. The Electrochemical Society (ECS) PRiME 2024 (6th-11th October, 2024, Honolulu, Hawaii Convention Center)
11. The Chemistry Research Day 2024 (18th September, 2024, Maynooth University)
12. RSC / ISE Early Career Researcher Symposium on Electrochemistry (30th January, 2025, Maynooth University)
13. The 76th Universities Chemistry Research Colloquium (16th-17th June, 2025, Maynooth University)